2009

Experimental and Numerical Assessments of Injury Criteria for Short-Duration, High-Force Impact Loading of the Tibia

Cheryl Elizabeth Quenneville

EXPERIMENTAL AND NUMERICAL ASSESSMENTS OF INJURY CRITERIA FOR SHORT-DURATION, HIGH-FORCE IMPACT LOADING OF THE TIBIA

(SPINE TITLE: INJURY CRITERIA FOR SHORT-DURATION HIGH-FORCE TIBIAL IMPACTS)

(Thesis format: Integrated-Article)

by

Cheryl Elizabeth Quenneville

Graduate Program in Engineering Science
Department of Mechanical and Materials Engineering

A thesis submitted in partial fulfillment
of the requirements for the degree of
Doctor of Philosophy

The School of Graduate and Postdoctoral Studies
The University of Western Ontario
London, Ontario, Canada
December, 2009

ABSTRACT

Short-duration, high-force loading of the lower leg occurs during a variety of events, including indirect (*i.e.,* in-vehicle) contact with landmines. To date, the majority of research on impact loading of the lower extremities has been conducted by the car crash industry. From this, the current standard for designing protective measures for high-impulse scenarios has been selected - a maximum axial load of 5.4 kN measured in an Anthropomorphic Test Device (ATD). This force value, however, gives no indication of the load duration or injury severity. Furthermore, its applicability to high-impulse situations, with higher forces over shorter durations, is not known. The overall objective of this thesis was to investigate the appropriateness of this value for short-duration impulsive loading of the tibia (*i.e.,* lower leg bone) using both cadaveric specimens and test surrogates. Surrogates that were considered for injury prediction were synthetic bones, ATDs, and finite element models.

Experimental testing was accomplished through the development of a pneumatic testing apparatus capable of applying axial loads to test specimens over a large range of magnitudes and velocities. This apparatus was validated to replicate the loading caused by anti-vehicular mine blasts, and was initially used to conduct load-to-failure tests on cadaveric tibias. A new injury criterion was proposed, with a higher force limit (7.9 kN) and inclusion of kinetic energy as a fracture risk factor. Synthetic composite bones were similarly tested, but demonstrated lower impact tolerance and non-biofidelic fracture patterns compared to cadavers. Critical load values from ATDs (12.6 kN) were determined which correspond to injury levels from the cadaveric tests.

To allow computer simulations of survivability analyses, a finite element model of a representative cadaveric specimen was developed using TrueGrid® and LS-Dyna® softwares. The model was evaluated by comparing to experimental results, with refinements to best represent the experimental axial load, load duration, and strains for both non-fracture and fracture scenarios.

Through experimental testing and development of a finite element model, this thesis investigated the injury criteria for tibias exposed to short-duration, high-force axial loading. Overall, this research will contribute to improved standards for better protection of occupants from lower leg injuries.

Keywords: tibia, impulse loading, impact test apparatus, lower limb, anthropomorphic test device, injury criteria, composite bone, fracture, test surrogate, anatomical finite element model, bone material properties, strain gauge analysis, *in-vitro* biomechanical testing.

CO-AUTHORSHIP

Each study in this thesis was a collaborative effort which could not have been completed without the assistance of others. The contributions that each individual made are detailed below.

CHAPTER 1: Cheryl Quenneville – wrote manuscript; Cynthia Dunning – reviewed manuscript.

CHAPTER 2: Cheryl Quenneville – study design, wrote manuscript; Gillian Fraser – study design; Cynthia Dunning – study design, reviewed manuscript.

CHAPTER 3: Cheryl Quenneville – study design, data collection and analysis, wrote manuscript; Gillian Fraser – study design; Stewart McLachlin – data collection; Cynthia Dunning – study design, reviewed manuscript.

CHAPTER 4: Cheryl Quenneville – study design, data collection and analysis, wrote manuscript; Gillian Fraser – study design; Cynthia Dunning – study design, reviewed manuscript.

CHAPTER 5: Cheryl Quenneville – study design, data analysis, wrote manuscript; Cynthia Dunning – study design, reviewed manuscript.

CHAPTER 6: Cheryl Quenneville – study design, data analysis, wrote manuscript; Cynthia Dunning – study design, reviewed manuscript.

CHAPTER 7: Cheryl Quenneville – wrote manuscript; Cynthia Dunning – reviewed manuscript.

ACKNOWLEDGEMENTS

I would like to begin by thanking my supervisor, Dr. Cynthia Dunning. You have been an exceptional advisor and mentor, and I am privileged to have worked with you and to know you. I truly appreciate your encouragement, especially through the setbacks (and there have been a couple!). You have made my graduate school experience a wonderful one – thank you.

I would also like to thank the people with whom I have had the opportunity to work through this project: Mr. Patrick Gallagher for the overall study conception; Mr. Clayton Cook and the members of the University Machine Services for help with the many iterations of the apparatus; Mr. Eugen Porter from the Electronics Shop for instrumentation assistance; Miranda Restorick for her project designing the bracket for the ATD; Marley Winfield for her assistance testing synthetic bones; and Dr. James Johnson and Dr. Thomas Jenkyn, members of my advisory committee, for their support. Your contributions to this work are greatly appreciated.

A big thank you to the members of the Jack McBain Biomechanical Testing Laboratory, past and present, who have made this experience so enjoyable: Angela, Stew, Yara, Mark, Becky, Brendon, Vega, Sarah, and Pencilla. It's been a blast! Special thanks to Stew McLachlin for his help through the frustrations of the experimental testing with the 'quirky' apparatus.

This project was conducted in an industrial partnership with General Dynamics Land Systems – Canada, and I would like to thank them for their financial support and expertise in this field. The contributions of Ms. Gillian Fraser and Mr. Brendon Beaton to this project were especially invaluable.

I would like to thank the Natural Sciences and Engineering Research Council of Canada, the Ontario Graduate Scholarships in Science and Technology, and the University of Western Ontario for the scholarship funding, which have allowed me to pursue this research which I have enjoyed so much.

Finally, I would like to thank my family for their never-ending support. To my parents, for their love and encouragement to pursue my dreams (yes, I will get a real job some day!), and my brother Scott for inspiring and pushing me – thank you. Gilles, thank you for being my number one supporter and best friend – I love you very much. You have all made this possible.

TABLE OF CONTENTS

LIST OF TABLES

LIST OF FIGURES

EXPERIMENTAL AND NUMERICAL ASSESSMENTS OF INJURY CRITERIA FOR SHORT-DURATION, HIGH-FORCE IMPACT LOADING OF THE TIBIA

(SPINE TITLE: INJURY CRITERIA FOR SHORT-DURATION HIGH-FORCE TIBIAL IMPACTS)

(Thesis format: Integrated-Article)

by

Cheryl Elizabeth Quenneville

Graduate Program in Engineering Science
Department of Mechanical and Materials Engineering

A thesis submitted in partial fulfillment
of the requirements for the degree of
Doctor of Philosophy

The School of Graduate and Postdoctoral Studies
The University of Western Ontario
London, Ontario, Canada
December, 2009

ABSTRACT

Short-duration, high-force loading of the lower leg occurs during a variety of events, including indirect (*i.e.,* in-vehicle) contact with landmines. To date, the majority of research on impact loading of the lower extremities has been conducted by the car crash industry. From this, the current standard for designing protective measures for high-impulse scenarios has been selected - a maximum axial load of 5.4 kN measured in an Anthropomorphic Test Device (ATD). This force value, however, gives no indication of the load duration or injury severity. Furthermore, its applicability to high-impulse situations, with higher forces over shorter durations, is not known. The overall objective of this thesis was to investigate the appropriateness of this value for short-duration impulsive loading of the tibia (*i.e.,* lower leg bone) using both cadaveric specimens and test surrogates. Surrogates that were considered for injury prediction were synthetic bones, ATDs, and finite element models.

Experimental testing was accomplished through the development of a pneumatic testing apparatus capable of applying axial loads to test specimens over a large range of magnitudes and velocities. This apparatus was validated to replicate the loading caused by anti-vehicular mine blasts, and was initially used to conduct load-to-failure tests on cadaveric tibias. A new injury criterion was proposed, with a higher force limit (7.9 kN) and inclusion of kinetic energy as a fracture risk factor. Synthetic composite bones were similarly tested, but demonstrated lower impact tolerance and non-biofidelic fracture patterns compared to cadavers. Critical load values from ATDs (12.6 kN) were determined which correspond to injury levels from the cadaveric tests.

To allow computer simulations of survivability analyses, a finite element model of a representative cadaveric specimen was developed using TrueGrid® and LS-Dyna® softwares. The model was evaluated by comparing to experimental results, with refinements to best represent the experimental axial load, load duration, and strains for both non-fracture and fracture scenarios.

Through experimental testing and development of a finite element model, this thesis investigated the injury criteria for tibias exposed to short-duration, high-force axial loading. Overall, this research will contribute to improved standards for better protection of occupants from lower leg injuries.

Keywords: tibia, impulse loading, impact test apparatus, lower limb, anthropomorphic test device, injury criteria, composite bone, fracture, test surrogate, anatomical finite element model, bone material properties, strain gauge analysis, *in-vitro* biomechanical testing.

CO-AUTHORSHIP

Each study in this thesis was a collaborative effort which could not have been completed without the assistance of others. The contributions that each individual made are detailed below.

CHAPTER 1: Cheryl Quenneville – wrote manuscript; Cynthia Dunning – reviewed manuscript.

CHAPTER 2: Cheryl Quenneville – study design, wrote manuscript; Gillian Fraser – study design; Cynthia Dunning – study design, reviewed manuscript.

CHAPTER 3: Cheryl Quenneville – study design, data collection and analysis, wrote manuscript; Gillian Fraser – study design; Stewart McLachlin – data collection; Cynthia Dunning – study design, reviewed manuscript.

CHAPTER 4: Cheryl Quenneville – study design, data collection and analysis, wrote manuscript; Gillian Fraser – study design; Cynthia Dunning – study design, reviewed manuscript.

CHAPTER 5: Cheryl Quenneville – study design, data analysis, wrote manuscript; Cynthia Dunning – study design, reviewed manuscript.

CHAPTER 6: Cheryl Quenneville – study design, data analysis, wrote manuscript; Cynthia Dunning – study design, reviewed manuscript.

CHAPTER 7: Cheryl Quenneville – wrote manuscript; Cynthia Dunning – reviewed manuscript.

ACKNOWLEDGEMENTS

I would like to begin by thanking my supervisor, Dr. Cynthia Dunning. You have been an exceptional advisor and mentor, and I am privileged to have worked with you and to know you. I truly appreciate your encouragement, especially through the setbacks (and there have been a couple!). You have made my graduate school experience a wonderful one – thank you.

I would also like to thank the people with whom I have had the opportunity to work through this project: Mr. Patrick Gallagher for the overall study conception; Mr. Clayton Cook and the members of the University Machine Services for help with the many iterations of the apparatus; Mr. Eugen Porter from the Electronics Shop for instrumentation assistance; Miranda Restorick for her project designing the bracket for the ATD; Marley Winfield for her assistance testing synthetic bones; and Dr. James Johnson and Dr. Thomas Jenkyn, members of my advisory committee, for their support. Your contributions to this work are greatly appreciated.

A big thank you to the members of the Jack McBain Biomechanical Testing Laboratory, past and present, who have made this experience so enjoyable: Angela, Stew, Yara, Mark, Becky, Brendon, Vega, Sarah, and Pencilla. It's been a blast! Special thanks to Stew McLachlin for his help through the frustrations of the experimental testing with the 'quirky' apparatus.

This project was conducted in an industrial partnership with General Dynamics Land Systems – Canada, and I would like to thank them for their financial support and expertise in this field. The contributions of Ms. Gillian Fraser and Mr. Brendon Beaton to this project were especially invaluable.

I would like to thank the Natural Sciences and Engineering Research Council of Canada, the Ontario Graduate Scholarships in Science and Technology, and the University of Western Ontario for the scholarship funding, which have allowed me to pursue this research which I have enjoyed so much.

Finally, I would like to thank my family for their never-ending support. To my parents, for their love and encouragement to pursue my dreams (yes, I will get a real job some day!), and my brother Scott for inspiring and pushing me – thank you. Gilles, thank you for being my number one supporter and best friend – I love you very much. You have all made this possible.

TABLE OF CONTENTS

LIST OF TABLES

LIST OF FIGURES

LIST OF APPENDICES

LIST OF ABBREVIATIONS, SYMBOLS, AND NOMENCLATURE

”	inch
°	degree
%	percent
2D	two-dimensional
3D	three-dimensional
α	level of significance
σ	stress
γ	shear strain
τ	shear stress
ε	strain
ρ	density
με	microstrain
μm	micrometer
υ	Poisson's ratio
A	age
AIS	Abbreviated Injury Scale
ANOVA	analysis of variance
AT	Achilles tension
AV	anti-vehicular
CAD	computer aided design
CLL	Complex Lower Leg
cm	centimeter
CT	Computed Tomography

DAQ	data acquisition system
DICOM	Digital Imaging and Communications in Medicine
E	elastic modulus
E_{tan}	tangent (plastic) modulus
F	force
F_c	critical force
f_c	cutoff frequency
FEA	finite element analysis
FSL	Frangible Surrogate Leg
FSLM	Frangible Surrogate Leg (Modified)
G	acceleration due to gravity
G	gender (in risk equation)
GPa	gigaPascal
HU	Hounsfield units
IARV	Injury Assessment Reference Values
IGES	Initial Graphics Exchange Specification
IR	infrared
J	Joule
kg	kilogram
KE	kinetic energy
kHz	kiloHertz
kN	kiloNewton
kVp	peak kilovoltage
LLth	Lower Leg Threshold
m	meter

mA	milliampere
M	moment
M_c	critical moment
mm	millimeter
ms	millisecond
MPa	megaPascal
N	Newton
NATO	North Atlantic Treaty Organization
NI	National Instruments
P	patched canal
P+, P-	power to a bridge circuit
PMMA	polymethyl-methacrylate
psi	pounds per square inch
PVC	polyvinyl chloride
R	loading rate
RTI	Revised Tibia Index
s	second
S+, S-	signal from a bridge circuit
STL	Stereolithography file format
TI	Tibia Index
TROSS	test rig for occupant safety system
txt	text file
V	volt
W	weight

CHAPTER 1 – Introduction

Overview: *Large energy pulses transferred through the floor from anti-vehicular (AV) landmine blasts can lead to debilitating injuries of the lower leg. Current protective standards are based on limits from car crash studies, whose type of loading has not been validated to be applicable to these scenarios. This introductory chapter details the bony anatomy of the lower leg and its vulnerability to in-vehicle AV mine blasts, surrogates that can be used to assess lower leg damage, impact injury limits that have been developed for the lower leg, and specific studies both experimental and finite element-based pertaining to the tolerance of the lower leg. It concludes with the study rationale, objectives, hypotheses, and a thesis overview.*[1]

1.1 THE LOWER LEG

The lower leg describes the region of the body below the knee, consisting of the shank (the region from the knee to the ankle joint) and the foot combined.

1.1.1 *BONY ANATOMY*

The two bones which make up the shank are the tibia and the fibula (Figure 1.1). The tibia is the larger of the two, and is the primary weight-bearing bone. The tibia articulates proximally with the femur of the thigh at the knee, and distally with the talus of the foot

[1] Due to the interdisciplinary nature of this work, a glossary of anatomical terms is included as Appendix A.

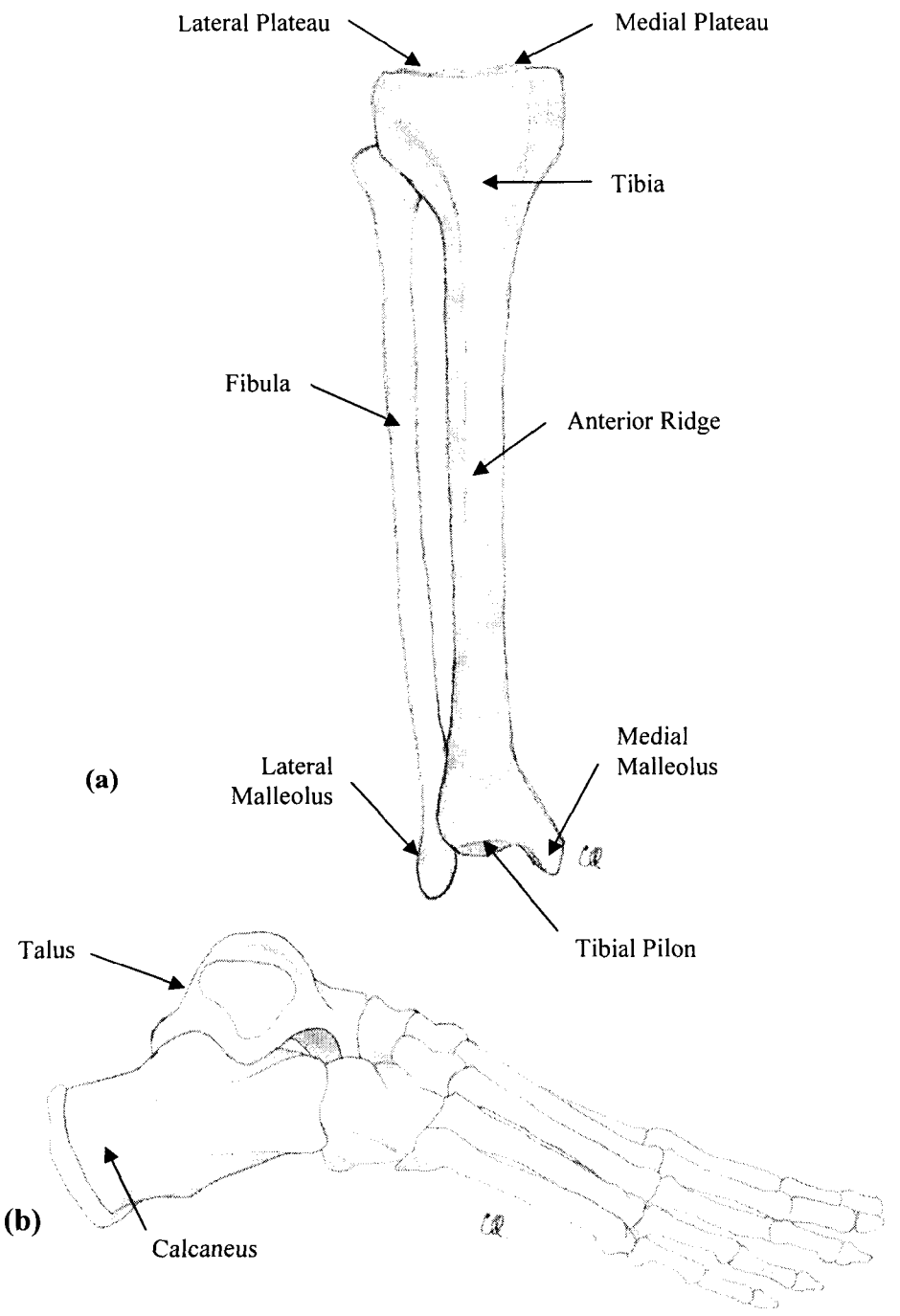

Figure 1.1: Lower Limb Anatomy
(a) Anterior view and **(b)** lateral view, right leg. The larger bone in the lower leg is the tibia, and the smaller bone is the fibula. The tibia articulates with the talus of the foot. Fractures of the calcaneus, talus and tibia are common in axial impacts.

at the ankle. Proximally the two articular regions are the medial and lateral plateaus. Along the anterior border of the tibia shaft is the sharp anterior ridge. At the distal end is the medial malleolus, a protrusion which serves as an attachment site for soft tissues. The distal region of the tibia, the pilon (or plafond), has a relatively flat surface where it articulates with the talus.

The fibula, located laterally within the shank, articulates with the tibia proximally and distally, forming tibiofibular joints; however, these joints have very little movement. The fibula does not contribute to the knee, but provides stabilization to the ankle joint via the talus (which, along with the distal tibia, forms the talocrural joint), and serves as the origin for several muscles. It has been estimated that the fibula carries approximately 7 - 15% of the axial load through the lower leg (Crandall *et al.*, 1996; Kuppa *et al.*, 2001b).

The talus is an irregularly shaped bone forming the lower part of the ankle joint that is largely covered with cartilage. The talus provides much of the range of motion of the ankle due to its joints (including the talocrural joint), and receives loading from the foot through contact with the calcaneus as well as from the tarsal bones of the foot.

1.1.2 *Bone Structure and Material Properties*

Bone is made up of two different microstructures – cortical and cancellous (Figure 1.2). The structure that is present depends on the location and function of the bone. Cortical (or compact) bone is the denser of the two. It forms a shell over bones, and is also the main component of the diaphysis (*i.e.*, shaft) of long bones. In the cortical structure, many microscopic cylindrical structures made mostly of collagen, called osteons, are tightly packed and aligned parallel to the major axis in long bones in order to

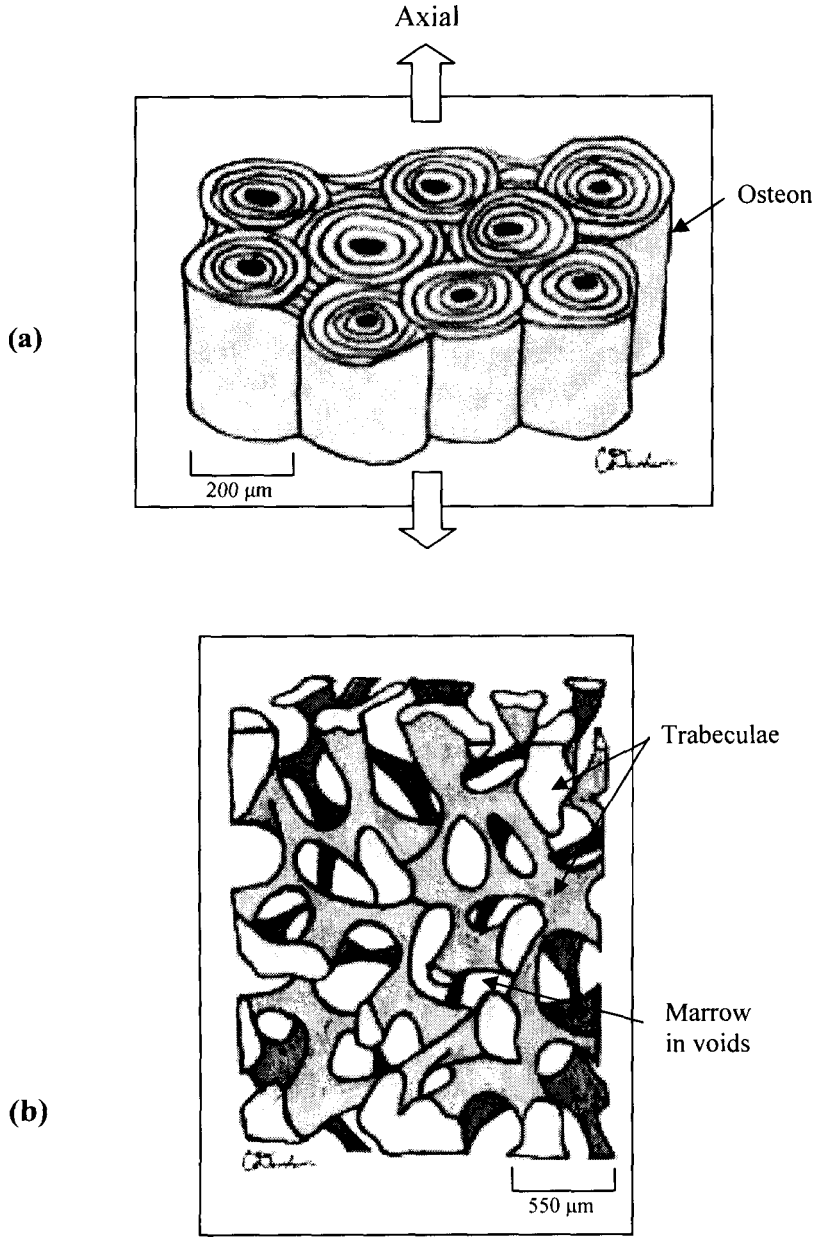

Figure 1.2: Bone Structures
(a) Cortical bone is made of many microscopic cylindrical structures called osteons, which are aligned axially to best support loads. **(b)** Cancellous bone is a lattice-like structure composed of struts of bone, called trabeculae, oriented in a web and filled with marrow. (Adapted from Dunham, 2005)

support axially-directed loads. Cancellous bone (also referred to as trabecular bone) is much less dense than cortical, and has a lattice-like structure. It is composed of small needle-like struts of bone called trabeculae, in a three-dimensional web. Cancellous bone forms the epiphyses (*i.e.,* ends) of bones, where loads are applied through joints in the body. Through the center of long bones is a medullary canal filled with marrow.

Bone is a complex material, and is inhomogeneous and anisotropic (*e.g.,* Marieb, 2004). It has been shown to display characteristics similar to elastic-plastic materials, including an elastic modulus, yield stress, plastic modulus, and ultimate stress (Burstein *et al.*, 1976) (Figure 1.3). Cortical bone is also viscoelastic, and as such the modulus and strength are approximately proportional to strain rate raised to the 0.06 power, as determined through compressive tests (Carter and Hayes, 1977). This can be attributed to the presence of the polymer collagen within cortical bone, and void collapse in cancellous bone. The presence of marrow in cancellous bone was similarly found to only affect the properties of bone at strain rates higher than 10 per second.

The properties of bone vary greatly in the literature, and are dependent on gender, age, location and method of testing. For example, the modulus of cortical bone in the literature has been reported to range from 12 – 21 GPa (Tannous *et al.*, 1996; Takahashi *et al.*, 2000), and for cancellous bone range from 250 – 530 MPa (Kim *et al.*, 2005; Beaugonin *et al.*, 1997). One study found that for 20 – 39 year olds, cortical bone of the tibia has an elastic modulus of 18.4 GPa, an ultimate tensile strength of 140 MPa, and an ultimate compressive strength of 159 MPa (Yamada, 1970). These properties tend to decrease by approximately 2 – 5% per decade of age (Burstein *et al.*, 1976). Cancellous

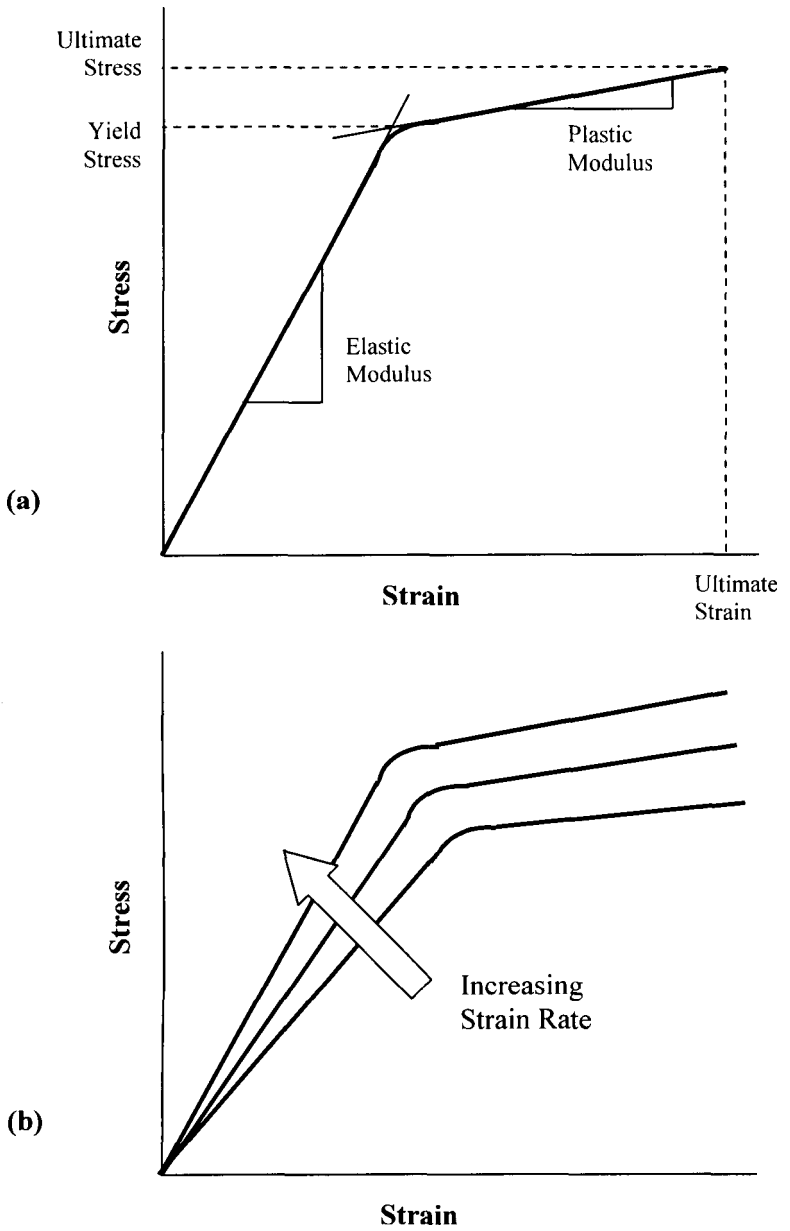

Figure 1.3: Bone Material Properties
(a) Bone has properties similar to elastic-plastic materials, and as such the stress-strain curve can be approximated as bilinear, including an elastic modulus and a plastic (or tangent) modulus. The yield stress defines the point of permanent deformation, and ultimate stress and strain occur at the point of fracture. **(b)** Increasing strain rate increases the slope (elastic modulus) as well as the yield stress.

bone of the tibia has been reported to have an elastic modulus of 445 MPa, with an ultimate strength of 5.3 MPa (Untaroiu *et al.*, 2005).

1.1.3 *HIGH ENERGY FRACTURES*

Fractures of the calcaneus, talus and tibia are especially devastating injuries due to the poor vascularization of the smaller bones of the foot. Pilon fractures of the distal tibia can be caused by the talus being driven into the tibia, as commonly associated with high-energy traumas. Due to its distance from the torso, the distal tibia has a relatively poor blood supply. Fractures of the distal tibia are often badly displaced due to low supporting musculature, and frequently are compound or open, with high risk of infections (Bergeron *et al.*, 2006). As a result of the severity of injuries and the low blood supply, fractures of this region can heal poorly, leading to impairment.

1.2 IN-VEHICLE MINE DETONATION LOADING

The primary cause of injury to the lower limb during an anti-vehicle (AV) mine blast is the energy transfer through the deformation of the floor, which can cause significant lower limb injuries (Manseau and Keown, 2005). While these injuries typically are not life-threatening, they can lead to long-term impairment or the need for lower limb amputation (Radonic *et al.*, 2004; Medin *et al.*, 1998). The resulting axial loading can lead to injuries similar to those from car crashes, but the loading conditions are quite different. AV blast impacts achieve higher forces over shorter durations than car crashes (<10 ms vs. > 100 ms) (van der Horst *et al.*, 2005), from which experimental results have formed the current basis for protective measures (*e.g.*, Funk *et al.*, 2002; Yoganandan *et*

al., 1996). Local floor accelerations and peak velocity changes may typically exceed 100 G as a result of an AV mine blast (Wang *et al.*, 2001), whereas car crashes have been reported to achieve accelerations of approximately 40 G (Bir *et al.*, 2008).

The loading as a result of an AV mine blast on the lower leg is not well quantified. Typical tibia loadings recorded during such blast events on light armoured vehicles have durations of approximately 10 – 20 ms and loading rates of approximately 1.5 – 5 kN/s (Manseau and Keown, 2005). Others have shown loading durations to be between 3 – 10 ms in duration (Bir *et al.*, 2008). One study analyzed an event where soldiers were injured (Medin *et al.*, 1998), and calculated that the vehicle had experienced an impulse of 25 kNs over 0.3 ms.

The Test Rig for Occupant Safety System (TROSS) was developed by IABG Germany to reproduce typical floor loadings as a result of AV mine blasts through the use of scaled detonations (Bir *et al.*, 2008). In 2003, TROSS was used to quantify the motion of the floor, and generated a velocity profile showing a peak velocity of 4.5 m/s occurring within 6 ms (Keown and Anctil, 2004).

1.3 Measurement Techniques

In order to assess the injury potential as the result of a blast, the strains, forces and accelerations experienced by the occupant need to be quantified. They can then be compared to established injury limits based on these measurable values. The following types of instrumentation are commonly used to assess the loading applied to the body.

1.3.1 *Strain Gauges*

Load through a structure such as bone can be measured using strain gauges applied to the surface. The most common type of strain gauge is a metallic foil gauge, which has a strain-sensitive pattern of wire sandwiched between two insulating sheets (Figure 1.4). Gauges must be securely attached to the object being studied, typically using a cyanoacrylate adhesive, in order to achieve an accurate measurement. As the object is deformed, the foil pattern is also deformed, causing the resistance of the wire to change proportionally to the strain. Strain gauges are appealing in their ability to measure the state of strain at a location, but are limited in the fact that strain can only be measured at discrete locations that are accessible for application.

Strain gauges are sensitive to strain in only one direction, and cannot be used to measure shear strain directly. To quantify the two plane strains and one shear strain, strain gauges can be combined to create a rosette (Figure 1.5). Considering a rosette with three gauges, a, b, and c at angles α, $\alpha+\beta$, and $\alpha+\beta+\gamma$ from the x-axis, these strains can be related to ε_x, ε_y, and γ_{xy} through the following equations (*e.g.*, Beckwith *et al.*, 1993):

$$\varepsilon_a = \frac{\varepsilon_x + \varepsilon_y}{2} + \frac{\varepsilon_x - \varepsilon_y}{2}\cos 2\alpha + \gamma_{xy}\sin 2\alpha \qquad \textbf{(Eq. 1.1)}$$

$$\varepsilon_b = \frac{\varepsilon_x + \varepsilon_y}{2} + \frac{\varepsilon_x - \varepsilon_y}{2}\cos 2(\alpha+\beta) + \gamma_{xy}\sin 2(\alpha+\beta) \qquad \textbf{(Eq. 1.2)}$$

$$\varepsilon_c = \frac{\varepsilon_x + \varepsilon_y}{2} + \frac{\varepsilon_x - \varepsilon_y}{2}\cos 2(\alpha+\beta+\gamma) + \gamma_{xy}\sin 2(\alpha+\beta+\gamma) \qquad \textbf{(Eq. 1.3)}$$

When a 45° rosette is used, and gauge 'a' is aligned with the x-axis, these equations simplify to:

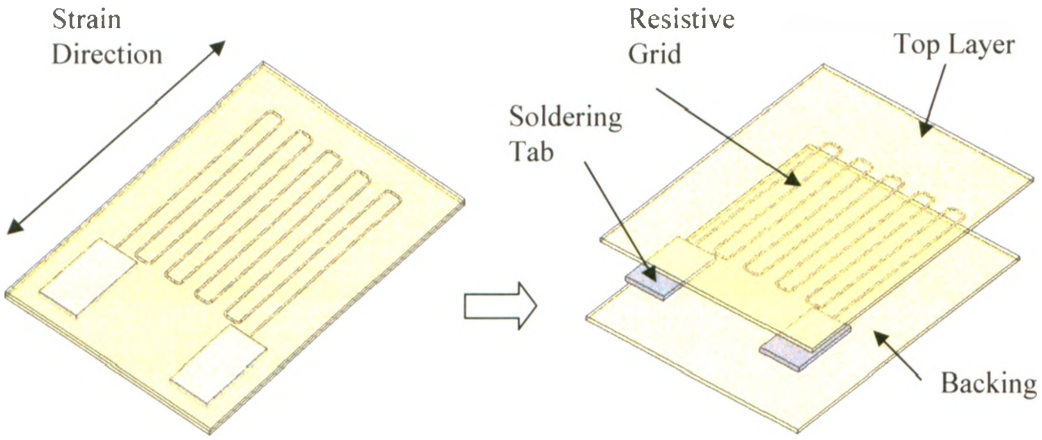

Figure 1.4: Strain Gauge Structure
A strain gauge consists of a protective backing, a resistive grid (whose resistance changes proportionately to the strain it experiences), and a top protective layer. Soldering tabs at the ends of the resistive grid are used to attach lead wires. Strain is measured along the longitudinal grid direction. (From Dunham, 2005)

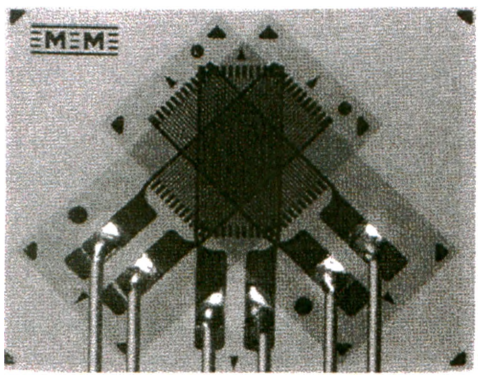

Figure 1.5: Strain Gauge Rosette
A rosette with three strain gauges at angles to one another allows for the full state of strain to be measured. (*Vishay Micro-Measurements*)

$$\varepsilon_x = \varepsilon_a \quad \textbf{(Eq. 1.4)}$$

$$\varepsilon_y = \varepsilon_c \quad \textbf{(Eq. 1.5)}$$

$$\gamma_{xy} = \varepsilon_b - \frac{\varepsilon_a + \varepsilon_c}{2} \quad \textbf{(Eq. 1.6)}$$

Once these values are known, they may be used to calculate stresses (σ_x, σ_y, τ_{xy}) or principal strains (ε_1, ε_2) as given below:

$$\varepsilon_{1,2} = \frac{\varepsilon_x + \varepsilon_y}{2} \pm \sqrt{\left(\frac{\varepsilon_x - \varepsilon_y}{2}\right)^2 + \left(\frac{\gamma_{xy}}{2}\right)^2} \quad \textbf{(Eq. 1.7)}$$

$$\frac{\gamma_{max}}{2} = \sqrt{\left(\frac{\varepsilon_x - \varepsilon_y}{2}\right)^2 + \left(\frac{\gamma_{xy}}{2}\right)^2} \quad \textbf{(Eq. 1.8)}$$

$$\alpha = -\frac{1}{2}\tan^{-2}\left(\frac{\gamma_{xy}}{\varepsilon_x - \varepsilon_y}\right) \quad \textbf{(Eq. 1.9)}$$

1.3.2 *Load Cells*

A load cell is an electronic transducer that converts force into an electric signal. Load cells are most commonly instrumented with strain gauges in various Wheatstone Bridge configurations, used to isolate and amplify different components of load. For example, an axial load cell might consist of four strain gauges, two aligned with the direction of loading and two perpendicularly oriented (Figure 1.6).

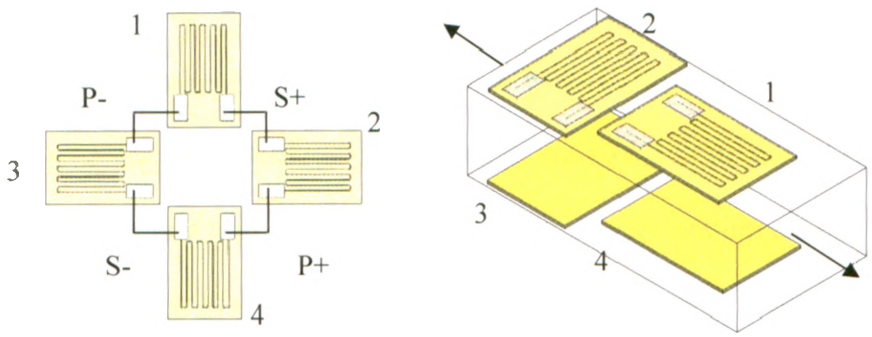

Figure 1.6: Wheatstone Bridge Circuit for Axial Load Cells
Through the combination and arrangement of several strain gauges, different components of load can be isolated and amplified, such as axial loading as shown. The gain from this bridge circuit is $2 + 2\upsilon$ (From Dunham, 2005)

1.3.3 *ACCELEROMETERS*

Accelerometers are sensors that detect the acceleration of a body relative to free fall, and are frequently used for dynamically measuring the motion and vibration of structures. They can be single or multi-axis, and are tuned to be sensitive to specific ranges of accelerations. The principle of operation of an accelerometer is the same as a mass-spring-damper system. When the mass experiences an external force such as gravity, it is displaced until it is balanced by the spring force. This displacement is measured most commonly via a capacitance change between fixed beams and beams mounted to the mass, but can also be measured using piezoresistors in the spring or through piezoelectric crystals. It is then converted into acceleration. The units of acceleration are m/s^2, but are commonly reported in units of g-force, or 'Gs', where 1 G equals 9.81 m/s^2 (acceleration due to gravity).

1.4 LOWER LEG SURROGATES

Measurement techniques such as those previously discussed are useful for evaluating loading of the human body when subjected to impacts. Often it is not practical or feasible to apply these tools direction to cadaveric specimens. For this purpose, surrogates representing the response of the human body are used to evaluate protective measures. These surrogates can be instrumented with various measurement systems, and in several cases can be reused for many tests, making them a consistent benchmark for evaluating loading of the body. However, their response needs to be correlated to the actual human response for them to be an appropriate method for assessing injury risk.

1.4.1 *ANTHROPOMORPHIC TEST DEVICES*

The current method for evaluating anti-tank land mine blast injuries involves the use of a Hybrid III (HIII) (Denton ATD, Inc, Rochester Hills, MI, USA) anthropomorphic test device (ATD) – commonly known as a crash test dummy. These devices were originally designed by the automotive industry to evaluate injury risk during frontal crashes. They are sized in both geometry and mass to represent different anthropometric populations, and the most commonly used is scaled to the dimensions of the 50th percentile male. In practice, ATDs are placed inside an actual vehicle and instrumentation on them is monitored while the vehicle is subjected to various explosive events.

1.4.1.1 DENTON LEG

The most commonly used ATD lower leg in automotive safety assessment is the Denton leg (Denton ATD, Inc, Rochester Hills, MI, USA). This leg is mandated to be instrumented with a 5-axis lower tibia load cell for AV mine blast tests, and is recommended to have a 5-axis upper tibia load cell included as well (Manseau, 2005). The Denton leg attaches to the knee of the HIII ATD via a clevis, and has a ball joint to approximate motion of the human ankle joints. It is a simple steel shaft that is mounted on an angle from the ankle to attach in front of the knee (Figure 1.7, right). The axial response of the Denton leg has been evaluated in comparison with cadaveric specimens in several studies (Crandall *et al.*, 1996; Kuppa *et al.*, 1998; Owen, 2001; Petit and Trosseille, 1999; Kuppa *et al.*, 2001a). It has been shown to induce bending moments under axial loading (Kuppa *et al.*, 2001a). Under pendulum loading, it was between 1.8

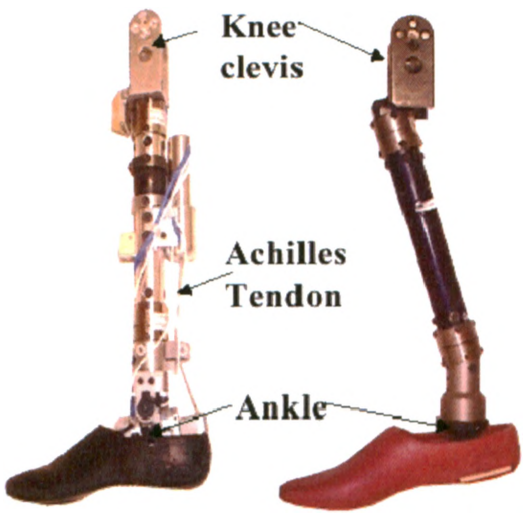

Figure 1.7: Mechanical Structure of the Thor-Lx and Denton Leg
The Thor-Lx (left) is the most recent attempt at a biofidelic Anthropomorphic Test Device. It includes more instrumentation than the Denton leg (right), as well as a component to represent the Achilles tendon, but the Denton remains the most widely used device for assessing injury risk to the lower leg. (Kuppa *et al.*, 2001a, see Appendix M for letter of permission)

and 2.8 times stiffer, had rise times 2 – 3 times faster, and showed greater rate dependency than cadaveric specimens (Crandall *et al.*, 1996; Kuppa *et al.*, 1998; Bir *et al.*, 2008). This has raised many concerns about the biofidelity of this ATD leg model, and led to further attempts to develop a more accurate representation.

1.4.1.2 THOR

The Test device for Human Occupant Restraint (THOR) ATD was developed by the National Highway Traffic Safety Administration to be a more biofidelic device than the Hybrid III. The lower extremity, the THOR-Lx, has improvements in both mechanical structure and level of instrumentation. The shaft of the THOR-Lx is straight, and includes a rubber element to allow a small amount of compression (Figure 1.7, left). An Achilles tendon is included to simulate the resistance provided by musculature of the lower leg often present when braking during car crashes. The THOR-Lx has the same knee clevis as the Denton leg, and as such is interchangeable on the Hybrid III ATD. There are two 5-axis load cells (one distal and one proximal) and a uniaxial load cell built into the Achilles tendon, as well as 3-axis rotary potentiometers in the ankle. Further instrumentation can include accelerometers in the foot and at two locations on the tibia.

Several studies have examined the response of this lower leg model to axial impact in order to evaluate its biofidelity (Kuppa *et al.*, 2001a; Owen, 2001). The THOR-Lx was found to have closer response to cadaveric specimens when tested using a pendulum system, with equivalent peak loads being accurately measured. During full-scale vehicle crashes, the THOR-Lx exhibited lower stiffness and slower rise times than the Denton

leg, proving to be more representative of cadaveric response. Despite this, the Denton model remains the most widely used leg currently.

1.4.2 *Synthetic Composite Bones*

Composite synthetic bones are widely used in orthopaedic research. They offer many advantages over cadaveric specimens, including low inter-specimen variability in both geometry and material properties, ready availability, and ease of handling, storage, and disposal. For these bones to be an appropriate surrogate for fracture testing, the fracture strength and failure mechanics need to be consistent with the natural bone response under impact conditions (Funk *et al.*, 2002; Yoganandan *et al.*, 1996).

1.4.2.1 Complex Lower Leg

The Complex Lower Leg (CLL) was designed by Defence Research and Development Canada for evaluation of anti-personnel landmine injury risk. This synthetic surrogate is made of polymeric bones (a tibia/fibula, talus, and calcaneus) encased in ballistic gelatin representing soft tissues, covered with a latex skin. Silicone rubber is used to make cartilage pads and a heel pad. The geometry was taken from the Visible Human Database (National Library of Medicine), and accounts for loading through the hind-foot via the calcaneus only. As such, there is no representation of the rest of the bones of the foot (Keown and Anctil, 2004), and a two piece calcaneus was included to provide symmetry about the two vertical axes. A tendon wraps the two calcanei to provide stability of the foot. The CLL is not instrumented with a load cell, but can be instrumented with strain gauges. To assess the biofidelity of these surrogates,

they were subjected to axial impact loads and assessed for damage (Manseau and Keown, 2005). The resulting injuries were compared to similar impact tests previously reported (Funk *et al.*, 2002). At low loading levels satisfactory results were found, but at high severity tests, representative of an AV mine blast, there was a lack of consistency in injury patterns and severity. As well, unrealistic fracture locations were observed. Recommendations for improvement were made (Manseau and Keown, 2005), but no known further versions of this leg have been produced to date.

1.4.2.2 Frangible Surrogate Leg

The Frangible Surrogate Leg (FSL) was designed by the Defense Science and Technology Organization of Australia in the late 1990s for the purposes of assessing protective measures for anti-personnel and anti-vehicular mine blasts (Footner *et al.*, 2006). This synthetic surrogate is also made of polymeric composite bones representing the lower leg and foot, connected by highly flexible polyamide glue (simulating cartilage), and encased in ballistic gelatin representing soft tissues.

The FSL has been used to assess the efficacy of foot protection for anti-personnel landmines (Bergeron *et al.*, 2001), and fractures were compared to cadaveric results previously reported (Harris *et al.*, 2000). It was found that the calcaneus was too strong, as it survived blasts known to cause injury. This study removed a portion of the tibia to insert a load cell, which may have altered the load response, and therefore a need for an integrated load cell was identified.

A modified FSL (FSLM) has since been developed which is instrumented with strain gauges and calibrated to act as a load cell that can measure both bending moments and

compressive loads. The FSLM was shortened for compatibility with a Hybrid III ATD, but the distal half (the foot and ankle region) remained unchanged. The response of the FSLM was evaluated under drop test and explosive loading, and softening of the glue of the joints was observed after the first impact. Large variations in response among legs were noted, and accuracy was assessed to be on the order of 15%, likely as a result of manufacturing and calibration difficulties (Footner *et al.*, 2006).

The latest version of this model is the MK IV FSL, which includes flat and tubular polymeric materials to simulate tendons. Biofidelity of these bones was assessed only qualitatively, based on previously reported experiences using cadaveric specimens, and was found to be somewhat limited in its ability to predict injuries (Bergeron *et al.*, 2006).

1.4.2.3 SAWBONES®

The most widely used commercially-available composite bones are Sawbones® (Pacific Research Laboratories, Inc., Vashon, WA, USA). The tibia models were first examined in their second generation version, which was made of fiberglass-fabric-reinforced epoxy and polyurethane foam (Cristofolini and Viceconti, 2000). The external and internal geometry of the bones were compared to cadaveric specimens, and were found to be relatively close, except for a difference in width of the diaphysis. They were subsequently compared under axial and torsional whole bone loading (potted in cement at both ends), as well as in bending in both anatomical planes. The bones were validated for bending, but were overly stiff under torsion and were too difficult to align for axial assessment. The third generation of tibias was manufactured using short-glass-fiber-reinforced epoxy as the cortical analogue in order to improve the uniformity of

mechanical properties, add greater anatomical detail, and facilitate easier fabrication (Heiner and Brown, 2001). An intramedullary canal was also introduced, which aided with alignment issues. These bones were similarly tested, and found to have lower variability under axial testing. Stiffnesses were found to reasonably approximate natural human bones from other studies.

The currently-available models are fourth generation, and are made using a short glass fiber reinforced epoxy resin injected around a core of rigid polyurethane foam (Figure 1.8). Changes were made to the cortical analogue to improve fracture toughness, fatigue life, tensile strength and modulus, and thermal stability (www.sawbones.com, visited October 12, 2009). Third generation bones were prone to crack formation and early fatigue failure, making them unsuitable for cyclic studies (Chong *et al.*, 2007). The fourth generation cortical analogue was tested for static mechanical properties, fracture toughness, and fatigue crack propagation resistance, and compared to the third generation and human properties from the literature. Strength and modulus were found to be close to human cortical bone (but still lower), as well as fracture toughness (within the range reported). The fatigue life of the fourth generation material was better than the third, but as synthetic materials cannot remodel like bone, higher fatigue life is always desired (Chong *et al.*, 2007). The fourth generation bones were also tested for whole-bone response in the same manner as the third generation ones were previously (Heiner, 2008), and were validated to be close to natural human structural properties for bending and torsion (axial stiffness values were not available for comparison). No known studies have looked at the fracture response of Sawbones® to impacts, as they have only been validated for quasi-static loading rates.

(a)

(b)

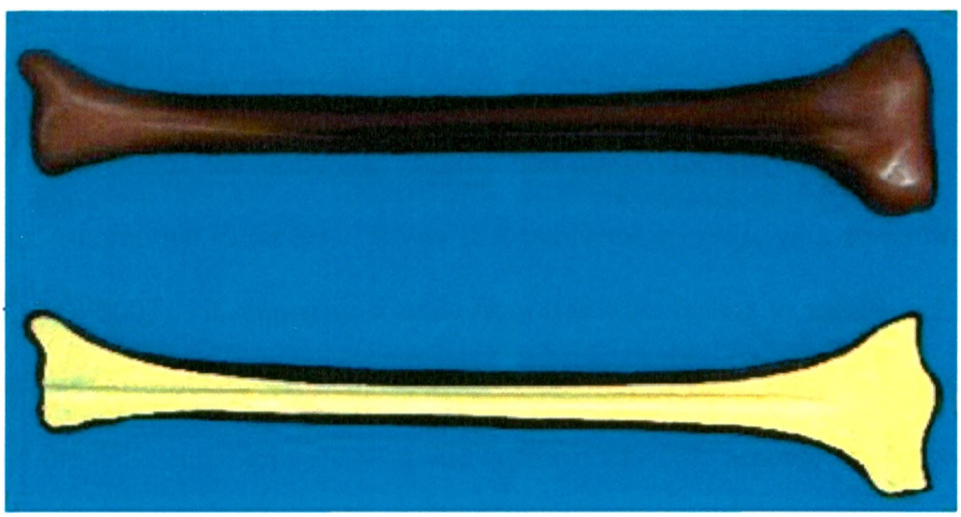

Figure 1.8: Sawbone® Synthetic Composite Tibia
Sawbone® composite tibias are made of a short fibre reinforced epoxy resin over a polyurethane foam core. Shown are a whole bone **(a)** and cross-section **(b)**. Bones are shown from an anterior view of a left specimen, with the distal end oriented to the left. (*www.sawbones.com*, see Appendix M for letter of permission)

1.5 EXISTING INJURY CRITERIA

Injury criteria have been developed for a variety of regions of the body. Those that pertain to the lower leg are described in detail below. Commonly used criteria that apply to other areas of the body have been included as Appendix B for completeness.

1.5.1 *ABBREVIATED INJURY SCALE*

In order to quantify the severity of a traumatic injury at any location in the body, the Abbreviated Injury Scale (AIS) can be used. The AIS was developed by the American Medical Association, the American Association for Automotive Medicine, and the Society of Automotive Engineers. It was first published in 1971, with several revisions since (NATO, 2007). It represents a scale from 0 to 6 according to anatomical injuries. The severities corresponding to the AIS scale levels are shown in Table 1.1. It should be noted that the AIS scores injuries only, and does not take into account the consequences of these injuries such as disabilities. AIS 2+ (moderate and greater) is considered to be the cutoff for acceptable potential injury in defense research (van der Horst *et al.*, 2005), as life-altering injuries are avoided. A 10% risk of AIS 2+ has been adopted as the protection limit by the North Atlantic Treaty Organization (NATO, 2007), and thus is the significant severity level for this project. Table 1.2 gives examples of injuries that may occur to the lower leg, along with an estimate of recovery time and risk of impairment.

1.5.2 *AO CLASSIFICATION*

Distal tibia fractures can be classified in order of severity using the AO universal classification system. Type A fractures consist of extra-articular injuries, which do not

Table 1.1: AIS Severity Levels
The AIS is a useful scale for assessing severity of an injury, and considers post-injury aspects such as quality of life. Injuries of AIS level 2 and above (corresponding to moderate and higher) are to be avoided in order to minimize life-altering effects (Bogosian and Der Avanessian, 2004).

AIS Level	Severity	Type of Injury
0	None	Non
1	Minor	Superficial
2	Moderate	Reversible injuries; medical attention required
3	Serious	Reversible injuries; hospitalization required
4	Severe	Life threatening; not fully recoverable without care
5	Critical	Non-reversible injury; not fully recoverable even with medical care
6	Virtually unsurvivable	Fatal

Table 1.2: Lower Leg Injuries
Injuries to the lower leg and their corresponding AIS level. AIS levels 2 and above have long recovery times and higher risks of long-term impairment (NATO, 2007).

Examples of Injuries	AIS	Recovery	Risk of Impairment
Ankle sprain	1	2 – 3 months	Low
Simple fracture of the tibia	2	3 months	Low
Simple or comminuted fracture of the talus	2	3 months or +	Medium
Simple or comminuted fracture of the calcaneus	2	3 months or +	Medium – High
Open fracture of the tibia	3	3 months or +	Low – Medium
Fracture of the fibula with affected artery or nerve	3	3 months or +	Medium – High
Traumatic amputation	4	3 months or +	High

interrupt the articular surface of the tibio-talar joint. Type B fractures are partial articular fractures, with some connection between the joint surface and the diaphysis. Type C can be considered the most devastating, and the most common type of pilon fracture, and consists of complete articular fractures, with no connection between the joint surface and the diaphysis of the tibia. Increasing severity on the AO classification scale can be associated with increasing difficulty of repair.

1.5.3 *TIBIA CRITERIA*

1.5.3.1 TIBIA INDEX

A method of evaluating the injury tolerance for leg shaft fractures commonly used in the automotive industry is the Tibia Index (TI) (Mertz, 1993). The TI is an injury tolerance criterion for combined bending and axial compressive loads on the tibia, where a value of 1.0 is the pass/fail threshold for injury.

The equation for calculating the Tibia Index is given as follows (Kuppa *et al.*, 2001b):

$$TI = \frac{F}{F_C} + \frac{M}{M_C} < 1 \qquad \textbf{(Eq. 1.10)}$$

where F is the measured compressive axial force (kN), and M is the measured bending moment (Nm) in the leg (defined as the resultant moment of the medial-lateral and the anterior-posterior moments). M_C and F_C, the critical values of bending moment and axial compressive force in the tibia, were recommended by Mertz (1993) to be equal to 225 Nm and 35.9 kN for the 50th percentile male. These values, however, have subsequently been changed as the result of further cadaveric and experimental testing to be 240 Nm for Mc and 12 kN for Fc (Kuppa *et al.*, 2001b), referred to as the "Revised Tibia Index". An RTI of 0.75 corresponds to a 10% probability of an AIS 2+ injury (NATO, 2007).

The Insurance Institute for Highway Safety (IIHS) (2004) uses adjusted bending moments to account for the fact that the shape of the Denton leg induces bending when exposed to pure axial forces (see Section 1.4.1.1). This adjustment was developed by Zuby *et al.* (2001), and is applied to moments about the *y*-axis. The adjusted bending moments as measured by the tibia load cells are calculated from the measured ones as follows:

$$M_{upperadj} = M_{uppermeas} - (F_z * 0.02832) \quad \textbf{(Eq. 1.11)}$$

$$M_{loweradj} = M_{lowermeas} + (F_z * 0.006398) \quad \textbf{(Eq. 1.12)}$$

1.5.3.2 Injury Assessment Reference Values

The IIHS published Injury Assessment Reference Values (IARV) for significant injury-related parameters (Insurance Institute for Highway Safety, 2004). IARVs refer to "a human response level below which a specified significant injury is considered unlikely to occur for the given size individual" (Mertz, 1993). For the lower leg, limits on the tibia axial force and foot accelerations were specified. The foot acceleration limit is 150 G, which is based on non-injurious volunteer tests. The IIHS defines this as good-acceptable, 200 G as acceptable-marginal acceleration, and 250 G as marginal-poor. Similarly, tibia axial forces levels are defined, with 8.0 kN as the recommended IARV (corresponding to marginal-poor), 6.0 kN is acceptable-marginal, and 4.0 kN is good-acceptable. IARVs must be used with caution, as they have not been investigated for all mechanisms of injury.

1.5.3.3 LOWER LEG THRESHOLD

The Lower Leg Threshold (LLth) was developed as a time-dependent lower leg injury criterion based on tibia loading duration (Nies, 2004). This criterion was developed to correlate lower leg injury with impulse magnitude and duration, an important factor not often included in tibia injury criteria which differs between AV mine-blast and car crash loading. Acceleration-injury data from Hirsch (1964) were used to develop this threshold, and 5 and 10% risk curves were generated for both acceleration and force-based limits (Figure 1.9). The LLth states that an acceleration limit of 20 G can safely be tolerated for durations longer than 20 ms (Nies, 2004). The previously proposed force limit of 5.4 kN (see section 1.5.3.1) corresponds well with loading durations on the order of 10 ms, but no further validation studies have been published on this injury threshold.

1.5.4 *REVIEW OF EXPERIMENTAL STUDIES EXAMINING LOWER LEG INJURY TOLERANCE*

Most of the previous research on the tolerance of the lower leg to axial impacts has been conducted for car crashes. These incidents are slower than in-vehicle AV mine blasts, and as such the proposed tolerances could be inappropriate for this application. However, they provide insight into parameters that affect the tolerance of the lower leg to impact, and form a basis for current injury standards in the defence community. The following studies (sorted from oldest to newest by research laboratory) have examined the injury tolerance of the lower leg to axial loading, and key findings are summarized in Table 1.3 at the end of this section.

(a)

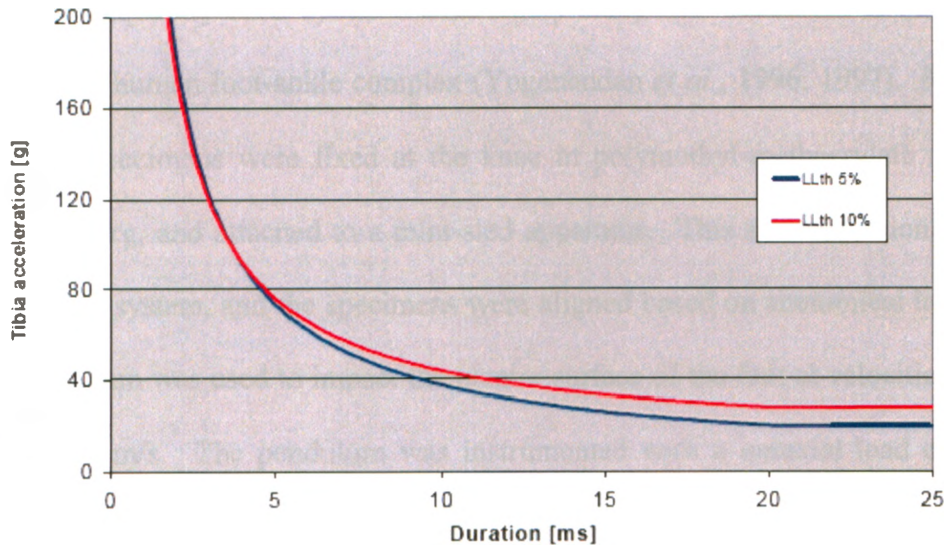

(b)

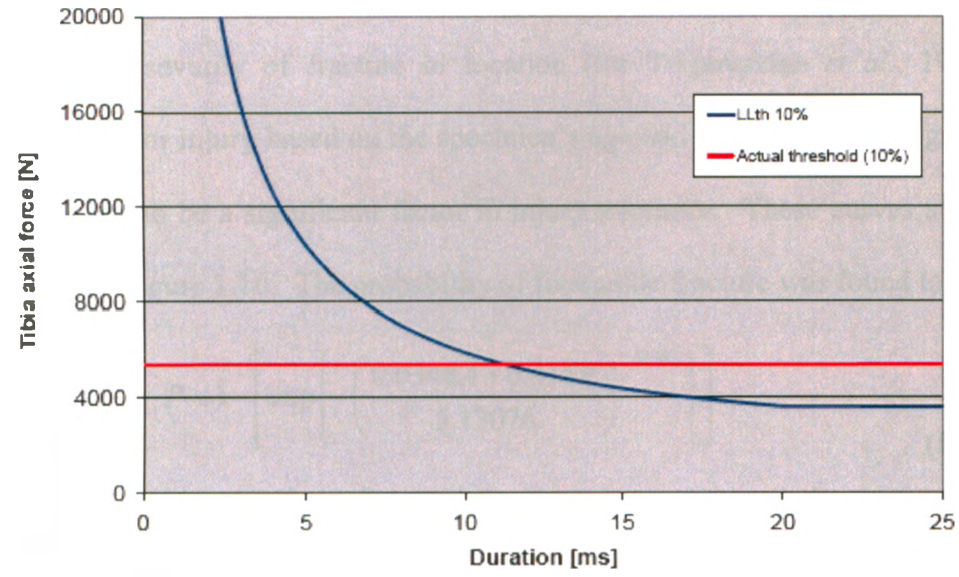

Figure 1.9: Lower Leg Threshold for Acceleration and Force
Injury tolerance curves are defined based on both **(a)** acceleration and **(b)** force levels. (NATO, 2007) See Appendix M for permission.

1.5.4.1 Medical College of Wisconsin: 1996-97

The most frequently cited dynamic axial injury study was conducted to quantify the tolerance of the human foot-ankle complex (Yoganandan *et al.*, 1996; 1997). Full lower leg cadaveric specimens were fixed at the knee in polymethyl-methacrylate (PMMA), ballasted to 16 kg, and attached to a mini-sled apparatus. This sled rode along a linear rail and bearing system, and the specimens were aligned based on anatomical landmarks. A 24 kg pendulum was used to impact the plantar surface of the foot at velocities ranging from 2.2 – 7.6 m/s. The pendulum was instrumented with a uniaxial load cell and a uniaxial accelerometer, and a second load cell was located at the proximal end of the sled (behind the PMMA block). Fracture forces ranged from 4.3 to 13.0 kN, but with no indication of the severity of fracture or location (for Yoganandan *et al.*, 1996). A probability curve for injury based on the specimen's age and impact force was generated, as age was found to be a significant factor in injury tolerance. These curves are shown for three ages in Figure 1.10. The probability of foot/ankle fracture was found to be:

$$P = 1 - \left[\exp\left\{ -\left(\frac{0.0348A + 0.415F}{5.13076} \right)^{7.42582} \right\} \right] \qquad \textbf{(Eq. 1.13)}$$

where A is the age in years and F is the tibia axial force in kN (from NATO, 2007). To select a tolerance value for protective measures, a 10% risk of injury for a 45 year old was chosen as most representative of the average military population, corresponding to a force level of 5.4 kN (NATO, 2007).

The data from Yoganandan *et al.* (1996) were analyzed by Kuppa *et al.* using a logistic regression analysis to define an alternate injury prediction equation (Kuppa *et al.*, 2001b). The probability of fracture as a function of lower tibia axial force:

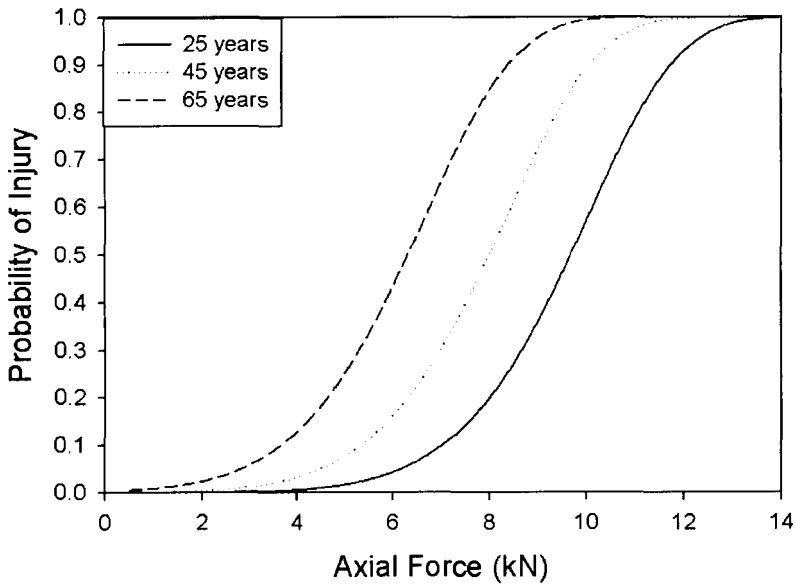

Figure 1.10: Injury Probability Curves by Age, Yoganandan Model
The injury risk equation from Yoganandan *et al.* (1996) was plotted for 25, 45, and 65 years to demonstrate the effect of age.

$$P = \frac{1}{1+\exp(4.572-0.670F)} \qquad \textbf{(Eq. 1.14)}$$

where F is the lower tibia axial force in N. This resulted in a force of 3.6 kN corresponding to a 10% risk of fracture. This equation is more straightforward in application, but does not include the effect of age on bone tolerance.

1.5.4.2 WAYNE STATE UNIVERSITY / NISSAN MOTOR CO: 1998

A study by Kitagawa *et al.* (1998) introduced the concept of including Achilles tension to simulate braking force in an attempt to create tibial pilon fractures. Paired cadaveric lower legs were potted at the proximal end of the tibia, and the Achilles tendon pulled with 1.8 kN of force. A rigid pendulum (mass = 18 kg) was used to impact the plantar surface of the foot at approximately 3 m/s. A load cell and accelerometer were mounted to the pendulum, and a 6-axis load cell fixed to the proximal end of the tibia. Average failure loads measured by the impactor and proximal tibia load cells for tibial pilon fractures were 4.9 and 7.2 kN, respectively, and 5.2 and 7.9 kN for calcaneus fractures. The distal tibia and the calcaneus were concluded to have strengths very close to each other.

1.5.4.3 CALIFORNIA POLYTECHNIC STATE UNIVERSITY: 2001

The objective of the study by Griffin *et al.* (2001) was to determine predictors of lower extremity injury as a result of anti-personnel landmines, and assess the efficacy of protective footwear. Twenty fresh-frozen cadavers were used, and instrumented with a proximal tibia load cell and strain gauges on the distal tibia and calcaneus. They were then loaded by placing the heel over a landmine. Impulse (defined as the area under the

force-time curve), loading rate, and pulse width were calculated. It was found that statistically significant predictors of pilon fractures are axial loading rate, axial impulse, axial peak force, and subject weight. This was formulated in terms of a risk of pilon fracture equation, given as:

$$p = \frac{1}{1+\exp(-8.39-0.078R+0.073W+5.2\times10^{-5}Fz)} \quad \textbf{(Eq. 1.15)}$$

where R is the axial loading rate (kN/ms), W is the subject weight (lbs), and Fz is the peak Z force (N). Based on this, probability curves were plotted for various loading rates, for a 75 kg subject, and an impulse of 30 Ns (the average value from the tests) (Figure 1.11). Loading rate was found to be the strongest predictor of pilon fracture, but rates tested were in the range of 5 – 116 kN/ms. As AV blast loading rates are typically below 5 kN/ms, the validity of this model is questionable.

1.5.4.4 Medical College of Wisconsin: 2001

Calcaneal fractures are a common injury to the lower extremity, and can heal poorly as a result of low vascularization. Seipel *et al.* (2001) subjected 22 cadaveric lower extremities to axial impacts representative of car crash events in an attempt to quantify the tolerance of the calcaneus. The impacting apparatus was the same pendulum system as in Yoganandan *et al.* (1996), and strikes occurred with velocities of 2.2 to 6.7 m/s, and with energies from 58 to 540 J. Fractures were created at forces ranging from 3.6 – 11.4 kN. A risk curve for calcaneal fracture was generated based on axial force, showing a 25% risk of fracture at a force of 4.0 kN, and 50% risk at 5.5 kN.

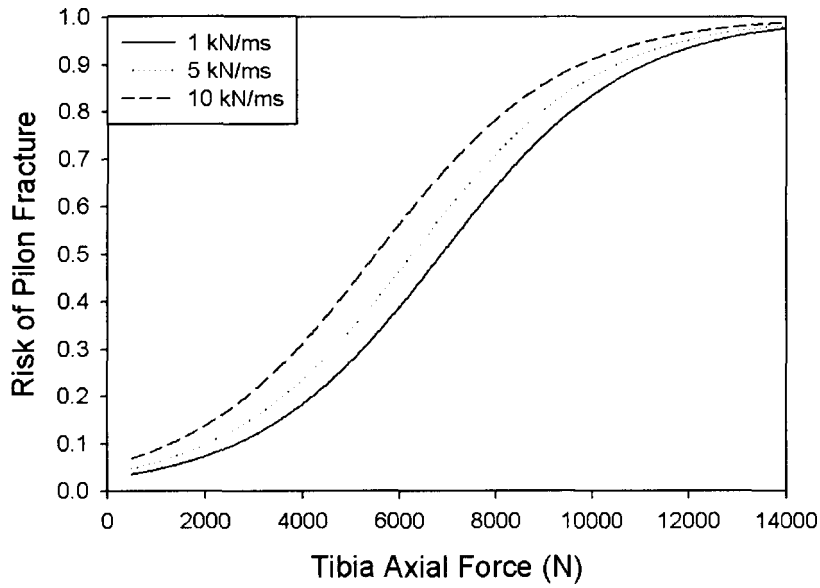

Figure 1.11: Risk of Pilon Fracture Curves, Griffin Model
Using the Griffin equation (2001), risk curves were generated for a 75 kg person at various loading rates.

1.5.4.5 UNIVERSITY OF VIRGINIA: 2002

One of the most comprehensive axial injury tolerance equations was developed by Funk *et al.* (2002). This study examined the axial response of intact lower legs to simulated car crash loading, with particular investigation into the effect of Achilles tension (representative of bracing prior to impact). Muscle pre-tensioning is not considered a factor in AV blast impacts, as the occupants do not expect the event, and muscle contraction is too slow to respond (NATO, 2007). Specimens were mounted in a test apparatus, and received axial impacts via a transfer piston resulting in footplate velocities of approximately 5 m/s. A load cell measured the load imparted to the footplate, and a tibia load cell was implanted in each specimen. A multivariate Weibull model was used to describe the probability of injury using the best subset of predictors:

$$P = 1 - \left[\exp\left\{-\exp\left(4.99 \ln F - 43.7 - 0.964G + 0.0793A - 0.0552W - 0.473AT\right)\right\}\right] \quad \textbf{(Eq. 1.16)}$$

where F is the tibia axial force in N, G is the subject gender (1 if male, 0 if female), A is the subject age in years, W is the subject body weight in kg, and AT is the Achilles tension in N. This equation is plotted for the average 45 year old male population in Figure 1.12.

1.6 FINITE ELEMENT ANALYSIS OF BONE

While cadaveric studies of lower leg injury tolerance are numerous, there are several limitations inherent in the type of testing. Due to limited numbers, only a small number of parameters can be examined with statistical significance, especially with this type of destructive testing. Computer modeling through the use of finite element analyses offers

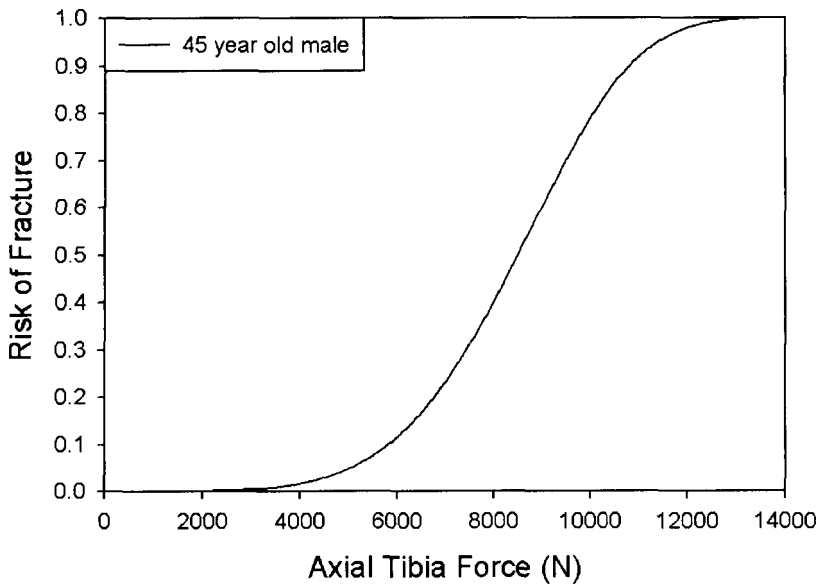

Figure 1.12: Injury Risk, Funk Model
Injury risk function for the American 50th percentile male at 45 years old, assuming no Achilles tension, using the equation from Funk *et al.* (2002).

Table 1.3: Summary of Previous Injury Tolerance Studies
The significant injury risk factors and recommended 10% injury risk force level (for an average male) are summarized. The current standard is highlighted in blue.

Study	Significant Injury Risk Factors	10% Injury Risk Force
Yoganandan *et al.* (1996, 1997)	Axial force, age	5.4 kN
Kuppa *et al.* (2001)	Axial force	3.6 kN
Kitagawa *et al.* (1998)	Axial force	-
Griffin *et al.* (2001)	Axial loading rate, axial impulse, axial peak force, subject weight	2.1 kN
Seipel *et al.* (2001)	Axial force	2.5 kN
Funk *et al.* (2002)	Axial force, gender, age, body weight, Achilles tension	5.8 kN

the advantage of being able to simulate a large number of loading protocols. It is also a primary method of injury assessment used by automotive and defence industry members.

1.6.1 *APPLICATION OF FINITE ELEMENT ANALYSIS*

Finite element analysis (FEA) is a powerful tool that can be used to analyze biomechanical response to loading (among other things). FEA consists of subdividing structures into simple shapes in order to compute the stresses and strains at any location through the structure. Once the finite element model has been validated, a primary advantage FEA has over cadaveric experimental testing is the ability to test multiple loading conditions on a single specimen, which is especially useful in destructive fracture analyses.

The geometric shapes used to construct the model are termed elements, and are joined together at points called nodes. The continuum of elements which forms the model is called a mesh. Once a mesh is built, material properties are assigned to the elements, and boundary conditions and loads can be applied. There are two main shapes of elements: tetrahedral and hexahedral (Figure 1.13). For dynamic simulations hexahedral elements have been shown to be computationally more accurate than tetrahedral elements (Untaroiu *et al.*, 2005). Within this element geometry there are two element structures that are frequently used, shells and solids. Shell elements have very small thickness relative to their other dimensions, and as such are useful for studies where stresses occur in-plane with the element. Shell elements are also less computationally intensive than solid elements, which allow for three-dimensional loading. Solid elements are used more

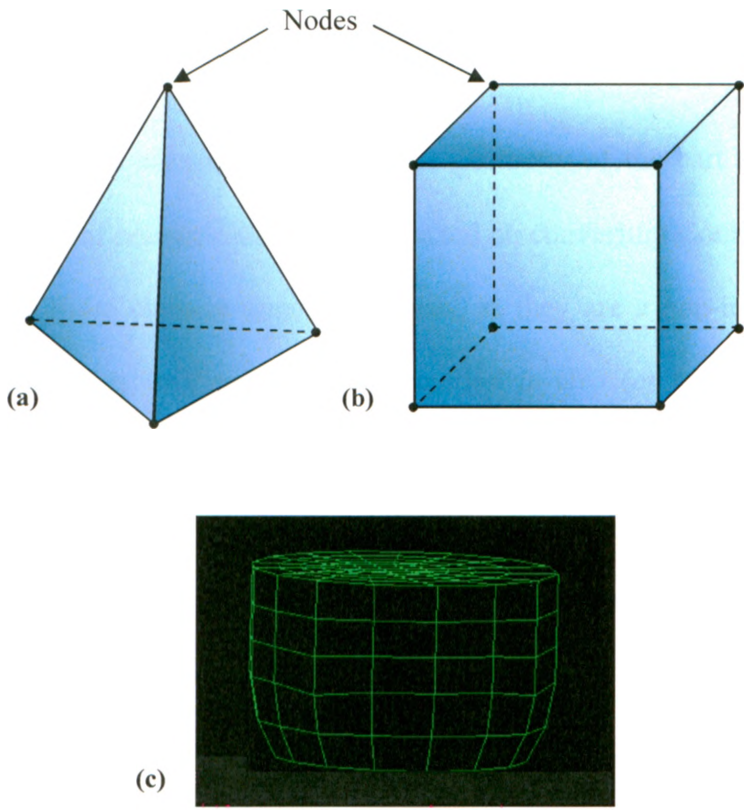

Figure 1.13: Tetrahedral and Hexahedral Elements
Two types of solid elements used in finite element modeling are **(a)** tetrahedral and **(b)** hexahedrals. Nodes are indicated with dots. The combination of elements forms a mesh **(c)**.

frequently for general finite element analyses, especially when the state of stress is unknown.

Once a model is built it can be analyzed, typically using a computer-based solver. Most of these solvers compute the displacements of the nodes of the mesh based on the stiffness of the structure and the applied loading, and also calculate the state of stress for each element.

The mesh requires accurately knowing the geometry of the part to be analyzed. A significant amount of research has been conducted on converting Computed Tomography (CT) scans into finite element models of bones, as they are a non-invasive method for obtaining geometry as well as density information *in-vivo* (or *in-vitro*) from which to develop patient-specific models (Taddei *et al.*, 2006). As such, the process has been well established, but is complex and time-consuming (Valle and Ray, 2005). The steps involved include extraction of the 3D bone surface from the CT images to establish the geometry of the model, generation of the finite element mesh based on these surface definitions, and assignment of mechanical properties to the mesh prior to application of simulated loads and boundary conditions. Due to the complicated geometry of bones, meshes created using automatic mesh generators are of a much lower quality than those manually generated (Valle and Ray, 2005). Analyses have been conducted to identify fracture locations of bones in finite element models; however, most studies simulate quasi-static and not dynamic loading (Imai *et al.*, 2006). The focus of the current thesis is dynamic, and as a review only these types of studies are described herein.

1.6.2 *PREVIOUS TIBIA IMPACT SIMULATIONS*

Most of the previous finite element models of the lower limb have been developed by the car crash industry. The existing models have several limitations in both development and validation. Numerous simplifications have been made as a result of the complex nature of this type of simulation, including geometrical and material property definitions. As well, validation has been limited due to the lack of experimental cadaveric testing for comparison purposes. A summary of key parameters is provided at the end of this section in Table 1.4.

1.6.2.1 GEORGE WASHINGTON UNIVERSITY / NHTSA: 1996

The most commonly referenced experimental study on axial impact tolerance of the lower leg (Yoganandan *et al.*, 1996) was the basis of validation of a finite element model by Tannous *et al.* (1996). A representative foot and ankle were digitized to generate IGES files describing the surface geometry of the bones. The bone was meshed using deformable 8-noded hexagonal solid elements, with an average thickness estimated for cortical bone. Both cortical and cancellous bone were considered to be homogenous, isotropic, and linear elastic, with the cortical modulus taken from the literature (Cowin, 1991) and the cancellous modulus based on average apparent density (Carter and Hayes, 1977). LS-Dyna® was used to run the simulation, with friction of contact between the bone and impactor selected to be 0.02, similar to that of cartilage. Non-injurious simulations were run, with a rigid plate impactor constrained to move only in one direction. At the proximal end a rigid mass simulated the weight of the experimental slider, and was similarly constrained. The forces were found to be higher than those

experimentally, but the shape and durations were in good agreement. Stresses and strains were compared to ultimate values from the literature used to evaluate fracture risk. A number of future improvements were identified, including the use of CT scans for more accurate geometry.

1.6.2.2 TOYOTA CENTRAL R&D LABS, INC. / WAYNE STATE UNIVERSITY: 2000

A full lower limb model was developed by Iwamoto *et al.* (2000) for the purposes of injury prediction during frontal automobile impacts. The geometry was taken from a 50th percentile male, and was modeled using crushable solid elements for cancellous bone and damageable shell elements for cortical bone, with properties from Yamada (1970). Joints were modeled with contacts and major ligaments and tendons. Simulations were run using the solver PAM-CRASH®, and were evaluated for validation purposes in comparison with quasi-static three-point bending tests (Yamada, 1970) and dynamic impact tests simulating braking (Kitagawa *et al.*, 1998). Force values were compared and showed generally good agreement, although some differences were noted. Fractures occurred in the calcaneus and the distal tibia, regardless of the Tibia Index (TI) being calculated to be less than 0.5 (suggesting no injury). The authors concluded that the TI may underestimate the injury in frontal impact. The material definition for this model was later improved through the development of an anisotropic inelastic constitutive model with damage evolution, strain rate dependency, and asymmetry of tension and compression, which showed improved results over the previous, more simplified isotropic elasto-viscoplastic material model as implemented in LS-Dyna® (Iwamoto *et al.*, 2005).

1.6.2.3 WAYNE STATE UNIVERSITY / FORD MOTOR COMPANY: 2001

A further finite element model of the lower limb was developed for automotive crash injury prediction, and validated against cadaveric tests (Beillas *et al.*, 2001). This model was developed from a CT scan of a 50th percentile male, and the internal and external boundaries of the cortical shell were identified, along with soft tissues. Shell elements were used to model the cortical bone, and cancellous bone was modeled using solid hexahedral elements. The two material types were joined using a tied contact interface in order to accelerate the meshing process. Both cortical and cancellous materials were modeled using an elastic-plastic material representation. Impact simulations were compared to previous studies in the literature (Haut and Atkinson, 1995; Banglmaier *et al.*, 1999). Injury locations were observed to correlate with experimental results, but crushing of the distal region (observed during cadaveric tests) could not be simulated due to the deletion of elements, and as such the failure appeared to be brittle.

1.6.2.4 UNIVERSITY OF VIRGINIA / GENERAL MOTORS: 2005

One of the most detailed reports of a validated finite element model of the leg was presented by Untaroiu *et al.* (2005). This model was built for the purposes of assessing pedestrian impacts, and the geometry of the bones and soft tissues were based on the Visible Human Male Project (The National Library of Medicine). Transverse contour lines were identified for the exterior and interior surfaces of the bones, and in the epiphyseal regions only the exterior contours obtained (assuming the interior was filled with cancellous bone). It was meshed using TrueGrid® (XYZ Scientific Applications, Inc, Livermore, CA, USA), a hexahedral mesh generator, and the diaphyseal cortical

bone and epiphyseal cancellous bone modeled with solid elements, and the epiphyseal cortical bone with shell elements. The solids and shells were joined using a transition region.

The mesh was verified for geometric parameters to assess its quality. LS-Dyna® (Livermore Software Technology Corp., Livermore, CA, USA) was used as the FE solver (more detail in Section 6.2.1). Cortical and cancellous bones were assumed to be isotropic elastic-plastic materials, and the cortical bone assigned a tangent stiffness of 100 MPa, and cancellous bone modeled as elastic-perfectly plastic. Strain rate sensitivity was included using explicit load curves. Assumptions made due to the limitations of the material models available included the material being isotropic and having properties equal in tension and compression. Fracture was modeled using element elimination (*i.e.*, an LS-Dyna® technique to be described in more detail in Chapter 6), and all elements formulated using one-point integration. The model was evaluated by comparing force-deflection curves for three-point bending with quasi-static and dynamic cadaveric tests from the literature (*e.g.*, Yamada, 1970).

1.7 STUDY RATIONALE

Axial impulse loading to the lower leg can lead to devastating injuries. Currently-applied injury criteria have yet to be examined for their applicability to the loading scenarios found in anti-vehicle blasts, and as such may not define appropriate protective limits. An investigation into the current injury threshold, along with evaluation of surrogates for assessing injury risk would help to better define the tolerance of the lower leg to impact, ultimately leading to better safety standards.

Table 1.4: Summary of Previous Impact Simulations
The key parameters used in previous studies are summarized here.

Study	Element Type	MAT type	Failure Criteria
Tannous *et al.* (1996)	Solids	Isotropic, linear elastic	Max principal strain
Iwamoto *et al.* (2000)	Cancellous: solids; cortical: shells	Isotropic, linear elastic	Max stress
Beillas *et al.* (2001)	Cancellous: solids; cortical: shells	Isotropic elastic-plastic	Element Elimination
Untaroiu *et al.* (2005)	Cancellous, diaphyseal cortical: solids; Epiphyseal cortical: shells	Isotropic elastic-plastic	Element Elimination

Through impact testing of isolated cadaveric tibias using a custom-built testing apparatus, it is expected that injuries of varying degrees can be created by adjusting the loading parameters (*i.e.,* force, momentum, energy). The regions of the tibia which are most susceptible to fracture as a result of axial compression will be identified, and strain data during fractures collected. It is hoped that by determining a relationship between loading parameters and injury level, an improved injury tolerance equation can be developed in order to identify safe loading limits for the lower leg.

Test surrogates which have the potential to be useful tools for quantifying injury risks will be similarly subjected to impact loading. The currently used Anthropomorphic Test Device, along with Sawbone® synthetic tibias will be assessed for their ability to represent cadaveric bone response. A validated finite element model of a representative tibia will be developed based on the results of the experimental testing as a final method for assessing injury risk. This model will be correlated to experimental data from impact tests. This will allow for further loading mechanisms to be analyzed without the costly and time consuming need for cadaveric testing, and can be used for future survivability analyses.

This research will provide further characterization of the shank and its material properties and fracture mechanisms. It will be used to define injury tolerance levels for occupants subjected to anti-vehicle land mines, which will be used in the development of protection systems, and ultimately to reduce lifestyle changing injuries and the need for traumatic amputations.

1.8 OBJECTIVES AND HYPOTHESES

The objectives of this thesis were:

1. To develop a testing apparatus that would allow ATD, cadaveric, and synthetic tibias to be subjected to various impact loads with momentum/energy being controlled independently of force;
2. To experimentally determine an injury criterion for the isolated tibia specific to short-duration high-force axial loading scenarios;
3. To investigate the applicability of the ATD and Sawbone® synthetic bone model for injury prediction; and
4. To develop a finite element model of a representative cadaveric specimen using computed tomography scans, and to directly compare it to experimentally-obtained data.

The corresponding hypotheses were:

1. An apparatus could be developed that would allow impacts to be applied with different energies, momentums, forces, and impulses, in order to vary these parameters independently.
2. The force tolerance of the tibia would be higher than previously reported whole-leg studies due to the shorter duration and isolation from other bones, and the injury tolerance of the tibia would be dependent on an additional parameter such as kinetic energy or momentum.

3. The ATD would be useful for measuring loads, but not for predicting fractures. The synthetic bone model would be too weak to be considered a biofidelic representation of the cadaveric tibia.
4. A finite element model of a cadaveric bone could be developed that matched the experimental tests in fracture pattern and location, load, load duration, and cortical bone strains.

1.9 THESIS OVERVIEW

This thesis is written in an integrated article format. Chapter 2 describes the testing apparatus that was developed and validated to allow impacts to be applied to specimens, along with the associated instrumentation. Chapter 3 outlines the experimental study that was conducted on cadaveric tibias to develop an axial injury criterion, with a comparison to ATD measured outputs. Chapter 4 describes the corresponding experimental study that was conducted on synthetic tibias to assess their ability to represent cadaveric bones. In Chapter 5 the methods that were used to create a finite element mesh from Computed Tomography scans are presented. Chapter 6 presents the finite element model that was generated and evaluated for a representative cadaveric tibia. Chapter 7 summarizes the conclusions of this thesis, as well as discusses potential future work related to these studies.

1.10 REFERENCES

Banglmaier, R.F., Dvoracek-Driskna, D., Oniang'o, T.E., and Haut, R.C. (1999) Axial compressive load response of the 90 degrees flexed human tibiofemoral joint. 43rd Stapp Car Crash Conference Proceedings.

Beaugonin, M., Haug, E., and Cesari, D. (1997) Improvement of numerical ankle/foot model: modeling of deformable bone. *Stapp Car Crash Journal.* **41,** 225-237.

Beckwith, T.G., Marangoni, R.D., and Lienhard V, J.H. (1993) Mechanical Measurements: Fifth Edition. Addison-Wesley Publishing, Reading, MA, USA.

Beillas, P., Begeman, P.C., Yang, K.H., King, A.I., Arnoux, P.J., Kang, H.S., Kayvantash, K., Brunet, C., Cavallero, C., and Prasad, P. (2001) Lower limb: advanced FE model and new experimental data. *Stapp Car Crash Journal.* **45,** 469-494.

Bergeron, D.M., Coley, G.G., Fall, R.W., and Anderson, I.B. (2006) Assessment of lower leg injury from land mine blast - Phase 1. TR 2006-051. Defence R&D Canada - Suffield.

Bergeron, D.M., Coley, G.G., Rountree, M.S., Anderson, I.B., and Harris, R.M. (2001) Assessment of foot protection against anti-personnel landmine blast using a frangible surrogate leg. UXO Forum 2001.

Bir, C., Barbir, A., Dosquet, F., Wilhelm, M., van der Horst, M.J., and Wolfe, G. (2008) Validation of lower limb surrogates as injury assessment tools in floor impacts due to anti-vehicular land mines. *Journal of Military Medicine* **173,** 1180-1184.

Bogosian, D. and Der Avanessian, H. (2004) Blunt trauma from blast-induced building debris. 31st Explosives Safety Seminar San Antonio, Texas.

Burstein, A.H., Reilly, D.T., and Martens, M. (1976) Aging of bone tissue: mechanical properties. *The Journal of Bone and Joint Surgery (American volume).* **58,** 82-86.

Carter, D.R. and Hayes, W.C. (1977) The compressive behavior of bone as a two-phase porous structure. *The Journal of Bone and Joint Surgery (American volume).* **59,** 954-962.

Chong, A.C., Miller, F., Buxton, M., and Friis, E.A. (2007) Fracture toughness and fatigue crack propagation rate of short fiber reinforced epoxy composites for analogue cortical bone. *Journal of Biomechanical Engineering* **129,** 487-493.

Cowin, C.S. (1991) The Mechanical Properties of Cortical Bone Tissue. In *Bone Mechanics* (Edited by Cowin, C.S.) Pp. 98-125. Boca Raton, FL., USA.

Crandall, J.R., Portier, L., Petit, P., Hall, G.W., Bass, C.R., Klopp, G.S., Hurwitz, S., Pilkey, W.D., Trosseille, X., Tarriere, C., and Lassau, J.-P. (1996) Biomechanical

response and physical properties of the leg, foot, and ankle. Society of Automotive Engineers, Inc.

Cristofolini, L. and Viceconti, M. (2000) Mechanical validation of whole bone composite tibia models. *Journal of Biomechanics* **33,** 279-288.

Dunham, C.E. (2005) Biomechanical assessments of synthetic and cadaveric distal humeri for laboratory-based investigations. M.E.Sc. Thesis, *The University of Western Ontario*.

Footner, M.J., Bergeron, D.M., and Swinton, R.J. (2006) Development and calibration of a frangible leg instrumented for compression and bending. Australian Government, Department of Defence. DSTO-TR-1829. Australia, Defence Science and Technology Organisation.

Funk, J.R., Crandall, J.R., Tourret, L.J., MacMahon, C.B., Bass, C.R., Patrie, J.T., Khaewpong, N., and Eppinger, R.H. (2002) The axial injury tolerance of the human foot/ankle complex and the effect of Achilles tension. *Journal of Biomechanical Engineering* **124,** 750-757.

Griffin, L.V., Harris, R.M., Hayda, R.A., and Rountree, M.S. (2001) Loading rate and torsional moments predict pilon fractures for antipersonnel blast mine loading. International IRCOBI Conference on the Biomechanics of Impacts, Isle of Man, UK.

Harris, R.M., Rountree, M.S., Griffin, L.V., Hayda, R.A., Bice, T., and Mannion, S.J. (2000) Final report of the lower extremity assessment program (LEAP 99-2) - Volume II. Fort Sam Houston Texas USA, U.S. Army Institute of Surgical Research Extremity Trauma Study Branch.

Haut, R.C. and Atkinson, P.J. (1995) Insult to the human cadaver patellofemoral joint: Effect of age on fracture tolerance and occult injury. 40th Stapp Car Crash Conference.

Heiner, A.D. (2008) Structural properties of fourth-generation composite femurs and tibias. *Journal of Biomechanics* **41,** 3282-3284.

Heiner, A.D. and Brown, T.D. (2001) Structural properties of a new design of composite replicate femurs and tibias. *Journal of Biomechanics* **34,** 773-781.

Hirsch, A.E. (1964) Man's response to shock motion. Report 1797. Washington, D.C., USA, David Taylor Bassin Model.

Imai, K., Ohnishi, I., Bessho, M., and Nakamura, K. (2006) Nonlinear finite element model predicts vertebral bone strength and fracture site. *Spine* **31,** 1789-1794.

Insurance Institute for Highway Safety. (2004) Frontal offset crashworthiness evaluation. Guidelines for rating injury measures.

Iwamoto, M., Miki, K., and Tanaka, E. (2005) Ankle skeletal injury predictions using anisotropic inelastic constitutive model of cortical bone taking into account damage evolution. Society of Automotive Engineers, Inc.

Iwamoto, M., Tamura, A., Furusu, K., Kato, C., Miki, K., Hasegawa, J., and Yang, K.H. (2000) Development of a finite element model of the human lower extremity for analyses of automotive crash injuries. In *2000-01-0621.* Computer Applications for Crash, Optimization, and Simulation Research, Society of Automotive Engineers, Detroit, MI, USA.

Keown, M. and Anctil, B. (2004) Review of lower leg injury criteria and physical surrogates. R03-15. Biokinetics and Associates Ltd.

Kim, Y.S., Choi, H.H., Cho, Y.N., Park, T.J., Lee, J.B., Yang, K.H., and King, A.I. (2005) Numerical investigations of interactions between the knee-thigh-hip complex with vehicle interior structures. *Stapp Car Crash Journal.* **49,** 85-115.

Kitagawa, Y., Ichikawa, H., King, A.I., and Levine, R.S. (1998) A severe ankle and foot injury in frontal crashes and its mechanism. Society of Automotive Engineers, Inc.

Kuppa, S., Haffner, M., Eppinger, R., and Saunders, J. (2001a) Lower extremity response and trauma assessment using the THOR-Lx/HIIIr and the Denton leg in frontal offset vehicle crashes. National Highway Traffic Safety Administration, The Netherlands.

Kuppa, S., Klopp, G.S., Crandall, J.R., Hall, G., Yoganandan, N., Pintar, F.A., Eppinger, R.H., Sun, E., Khaewpong, N., and Kleinberger, M. (1998) Axial impact characteristics of dummy and cadaver lower limbs. Society of Automotive Engineers, 98-S7-O-10.

Kuppa, S., Wang, J., Haffner, M., and Eppinger, R. (2001b) Lower extremity injuries and associated injury criteria. Proceedings of the 17th International Technical Conference on Enhanced Safety of Vehicles Paper 457. Amsterdam, Netherlands.

Manseau, J. (2005) Injury assessment method proposal for vehicle mine protection testing. TM 2004-241. Defence Research & Development Canada - Valcartier.

Manseau, J. and Keown, M. (2005) Evaluation of the Complex Lower Leg (CLL) for its use in anti-vehicular mine testing applications. International IRCOBI Conference, Prague, Czech Republic.

Marieb, E.N. (2004) *Human Anatomy & Physiology.* Pearson Benjamin Cummings, San Francisco, CA, USA.

Medin, A., Axelsson, H., and Suneson, A. (1998) The reactions of the crew in an armoured personnel carrier to an anti-tank mine blast. Defence Research Establishment. FOA-R-98-00720-310-SE.

Mertz, H. (1993) Anthropomorphic Test Devices. In *Accidental Injury, Biomechanics, and Prevention* (Edited by Nahum,A.) Springer-Verlag.

NATO. (2007) Test Methodology for Protection of Vehicle Occupants against Anti-Vehicular Landmine Effects. Final Report of HFM-090 Task Group 25.

Nies, T.I. (2004) Mine-clearing vehicle MINEWOLF: Biomechanical assessment of mine-clearing tests. WTD 91: German Federal Armed Forces Technical Center for Weapons and Ammunition. 91-400-058/04.

Owen, C. (2001) Requirements for the evaluation of the risk of injury to the ankle in car impact tests. National Highway Traffic Safety Administration, The Netherlands.

Petit, P. and Trosseille, X. (1999) Comparison of the THOR, HYBRID III and cadaver lower leg dynamic responses in dorsiflexion.

Radonic, V., Giunio, L., Biocic, M., Tripkovic, A., Lukcic, B., and Primorac, D. (2004) Injuries from antitank mines in southern Croatia. *Journal of Military Medicine.* **169,** 320-324.

Seipel, R.C., Pintar, F.A., Yoganandan, N., and Boynton, M.D. (2001) Biomechanics of calcaneal fractures: a model for the motor vehicle. *Clinical Orthopaedics and Related Research.* (388):218-224.

Taddei, F., Cristofolini, L., Martelli, S., Gill, H.S., and Viceconti, M. (2006) Subject-specific finite element models of long bones: An in vitro evaluation of the overall accuracy. *Journal of Biomechanics.* **39,** 2457-2467.

Takahashi, Y., Kikuchi, Y., Konosu, A., and Ishikawa, H. (2000) Development and validation of the finite element model for the human lower limb of pedestrians. *Stapp Car Crash Journal* **44**.

Tannous, R.E., Bandak, F.A., Toridis, T.G., and Eppinger, R. (1996) A three-dimensional finite element model of the human ankle: development and preliminary application to axial impulsive loading. Society of Automotive Engineers, Inc.

Untaroiu, C., Darvish, K., Crandall, J., Deng, B., and Wang ,J.T. (2005) A finite element model of the lower limb for simulating pedestrian impacts. *Stapp Car Crash Journal.* **49,** 157-181.

Valle, L. and Ray, M.H. (2005) Development and validation of a 50th percentile male human femur: Attachment A. Worcester Polytechnic Institute. Worcester, MA, National Highway Traffic Safety Administration.

van der Horst, M.J., Simms, C.K., van Maasdam, R., and Leerdam, P.J.C. (2005) Occupant lower leg injury assessment in landmine detonations under a vehicle. IUTAM Symposium on Impact Biomechanics, Dublin, Ireland.

Wang, J., Bird, R., Swinton, B., and Krstic, A. (2001) Protection of lower limbs against floor impact in army vehicles experiencing landmine explosion. *Journal of Battlefield Technology* 4[3], 8-12.

Yamada, H. (1970) *Strength of biological materials*. The Williams & Wilkins Company, Baltimore, MD, USA.

Yoganandan, N., Pintar, F.A., Boynton, M., Begeman, P., Prasad, P., Kuppa, S., Morgan, R.M., and Eppinger, R. (1996) Dynamic axial tolerance of the human foot-ankle complex. Society of Automotive Engineers, Inc. 962426, 207-218.

Yoganandan, N., Pintar, F.A., Kumaresan, S., and Boynton, M. (1997) Axial impact biomechanics of the human foot-ankle complex. *Journal of Biomechanical Engineering* **119,** 433-437.

Zuby, D.S., Nolan, J.S., and Sherwood, C.P. (2001) Effect of Hybrid III geometry on upper tibia bending moments. Society of Automotive Engineers. Biomechanics Research and Development (SP-1577), 1-14. Warrendale, PA, USA.

CHAPTER 2 – Development of a Pneumatic Test Apparatus

Overview: *This chapter details the development and validation of the custom-built testing apparatus to be used for the experimental studies found in Chapter 3 and Chapter 4.* [2]

2.1 INTRODUCTION

Numerous previous studies have quantified tolerance values for lower leg injuries (Kuppa *et al.*, 2001; Funk *et al.*, 2002; Griffin *et al.*, 2001; Seipel *et al.*, 2001; Yoganandan *et al.*, 1996). Based on the work of Yoganandan *et al.* (1996), NATO (2007) has adopted a standard for vehicle mine testing to be a maximum axial compressive load of 5.4 kN. This force value, however, was determined from cadaveric tests performed to mimic a car crash event (slower in duration than AV mine events), (Yoganandan *et al.*, 1996; Yoganandan *et al.*, 1997). It is therefore desirable to investigate the appropriateness of this load value for controlled short-duration high-impulse scenarios.

AV mine blast events have been shown to occur between 3 – 10 ms, and have been simulated in the range of 5 – 12 m/s (Bir *et al.*, 2008; Wang *et al.*, 2001). Axial tibia injuries have been shown in previous studies to occur for forces up to 12 kN (Yoganandan *et al.*, 1996). These parameters comprise the range for investigation in the current study. In addition to force, the current authors have postulated that impact velocity may be a secondary and important injury factor, as it influences both momentum

[2] A version of this work has been published: Quenneville CE, Fraser GS, and Dunning CE. (2010). Development of an Apparatus to Produce Fractures From Short-Duration High-Impulse Loading With an Application in the Lower Leg, *Journal of Biomechanical Engineering* (132): 014502.

and energy imparted to the lower leg. Therefore, it is of interest to be able to impart a range of impact forces with varied velocity levels to examine the possibility of velocity-dependency.

In order for the effect of these factors on injury tolerance to be examined, a controllable test apparatus is required. The devices used to conduct the previous studies were either pendulum or piston-driven (Section 1.5.3). Some specimens were mounted on bearings, and free to move following impact (Yoganandan *et al.*, 1996), while others had the knee rigidly held (Owen, 2001; Funk *et al.*, 2002). Instrumentation on the test devices often included load cells, which could be located between the impactor and the foot (Funk *et al.*, 2002) or at the proximal mounting of the knee (Yoganandan *et al.*, 1996). The high-impulse loading being examined in the current study achieves higher speeds and forces over shorter durations than the previous studies, and as such a robust and controllable specialized test apparatus instrumented to fully quantify the events is required.

The purpose of this study was to design and develop a testing apparatus that applies controlled impulse loads over a large range of magnitudes and velocities to cadaveric, synthetic, or Anthropomorphic Test Device (ATD) tibias; and to evaluate the capability of this system to recreate an AV mine blast scenario.

2.2 TEST APPARATUS

The apparatus described in this chapter is composed of several systems (Figure 2.1). The mechanical structure consists of the testing area, and is operated using a system of pneumatics. Electronic instrumentation on the structure is used to collect data using a

(a)

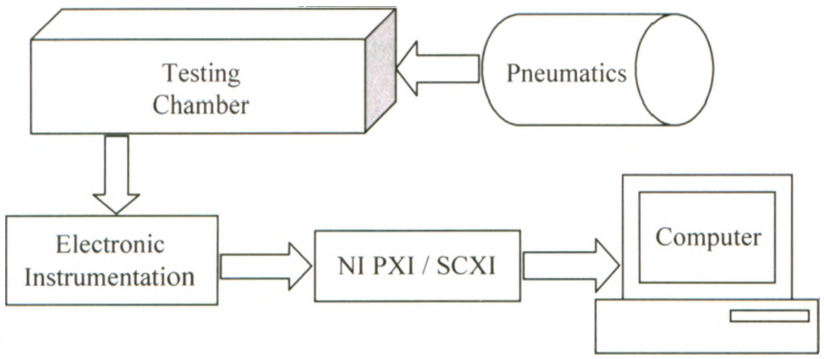

(b)

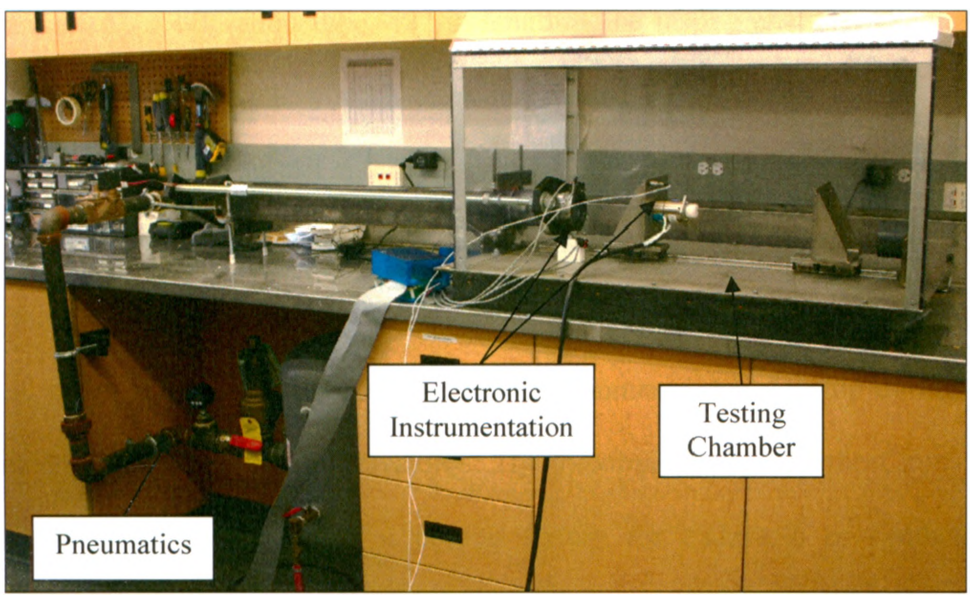

Figure 2.1: Test Apparatus Systems
A schematic **(a)** and photograph **(b)** of the test apparatus are given. Tests were conducted within the mechanical structure, which operated off a pneumatic system. Electronic instrumentation on the structure was measured using a National Instruments (NI) PXI data acquisition system complete with a SCXI 1010 chassis, and recorded on a computer.

National Instruments data acquisition system (NI – PXI 1050 and SCXI 1010) via a computer and custom-written LabVIEW® programming. Each of the subsystems will be discussed in detail below. The step-by-step operation of the apparatus is detailed in Appendix C.

2.2.1 *MECHANICAL STRUCTURE*

The apparatus consists of a pneumatic system connected to a testing chamber via a 3" diameter Lexan® acceleration tube, 42" in length. The testing chamber (Figure 2.2) is made of a 24" x 36" stainless steel sheet surrounded by protective Lexan® shielding. This sheet supports a linear rail and ball bearing system, which connects to two brackets used to support both ends of a test specimen in a horizontal orientation (see Appendix D for Technical Drawings). Each bracket is attached to two bearings separated by 1" using a plate in order to counteract the strong bending moments that develop during impact, thus protecting the bearings from breaking. The proximal bracket (furthest from impact) has attachment points for either a potting fixture for cadaveric or synthetic bone specimens, or an angled support for an ATD lower leg (Figure 2.3). The details of the design of the angled support can be found in Restorick (2007). The distal bracket, which receives the impulse, is covered with a piece of ½" urethane foam (E = 2.5 MPa) in order to control the duration of load application. The impulse is transferred from the distal bracket to the distal surface of the tibia via an artificial talus made of polyethylene that attaches to the load cell (see section 2.2.3). The mounting plate for the talus allows precise adjustment of the location to best sit within the articular surface of the distal tibia,

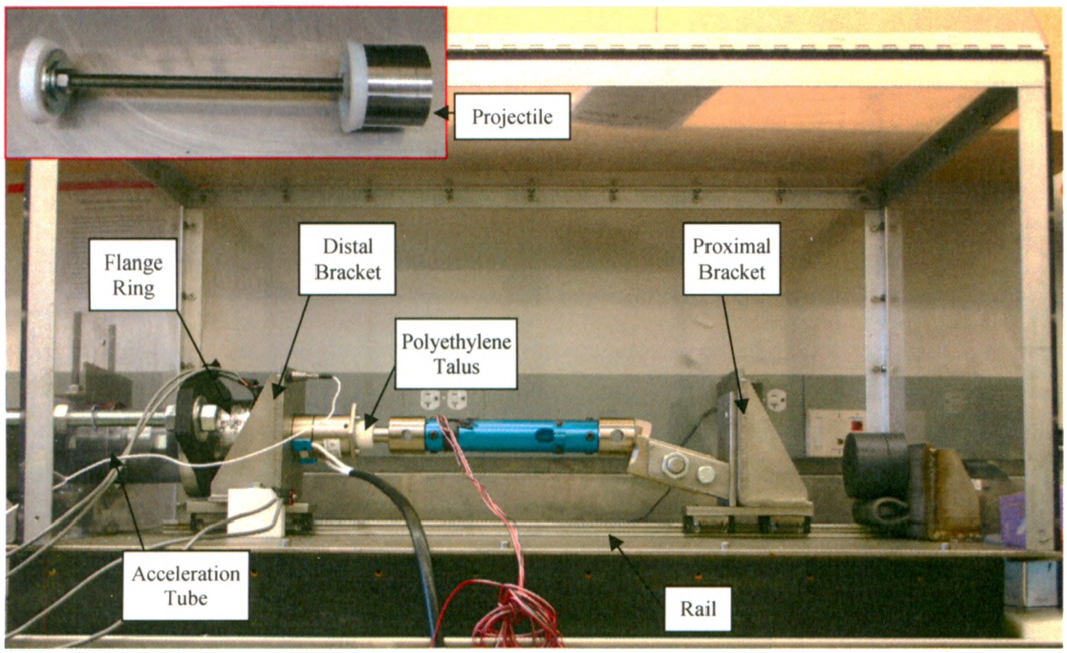

Figure 2.2: Testing Chamber
A projectile (inset) passes through the acceleration tube and strikes the distal bracket. Both the distal and proximal brackets travel on bearings on a rail, and support a lower limb specimen. The impulsive load is passed to the specimen via a polyethylene talus. The flange ring restricts the projectile from fully exiting the tube. The entire chamber is enclosed in Lexan shielding, with a hinged front door for access to the specimen.

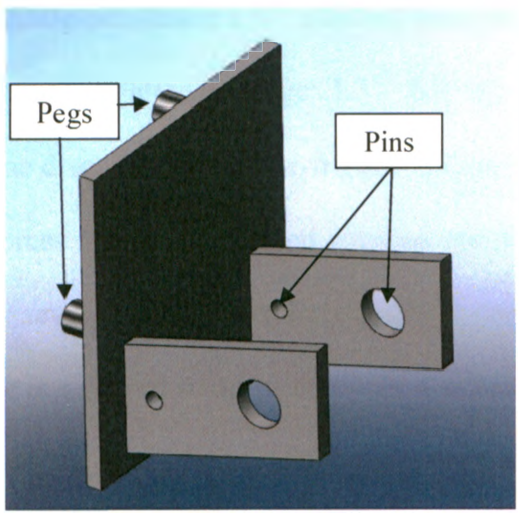

Figure 2.3: Angled Bracket for ATD Attachment
The knee clevis of the ATD lower leg was mounted on the proximal bracket via two pegs on the back of the angled bracket, which held the leg in a horizontal orientation using two pins.

and the edges are rounded to eliminate any sharp contact points that may act as stress concentrators.

A projectile (Figure 2.2, inset) is propelled through the acceleration tube, and supplies the required impulse to the distal end of the specimen. The distance it travels along the tube can be varied between 5 – 85 cm, thereby altering its exit velocity at a given pressure level. This projectile consists of a ¾" stainless steel threaded rod with a number of discs, allowing its mass to be altered (range: 1.3 – 6.8 kg). At the back end of the projectile is a polyethylene disc, ensuring a low-friction sliding fit within the acceleration tube. Due to the large forces that develop when arresting the projectile after impact, the front end is supported by several 3" steel Fender washers instead of a polyethylene disc. The front of the projectile is a curved stainless steel disc that ensures a consistent point of impact. At the exit end of the acceleration tube is an aluminum flange ring, which fits over the end of the acceleration tube, but has a lip that is sized to allow the front of the projectile to strike the bracket, but not fully exit the tube (*i.e.* as a safety precaution). Again, due to the large forces required to arrest the projectile, the flange ring is clamped to the pneumatics using two reinforcing pieces connected by 1" steel threaded rods, effectively sandwiching the acceleration tube between the flange ring and the pneumatic system.

2.2.2 *Pneumatic System*

The pneumatics supply a fast burst of pressurized air to propel the projectile through the acceleration tube (Figure 2.4). The system uses 100 psi air fed through an electrically-controlled pressure regulator (500-AG, ControlAir Inc., Amherst, NH, USA)

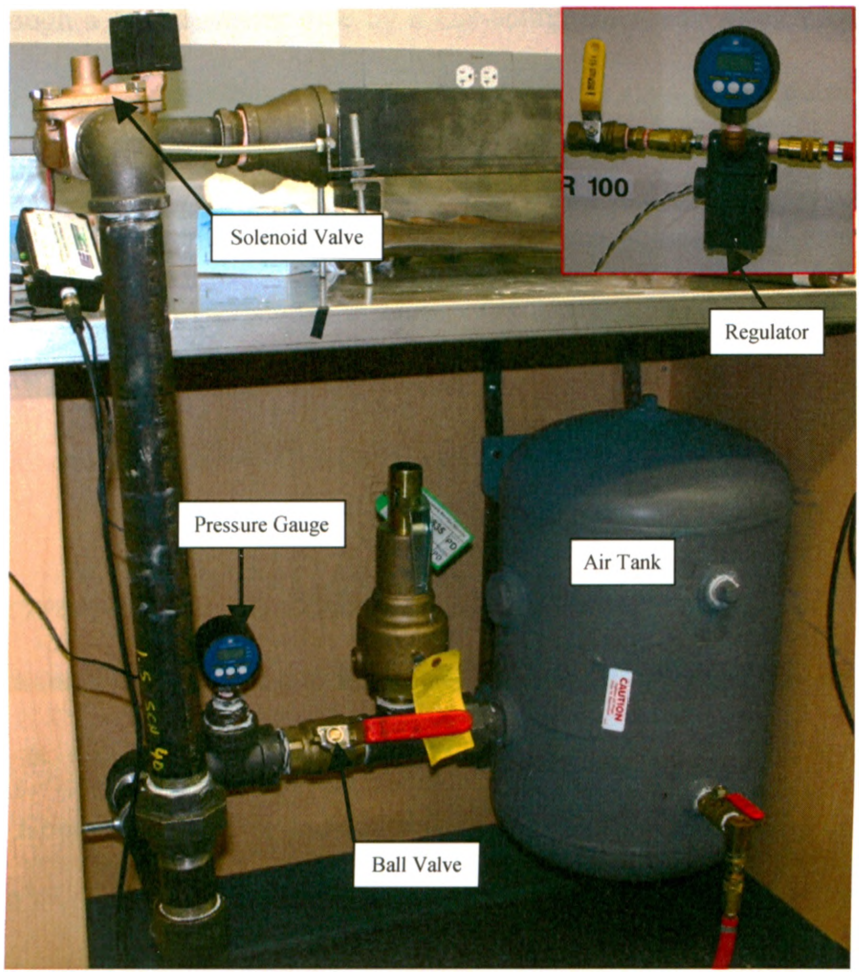

Figure 2.4: Pneumatics of the Test Apparatus
Air at 100 psi is supplied to the regulator, which controls the pressure to the air tank. A ball valve is included for safety purposes, and the pressure of the air prior to release is recorded from the digital pressure gauge. A fast-acting solenoid valve releases the air to the acceleration tube.

to an air tank (capacity = 13 gallons). This regulator operates by providing a pressure that is proportional to an input voltage, which is generated using a LabVIEW® program (National Instruments, Austin, TX, USA) (Appendix E). Compressed air is released from the tank through a 1.5" diameter pipe by a fast-acting solenoid valve (VXR2380, SMC Corporation, Tokyo, Japan) that is electronically triggered via a 5VDC pulse. The signal to activate the valve is generated using a second LabVIEW® program (Appendix E) that connected to an electronics control box built by the University Electronics Shop (Appendix F). This 5VDC signal is output for 0.25s, as this provides a consistent pressure for the entire duration of the projectile's travel. Varying the pressure allows further control over the projectile's exit velocity.

2.2.3 *ELECTRONIC INSTRUMENTATION*

The apparatus is instrumented to fully quantify each test (Figure 2.5). Attached to the flange ring at the end of the acceleration tube are two reflective optical sensors (HOA0149, Honeywell Sensing and Control, Golden Valley, MN, USA) that determine the projectile's velocity immediately prior to impact. These optical sensors consist of an infrared (IR) emitting diode and a phototransistor, which responds to the IR light when a reflective object passes in front of it. The velocity of the projectile is determined using a microcontroller program which detects the difference in activation times between the two reflective sensors, and is subsequently divided by their separation distance. This was integrated into the electronics box that was built by the Electronics Shop at The University of Western Ontario (Appendix F). The calculated time is outputted in two ways: firstly, as a voltage signal that was proportional to the time (1 V = 4 ms), and

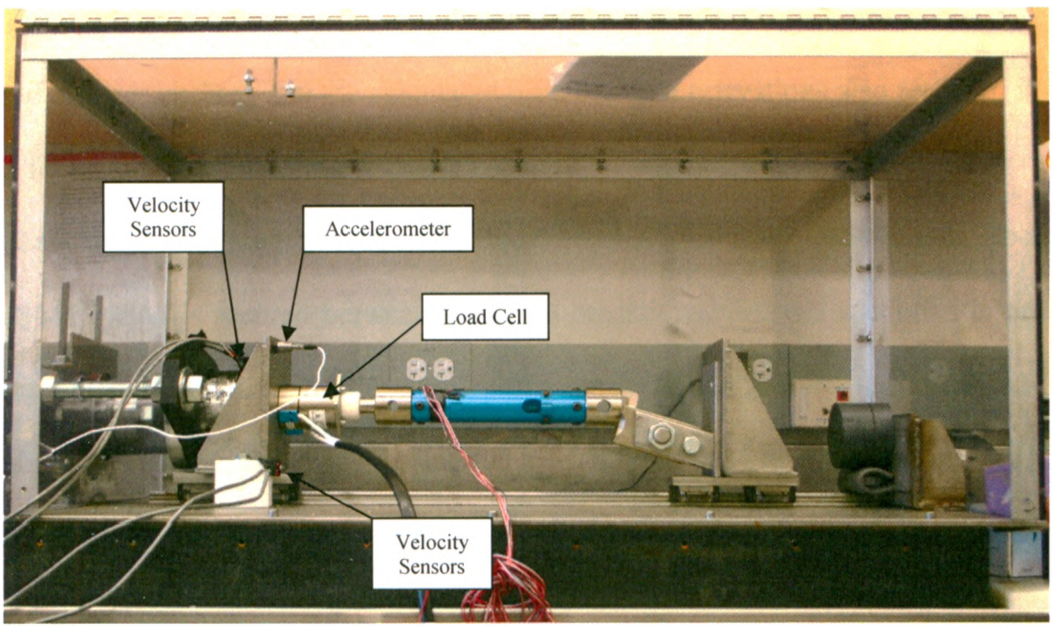

Figure 2.5: Electronic Instrumentation of Apparatus
The flange ring was instrumented with optical sensors to detect the velocity of the projectile immediately prior to impact. A second set of sensors was used to measure the velocity of the distal bracket immediately following impact. The distal bracket was instrumented with a uniaxial accelerometer, and load was transferred to the tibia via a six-degree-of-freedom load cell. All signals were recorded at 15 kHz.

secondly as a 5 V square pulse of 1000x the duration in length. Both methods were collected separately for redundancy. A second set of velocity sensors is attached to the base of the testing chamber via a polyethylene block in order to measure the velocity of the distal bracket immediately following impact. These sensors are connected to a second electronics box, and the calculated time between activations also recorded in both ways for redundancy.

A six degree-of-freedom load cell (Model 1914D, Robert A. Denton, Inc., Rochester Hills, MI, USA) is secured between the distal bracket and the test specimen in order to measure the load imparted to the tibia, with a maximum axial force limit of 22 kN. By locating it adjacent to the specimen inertial effects of the load cell were minimized. Also mounted to the distal bracket is a 500 G uniaxial accelerometer (PCB Piezotronics, Depew, NY, USA), selected based on accelerations reported in Nies (2004).

The signals from the instrumentation (two sets of velocity sensors, load cell, and accelerometer) are fed to the electronics box and passed through a ribbon cable to a data acquisition system (PXI 1050 / SCXI 1010, National Instruments, Austin, TX, USA). This operated in conjunction with a custom-written LabVIEW® program (National Instruments, Austin, TX, USA) at a sampling rate of 15 kHz (Appendix E). The entire impact event is also recorded using a black and white high speed camera (Motionscope M2, Redlake Inc., Tucson, AZ, USA) at 1000 frames per second.

2.2.4 *VALIDATION PROTOCOL*

To verify the apparatus' ability to create a suitable impulse (*i.e.* 1 – 12 kN, 5 – 10 m/s, 3 – 10 ms duration) (Wang *et al.*, 2001), a test protocol was developed to examine

the role of the independent variables (pressure, projectile mass, and projectile travel distance) on the dependent variables of interest (projectile exit velocity, force imparted to the distal leg, and acceleration of the distal bracket). Three projectile masses (1.3, 3.9 and 6.8 kg) were each tested at a minimum of 4 different pressures (range: 6 – 17 psi) from three initial starting distances (24, 40 and 56 cm from the end of the acceleration tube). All tests were performed against a Denton ATD lower leg (Robert A. Denton, Inc., Rochester Hills, MI, USA) (Appendix G), which can be exchanged for a cadaveric or synthetic bone in future tests without altering the test setup. The load cells in the ATD tibia were removed and replaced with structural blanks in order to protect the lower load limits of these components. The momentum and kinetic energy that could be applied to a specimen as a result of these impacts were calculated from the measured impact velocity. System repeatability was quantified by the standard deviation in both velocity and force over five trials for a single pressure and travel distance for each mass (8.6 psi and 40 cm, respectively). A custom-written LabVIEW® program (National Instruments, Austin, TX, USA) calculated the momentum and energy of the projectile, as well as filtered the acceleration signal (f_c = 1000 Hz) and integrated the force in the axial direction to compute the impulse received by the tibia (Appendix E).

2.3 RESULTS

For all mass-distance combinations, projectile velocity varied quadratically with pressure (Figure 2.6, $R^2 > 0.99$), and force also varied quadratically with pressure (Figure 2.7, $R^2 > 0.96$). Overall, the projectile exit velocities ranged between 1.3 and 10.2 m/s. The axial forces imparted to the load cell ranged between 1.2 and 15.9 kN; however, the

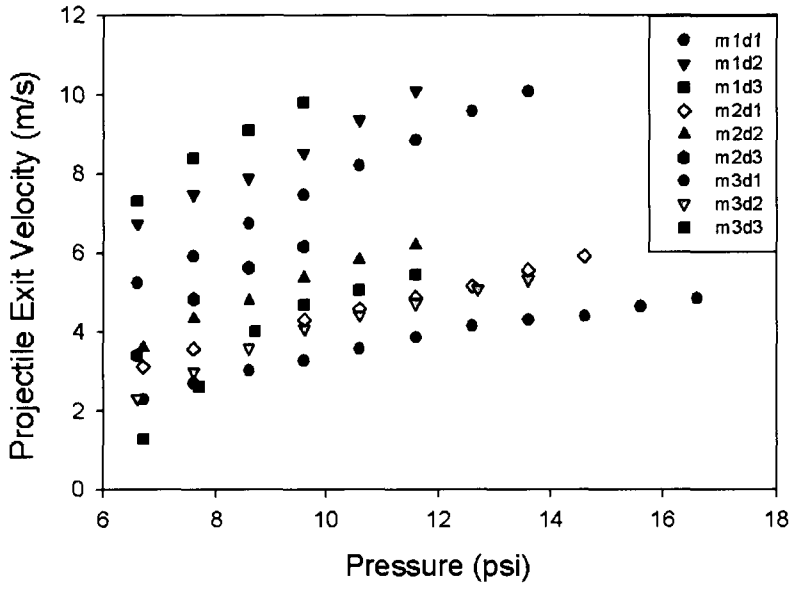

Figure 2.6: Effect of Pressure on Projectile Exit Velocity
Projectile velocity was quadratically dependent on pressure ($R^2 > 0.99$) and is presented for each mass (m1 = 1.3, m2 = 3.9, and m3 = 6.8 kg) over the three travel distances (d1 = 24, d2 = 40, and d3 = 56 cm). Velocity decreased with increased projectile mass and increased with distance.

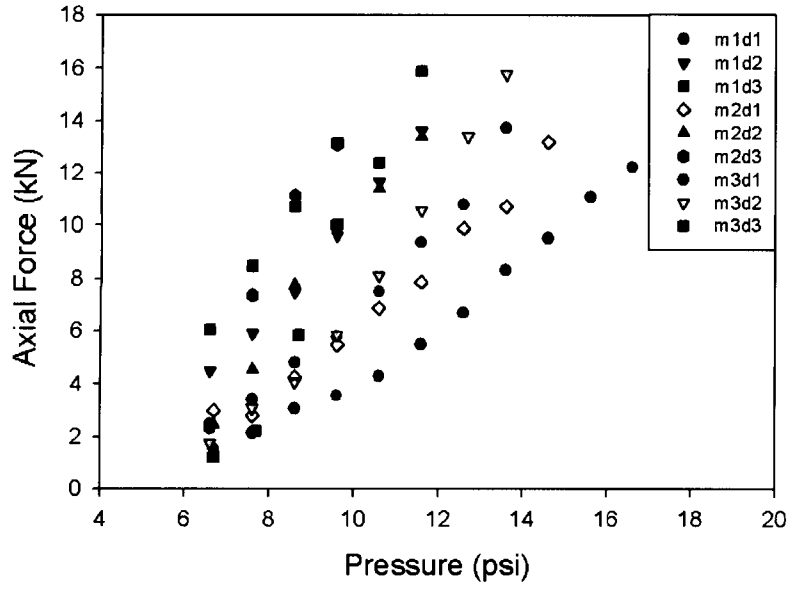

Figure 2.7: Effect of Pressure on Axial Force
Axial force varied quadratically with pressure ($R^2 > 0.96$) for each mass (m1 = 1.3, m2 = 3.9, and m3 = 6.8 kg) over the three travel distances (d1 = 24, d2 = 40, and d3 = 56 cm). Axial force decreased with increased projectile mass and increased with travel distance.

magnitude of force is dependent upon the properties of the specimen being impacted, and as such these values are applicable only to the currently-tested ATD lower leg. Increasing projectile mass for a given pressure decreased both velocity and force; whereas increasing travel distance increased both velocity and force. The standard deviation among repeated trials ranged between 0 – 2% for exit velocity and 2 – 7% for force. The durations of the applied impulses over the entire range of testing were between 2.9 and 13.1 ms. At the repeated tests, the average impact duration was 6.0 ms, with a standard deviation of 0.5 ms.

Figure 2.8 shows that for a given exit velocity, force can be controlled by varying the mass of the projectile. Against the ATD lower leg, a force of 5.4 kN (*i.e.,* the current injury limit for the lower leg) can be achieved at velocities of 3.7, 4.3 or 7.0 m/s for the masses tested. Similar relationships are achieved when examining force versus momentum applied to the leg (Figure 2.9), with momentums being created between 6.8 and 37.1 Ns. For the current injury limit of a force of 5.4 kN, momentums can be created at 9.1, 16.6, and 24.7 Ns (with the highest being achieved using the heaviest mass). This allowed a 63% variation in momentum applied to the specimen. These momentums created corresponding impulses (as measured by integrating the force-time curve from the load cell) that ranged from 1.9 to 14.7 Ns.

Kinetic energies that were imparted to the leg ranged from 5.6 to 101.0 J. Figure 2.10 graphs kinetic energy versus impact force, which has a quadratic relationship ($R^2 > 0.97$) and was dependent on projectile mass but not travel distance. The current injury standard of 5.4 kN could be generated with kinetic energies of 32.5, 35.5, or 46.1 J for the current masses tested.

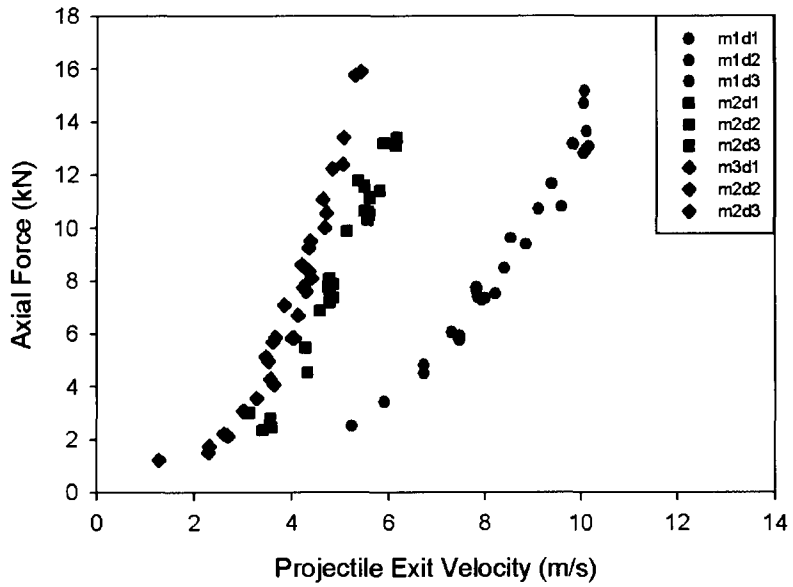

Figure 2.8: Effect of Projectile Exit Velocity on Axial Force
Axial force was quadratically dependent on projectile velocity ($R^2 > 0.97$) for each mass (m1 = 1.3, m2 = 3.9, and m3 = 6.8 kg) over the three travel distances (d1 = 24, d2 = 40, and d3 = 56 cm). Axial force increased for a given exit velocity with increasing projectile mass, but was unaffected by travel distance.

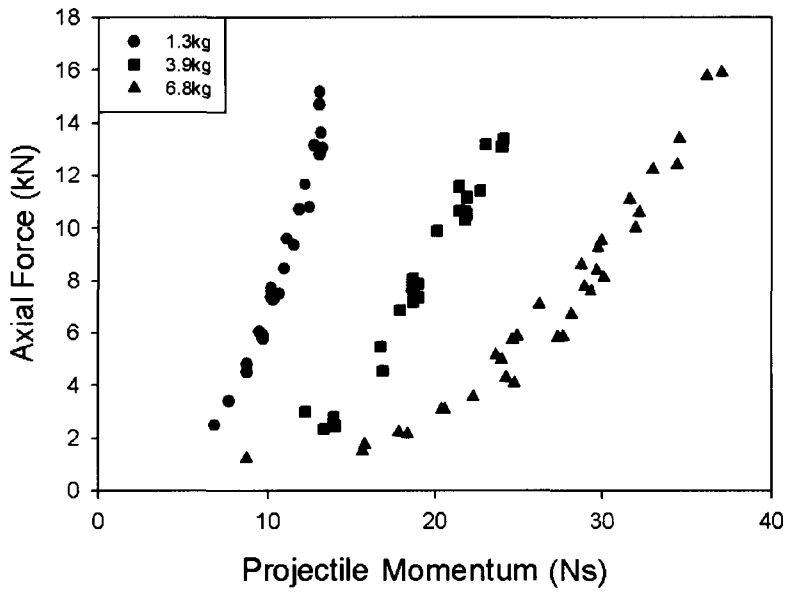

Figure 2.9: Effect of Projectile Momentum on Axial Force
Axial force was quadratically dependent on projectile momentum ($R^2 > 0.95$). The highest momentum for a given force was achieved using the heaviest projectile mass.

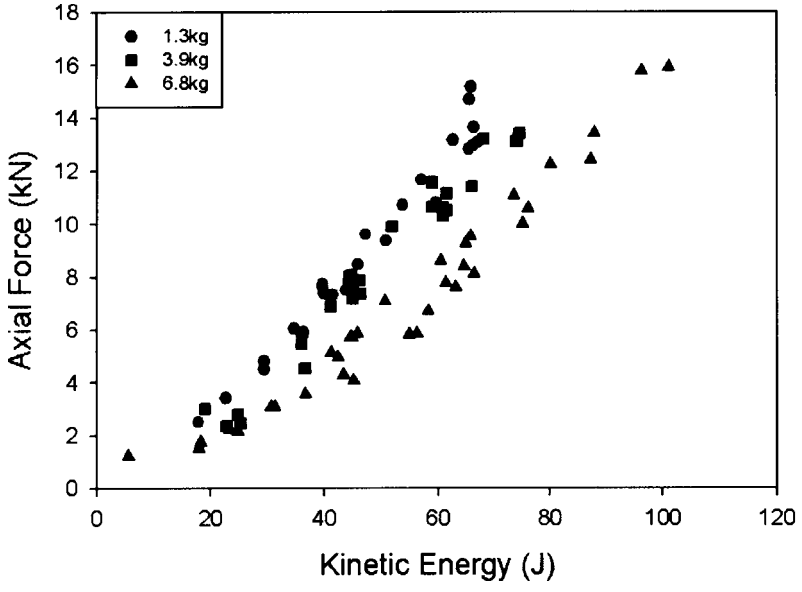

Figure 2.10: Effect of Kinetic Energy on Axial Force
Axial force was quadratically dependent on kinetic energy ($R^2 > 0.97$). The relationship was dependent on projectile mass, but not on distance.

Distal bracket velocities ranged from 0.46 m/s to 2.28 m/s (Figure 2.11), and were linearly related to exit velocity, for a given mass ($R^2 > 0.90$). As mass increased, the distal bracket velocity for a given exit velocity increased, due to the increased momentum input to the system.

While accelerations were collected, they were lower than previously anticipated (ranging from 0.25 to 11.01 G), and were therefore highly unreliable and inconsistent. It is hypothesized that this is the result of working in the lowest portion of the range of the accelerometer. As such, acceleration data are not presented here.

2.4 DISCUSSION

Lower leg damage resulting from high-impulse loading can be lifestyle-altering. By properly defining thresholds, these devastating injuries may be avoided through the design of appropriate protective measures. This device is an important tool in this assessment, as it will allow experimental tests covering a span of impulse levels to be conducted in a controlled environment, correlating injuries to applied loading.

A number of previous systems have been used to investigate the injury tolerance of the lower limb. These systems were typically operated at slower velocities (2.2 to 7.6 m/s) (Yoganandan *et al.*, 1996; Funk *et al.*, 2002) than are anticipated to be required in the current research. These studies have also not reported load durations that occurred during their testing. McKay (2008) identified that impact velocity is a critical factor and found that 8.4 m/s and 10.8 m/s produces a 10% and 50% probability of severe leg injury, respectively. However, further details on this (including impact duration and injury location) have yet to be published.

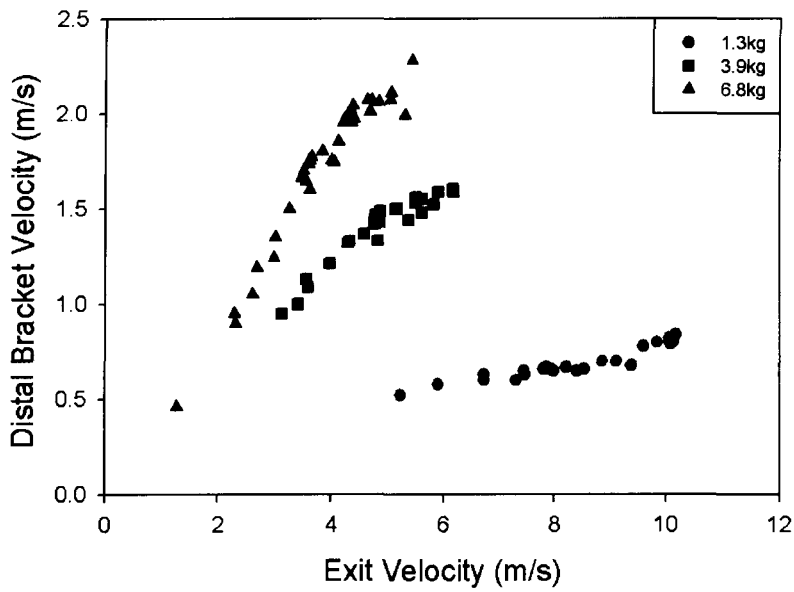

Figure 2.11: Relationship Between Exit Velocity and Distal Bracket Velocity

Distal bracket velocity was linearly dependent on exit velocity and projectile mass (due to momentum balance) ($R^2 > 0.90$).

For indirect mine blast events in particular, velocities are known to be approximately 5 - 12 m/s (Manseau and Keown, 2005; Wang *et al.*, 2001) and current injury limits suggest forces must be below 5.4 kN (NATO/PfP, 2006). Others have shown lower leg injuries to occur for axial forces between 4.5 and 10.1 kN (Yoganandan *et al.*, 1996). Validation of this device shows that it is capable of producing impulse events within the range of these parameters in a controlled, repeatable manner.

While the lower velocity and force limits of this device have been defined within this testing protocol, the upper limits have not. By further increasing the pressure and/or distance to the system's maximums (60 psi and 85 cm, respectively), the device can impart larger forces at higher velocities, but this could not be tested without exceeding the safe operating limits of the load cell. The accelerometer used in the present study was selected for a high level of accelerations, based on the acceleration limits proposed in the Lower Leg Threshold (Figure 1.9). Accelerations attained in the present study were much lower than anticipated, resulting in low-quality signals being collected.

This device is able to apply impact loads to specimens over a wide range of forces, velocities and momentums. Tests over longer loading durations could be performed by increasing the thickness of the foam on the distal bracket, which would allow for simulations of various alternate injury events. This apparatus will serve as a powerful tool for linking human injuries to the outputs obtained from an Anthropomorphic Test Device, the current standard for injury prediction. It will also be useful for evaluating potential surrogates such as synthetic bones for studies of these events. It will be used in future studies to quantify the fracture strength of cadaveric tibias (Chapter 3) and develop an injury criterion specifically for these short-duration high-impulse events.

2.5 REFERENCES

Funk, J.R., Crandall, J.R., Tourret, L.J., MacMahon, C.B., Bass, C.R., Patrie, J.T., Khaewpong, N., and Eppinger, R.H. (2002) The axial injury tolerance of the human foot/ankle complex and the effect of Achilles tension. *Journal of Biomechanical Engineering* **124,** 750-757.

Griffin, L.V., Harris, R.M., Hayda, R.A., and Rountree, M.S. (2001) Loading rate and torsional moments predict pilon fractures for antipersonnel blast mine loading. International IRCOBI Conference on the Biomechanics of Impacts, Isle of Man, UK.

Kuppa, S., Wang, J., Haffner, M., and Eppinger, R. (2001) Lower extremity injuries and associated injury criteria. Proceedings of the 17th International Technical Conference on Enhanced Safety of Vehicles Paper 457. Amsterdam, Netherlands.

Manseau, J. and Keown, M. (2005) Evaluation of the Complex Lower Leg (CLL) for its use in anti-vehicular mine testing applications. IRCOBI, Prague, Czech Republic.

McKay, B. (2008) Lower Extremity. Blast Injury Symposium, Wayne State University, Michigan, USA.

NATO. (2007) Test methodology for protection of vehicle occupants against anti-vehicular landmine effects. Final Report of HFM-090 Task Group 25.

NATO/PfP. (2006) Procedures for evaluating the protection level of logistic and light armoured vehicles, Volume 2. AEP-55, Vol 2. Allied Engineering Publication.

Nies, T.I. (2004) Mine-clearing vehicle MINEWOLF: Biomechanical assessment of mine-clearing tests. WTD 91: German Federal Armed Forces Technical Center for Weapons and Ammunition. 91-400-058/04.

Owen, C. (2001) Requirements for the evaluation of the risk of injury to the ankle in car impact tests. National Highway Traffic Safety Administration, The Netherlands.

Restorick, M. (2007) The response of an Anthropomorphic Test Device to high impact loads. 4th year Mechanical Engineering thesis, The University of Western Ontario.

Seipel, R.C., Pintar, F.A., Yoganandan, N., and Boynton, M.D. (2001) Biomechanics of calcaneal fractures: a model for the motor vehicle. *Clinical Orthopaedics and Related Research.* (388):218-224.

Wang, J., Bird, R., Swinton, B., and Krstic, A. (2001) Protection of lower limbs against floor impact in army vehicles experiencing landmine explosion. *Journal of Battlefield Technology* **4**[3], 8-12.

Yoganandan, N., Pintar, F.A., Boynton, M., Begeman, P., Prasad, P., Kuppa, S., Morgan, R.M., and Eppinger, R. (1996) Dynamic axial tolerance of the human foot-ankle complex. Society of Automotive Engineers, Inc. 962426, 207-218.

Yoganandan, N., Pintar, F.A., Kumaresan, S., and Boynton, M. (1997) Axial impact biomechanics of the human foot-ankle complex. *Journal of Biomechanical Engineering* **119,** 433-437.

CHAPTER 3 – Injury Tolerance Criteria for Short-Duration Axial Impulse Loading of the Tibia

Overview: *This chapter details the experimental study conducted to quantify the injury tolerance of the isolated cadaveric tibia. Using the apparatus from Chapter 2, injury parameters such as force, momentum and energy were examined. The results from this study will be used for the assessment of surrogates such as the Sawbone® synthetic tibia, evaluated in Chapter 4.*[3]

3.1 INTRODUCTION

Axial loading of the lower leg during short-duration impulse loading events, such as ejection seat and parachute landings, or in-vehicle landmine blasts, can cause significant lower leg injuries. While these injuries typically are not life-threatening, they can lead to long-term impairment or the need for lower leg amputation (Radonic *et al.*, 2004; Medin *et al.*, 1998). To date, most of the research investigating the axial injury tolerance levels of the lower limb has been conducted by the car crash industry (*e.g.* Funk *et al.*, 2002; Yoganandan *et al.*, 1996). Impulsive events of interest to the current investigation achieve higher forces over shorter durations than car crashes (< 10 ms vs. > 100 ms) (van der Horst *et al.*, 2005), and as such, investigation into the applicability of the current injury criterion is required.

[3] A version of this work has been submitted for publication: Quenneville CE, McLachlin SD, Fraser GS, and Dunning CE. Injury Tolerance Criteria for Short-Duration Axial Impulse Loading of the Tibia. *Journal of Trauma, Injury, Infection and Care*, September 2009, and was presented at the American Society of Biomechanics Meeting, University Park, PA, USA, August 2009.

Several previous studies have attempted to identify such injury tolerance levels for the shank by developing various lower leg models (Funk *et al.*, 2002; Yoganandan *et al.*, 1996; Griffin *et al.*, 2001; Kuppa *et al.*, 2001; Seipel *et al.*, 2001). These studies, using post-mortem human specimens, proposed peak axial force criteria ranging from 2.4 kN (Seipel *et al.*, 2001) to 5.5 kN (Funk *et al.*, 2002), corresponding to a 10% risk of fracture. The current standard used for assessing lower leg risk to short-duration impulsive loading comes from protective measures for anti-vehicular (AV) landmines (NATO, 2007) and uses the risk curve generated by Yoganandan *et. al.* (1996). This is a maximum axial compressive load of 5.4 kN, as measured with an Anthropomorphic Test Device (ATD), which corresponds to a 10% risk of moderate injury in cadaveric subjects.This force value, however, gives no indication of the duration of load application (*i.e.,* impulse). As well, this load value was taken from cadaveric tests and directly applied to ATD measurements, with no adjustment for the difference in stiffness and load response between the ATD and cadaveric specimens. It should be noted that these previous studies used whole lower-leg specimens, and as such fractures occurred in areas including the calcaneus, talus, and tibia. The variation in strength of these bones, combined with the degrees of freedom involved in consistently orienting specimens for axial loading suggests that these injury criteria may not accurately represent the tolerance of the tibia alone.

The purpose of this study was to investigate the applicability of the current injury standard to short-duration high-impulse loading scenarios, specifically for the tibia. Through the use of paired specimens, other potential factors controlling injury risk will be examined. The hypotheses of this study were: 1) that the injury tolerance of the

isolated tibia to short-duration axial loading is higher than in previous studies, and 2) that secondary parameters such as momentum or kinetic energy are significant for fracture tolerance in addition to force.

3.2 SPECIMENS

Impact testing was conducted on fourteen (*i.e.,* seven pairs) fresh-frozen isolated cadaveric tibias stripped of all soft tissues, from males with a mean age of 48 ± 5 years (range: 41 – 57 years). The mean height of donors was 184.6 ± 6.3 cm, and the mean body mass was 80.0 ± 19.0 kg (see Table H.1 for donor information). Paired specimens were used to allow side-by-side comparison of the force-momentum-kinetic energy relationships. Specimens were tested within eight hours of being thawed.

Each tibia was supported in a vertical orientation with the proximal end centered within a section of 4" PVC tube (Figure 3.1). Proper alignment was achieved based on the anterior ridge of the tibia at mid-shaft and the center of the medial malleolus being aligned with laser levels attached to the potting fixture at 90° to one another. The proximal end of the tibia was then embedded in cement to a depth of 2", and allowed to cure. The anterior laser line was transcribed onto the surface for alignment of strain gauges, and the PVC pot flipped end-for-end and the void in the cement beneath the specimen was filled in and levelled with more cement. Each potted specimen was then weighed.

Specimens were instrumented with tri-axial stacked strain gauge rosettes (C2A-13-125WW-350, Vishay Micro-Measurements, Raleigh, NC, USA) along the anterior line as transcribed from the laser in order to characterize the strain patterns during impact (see

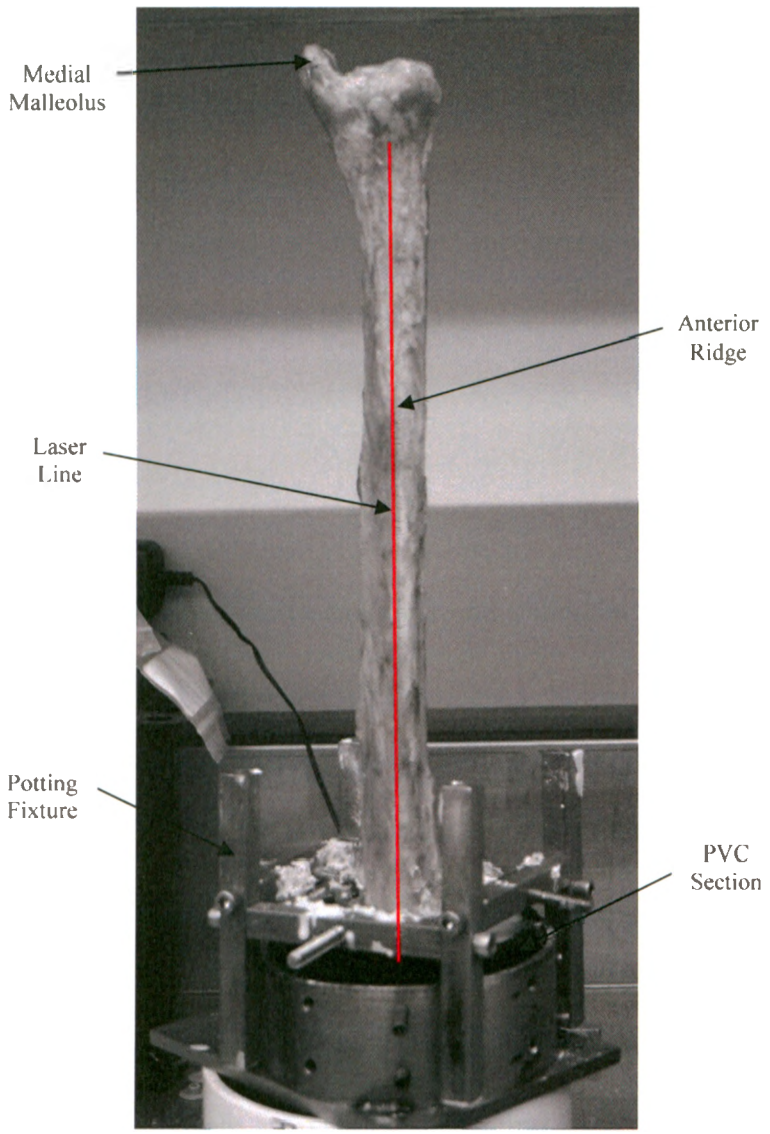

Figure 3.1: Alignment and Potting
Each tibia was supported vertically using a potting fixture, aligned using a laser level based on anatomical landmarks, and embedded in a section of PVC pipe using cement. The anterior laser line was then transcribed onto the surface of the bone.

Appendix I for application protocol). Three rosettes were located distally, with the first being located 6 mm from the tibial plafond, and the second and third similarly spaced with 6 mm gaps between gauges (Figure 3.2). A fourth rosette was located approximately 1 cm from the surface of the cement at the proximal end, in order to determine strain changes over the length of the bone. The centre gauge of each rosette was aligned with the anterior laser from potting, and each gauge was independently wired into a quarter-bridge completion circuit (SCXI 1314, National Instruments, Austin, TX, USA).

3.3 Test Protocol

The impacting apparatus previously designed and validated to apply short-duration axial forces to the tibias with varying momentum levels (Chapter 2) was used. The distal end of the tibia rested against an artificial talus machined from polyethylene attached to the load cell on the distal bracket. A travel distance of 40 cm was used for all tests, and the distal bracket was covered with a ½" piece of urethane foam to control the loading impact duration.

The force that develops during an impact is dependent on the stiffness of the object being struck, and so force levels are variable and unpredictable for cadaveric bones. Therefore kinetic energy levels of the projectile were used as the target inputs as these were controllable. To determine appropriate loading levels, preliminary testing was conducted on two pairs of specimens (Protocol 1), which impacted specimens in energy increments of 50 J (Table 3.1a). To vary the momentum applied to the specimens by the projectile, and allow examination of this variable as an injury risk factor, one specimen

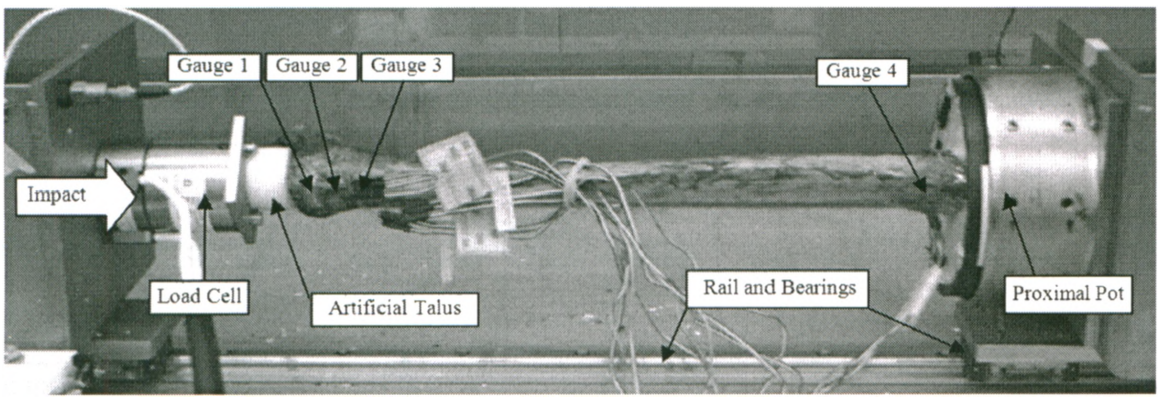

Figure 3.2: Instrumented Cadaveric Tibia in Testing Configuration
Each tibia was embedded proximally in cement in the proximal pot, and instrumented along the anterior line with triaxial strain gauge rosettes. The three distal gauges (Gauges 1-3) were spaced 6 mm apart, and the proximal gauge (Gauge 4) was 1 cm from the cement surface. The impact load (shown with an arrow) was transferred to the distal articular surface via a polyethylene talus mounted on a load cell.

Table 3.1: (a) Protocol 1, and (b) Protocol 2
Kinetic energy levels were selected as the target inputs, as they were controllable and would result in different momentums for the two projectile masses.

(a)

		3.9 kg Projectile		6.8 kg Projectile	
Test #	Target Energy (J)	Target Velocity (m/s)	Target Momentum (Ns)	Target Velocity (m/s)	Target Momentum (Ns)
1	50	5.1	20	3.8	26
2	100	7.2	28	5.4	37
3	150	8.8	34	6.6	45
4	200	10.1	39	7.7	52
5	250	11.3	44	8.6	58

(b)

		3.9 kg Projectile		6.8 kg Projectile	
Test #	Target Energy (J)	Target Velocity (m/s)	Target Momentum (Ns)	Target Velocity (m/s)	Target Momentum (Ns)
1	150	8.8	34	6.6	45
2	250	11.3	44	8.6	58
3	300	12.4	48	9.4	64

from each pair was tested using a 3.9 kg (light) projectile mass, and the contralateral tested using a 6.8 kg (heavy) projectile mass, with right-left selection randomized. This protocol suggested that failure (defined as a fracture separating the tibia into at least two distinct pieces) would occur in the 200 – 250 J range, with two specimens failing at 200 J and two specimens failing at 250 J. Protocol 2 was then developed using the same two masses, which impacted the remaining five pairs of specimens in energy increments of 100 J, starting at 150 J (Table 3.1b). This was selected in an effort to limit each specimen to only two impacts (one pre-fracture and one at failure), minimizing any cumulative damage effects.

As injury risk is often assessed using an ATD, and the current protective standard is based on ATD loading, a Hybrid III Anthropomorphic Test Device tibia (Denton ATD Inc., Rochester Hills, MI, USA) was similarly impacted to define its velocity-force response curve. The relationship between cadaveric response and this standard injury assessment tool was thus quantified.

Impulse to the tibia was calculated by integrating the force-time profile from the load cell over the impact duration. Results were analyzed using paired t-tests to determine differences in force, momentum and kinetic energy levels at fracture between the two test masses, and a one-way ANOVA was used to determine differences between Protocol 1 and Protocol 2 (50 J and 100 J increments, respectively). Statistical tests were performed with significance defined at $\alpha = 0.05$. A best subsets regression analysis was performed to determine the variables that predicted injury risk and the associated equation. A multivariate Weibull model was used to establish a probability of injury curve based on

the injury risk equation, as well as based on axial force for comparison with previous studies.

3.4 RESULTS

In each specimen, fracture occurred in the distal region (Figure 3.3), and primarily corresponded to damage at the 'C' level of the AO scale (see Section 1.5.2). The force-time curve for a representative specimen is shown in Figure 3.4. The light mass (3.9 kg) caused average peak impact forces of 12563 ± 1982 N, and the heavier mass (6.8 kg) caused average peak impact forces of 12581 ± 2277 N (Figure 3.5). There were no differences in peak force between the two masses tested ($p = 0.98$). The two pairs that were impacted using Protocol 1 (increasing impacts in 50 J steps) had a peak load that was not different from those impacted using Protocol 2 ($p = 0.80$). Overall impact time durations averaged 3.7 ± 0.9 ms, and imparted an average impulse of 17.6 ± 3.7 Ns to the tibia at failure.

The average impact velocity to cause fracture was 11.0 ± 1.1 m/s for the 3.9 kg mass, which was higher than the 8.4 ± 0.5 m/s for the 6.8 kg mass ($p = 0.03$). These corresponded to impact momentums of 43.0 ± 4.4 Ns and 57.1 ± 3.6 Ns and kinetic energies of 239 ± 45 J and 241 ± 30 J for the light and heavy masses, respectively (Table 3.2). Momentum was different between projectile masses ($p < 0.001$); however, kinetic energy was not ($p = 0.94$).

Principal strains were calculated from the strain gauge rosettes for each test using Eq. 1.7. Many of the gauges were damaged during the fracture strike; as such the principal strains during the 150 J impact tests were averaged for all specimens that survived the

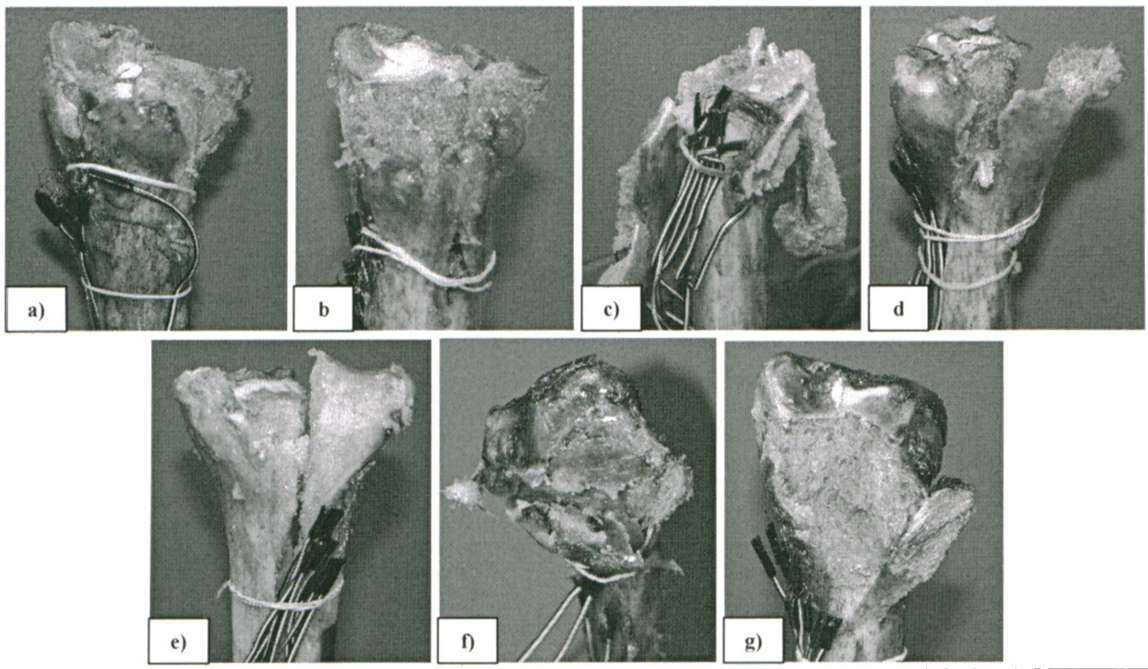

a) 06-06037R	b) 08-07033R	c) 08-07024R	d) 08-07085R	e) 08-08009R	f) 06-08044R	g) 06-10081R
40.16 mm	41.78 mm	41.88 mm	42.05 mm	43.06 mm	41.27 mm	41.63 mm

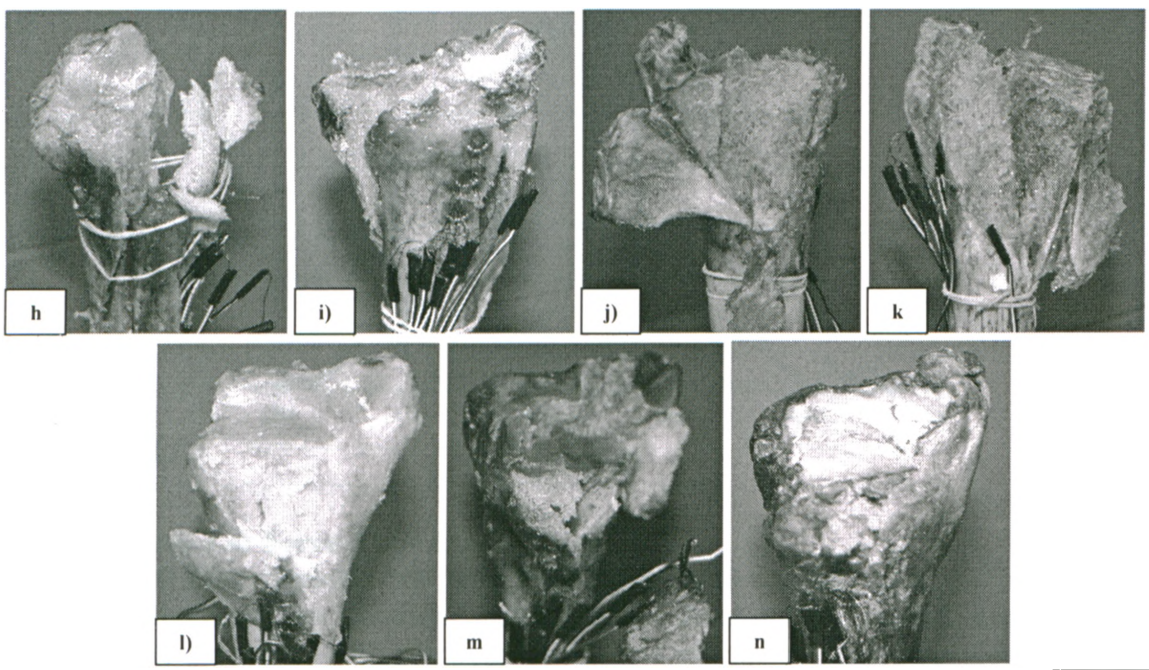

h) 06-06037L	i) 08-07033L	j) 08-07024L	k) 08-07085L	l) 08-08009L	m) 06-08044L	n) 06-10081L
41.40 mm	39.34 mm	41.26 mm	42.09 mm	41.33 mm	40.64 mm	41.98 mm

Figure 3.3: All Specimens Post-Fracture
Photos were taken of all specimens, and their distal width measured prior to testing and presented in mm. See Appendix N for width information.

a)

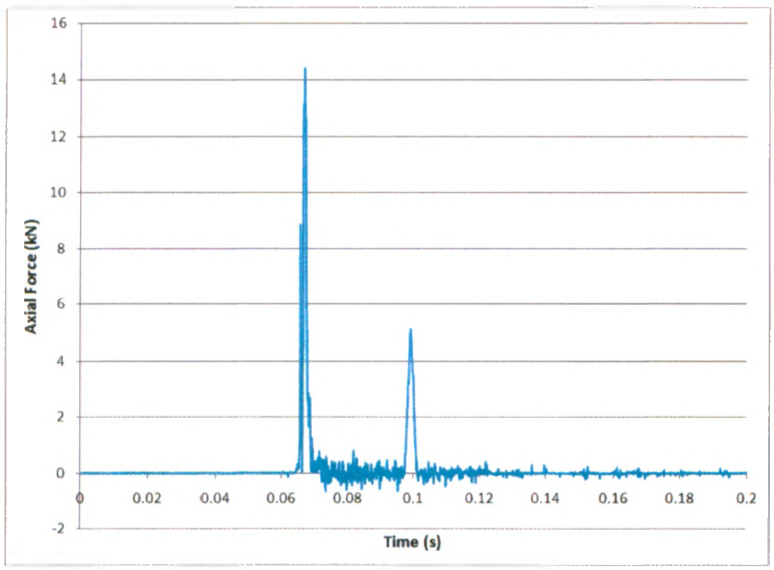

b)

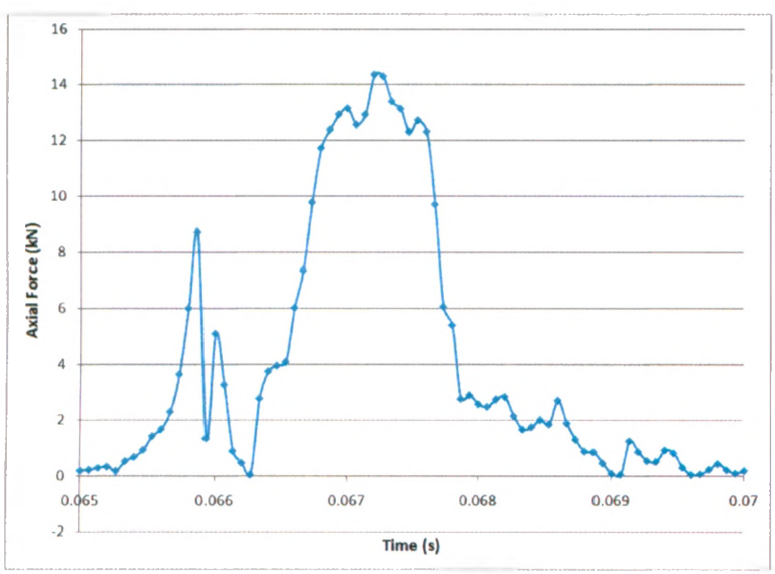

Figure 3.4: Force-Time Curve
Axial force is plotted vs. time for a representative impact test. **a)** Curve for the entire test duration, showing initial strike and the second, smaller strike associated with stopping the moving specimen. **b)** Enlargement of the force during the initial impact event.

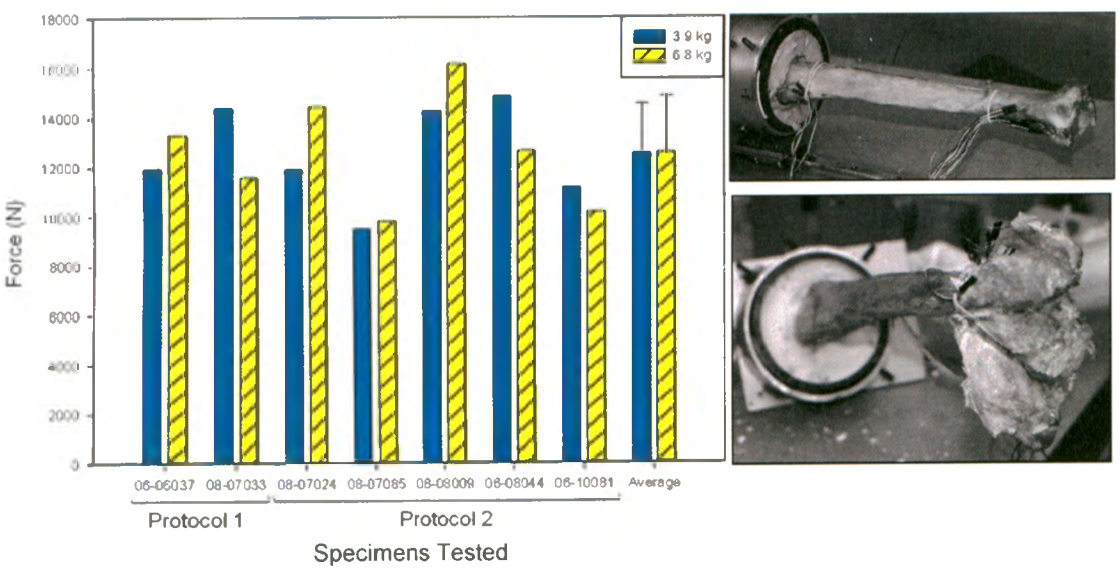

Figure 3.5: Peak Impact Force
Across both protocols the 3.9 kg mass caused average peak impact forces of 12563 ± 1982 N, and the 6.8 kg mass caused average peak impact forces of 12581 ± 2277 N. These forces resulted in substantial distal fractures, as shown to the right (intact, top; fractured, bottom).

Table 3.2: Specimen Data and Fracture Information
Each factor as well as specimen age, height and weight (Appendix H; Table H.1) was examined for statistical significance in failure.

3.9 kg mass	Specimen	Velocity (m/s)	Kinetic Energy (J)	Momentum (Ns)	Force (N)	Impulse (Ns)
1	06-06037	11.08	239.4	43.2	11936	10.4
	08-07033	11.37	252.1	44.3	14375	19.4
2	08-07024	11.00	236.0	42.9	11895	-
	08-07085	11.47	256.5	44.7	9481	12.6
	08-08009	11.29	248.6	44.0	14257	19.6
	06-08044	12.29	294.5	47.9	14831	19.8
	06-10081	8.68	146.9	33.9	11168	18.5
Average (±S.D.)		11.03 (1.12)	239.1 (45.0)	43.0 (4.3)	12563 (1982)	16.7 (4.1)

6.8 kg mass	Specimen	Velocity (m/s)	Kinetic Energy (J)	Momentum (Ns)	Force (N)	Impulse (Ns)
1	06-06037	7.63	197.9	51.9	13307	15.2
	08-07033	7.83	208.5	53.2	11586	17.6
2	08-07024	8.60	251.5	58.5	14435	18.5
	08-07085	8.48	244.5	57.7	9791	19.7
	08-08009	8.38	238.8	57.0	16131	25.1
	06-08044	9.18	286.5	62.4	12637	16.8
	06-10081	8.70	257.3	59.2	10182	15.8
Average (±S.D.)		8.4 (0.53)	240.7 (29.9)	57.1 (3.6)	12581 (2277)	18.4 (3.3)

trial, less the two with data collection errors (n = 11) (Figure 3.6). Principal strains ranged from 0.0002 to 0.0041 strain, and were highest at the second gauge from the distal end (Gauge 2). Individual strain data for each specimen are included in Appendix H (Tables H.2 and H.3).

To determine the most appropriate survival equation, the effect of each variable was tested using a best subsets regression. Factors that were examined included projectile mass, projectile velocity, impact momentum, impact kinetic energy, impact duration, impulse, axial force, donor age, height, and body mass. From these variables, the adjusted R^2 was used to determine the best model, which included the natural log of axial force (F) in Newtons ($p = 0.003$), kinetic energy (KE) in joules ($p < 0.001$), age in years ($p = 0.008$) and height of donor in centimeters ($p = 0.017$) as significant independent variables (Eq. (3.2)).

$$Injury\ risk = -2.123 - 0.666 * \ln(F) + 0.0104 * KE + 0.0397 * Age + 0.026 * Height \quad \textbf{(Eq. 3.2)}$$

This model proved to be a good fit of the data (standard $R^2 = 0.73$, adjusted $R^2 = 0.69$). All variables independently contributed to the equation ($p < 0.05$). A Weibull analysis was performed to develop a survivability curve based on this risk equation (Figure 3.7) ($R^2 = 0.95$). As force is usually the primary factor measured during an impact (Yoganandan *et al.*, 1996; Kuppa *et al.*, 2001; Griffin *et al.*, 2001; Funk *et al.*, 2002), a second Weibull analysis was performed to develop a survivability curve for applied axial force only. This indicated that a 10% risk of failure corresponded to a load of 7.9 kN ($R^2 = 0.86$). Previous injury risk equations based on axial force were graphed for comparison (Figure 3.8). Tibia Index values were also computed for both the non-fracture and fracture tests (Table 3.3).

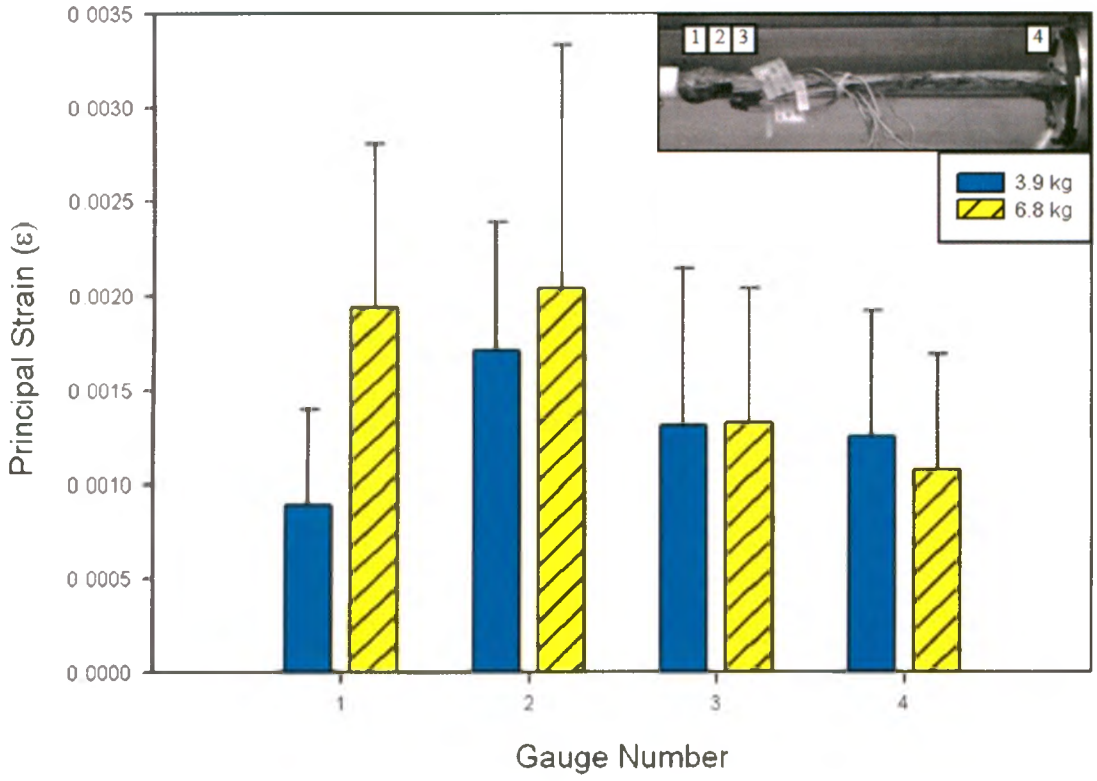

Figure 3.6: Principal Strains at 150 J Impact Tests
Peak strains during the 150 J impact test were averaged for all specimens (except the one which fractured). Strain values and standard deviations are presented for the four levels of gauging (1-3 are distal, and 4 is proximal, as shown in the inset).

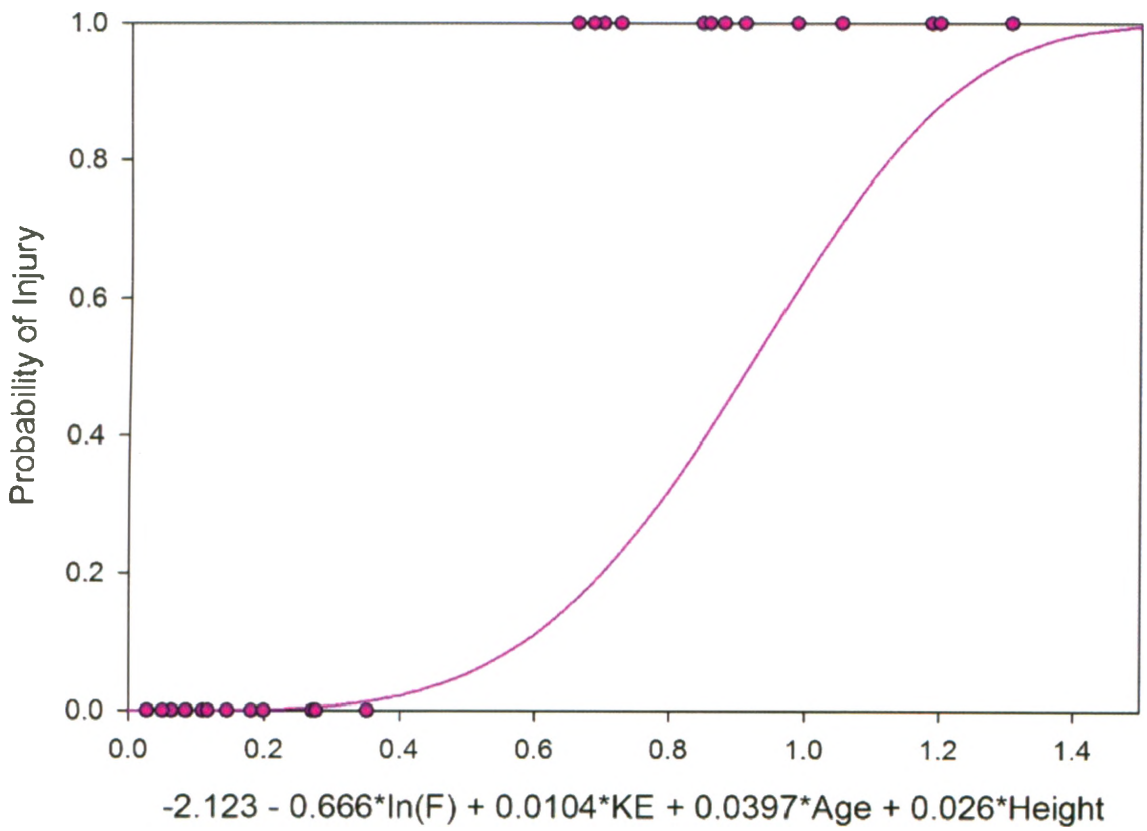

Figure 3.7: Probability Distribution for Injury
Probability of injury is a function of the natural log of axial force (F) in Newtons, kinetic energy (KE) in joules, age of the donor (in years) and height of the donor (in centimeters).

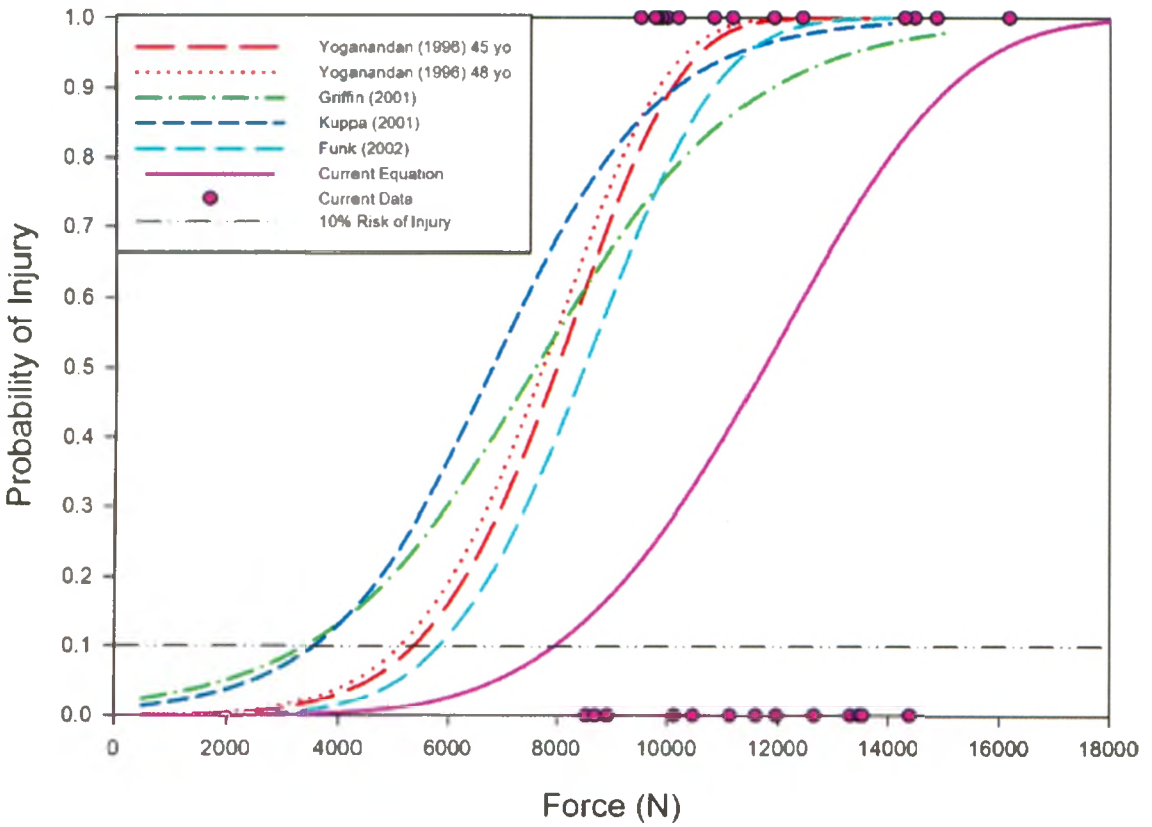

Figure 3.8: Comparison of Injury Risk Equations
Injury probability curves based on force only from previous studies are shown, along with 10% risk of injury line. The current force-based equation was developed from the shown data points using a Weibull analysis.

Table 3.3: Tibia Index Values
TI Values were computed using F_c = 12 kN and M_c = 240 Nm for both non-fracture and fracture tests.

Specimen	TI (Non-Fracture)	TI (Fracture)
08-07033R	1.48	1.76
08-07033L	1.37	1.27
08-07024L	-	-
08-07024R	1.14	1.66
08-07085R	1.07	1.28
08-07085L	1.19	1.35
08-08009R	1.30	1.86
08-08009L	1.51	1.90
06-08044R	1.94	1.98
06-08044L	1.60	1.22
06-10081L	-	1.37
06-10081R	1.17	1.32

Forces against the ATD measured as much as 2.8 times those measured during cadaveric impacts for the same impact conditions (*i.e.,* projectile mass and velocity). As exact duplication of the test protocol ran the risk of damaging the load cell (load limit = 11 kN), a velocity-force curve was generated for the ATD response at low velocities and extrapolated to the higher levels tested in the cadaveric specimens (Figure 3.9). For the 150 and 250 J tests run in the current study, an ATD would receive loads of approximately 31 kN and 67 kN. The kinetic energy corresponding to the 7.9 kN force limit as measured in a cadaveric tibia was used to predict the analogous forces that would develop in an ATD, and found to be 12.6 kN.

3.5 Discussion

This study subjected pairs of isolated cadaveric tibias to short-duration (< 10 ms) axial impulse loads for the purpose of re-evaluating the current injury criterion. Impact time durations, velocities, and loading rates were consistent with those measured during AV landmine blasts (Wang *et al.*, 2001; NATO, 2007), and fractures were achieved in all specimens. The injuries were mostly of the 'C' level on the AO scale, which is clinically relevant. These tests were conducted on younger, male specimens, representative of the population most frequently exposed to anti-vehicle land mine blasts. This allowed the current injury standard to be examined, and secondary criteria identified for the development of an injury risk curve.

Previous efforts to develop an injury criterion for the lower leg have been conducted on full lower leg specimens. By focusing on isolated tibias, the current study has been able to identify the tolerance of this bone specifically, reducing the degrees of freedom

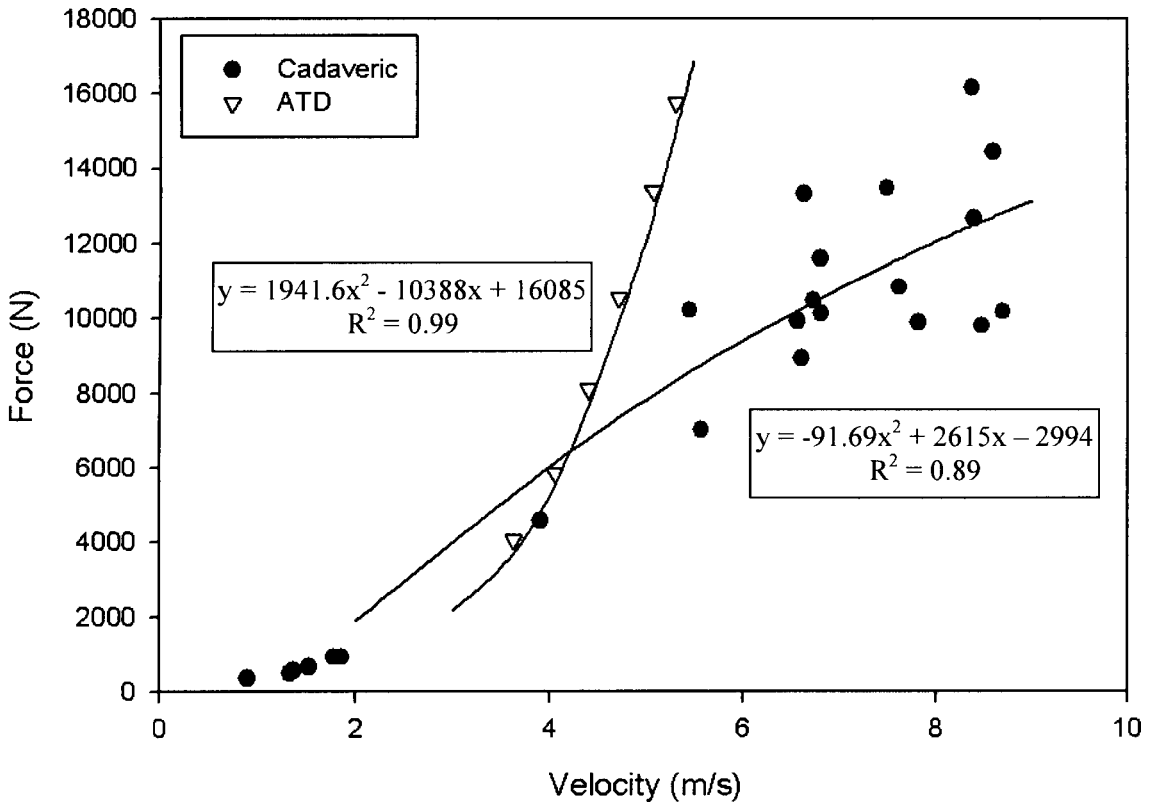

Figure 3.9: Velocity-Force Curves for Cadaveric and ATD Tibias
Non-injurious tests using the 6.8 kg mass were used to extrapolate load response for the cadaveric and ATD tibias for the target energies, as well as the proposed injury criterion of 7.9 kN.

and complexity of alignment that is present in full lower leg testing. However, this study gives no indication of injury risk to bones such as the talus and calcaneus, which are often damaged during these types of loading events. Injury limits that take these into account could therefore be lower, and should be examined in future studies. The impact protocols were designed to minimize the number of strikes to each specimen prior to failure, but there was the potential for cumulative injury effects. However, the lack of statistical difference between the peak forces attained in Protocol 1 (50 J steps), which had twice the number of strikes of Protocol 2 (100 J steps), suggests that the number of strikes likely had no cumulative damaging effects on the specimens.

The peak forces required to cause fractures in the present study were higher than those attained in previous studies designed to simulate car crash injuries. This resulted in a 10% risk of injury corresponding to 7.9 kN; higher than those proposed in previous studies of 5.4 kN (Yoganandan *et al.*, 1996), 3.6 kN (Kuppa *et al.*, 2001), 2.7 kN (Griffin *et al.*, 2001), 2.4 kN (Seipel *et al.*, 2001) and 5.5 kN (Funk *et al.*, 2002). Differences between the current and previous results may be partially attributed to testing variations, including impact velocities and masses, anatomical alignment of the lower leg, testing of full lower legs versus isolated tibias, and the use of factors such as age, gender, body mass, and Achilles tension in the development of risk curves (Table 3.4). The inclusion of tibia load cells via osteotomies (Funk *et al.*, 2002) may have also altered the overall response of the tibia, as well as inducing artifactual fractures. Previous studies also gave no indication of injury severity.

Momentum to cause fracture was significantly different between different projectile masses, but kinetic energy was not. The momentums achieved in the present study also

Table 3.4: Summary of Test Parameters From Previous Studies

Study	Impact Velocity (m/s)	Impactor Mass (kg)	Fracture Force (kN)
Yoganandan *et al.* (1996, 1997)	2.2 – 7.6	24	4.3 – 13.0
Kitagawa *et al.* (1998)	3	18	4.9 (average)
Seipel *et al.* (2001)	2.2 – 6.7	24	3.6 – 11.4
Funk *et al.* (2002)	5	- (piston)	3.8 – 11.9

are on the low end of those reported by Yoganandan *et al.* (1996), which the current authors have calculated to range from 82 – 182 Ns. This variation suggests that fracture is not controlled by a specific momentum level. Kinetic energy at failure had no differences between the light and heavy masses, and was in the same range as those found by Yoganandan *et al.* (1996), which ranged from 139 – 693 J, even though the current study achieved higher fracture forces. The best subsets regression analysis also found kinetic energy to be a significant factor in failure, and as such kinetic energy should be considered an important factor to consider in injury risk assessment, in addition to force. While this may provide a more accurate injury risk curve, kinetic energy is not a factor that is easily or often measured in experimental tests, suggesting additional measurement may be necessary for accurate injury prediction. In the injury risk equation (Eq. 3.2) the coefficient of axial force is negative, which may appear counter-intuitive. This demonstrates the inherent link between force and kinetic energy, as the increase in the kinetic energy term of the equation more than compensates for the negative effect of the force term. This is the first known study to propose the use of kinetic energy and height as terms in an injury risk curve.

Based on the developed injury risk curves in the current study, the accepted injury standard of 5.4 kN used for these events corresponds to a 2% risk of injury. This suggests that the previously adopted force limit may be too conservative for short-duration impacts of the isolated tibia. It is possible that higher forces were tolerated due to the decreased loading duration in the current impact events, and this may indicate that impulse (characterized by integrating the force profile over the impact time) could be an important factor in the injury tolerance of the tibia if compared with car crash data.

Impulse values are included here, but were not reported in previous studies, and so cannot be compared. This would be an important subject for future research on the lower leg, requiring further testing of additional specimens.

The artificial talus used in the present study was the same for each specimen, and had a diameter of 32 mm. This meant that the testing apparatus was consistent among specimens, but may have led to tibia-talus size mismatching. The diameter of each tibia was thus measured to determine if any relationship between size and injury existed, but none was observed. This simplification was therefore determined to be acceptable.

Denton ATD legs are the current method used in a variety of industries to assess injury risk to the lower leg. Due to their increased stiffness, an adjustment factor must be included to relate the measured loads to those which would have developed during impact of human bone. Previous studies have found ATD to cadaveric ratios between 1.8 and 2.8 (Bir *et al.*, 2008; Kuppa *et al.*, 1998). The present study attained a ratio of ATD to cadaveric forces up to 2.8, which agrees with these previous studies. The present study found a 10% risk of tibia injury would register as an ATD force of approximately 12.6 kN, which is 2.3 times the currently used limit of 5.4 kN as measured with an ATD. This new value may be a more appropriate force-based injury criterion when risk is assessed using an ATD. It should be noted, however, that the load cells that are sold with this ATD are not of a large enough capacity to tolerate these loads (maximum of 11.12 kN), and as such would need to be modified in order to protect them from damage. The Tibia Index values computed for both the non-fracture and fracture tests all exceeded the critical value of 1, indicating that this is not a useful criterion for assessing this type of injury risk. The Lower Leg Threshold (LLth) (section 1.5.2.3) was qualitatively

evaluated for the average load duration of 3.7 ms (due to the lack of a published equation for the threshold) to be approximately 13.5 kN. This value is higher than the 7.9 kN recommended in the present study, and as such may be inappropriate for this application.

This study isolated the fracture tolerance of the cadaveric tibia under short-duration (<10 ms) axial impulse loading. For these types of events, it has been shown that higher forces can be withstood prior to fractures occurring, and suggests that a higher injury limit may be acceptable for these loading profiles. It is the first study of its kind to propose the use of kinetic energy and impulse to further define the injury criteria for the lower leg. A revised injury force standard has been proposed for short-duration loading, along with the corresponding load values that would be measured using an ATD for this injury risk level. Significant progress has also been made toward defining energy and impulse-based secondary injury criteria.

3.6 REFERENCES

Bir, C., Barbir, A., Dosquet, F., Wilhelm, M., van der Horst, M.J., and Wolfe, G. (2008) Validation of lower limb surrogates as injury assessment tools in floor impacts due to anti-vehicular land mines. *Journal of Military Medicine* **173,** 1180-1184.

Funk, J.R., Crandall, J.R., Tourret, L.J., MacMahon, C.B., Bass, C.R., Patrie, J.T., Khaewpong, N., and Eppinger, R.H. (2002) The axial injury tolerance of the human foot/ankle complex and the effect of Achilles tension. *Journal of Biomechanical Engineering* **124,** 750-757.

Griffin, L.V., Harris, R.M., Hayda, R.A., and Rountree, M.S. (2001) Loading rate and torsional moments predict pilon fractures for antipersonnel blast mine loading. International IRCOBI Conference on the Biomechanics of Impacts, Isle of Man, UK.

Kuppa, S., Klopp, G.S., Crandall, J.R., Hall, G., Yoganandan, N., Pintar, F.A., Eppinger, R.H., Sun, E., Khaewpong, N., and Kleinberger, M. (1998) Axial impact characteristics of dummy and cadaver lower limbs. Society of Automotive Engineers, 98-S7-O-10.

Kuppa, S., Wang, J., Haffner, M., and Eppinger, R. (2001) Lower extremity injuries and associated injury criteria. Proceedings of the 17th International Technical Conference on Enhanced Safety of Vehicles Paper 457. Amsterdam, Netherlands.

Medin, A., Axelsson, H., and Suneson, A. (1998) The reactions of the crew in an armoured personnel carrier to an anti-tank mine blast. Defence Research Establishment. FOA-R-98-00720-310-SE.

NATO. (2007) Test methodology for protection of vehicle occupants against anti-vehicular landmine effects. Final Report of HFM-090 Task Group 25.

Radonic, V., Giunio, L., Biocic, M., Tripkovic, A., Lukcic, B., and Primorac, D. (2004) Injuries from antitank mines in southern Croatia. *Journal of Military Medicine.* **169,** 320-324.

Seipel, R.C., Pintar, F.A., Yoganandan, N., and Boynton, M.D. (2001) Biomechanics of calcaneal fractures: a model for the motor vehicle. *Clinical Orthopaedics and Related Research* (388):218-224.

van der Horst, M.J., Simms, C.K., van Maasdam, R., and Leerdam, P.J.C. (2005) Occupant lower leg injury assessment in landmine detonations under a vehicle. IUTAM Symposium on Impact Biomechanics. Dublin, Ireland.

Wang, J., Bird, R., Swinton, B., and Krstic, A. (2001) Protection of lower limbs against floor impact in army vehicles experiencing landmine explosion. *Journal of Battlefield Technology* 4[3], 8-12.

Yoganandan, N., Pintar, F.A., Boynton, M., Begeman, P., Prasad, P., Kuppa, S., Morgan, R.M., and Eppinger, R. (1996) Dynamic axial tolerance of the human foot-ankle complex. Society of Automotive Engineers, Inc. 962426, 207-218.

CHAPTER 4 – Evaluation of Synthetic Composite Tibias for Fracture Testing Using Impact Loads

Overview: *This chapter details the experimental testing of synthetic composite tibias using the apparatus developed in Chapter 2, and using the methods described in Chapter 3. The results are compared to those from the experimental cadaveric testing to assess their ability to represent the response of natural bone to impact loads causing fracture.*[4]

4.1 INTRODUCTION

Composite synthetic bones are widely used in orthopaedic research. They offer many advantages over post-mortem human specimens, including low inter-specimen variability in both geometry and material properties, ready availability, and ease of handling, storage, and disposal. Fourth generation models of Sawbones® (Pacific Research Laboratories, Inc., Vashon, WA, USA) are made using a short glass fibre reinforced epoxy resin injected around a core of rigid polyurethane foam (see Figure 1.8). These composite bones have been previously validated to replicate natural bone response at a quasi-static rate (Heiner, 2008).

Fracture studies for the purpose of injury prediction due to impulsive loading are an important area of research that could benefit from the advantages of synthetic bones. For these bones to be an appropriate surrogate, the fracture strength and failure mechanics

[4]A version of this work has been submitted for publication: Quenneville CE, Fraser GS, and Dunning CE. Evaluation of Synthetic Composite Tibias for Fracture Testing Using Impact Loads, *Journal of Engineering in Medicine: Proceedings of the Institution of Mechanical Engineers, Part H*, September 2009, and was presented at the American Society of Biomechanics Meeting, University Park, PA, USA, August 2009.

need to be consistent with the natural bone response under impact conditions (Yoganandan *et al.*, 1996; Funk *et al.*, 2002).

The purpose of this study was to evaluate the current fourth generation of Sawbones® tibias for fracture tolerance and strain distribution when exposed to short-duration axial impacts. Additionally, the effects of varied impact momentum and energy levels on failure were examined and compared to previous cadaveric data (Chapter 3).

4.2 Specimen Preparation

Impact testing was conducted on nine large Sawbone® tibias (Model #3402). Eight of the specimens were the manufacturer's standard model, with an open canal and hole in the distal cortex. The ninth bone had the canal filled with polyurethane foam and the distal hole patched with epoxy resin by the manufacturer, to allow the effect of the stress concentration of the canal to be examined. Each tibia was anatomically aligned, potted in cement, and instrumented with triaxial strain gauge rosettes in the same method as in Chapter 3 (Figure 4.1).

4.3 Test Protocol

The test apparatus detailed in Chapter 2 was used to apply axial impact loads to the tibias. As noted in Chapter 3, impact force is specimen-dependent, and could therefore not be used as the input target for testing. Therefore, kinetic energy levels were targeted. Four standard specimens were tested using a 3.9 kg (light) projectile mass and four standard specimens plus the canal-filled specimen were tested using a 6.8 kg (heavy) projectile mass. Energy values for the impacts were based on a preliminary test

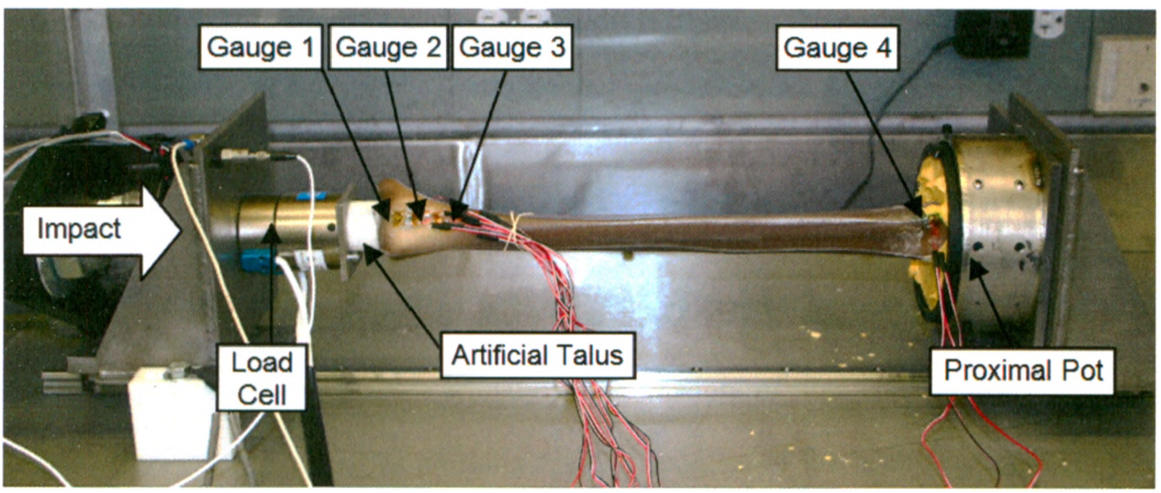

Figure 4.1: Instrumented Synthetic Tibia in Testing Configuration
Each synthetic tibia was embedded proximally in cement, and instrumented along the anterior line with triaxial strain gauge rosettes. The three distal gauges (Gauges 1-3) were spaced 6 mm apart, and the proximal gauge (Gauge 4) was approximately 1 cm from the cement surface. The impact load (shown with an arrow) was transferred to the distal articular surface via a polyethylene talus mounted on a load cell.

specimen, which fractured at 50 J, and were therefore increased in 20 J steps to average three strikes before failure, in an effort to minimize cumulative damage effects (Table 4.1). Failure was defined as a fracture separating the tibia into at least two distinct pieces. A Weibull analysis was used to establish a probability of injury curve based on axial force at failure. Results were also analyzed using paired t-tests to determine differences in failure energy and momentum levels based on the masses tested ($\alpha = 0.05$).

4.4 RESULTS

Failure occurred in all specimens, with damage concentrated in the distal region, and primarily corresponding to the 'B' level of the AO scale (see Section 1.5.2). Damage occurred in two manners concurrently: delamination of the epoxy resin from the polyurethane foam, as well as breaking apart of sections of the bone (Figure 4.2). The 3.9 kg mass caused average peak forces of 4702 ± 509 N, and the 6.8 kg mass caused average peak impact forces of 5718 ± 642 N (Figure 4.2). These differences were just at the level of significance ($p = 0.05$). The specimen with the canal filled fractured at a peak force of 5761 N, which was not different than the standard specimens obtained from the manufacturer ($p = 0.95$). A Weibull analysis based on axial force at failure was conducted in order to generate a survivability curve for the synthetic composite bones (Figure 4.3). This curve had an $R^2 = 0.97$.

Impact durations averaged 7.85 ± 0.67 ms, and imparted an average impulse of 14.65 ± 1.28 Ns to the distal end of the tibia (Figure 4.4). The average impact velocity to cause fracture was 5.64 ± 0.02 m/s for the light mass, which was higher than the 4.65 ± 0.31 m/s needed for the heavy mass ($p = 0.03$). Average impact momentums of 22.0 ± 0.1 Ns

Table 4.1: Test Protocol for Two Masses Used
Kinetic energies were targeted to be the same for both masses, allowing for investigation of both energy and momentum as fracture risk parameters. Tests were increased in 20 J steps to minimize cumulative effects.

		Light Mass (3.9 kg)		Heavy Mass (6.8 kg)	
Test #	Target Energy (J)	Velocity (m/s)	Momentum (Ns)	Velocity (m/s)	Momentum (Ns)
1	20	3.20	12.5	2.43	16.5
2	40	4.53	17.7	3.43	23.3
3	60	5.55	21.6	4.20	28.6
4	80	6.41	25.0	4.85	33.0

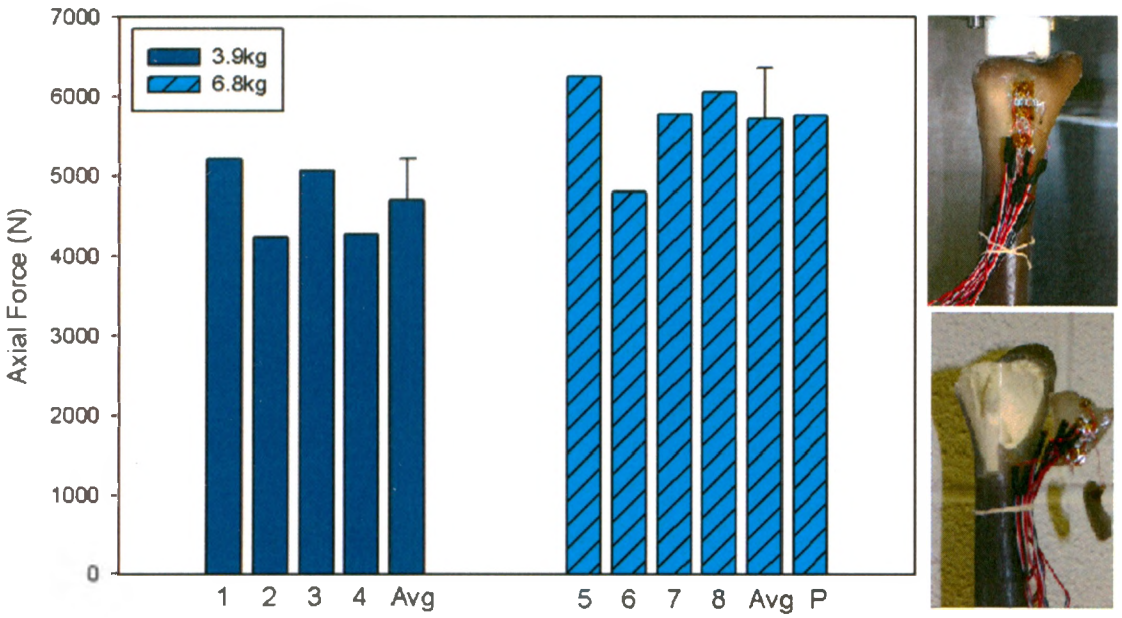

Figure 4.2: Peak Axial Impact Force
Damage was concentrated in the distal region of each specimen (right, upper is pre-test, lower is post-test), and consisted of both shattering of the epoxy resin as it delaminated from the polyurethane foam, as well as fracture of the foam into multiple pieces. The 3.9 kg mass caused average peak forces of 4702 ± 509 N, and the 6.8 kg mass caused average peak forces of 5718 ± 642 N ($p = 0.05$). The specimen with the patched canal (P) was struck with the 6.8 kg mass, and fractured at a force of 5761 N.

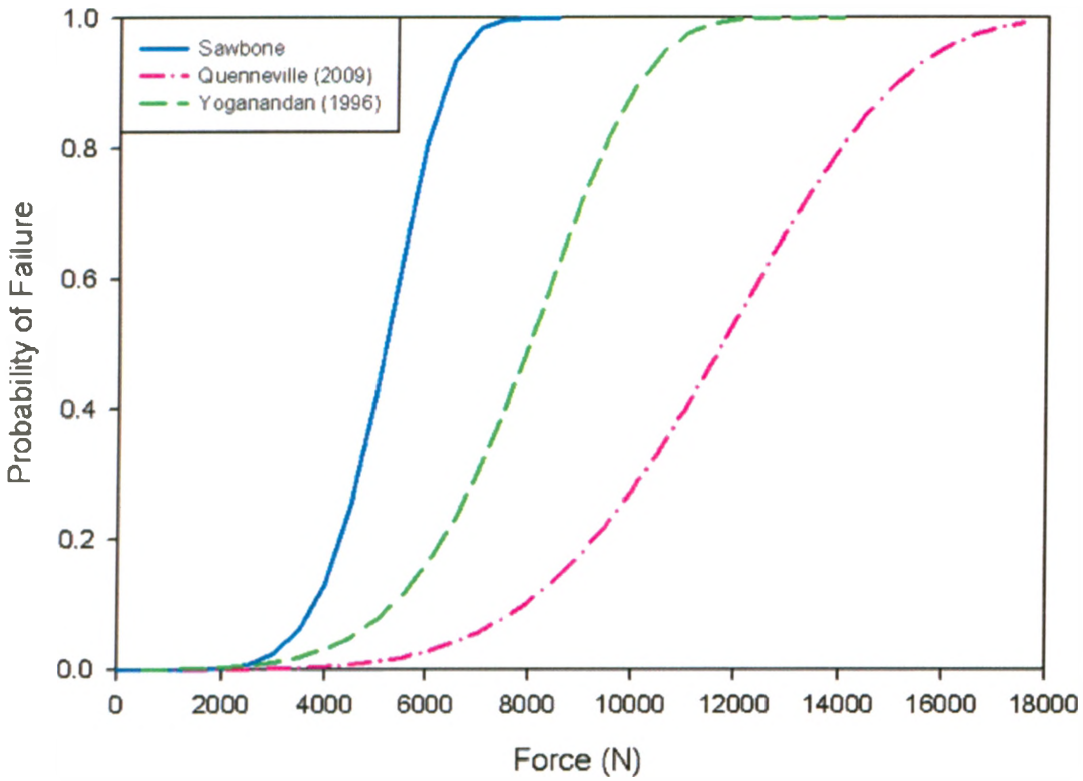

Figure 4.3: Survivability Curves for Synthetic and Cadaveric Tibias
A Weibull analysis generated a survivability curve for the specimens tested based on axial force. The curves from the previously tested cadaveric specimens (Chapter 3) and the current standard from the literature (Yoganandan *et al.*, 1996) are also plotted for comparison.

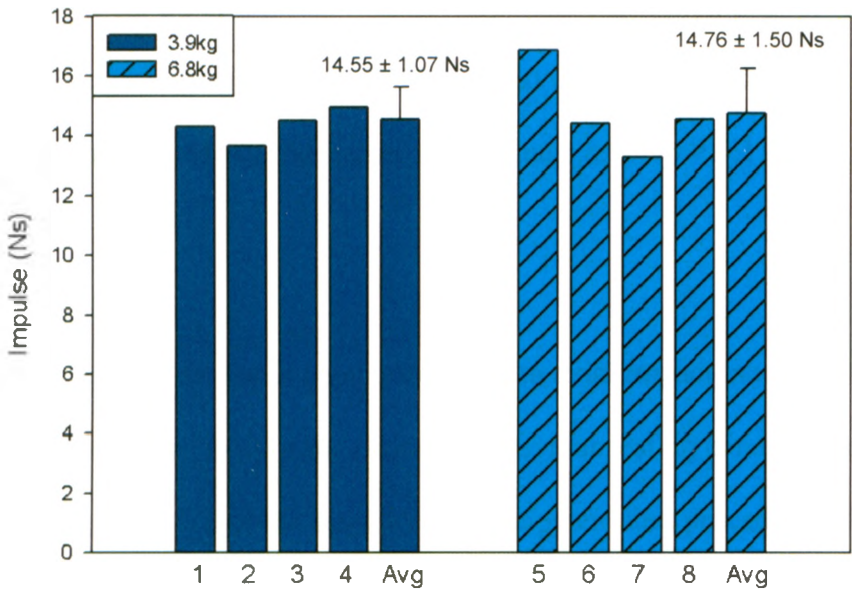

Figure 4.4: Impulse at Fracture
Impulse was computed by integrating the axial force signal (Fz) over the impact duration. The average impulse for all specimens was 14.55 Ns, with a range of 13.27 to 16.85 Ns.

and 31.6 ± 2.1 Ns, and kinetic energies of 61.9 ± 0.4 J and 73.8 ± 9.8 J occurred for the light and heavy masses, respectively. Momentum and kinetic energy were different between projectile masses ($p = 0.03$).

Principal strains were calculated from each strain gauge rosette for the 40 J impact tests, and averaged for all specimens (Figure 4.5). The highest strains were recorded at the distal-most gauge level (averaging 4000 με), and decreased proximally. There were no differences in strain between the masses at any gauge level ($p > 0.11$).

4.5 DISCUSSION

This study subjected synthetic composite tibias to axial impact loading representative of short-duration impulses in the same manner as previous testing conducted on cadaveric tibias (Chapter 3). The use of the same testing equipment and procedures allowed for a true comparison between synthetic and cadaveric bones. This is the first study to examine the impact fracture characteristics of composite bones. Previous generations of these synthetic composite bones were examined under quasi-static loading rates (Cristofolini *et al.*, 1996; Cristofolini and Viceconti, 2000; Heiner and Brown, 2001). They were found to have low inter-specimen variability, and reasonably approximated the response of cadaveric bones. The material properties of the cortical analogue were changed in the current fourth generation in an attempt to provide better fatigue resistance. These models have previously been validated a surrogate for biomechanical experiments (Heiner, 2008), but also only at quasi-static loading rates. The fracture tolerance of the cortical analogue has previously been examined, with the current material having a higher ultimate strength than previous models, but still lower than cortical bone (Chong

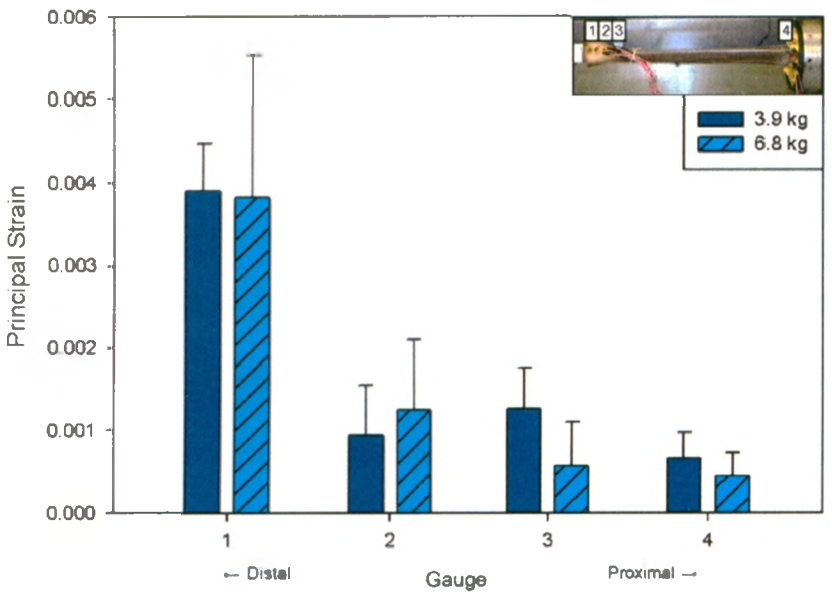

% Difference (Synthetic / Cadaveric)		
Gauge	3.9 kg	6.8 kg
1	437%	197%
2	55%	62%
3	98%	43%
4	53%	42%

Figure 4.5: Principal Strains at 40 J Impact Tests
Peak principal strains during the 40 J impact test were averaged. Strain values are presented for the four levels of gauging (1-3 are distal, and 4 is proximal, as shown in the inset). There were no differences between the masses ($p > 0.11$). Strain values in the synthetic tibias were higher than those in the cadaveric tibias (Chapter 3) at the distal-most gauge level, but lower at all other gauges, as detailed in the table shown to the right.

et al., 2007). The overall failure response of the synthetic bones was found in the current study to differ greatly from that of cadaveric bones.

Fracture force was found to vary with projectile mass; however, with a $p = 0.05$, this is just within the significant range. Impact velocity, momentum, and kinetic energy at failure were all mass-dependent, and as no single injury level was identified for these parameters, this suggests that they are not factors which define the fracture tolerance of these synthetic tibias. All of these parameters had noticeably low variation among specimens, demonstrating one of the desirable features of synthetic bones.

Previous testing of cadaveric tibias (Chapter 3) showed that force and kinetic energy were significant factors in the definition of fracture tolerance. The average force at fracture for the synthetic bones was 37 – 45% of that for the cadaveric tibias, and the average kinetic energy at fracture for the synthetic bones was 26 – 31% of that for the cadaveric specimens. A Weibull analysis based on axial force at failure was conducted in order to generate a survivability curve to be compared to those generated based on previous cadaveric studies (Yoganandan *et al.*, 1996; Chapter 3). The synthetic curve lies to the left of both of these previous studies, demonstrating its lower resistance to fracture (Figure 4.3).

It was hypothesized that the lower fracture tolerance of these synthetic bones could be the result of a stress concentration around the canal; however, patching with epoxy resin provided no improvement. Through the course of testing, it was observed that the distal articular surface of the composite tibias had a convex curvature, which differed from the flat or concave geometry observed on the cadaveric tibias. This curvature could have resulted in point loading from the artificial talus, thus lowering the resistance to failure.

It is recommended that future generations of these synthetic composite tibias include a revision to the distal geometry to better match the concave nature of the distal articular surface.

In comparison to a previous study with cadaveric specimens (Chapter 3), strains in the synthetic bones were higher than those in the cadavers at the distal-most gauge level, but were lower at all other gauge levels. This shows the difference in overall response between the two types of tibias to impact loads. The higher strains at the distal-most level could also possibly be attributed to the geometry of the distal region.

As discussed in Chapter 1, Sawbones® are not the only synthetic composite bone model available to researchers, but they are widely used in orthopaedic research. Models such as the Complex Lower Leg (CLL) and Frangible Surrogate Leg (FSL) were not examined in the current study due to their limited availability, but it is possible that they may have more biofidelic response to this type of axial impact loading, and could be examined in future studies.

The current fourth generation synthetic composite tibias do not accurately represent the response of natural tibias to axial impact loading of this short-duration nature. Studies with slower loading rates (such as car crash simulations) may yield different results. The relatively low tolerance to impact loads, parameters that dictate fracture response, and modes of failure are all different from those found in cadaveric bone. Were it not for the difference in failure mechanisms, a scaling factor could possibly have been applied to the forces experienced by these synthetic bones to represent those of cadaveric bones. As such, they cannot be recommended as a tool for injury investigations under impact loads.

4.6 REFERENCES

Chong, A.C., Miller, F., Buxton, M., and Friis, E.A. (2007) Fracture toughness and fatigue crack propagation rate of short fiber reinforced epoxy composites for analogue cortical bone. *Journal of Biomechanical Engineering* **129,** 487-493.

Cristofolini, L. and Viceconti, M. (2000) Mechanical validation of whole bone composite tibia models. *Journal of Biomechanics* **33,** 279-288.

Cristofolini, L., Viceconti, M., Cappello, A., and Toni, A. (1996) Mechanical validation of whole bone composite femur models. *Journal of Biomechanics* **29,** 525-535.

Funk, J.R., Crandall, J.R., Tourret, L.J., MacMahon, C.B., Bass, C.R., Patrie, J.T., Khaewpong, N., and Eppinger, R.H. (2002) The axial injury tolerance of the human foot/ankle complex and the effect of Achilles tension. *Journal of Biomechanical Engineering* **124,** 750-757.

Heiner, A.D. (2008) Structural properties of fourth-generation composite femurs and tibias. *Journal of Biomechanics* **41,** 3282-3284.

Heiner, A.D. and Brown, T.D. (2001) Structural properties of a new design of composite replicate femurs and tibias. *Journal of Biomechanics* **34,** 773-781.

Yoganandan, N., Pintar, F.A., Boynton, M., Begeman, P., Prasad, P., Kuppa, S., Morgan, R.M., and Eppinger, R. (1996) Dynamic axial tolerance of the human foot-ankle complex. Society of Automotive Engineers, Inc. 962426, 207-218.

CHAPTER 5 – Generation of a Finite Element Mesh of a Cadaveric Tibia

Overview: *Finite element models can be a useful companion to cadaveric testing for computer simulations of impact loading. These models allow experimental testing (such as that conducted in Chapter 3) to be replicated under a variety of conditions. A high quality model, however, is important for obtaining accurate results. This requires careful development, with attention given to proper geometric representation of the bone. This chapter details the techniques used to develop a finite element mesh of a cadaveric tibia from CT scans using the software packages Mimics® and TrueGrid®, and evaluation of its quality.*

5.1 INTRODUCTION

Cadaveric specimens are one method often used to assess risk of injury due to impact loading. Destructive testing, such as that conducted in Chapters 3 and 4, limits the number of impact tests that can be conducted on a single specimen. Validated finite element models developed for the purpose of assessing injury risk would therefore be advantageous. A variety of impact loading conditions (*i.e.*, different impulses, input energies, etc.) could be evaluated for the stresses and strains that develop within the bone.

In order to obtain accurate outputs from models run using finite element analysis, a high quality mesh must be developed. Due to the complex geometry inherent in bones, elements with large amounts of distortion often occur, and are potential sources of low accuracy or instability of a solution (Valle and Ray, 2005). Surprisingly, in dynamic

modeling only one known previous study presents an assessment of the quality of the mesh used (Untaroiu *et al.*, 2005). This raises concerns about the applicability of results from other studies where the mesh has not been so carefully constructed or evaluated.

This chapter details the development of a representative finite element model of the tibia. Its response to short-duration, high-force axial loading will be validated in Chapter 6 via comparison with results from cadaveric testing (Chapter 3). The model was produced using Mimics® (Materialise, Leuven, Belgium) to extract the geometry of the bone from Computed Tomography (CT) scans, TrueGrid® (XYZ Scientific Inc., Livermore, CA, USA) to build a hexahedral mesh defining the different components required for the simulation, and exported in LS-DYNA® format (LSTC, Livermore, CA, USA) for future analysis. Detailed instructions on the step-by-step process used to generate the model using the various software packages are given in Appendix J, and the overall process is described below.

5.2 CT Scanning

CT scans were taken of each of the cadaveric specimens tested experimentally prior to impact loading. All specimens had been potted proximally in a PVC pipe filled with dental cement, and instrumented with strain gauges before scanning. Axial scans were taken using a GE LightSpeed VCT (General Electric Healthcare, Chalfont St. Giles, United Kingdom), with 120 kVp and 100 mA, with a 0.625 mm slice thickness.

From the fourteen CT scans obtained, one representative specimen was selected from which to build the finite element model. Selection was based on an evaluation considering donor age, height and weight, and the impact force required to achieve

fracture during the experimental testing phase. In an effort to choose the specimen that would be most representative, the specimen for which these variables most closely matched the average values of all specimens tested was chosen. This was specimen 08-07033R (Table 5.1).

5.3 SURFACE GEOMETRY EXTRACTION AND ALIGNMENT

The CT scan images from 08-07033R were imported into Mimics® medical imaging software (Materialise, Leuven, Belgium) (Figure 5.1). A mask was applied to the scan to threshold the bone based on the Hounsfield Units (HU) of each voxel. This identified the densest region, which was then defined as cortical bone (HU between 492 and 2561). The mask required minimal manual manipulation for each scan slice, such that a single region was defined for the cortical bone (*i.e.,* fill in missing voxels and remove extraneous ones). Polylines were then generated based on the mask, creating a line on the exterior and interior of the cortical regions (Figure 5.2). The exterior and interior polylines were moved to separate sets, and they were cavity filled with 3D solids (Figure 5.3). These solids were then exported as STL files. STL was selected as the format for surface representation of the bone as it allowed for the best capture of the geometry without artificially smoothing the curvature, as would have occurred using an IGES file. While IGES is the standard CAD format, it only does wireframes and surfaces, not solids. STL files contain triangular facets that represent 2D or 3D shapes.

The inner region (as defined by the interior polylines) was broken into two material types – cancellous bone near the distal and proximal ends, and marrow filling the intramedullary canal. Anatomically, this transition is not clearly defined, with portions of

Table 5.1: Selection of Most Representative Specimen
Specimens were ranked according to their force at fracture, height, weight, and age of donor being closest to the average of all specimens tested. From this, specimen 08-07033R was selected to be the most representative of the average population, and formed the basis of the finite element model.

Specimen	Force (N):	F Rank:	Height (cm)	H Rank:	Weight (kg):	W Rank:	Age (yrs):	A Rank:	SUM:	OVERALL RANK:
06-06037L	9929	6	180.3	7	67.6	7	57	13	33	9
06-06037R	10820	4	180.3	7	67.6	7	57	13	31	7
08-07033R	**12405**	**3**	**185.4**	**1**	**78.0**	**1**	**49**	**1**	**6**	**1**
08-07033L	9862	7	185.4	1	78.0	1	49	1	10	3
08-07024L	11895	1	185.4	1	70.3	5	49	1	8	2
08-07024R	14435	12	185.4	1	70.3	5	49	1	19	4
08-07085R	9481	10	188.0	5	59.6	11	47	7	33	9
08-07085L	9791	8	188.0	5	59.6	11	47	7	31	7
08-08009R	14257	11	190.5	9	114.5	13	47	7	40	12
08-08009L	16131	14	190.5	9	114.5	13	47	7	43	14
06-08044R	14831	13	172.7	13	73.5	3	41	11	40	12
06-08044L	9745	9	172.7	13	73.5	3	41	11	36	11
06-10081L	11168	2	190.5	9	96.2	9	49	1	21	5
06-10081R	10181	5	190.5	9	96.2	9	49	1	24	6
Average:	11781		184.7		80.0		48			

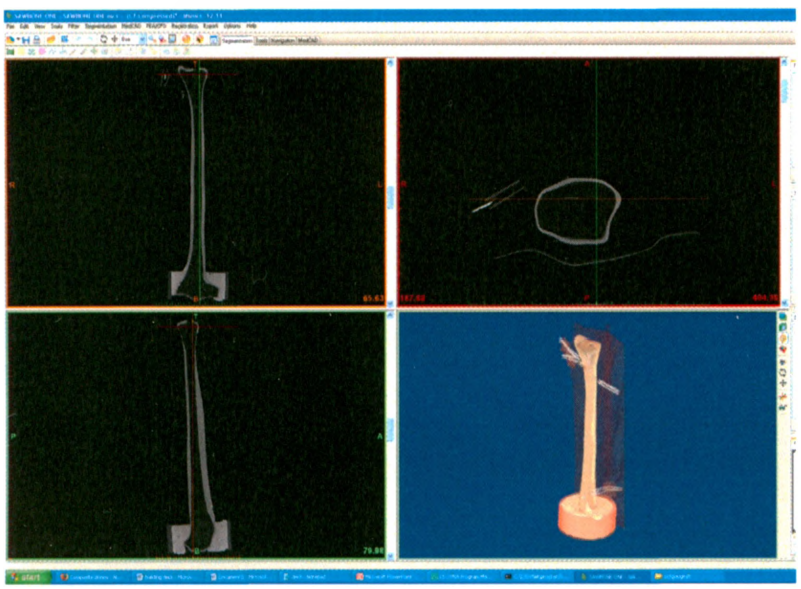

Figure 5.1: CT Scan of Tibia
The selected specimen was imported into Mimics® medical imaging software, which allowed the bone to be viewed in three planes (top left = frontal plane, top right = transverse plane, bottom left = sagittal plane), and thresholding conducted to isolate cortical bone based on Hounsfield Unit.

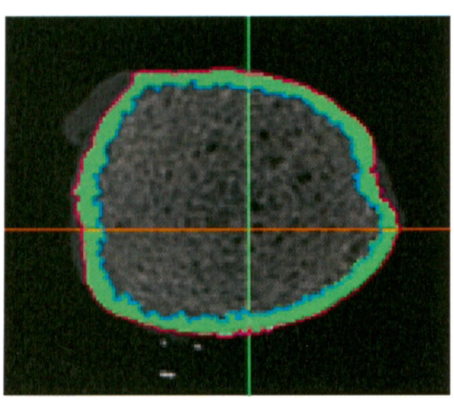

Figure 5.2: Cortical Mask and Corresponding Polylines
The region corresponding to the density of cortical bone was separated using a mask (green), and polylines generated to identify the exterior (purple) and interior (blue) contours.

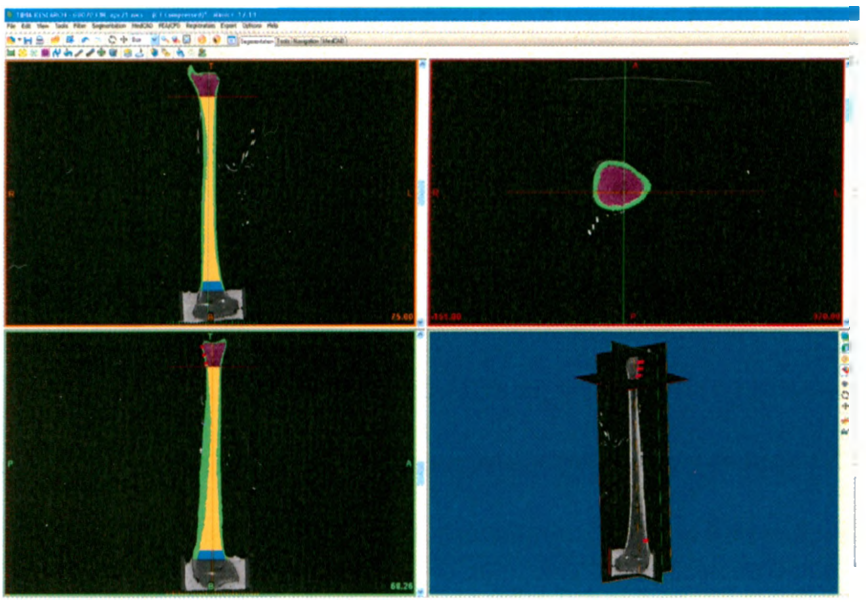

Figure 5.3: 3D Solids
A 3D solid was generated representing the cortical bone based on the polyline contours (green), and others similarly generated for the cancellous (purple and blue) and marrow (orange) regions of the specimen.

cancellous bone appearing in varying amounts throughout the canal, and pockets of marrow extending into the epiphyses of cancellous bone. As such, it is very difficult to draw a distinction between these two regions. As an assumption, two axial locations were selected as the boundaries between canal and cancellous bone regions: one between the distal cancellous bone region and the marrow, and a second between the marrow and the proximal cancellous bone region. These axial locations were defined as the first (*i.e.,* distal) and last (*i.e.,* proximal) CT slice images that were not entirely filled with cancellous bone. While this may have underestimated the portion of cancellous bone slightly, the structural contribution of the cancellous region over the thickness of a slice or two is not substantial, and was considered to be an acceptable simplification. As was previously done for the exterior surfaces, the relevant polylines were copied into distinct sets for each material region, and filled with 3D solids. These solids were also exported as STL files.

To allow comparison between finite element model strains and those obtained experimentally, the locations of the strain gauges on the bone were needed. These were identified in Mimics® by the position of the solder balls on the strain gauge rosettes that were visible in the CT scans (Figure 5.4). These points were subsequently exported as a txt file containing their *x-y-z* positions.

Because the long axis of the specimen was not perfectly aligned with the axis of the CT scanner, the angle between the side of the PVC pot and the axial axis of the scan was measured in both the frontal and sagittal planes (Figure 5.5). This allowed for any offset in angle to be corrected in the finite element simulation, such that it would correspond to

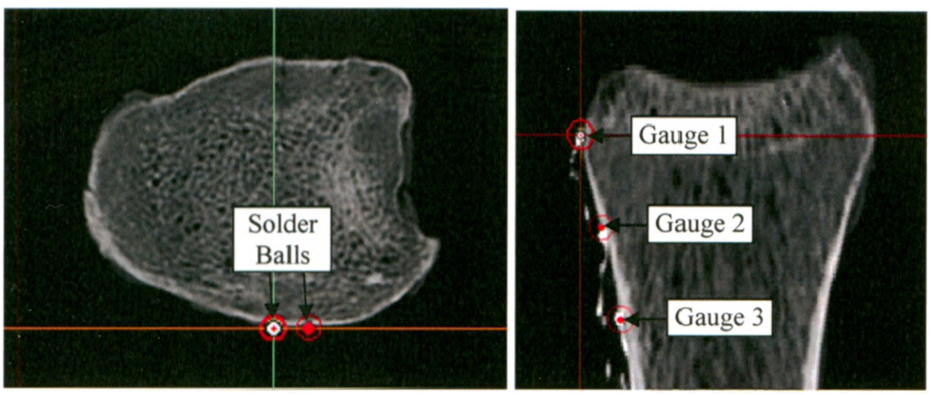

Figure 5.4: Identification of Strain Gauges
Points were defined in Mimics® at the center of the two outer solder balls for each strain gauge rosette (left = transverse plane, right = frontal plane), and were exported as *x-y-z* coordinates to a txt file.

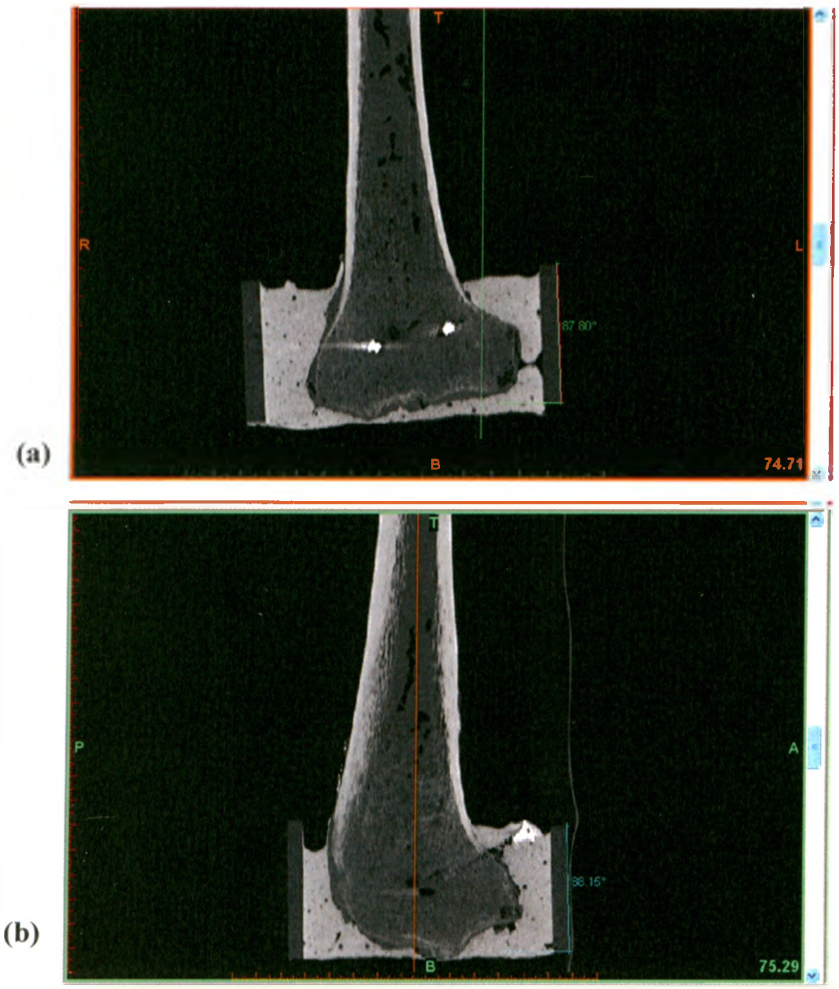

Figure 5.5: Identification of Angle of Tip
Deviations from the *z*-axis based on the sides of the PVC pot were calculated in two planes: **(a)** frontal and **(b)** sagittal.

the experimental setup in which the bone was supported horizontally and subjected to axial impact.

5.4 MESH GENERATION

5.4.1 *MESHING TECHNIQUES*

The mesh of the bone was created using TrueGrid® mesh generator (XYZ Scientific Inc., Livermore, CA, USA). TrueGrid® is a high quality hexahedral meshing program that allows the user to manipulate the mesh through the use of curves and surfaces. It uses a projection method to allow the mesh to best match the geometry of the part being built. This involves the creation of blocks of mesh, which are manipulated and positioned prior to being "projected" to surfaces and curves. This projection method allows small gaps and imperfections to be easily accommodated. The mesh is constructed using a block structure, where each block consists of numerous elements interconnected by nodes. Each block has six faces, which are connected by edges, which join at the corners to form vertices. Many blocks are used to build the mesh structure, and are separated by partitions. Partitions allow each block to be assigned a differing number of elements, as well as different material properties. Figure 5.6 shows the working environment of TrueGrid®, with the computational view (which shows the block structure) on the right and the physical view (which shows the positions and shapes of the elements) on the left.

As there are many areas of high curvature in the geometry of the tibia, it was important to select the appropriate topology to be used for the mesh. Figure 5.7 shows how applying a hexahedral mesh to a circular cross-section can result in elements that are

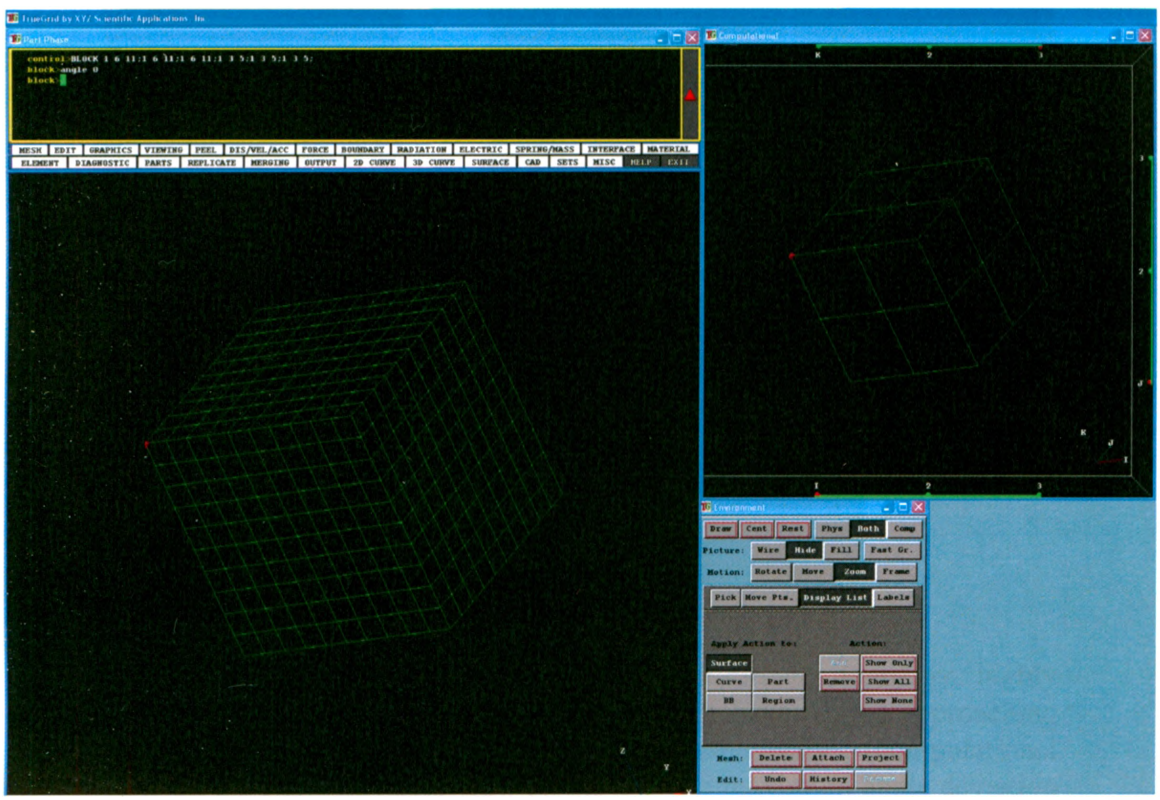

Figure 5.6: TrueGrid® Environment
Blocks of elements are built and manipulated using the computational view (right), and the positions and shapes of the elements relative to other parts and elements and nodes are shown in the physical view (left). At the top is the dialog box for inputting commands.

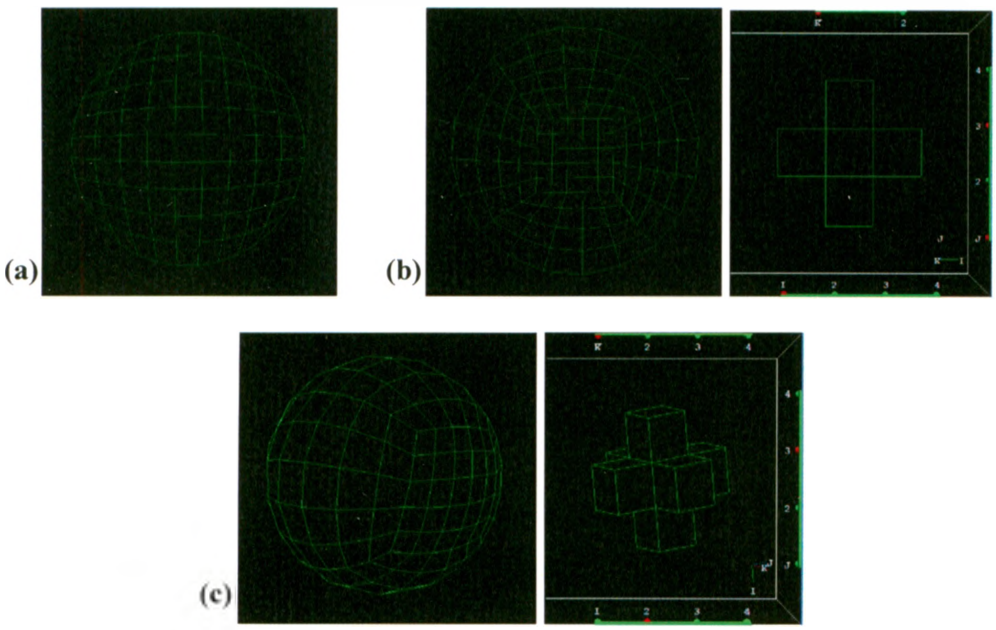

Figure 5.7: The Butterfly Technique
(a) When a hexahedral mesh is applied to a circular topology, highly distorted elements occur at the corners, which have angles approaching 180°. **(b)** By combining several blocks in a "butterfly", (computational view on the right, physical view on the left) the maximum angle deviation can be reduced substantially. **(c)** When this is translated into 3D and multiple butterflies applied, a sphere can be correctly meshed with minimal angle deviations.

extremely distorted, with distortion angles up to 180° at the corners. To reduce this distortion, multiple blocks are combined in what is known as the "butterfly technique". To build a butterfly, a grid of three blocks by three blocks is built, and the corner blocks removed. The corners of the remaining exterior blocks are then manually moved to be at approximately a 45° angle. After the initial positioning of the vertices, the faces where the corner blocks were removed are then glued together using a block boundary command. This results in a mesh where the most distorted elements are significantly improved.

5.4.2 *TIBIA MESHING*

The STLs that were exported from Mimics® were imported into TrueGrid® as surfaces (Figure 5.8). The surfaces were rotated as required to align the longitudinal axis with the direction of loading (*i.e.,* the angle correction mentioned in Section 5.3). Meshing was started from the distal portion of the bone as this had the most anatomical detail, the highest degree of curvature, and was the area of most interest. The interior cancellous and marrow regions were meshed first, before the cortical layer was added.

The topology of the distal-most region was similar to a cylinder, and as such butterflies were used at each quadrant of the bone. 3D splines were interactively created along the distal ridge around the circumference of the bone at both the cortical and cancellous levels to attach the edge to the outermost area of the bone. Further splines were created along the length of the bone at each quadrant (Figure 5.9). The inner cancellous region was projected to the inner STL surface, and several smoothing algorithms applied to the surfaces (to relax the faces) and volumes (to uniformly smooth

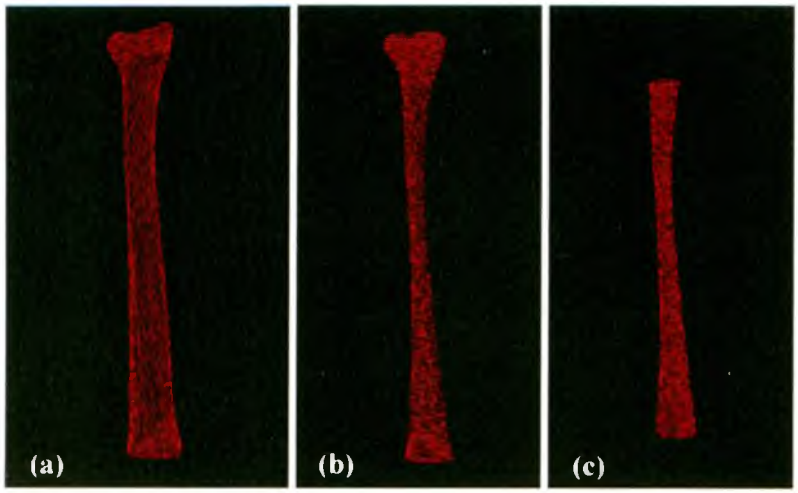

Figure 5.8: STL Surfaces in TrueGrid®
STL surfaces describing **(a)** the exterior of the cortical bone, **(b)** the interface between cortical and cancellous bone, and **(c)** the region defining the intramedullary canal.

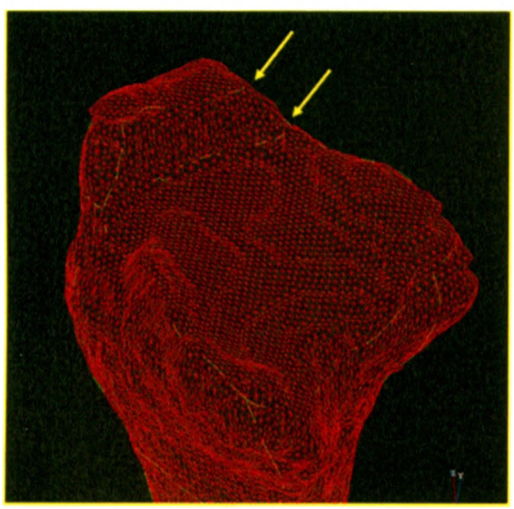

Figure 5.9: Generation of Splines in TrueGrid®
Splines were generated along areas of high curvature based on the STLs for attachment of the edges of blocks.

the regions) of the bone. Blocks were then added to the exterior of the cancellous region to represent the cortical bone. Due to the small thickness, a single element depth was used, and splines were similarly used to control the placement of the edges of the blocks. The cortical region was projected to the outer STL surface, and smoothing algorithms applied. The distal region of the bone has large changes in geometry, and so the distal-most section focused on the epiphysis prior to where it started to taper. An *x-y* surface was generated that marked this level, and the proximal edges of each of the regions were attached to it. A relatively fine mesh was used to characterize the detail present in this region, resulting in 4480 brick elements. The distal-most region of the tibia mesh can be seen in Figure 5.10.

The second most-distal region was constructed as a second part attached to the first, but incorporated a transition zone joining the two (Figure 5.11). This transition zone reduced the number of elements by a factor of two in each of the *x* and *y*-directions due to the narrowing of the bone's geometry. This reduced the number of distorted elements, and also improved the aspect ratio (which was high due to fitting a large number of elements through a relatively small corridor). The second level continued until the point where the transition from cancellous to marrow was defined. The diaphysis of the bone was continued in the same manner, with similar smoothing algorithms as previously described. At the proximal end a transition zone was again incorporated due to the expansion of the geometry, resulting in twice as many elements in each of the *x* and *y*-directions. The complete mesh is shown in Figure 5.12. A merge tolerance was applied to eliminate duplicate nodes between the parts, resulting in a continuous mesh for the bone with 14848 linear 8-node hexahedral elements.

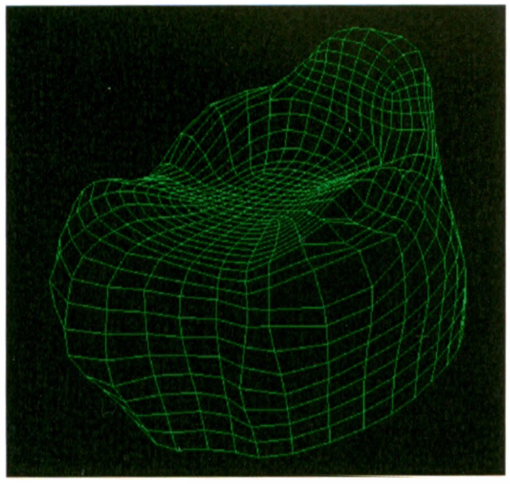

Figure 5.10: Distal-Most Mesh
The mesh was started at the distal end due to the high changes in geometry and interest in this area. Faces of the mesh were projected to the STL surfaces representing the bone's geometry.

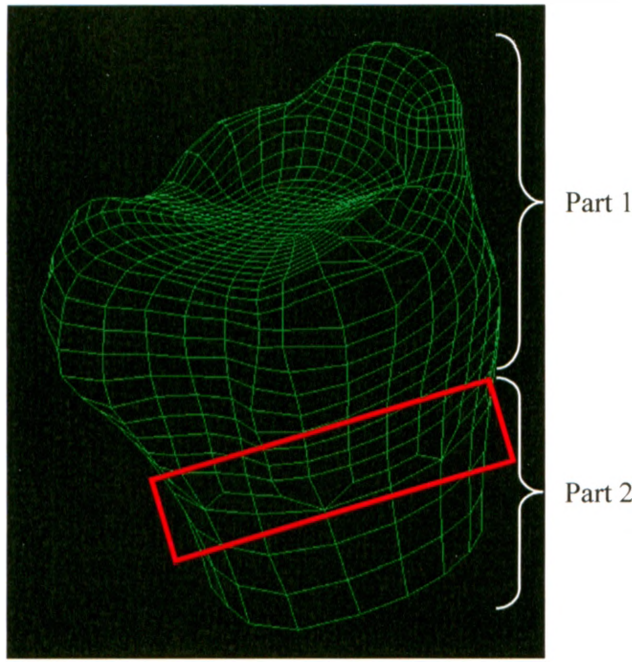

Figure 5.11: Transition Region
A transition zone (highlighted in red) between the distal-most part and the second part was used to reduce the number of elements that would become distorted as the cross-section of the bone tapered. The number of elements was reduced by a factor of two in each direction.

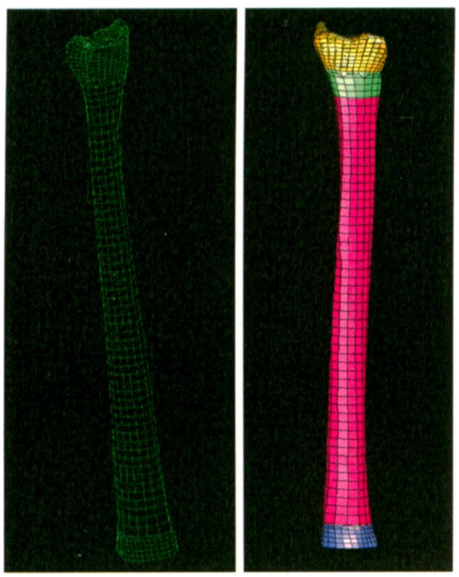

Figure 5.12: Complete Bone Mesh
The complete bone mesh consisted of 14848 hexahedral solid elements, with mesh density higher at the distal and proximal ends. The coloured regions represent the different parts that were built to achieve proper meshing.

5.4.3 *MESH EVALUATION*

Several diagnostic techniques were used to evaluate the quality of the mesh prior to analysis. The Jacobian of an element is a measure of its deviation from an ideally shaped element (computed as the determinant of the Jacobian matrix). The Jacobian of an extremely distorted element becomes negative, and will prevent analysis from continuing. The Jacobian was measured for each element in the bone mesh, and ranged from 0.102 to 8.001, with a mean of 0.7. The criterion for Jacobian in this study was that it be a positive value, and preferably greater than 0.25 (Untaroiu *et al.*, 2005). The Jacobian distribution can be seen in Figure 5.13, with elements with the smallest Jacobians (those less than 0.2 and therefore most at risk of failure) highlighted.

The orthogonality of the mesh (measured as the interior angle deviation from 90°) was also assessed, as elements that have large deviations can have unrealistic deformation responses. The deviation angle in the current mesh was found to range from -77° to 87° (corresponding to interior angles of 13° to 177°). The orthogonality distribution can be seen in Figure 5.14, and the goal was to avoid angular deviation values greater than an absolute magnitude of 70° (highlighted in pink in the figure for diagnostic purposes). The mean deviation angle was approximately zero, and the small number of distorted elements occurred primarily at the transition zones. It was not possible to completely eliminate elements with large deviation angles, although attempts were made to minimize the number present.

The final method of mesh quality assessment was aspect ratio. In TrueGrid®, the aspect ratio is computed as the ratio of the longest diagonal to the shortest diagonal in the element. For a solid element, the most numerically accurate solution is obtained when

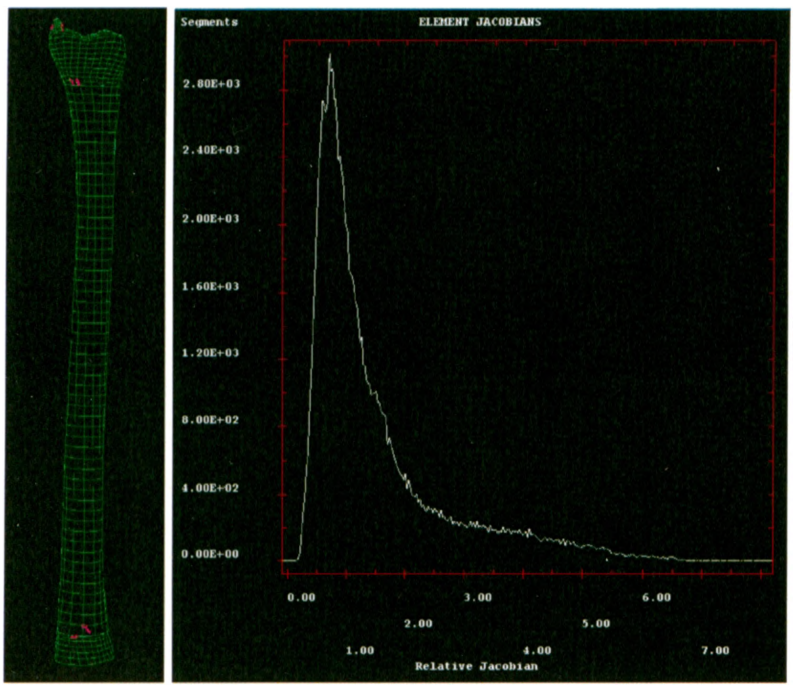

Figure 5.13: Element Jacobians
The average Jacobian in the mesh was 0.7, with a range of 0.1 to 8.0, Jacobians less than 0.2 are shown in pink. The closer to zero a Jacobian, the higher the risk of the simulation failing.

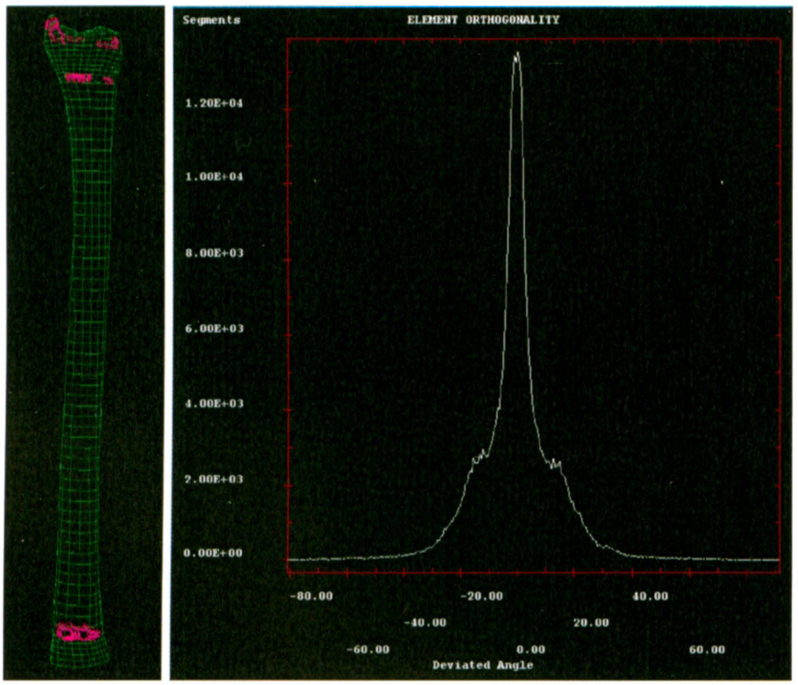

Figure 5.14: Element Orthogonality – Deviation Angle
Element angles deviation from 90° are shown in the distribution graph to the right. The average angle of deviation was zero, ranging from -77° to 87°. Elements with angles deviated between 70 – 90° (interior element angles less than 20° or greater than 160°) are shown in pink.

the elements' edges are equal in length. However, due to irregular geometry and features, this is not always possible, and when large differences occur the accuracy is reduced. Aspect ratios were found to range from 1.1 to 13.4. Ratios greater than 10 were to be avoided (Untaroiu *et al.*, 2005), and were only present in a small number of the elements in the final mesh and in regions of little interest (Figure 5.15). After the bone mesh was deemed of a sufficient quality, meshing of the other components (*i.e.*, projectile, brackets, talus and foam) could proceed.

5.4.4 *OTHER COMPONENTS*

Experimentally, the load applied to the distal surface of the tibia was transmitted via an artificial polyethylene talus. This was located to touch the articular surface, and adjusted to best sit within the distal curvature. For the finite element analysis, this talus was modeled as a distinct part using TrueGrid®. From the CT scan in Mimics®, a circle with the same diameter as the talus was drawn on an axial slice best approximating where the talus would have been centered. The *x-y-z* coordinates of this circle were exported as a txt file. A cylinder was created as a surface in TrueGrid® that matched this, and the talus part was generated such that it didn't touch the surface of the bone (Figure 5.16). From the surface of the talus, another part was extruded to represent the distal bracket. The geometry of the steel bracket was not modeled, only a block was constructed to represent the mass, as deformations of the bracket were presumed to be negligible. Off the distal bracket was built a third part representing the urethane foam used in testing to control the duration of load application. Another part was built just off the surface of the foam (but not attached) representing the projectile (with its front curvature matching that

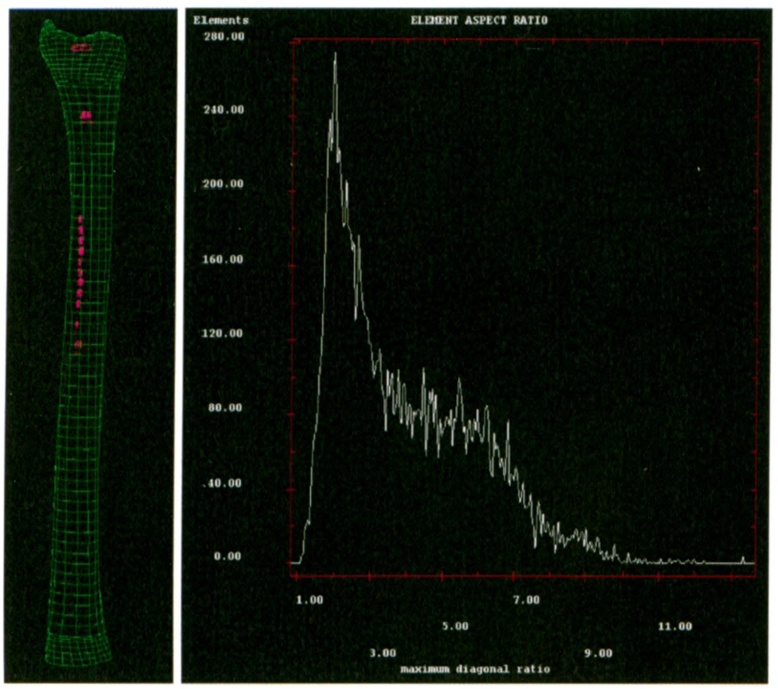

Figure 5.15: Aspect Ratio
Aspect ratios ranged from 1.1 to 13.4, with a mean of 2. Element aspect ratios are shown, with those greater than 10 highlighted in pink.

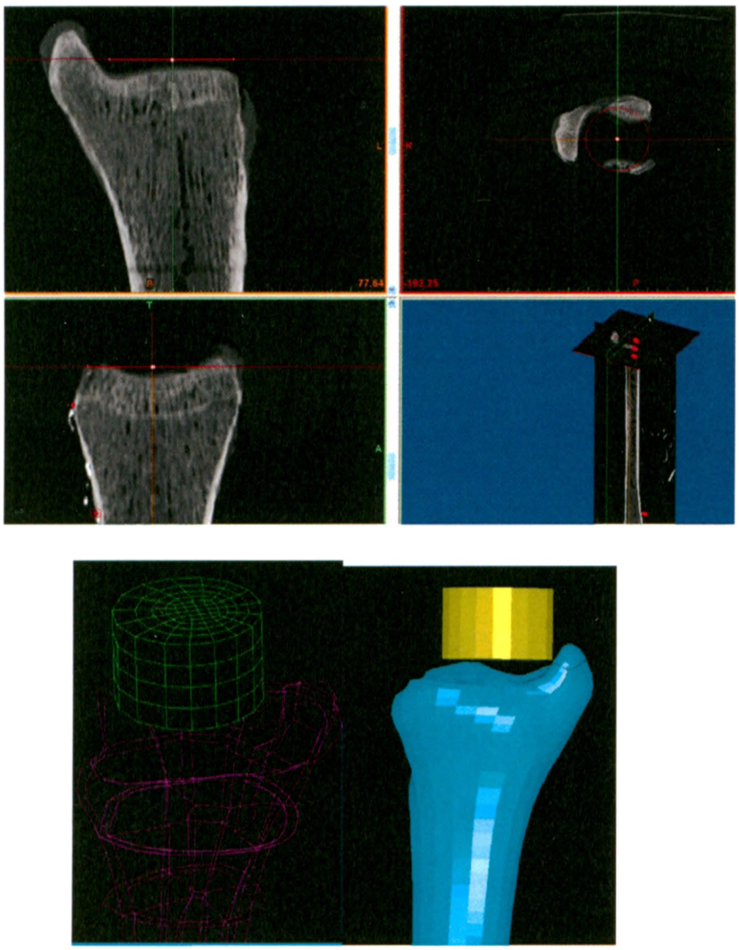

Figure 5.16: Creation of the Talus
A circle was stamped on the CT scan representing the best fit as would have been done experimentally. The coordinates of this circle were used to build a cylinder in TrueGrid® representing the talus.

of the projectile used experimentally). Finally, a block was built at the surface of the proximal cut end of the tibia, representing the proximal bracket. All components are shown in Figure 5.17, with a comparison to experimental setup. The TrueGrid® file for creating the mesh is included as Appendix K. The entire setup was exported in LS-Dyna® format. The model was then imported into LS-PrePost® (the preprocessor for LS-Dyna®, and the parts initialized to be in contact with one another. The elements representing the strain gauges were also identified using the *x-y-z* coordinates (from Section 5.3) and assigned to separate sets for each gauge.

5.5 SUMMARY

Finite element models are a potentially useful tool for assessing injury risk to the body through simulations. Previous studies have used these models to predict lower limb response to impulsive loading (*e.g.*, Iwamoto *et al.*, 2000; Beillas *et al.*, 2001; Untaroiu *et al.*, 2005), but with very little or no assessment of the quality of the mesh. Elements which have large aspect ratios or which are highly distorted are sources of error which may result in poor accuracy or instability of the analysis (Valle and Ray, 2005).

The mesh described in this chapter was developed with accurate representation of the bone geometry being the highest priority. The geometry of the bone regions was directly computed from CT scans, and through control curves and the projection method a mesh was built that represents these surfaces. Most elements met the diagnostic targets, and were deemed to be of sufficient quality to properly characterize the bone. All of the relevant components used in the experimental tests (Chapter 3) were also meshed and aligned with the long axis of the bone. This mesh will be used in Chapter 6 to simulate the impact tests that were conducted experimentally, which will complete the evaluation

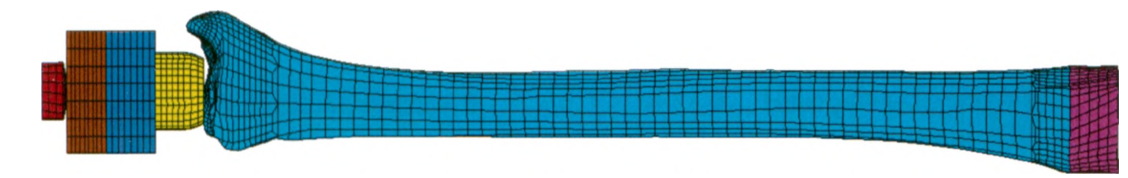

(a)

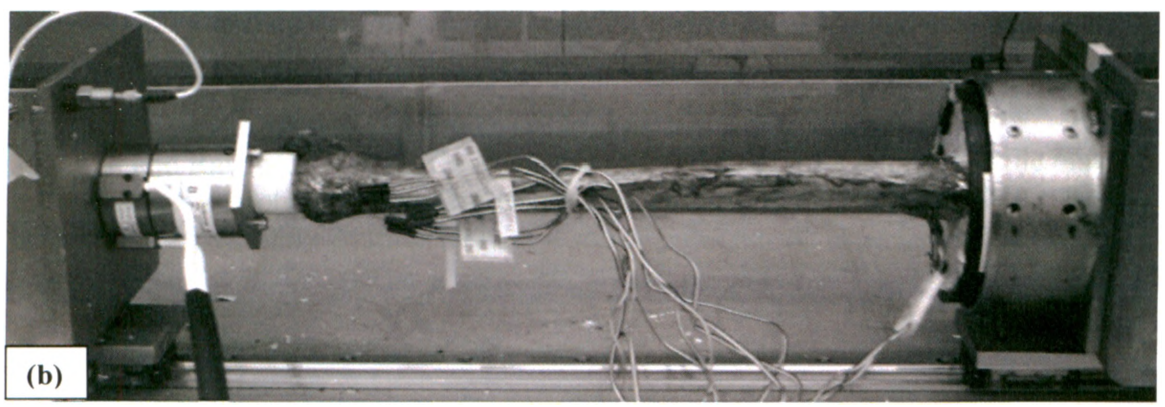

(b)

Figure 5.17: Completed Mesh of all Components Compared to Experimental Setup

(a) From left to right: projectile (red), foam (brown), distal bracket (dark blue), talus (yellow), tibia (light blue), and proximal bracket (purple). The components were all attached together except for the projectile-foam and the talus-bone interfaces. **(b)** Experimental setup with corresponding components (projectile and foam not shown).

of the model as a tool for injury prediction applications.

5.6 REFERENCES

Beillas, P., Begeman, P.C., Yang, K.H., King, A.I., Arnoux, P.J., Kang, H.S., Kayvantash, K., Brunet, C., Cavallero, C., and Prasad, P. (2001) Lower limb: advanced FE model and new experimental data. *Stapp Car Crash Journal.* **45,** 469-494.

Iwamoto, M., Tamura, A., Furusu, K., Kato, C., Miki, K., Hasegawa, J., and Yang, K.H. (2000) Development of a finite element model of the human lower extremity for analyses of automotive crash injuries. In *2000-01-0621.* Computer Applications for Crash, Optimization, and Simulation Research, Society of Automotive Engineers, Detroit, MI, USA.

Untaroiu, C., Darvish, K., Crandall, J., Deng, B., and Wang, J.T. (2005) A finite element model of the lower limb for simulating pedestrian impacts. *Stapp Car Crash Journal.* **49,** 157-181.

Valle, L. and Ray, M.H. (2005) Development and validation of a 50th percentile male human femur: Attachment A. Worcester Polytechnic Institute. Worcester, MA, National Highway Traffic Safety Administration.

CHAPTER 6 – Finite Element Model of a Tibia for Impact Analysis

Overview: *This chapter provides details on the finite element simulations of the experimental testing of one cadaveric specimen from Chapter 3, using the mesh developed in Chapter 5. The iterative process followed to obtain the model that is most representative of the response of the experimental results is described in detail.*

6.1 INTRODUCTION

Experimental testing of cadaveric specimens may provide the most realistic representation of the natural human response to loading, but they are often not a practical option for injury assessment, particularly in an industrial setting. Automotive and defence manufacturers conduct the majority of their designs and safety assessments using computer simulations; as such, finite element models offer a useful method for evaluating injury risk. The models are advantageous in that they allow a variety of experimental variables to be investigated simulating destructive tests relatively quickly and at a relatively low cost once properly developed. These provide an alternative for injury assessment that can be implemented in survivability analyses.

Development of a good quality mesh (as discussed in Chapter 5) is extremely important for obtaining accurate results, but many other parameters need to be properly determined in the model construction. A critical component of a finite element model that must be decided *a priori* is the selection of appropriate material properties for bone. Accepted values for bone material properties vary through the literature (*e.g.*, Tannous *et*

al., 1996; Takahashi *et al.*, 2000). In some cases, the properties are allowed to vary throughout the bone, based on a density-elastic modulus relationship, where the density is obtained via a CT scan on an element-by-element basis (*e.g.,* Taddei *et al.*, 2006; Austman *et al.*, 2008). Alternatively, the bone is divided into gross regions (*i.e.,* cortical vs. cancellous) and each region is assigned a bulk property. Due to the complex computational nature of dynamic tests, the latter method (*i.e.,* bulk properties) is typically selected (*e.g.,* Iwamoto *et al.*, 2000; Untaroiu *et al.*, 2004). However, the range of bulk properties found in the literature is great, and the properties chosen to be modeled (*i.e.,* the inclusion of a plastic region or strain rate effects) also vary from study to study. A further parameter that requires definition in a model is the element formulation (*i.e.,* single-point or multi-point integration), which dictates how the stress is computed through an element. The appropriateness of bone material definition has received little attention in the literature, and further investigation is required.

Several previous studies have attempted to generate an injury-predicting finite element model (Tannous *et al.*, 1996; Iwamoto *et al.*, 2000; Takahashi *et al.*, 2000; Beillas *et al.*, 2001; Kim *et al.*, 2005; Untaroiu *et al.*, 2005), but with very little validation. This would involve comparing the response of the model to that measured experimentally for the same loading and boundary conditions. The material properties can be varied within the range reported in the literature until best agreement is achieved. Comparisons can be made for both low-force (non-fracture) and high-force (fracture) tests.

The purpose of this study was to construct a finite element model based on a representative cadaveric tibia selected from the experimental impact tests (Chapter 3),

and meshed using TrueGrid® software (Chapter 5). Axial load magnitude, duration, velocity, impulse, and bone strains were compared to experimentally-obtained values and failure criteria were examined for obtaining the most representative model.

6.2 MATERIALS AND METHODS

6.2.1 SOFTWARE OVERVIEW

The dynamic finite element software used in this study was LS-Dyna® (LSTC, Livermore, CA, USA). LS-Dyna® is widely used in the automotive and defence industries due to its ability to handle large strain dynamic simulations. This makes it a good solver for examining crashworthiness. The first version of LS-Dyna® was DYNA3D, which was initially developed in 1976. This was developed into the commercial software package LS-Dyna® in 1988, and has since undergone many iterations and further developments. The complimentary model editor and post-processor for the LS-Dyna® solver is LS-PrePost®, which is used for initial setup of the model and plotting of outputs following simulation. Outputs can be in the form of 2D plots, 3D plots, and animations.

The LS-Dyna® solver runs text files called decks as the input code, which follow a specific format. Each command in the deck (*e.g.*, material definition, boundary condition, etc.) is termed a "card", and has a pre-defined structure for parameter input. There are over 150 different material models available for solids and shells (MAT #), and the descriptions are available in the LS-Dyna® Keyword User's Manual (LSTC, 2003). Numerous solid element formulations are likewise available, which affect how the stress is computed through an element. These include the default constant stress solid

(ELFORM 1), which has a single integration point, the fully integrated selective reduced solid (ELFORM 2), which has eight integration points, and the fully integrated quadratic 8 node element with nodal rotations (ELFORM 3), which has fourteen integration points. These are listed in increasing accuracy as well as computational cost.

6.2.2 DECK CREATION

The mesh developed in Chapter 5 and output in LS-Dyna® format (Appendix K) was used for the finite element model described within this chapter. Several commands had to be manually written into the deck for proper functioning. All units were selected to be consistent, with mm, ms, kg, and kN. Each component (cortical bone, cancellous bone, marrow, talus, distal bracket, foam, proximal bracket, projectile) was assigned a unique part, section, and material number.

As the nodes between the foam/distal bracket and distal bracket/talus were coincident and merged, they formed a continuous mesh, so no contact parameters were required. Contact was defined between the projectile and foam; an automatic surface-to-surface contact prevented nodes of one part from penetrating the surface of the other. A similar contact was defined between the talus and cortical bone, as well as between the talus and cancellous bone (for trials involving fracture). An additional contact card was defined preventing the nodes of the foam from penetrating its own faces (contact interior).

Boundary conditions were also written into the deck. The projectile, distal and proximal bracket parts were constrained to only move in the z-direction, mimicking the motion along the rail in the experimental setup (see Section 2.2.1). The projectile was given an initial velocity in the z-direction equal to the velocity achieved in the

experimental testing. This velocity was varied, so as to mimic the testing conditions for both the non-fracture and fracture tests (8.58 m/s and 11.37 m/s, respectively, corresponding to input target energies of 150 J and 250 J). A force was applied to the distal bracket in the negative *z*-direction to simulate the frictional forces that develop as a result of the large bending moment resisted by the bearings. The magnitude of this force was estimated using a frictional coefficient of 0.5, which was selected based on the measured distal bracket velocity (against the ATD leg in Chapter 3) compared to the theoretical velocity in a perfectly elastic collision. Outputs were written to record the nodal forces at the talus, and element information for each of the strain gauge sets described in Section 5.5.

6.2.3 Experimental Components

The components used in the experimental testing were defined based on their known material properties.

6.2.3.1 Rigid Components

There were three stainless steel components in the current model – the projectile and the distal and proximal brackets. The projectile was modeled using the curvature of the experimental projectile, but the brackets were modeled as blocks as their purpose was purely for inertial effects. As stainless steel is more than 10 times as stiff as cortical bone, it was decided that these components would experience negligible deformations, and could therefore be modeled using rigid materials (LS-Dyna® material model MAT 20). This has the advantage of reducing computational complexity, as the nodes in these

parts do not move relative to each other. The volumes of each "block" of rigid material were measured using LS-PrePost® and densities were assigned as needed to achieve masses matching the corresponding components used experimentally.

6.2.3.2 Polyurethane Foam

Simulation of foam is challenging due to the variability in material properties and the large deformations that can be experienced. Several material models exist in LS-Dyna® for modeling foams. A low density foam model is recommended as an appropriate formulation that has shown good correlation with physical test values (Sambamoorthy and Halder, 2001). This model is appropriate for simulating highly compressible, low density foams, and typically is used for seat cushions (LSTC, 2003). However, this resulted in unrealistically large compressions during initial trials of the model due to the concentrated load application. As such, the polyurethane was modeled as a simple elastic material, and the modulus was determined from experimental testing on the foam in an Instron® materials testing machine (*i.e.*, E = 2.5 MPa). A selective reduced integrated solid element formulation was used for the foam (ELFORM 2), which is recommended as it prevents pressure locking (Sambamoorthy and Halder, 2001).

6.2.3.3 Polyethylene Talus

The artificial talus was machined from high-density polyethylene, and was modeled using an elastic material model. The talus experienced relatively small deformations during the tests (on the order of 2 μm), but could not be modeled as a rigid material since such materials do not provide force output in LS-Dyna®, and this was the required

location for force measurement. A constant stress solid element formulation (ELFORM 1), the least computationally intensive, was used for this component to increase analysis speed due to the relatively small deformations experienced.

6.2.4 BONE OPTIMIZATION

The representation of cortical and cancellous bone in previous LS-Dyna® studies has varied greatly. For this purpose, numerous parameters were investigated in order to assess their influence on the bone response (Figure 6.1), with the aim of optimizing the model to best represent the experimental response.

6.2.4.1 MATERIAL PROPERTIES

The properties required to define the cortical bone model were the density, elastic modulus, Poisson's ratio, yield stress, and tangent modulus. Densities from the literature ranged from 1500 to 2100 kg/m^3 (Beillas *et al.*, 2001; Kim *et al.*, 2005), with the most commonly used value approximately 1850 kg/m^3 (Tannous *et al.*, 1996; Beaugonin *et al.*, 1997; Beillas *et al.*, 2001). The elastic modulus used for previous tibia models ranged from 12 – 20 GPa (Tannous *et al.*, 1996; Beaugonin *et al.*, 1997). As the specimen being modeled was from a young donor, an elastic modulus of 20 GPa was selected. This is similar to the modulus reported by Yamada *et. al.* (1970). Poisson's ratio in nearly all previous finite element tibia studies is 0.3 (*e.g.* Untaroiu *et al.*, 2005), and was used for the present model as well. The yield stress of cortical bone has been consistently reported in the literature to be approximately 0.120 – 0.129 GPa (Burstein *et al.*, 1976; Untaroiu *et al.*, 2005). Again, due to the specimen being from a young donor, the yield

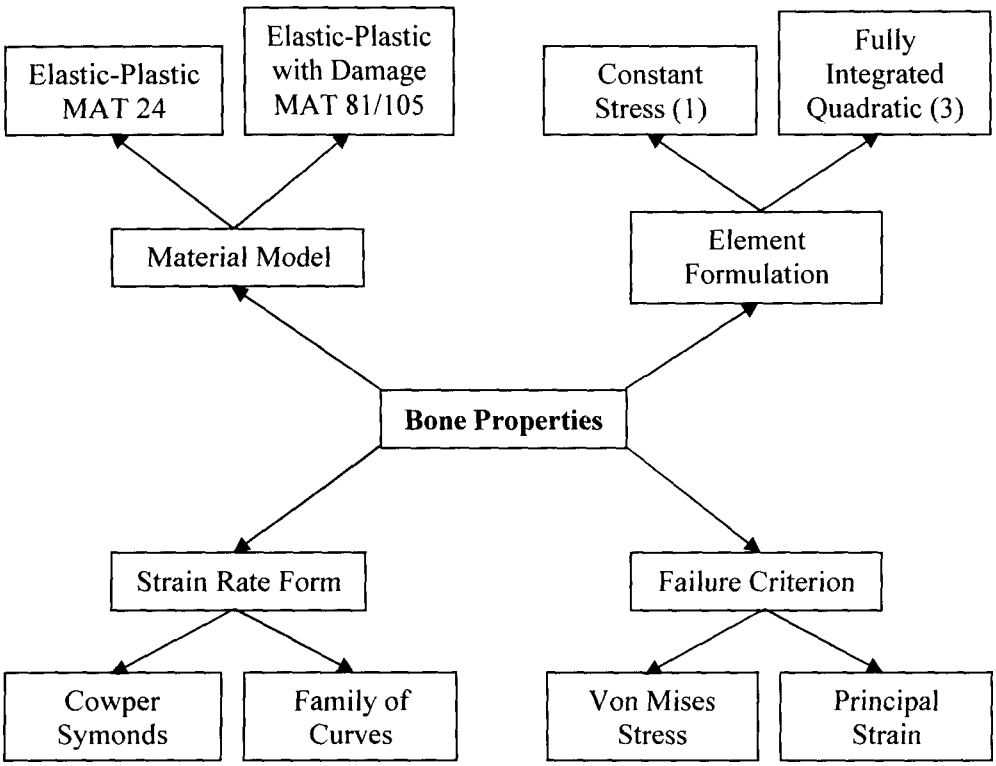

Figure 6.1: Parameters Investigated for Bone Properties
Two material models, two element formulations, two strain rate effect formulations, and two failure criteria were examined to determine the optimal bone properties.

stress was selected to be at the upper end, at 0.129 GPa. The plastic modulus (E_{tan}) was selected as 1 GPa (Burstein *et al.*, 1976), which is the recommended value of 5% of the elastic modulus (Imai *et al.*, 2006).

The same properties were defined for the cancellous bone component. Densities from the literature ranged from 454 to 1500 kg/m^3 (Beaugonin *et al.*, 1997; Kim *et al.*, 2005), with the most commonly used value approximately 1000 kg/m^3 (Untaroiu *et al.*, 2005). The elastic modulus in previous tibia models ranged from 0.25 – 0.53 GPa (Beaugonin *et al.*, 1997; Kim *et al.*, 2005), and 0.5 GPa was selected due to specimen age. Poisson's ratio was again selected to be 0.3 and yield stress was defined as 10 MPa (Kim *et al.*, 2005). The plastic modulus (E_{tan}) was selected as 5% of the elastic modulus (*i.e.*, 0.025 GPa).

Marrow is often neglected in finite element models of bone due to its low load transmission properties. However, the presence of this material can have an effect on the bone response to high strain rate loading (Carter and Hayes, 1977), and as such was included in the present study. Marrow was defined simply as an elastic material, with a density of 1000 kg/m^3, a modulus of 20 MPa, and a Poisson's ratio of 0.499 (Peng *et al.*, 2006).

6.2.4.2 Material Model

In previously-reported finite element models, cortical and cancellous bone have been modeled as one of three LS-Dyna® material types: linear elastic (MAT 1), elastic-plastic (MAT 24) and elastic-plastic with damage (MAT 81 and MAT 105 for cortical and cancellous, respectively). Linear elastic models were used in early modeling of this type

(Tannous *et al.*, 1996; Beaugonin *et al.*, 1997). This had the limitations of no yielding, no plastic deformation, and no strain rate effects. To better model bone, an elastic-plastic material model has become the new standard (Beillas *et al.*, 2001; Untaroiu *et al.*, 2005). This material consists of a bilinear modulus curve, with optional inclusion of strain rate effects (LSTC, 2003). A final material model that was used in a previous study was elastic-plastic with damage effects (Kim *et al.*, 2005). This included all the parameters of the previous material, but formulated with continuum damage mechanics, and includes a failure strain. Once the plastic strain in an element reaches this level, the element is deleted and no longer bears any load. It is hypothesized that this could realistically mimic fractures. For the elastic-plastic with damage model, a failure strain of 0.016 was used as the element deletion criteria for cortical bone, and 0.134 for cancellous bone (Untaroiu *et al.*, 2005). The elastic-plastic and the elastic-plastic with damage materials were both investigated in the current work.

6.2.4.3 Element Formulation

A constant stress solid element formulation (ELFORM 1) offers the fastest analysis speed (due to its low computational requirements), but is at risk of a phenomenon called hourglassing. The stress in this type of element is only computed at the center of the element, and as such the element may experience deformation that results in a state of zero stress. The use of this type of element is preferable if the accuracy sacrificed is minimal, due to the reduction in simulation time.

An element formulation which is not prone to hourglassing is the fully integrated quadratic 8 node element with nodal rotations (ELFORM 3). This element formulation

has fourteen integration points, and as such can be more accurate (and computationally expensive) than the constant stress type (Valle and Ray, 2005).

6.2.4.4 Strain Rate Formulation

Bone is a viscoelastic material, and therefore has a variable response depending on strain rate. Two different strain rate effect formulations were examined in this thesis. The first was the Cowper-Symonds model, which scales the yield stress according to the factor:

$$1+\left(\frac{\dot{\varepsilon}}{C}\right)^{1/p} \qquad \textbf{(Eq. 6.1)}$$

Where $\dot{\varepsilon}$ is the strain rate, C = 360.7, and p = 4.605 (LSTC, 2003; Iwamoto *et al.*, 2005) for both cortical and cancellous bone components (Figure 6.2). The second strain rate formulation examined was through the definition of a family of curves for a series of strain rates. These curves have been previously defined for the tibia (Untaroiu et al., 2004) (Figure 6.3). Intermediate strain rates are found by interpolating between the curves defined, and strain rates above the maximum level provided (1/s) use the highest curve. This strain rate formulation was only tested for cortical bone, as a set of strain rate curves for cancellous bone were not presented in the literature.

6.2.4.5 Failure Criteria

Maximum principal strain and Von Mises stress have both been previously used as failure criteria for finite element models which do not simulate fracture via element deletion (Takahashi *et al.*, 2000; Untaroiu *et al.*, 2005). The applicability of these parameters to assess the fracture risk in the present model was examined by plotting the

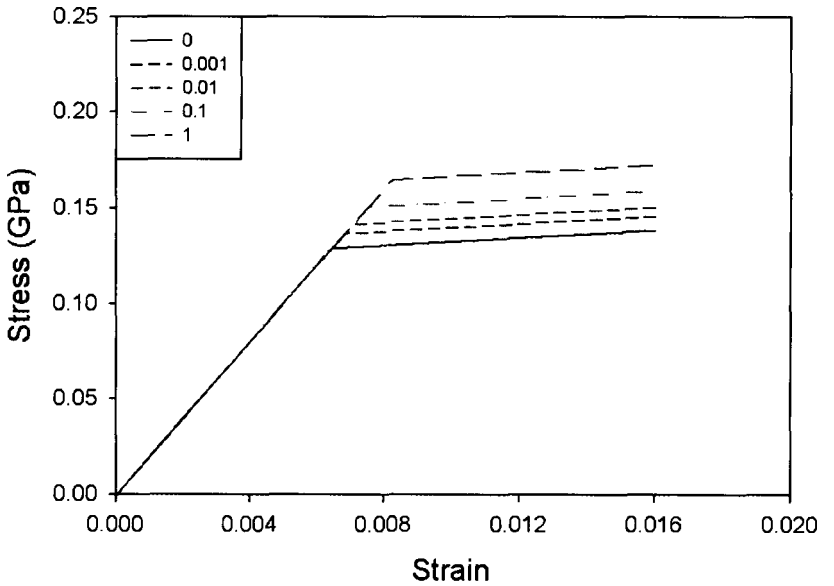

Figure 6.2: Cowper-Symonds Strain Rate
A series of strain rate curves (s^{-1}) demonstrates the Cowper-Symonds strain rate effect model (Eq. 6.1), which alters the yield stress only.

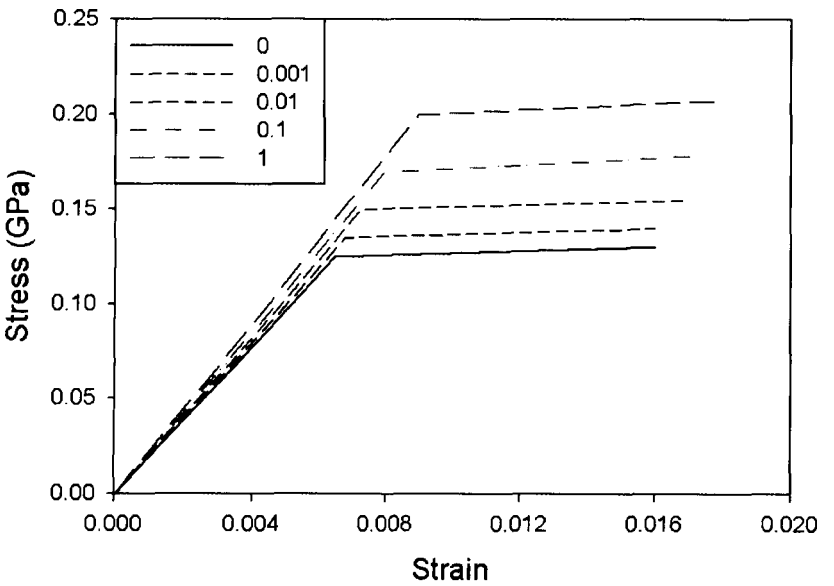

Figure 6.3: Strain Rate Family of Curves
A series of strain rate curves (s^{-1}) was defined based on a previous study (Untaroiu *et al.*, 2004). Strain rates above the maximum rate defined (1/s) used the curve for the 1/s rate.

maximum principal strain and the Von Mises stress for the non-fracture (*i.e.*, 150 J) and fracture (*i.e.*, 250 J) simulations. The critical strain level in cancellous bone was 0.134, and for cortical bone was 0.016 (Takahashi *et al.*, 2000; Untaroiu *et al.*, 2005). The ultimate stress for the cancellous region was 5.3 MPa, and for the cortical bone was 134 MPa (Untaroiu *et al.*, 2005). The injury risk equation developed in Chapter 3 (Eq. 3.2) was also applied to assess the simulations (using the peak axial force, applied kinetic energy, and height and age of the specimen donor).

6.2.5 Summary

The values used for the components described in Sections 6.2.3 and 6.2.4 are summarized in Table 6.1.

6.3 Results

Several outputs formed the basis of comparison between the finite element simulations and the experimental tests (Chapter 3). The axial force (as measured at the talus node set and with the load cell) and impact duration were the primary basis of comparison, as this is what has been used in previous studies. The values presented throughout this section are given with their percentage of experimental value in brackets immediately following. The corresponding impulses and distal bracket velocities were also examined, and the principal strains calculated for the locations of the strain gauges (for the non-fracture test only, as was done in Chapter 3). These points of comparison were used to select the set of properties for the bone that best matched the impact tests simulated. For the best model parameters selected, failure criteria (Von Mises stress and

Table 6.1: Material Properties
Properties for the tibia were taken from the literature, and the brackets and projectile were modeled with properties of steel and densities calculated to give the appropriate masses to the general blocks built in the mesh (both 6.8 kg and 3.9 kg projectile properties are included).

	Mass Density (kg/m^3)	Rigid Part Volume (mm^3)	Elastic Modulus (MPa)	Plastic Modulus (MPa)	Poisson's Ratio	Yield Stress (MPa)
Cortical Bone	1850	-	20000	1000	0.3	129
Cancellous Bone	1000	-	500	26.5	0.3	10
Marrow	1000	-	20	-	0.499	-
Polyethylene Talus	1000	-	1700	-	0.35	-
Distal Bracket	9590	44995	210000	-	0.3	-
Foam	40	-	2.5	-	0.2	-
Proximal Bracket	147600	37964	210000	-	0.3	-
Projectile (6.8 kg)	1690000	4017	210000	-	0.3	-
Projectile (3.9 kg)	971000	4017	210000	-	0.3	-

maximum principal strain) and the injury risk equation developed in Chapter 3 were evaluated.

6.3.1 Bone Material Model

The evaluation of material models was conducted using the fully integrated element formulation (ELFORM 3) and Cowper-Symonds strain rate effects.

6.3.1.1 Elastic-Plastic Material

The elastic-plastic material model achieved a peak axial force for the non-fracture simulation of 8.9 kN (74% of experimental), over a time duration of 3.2 ms (89%) (Figure 6.4). This resulted in an applied impulse, calculated by integrating the force-time curve, of 14.5 Ns (91%). The velocity of the distal bracket in the simulation was 2.45 m/s (122%).

For the fracture simulation, this model reached a peak force of 15.1 kN (121%), over a time duration of 3.1 ms (103%) (Figure 6.5). The corresponding impulse was 23.8 Ns (123%). The velocity of the distal bracket was 4 m/s (400%).

6.3.1.2 Elastic-Plastic With Damage Material

The elastic-plastic with damage material model (which allowed element erosion) resulted in elements being deleted in both the non-fracture and fracture tests (Figure 6.6). Because the eroded elements could no longer carry any load, the axial force resulting from these tests was vastly different from those found experimentally (2.8 kN (23%) for the non-fracture, 4.4 kN (35%) for the fracture) (see Figures 6.4 and 6.5). Due to this

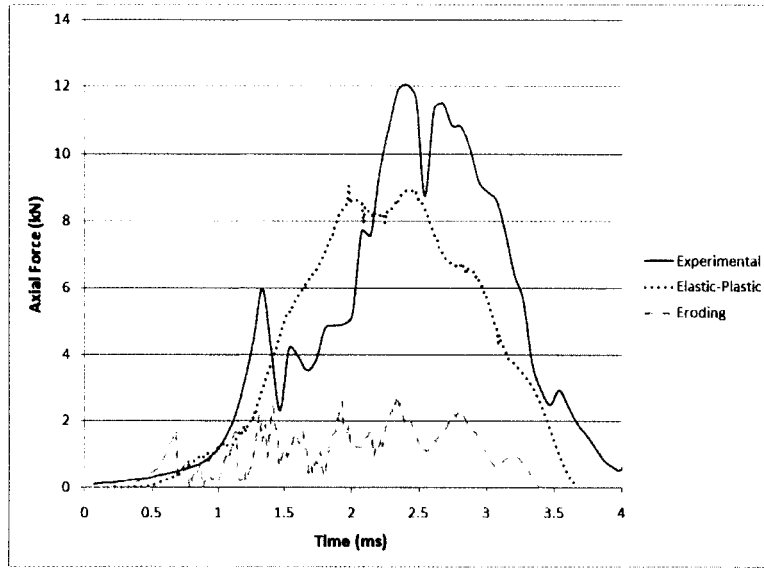

Figure 6.4: Axial Force for Material Models, Non-Fracture
The peak force using the elastic-plastic material model was 74% of that attained experimentally, whereas the peak force using the elastic-plastic with damage material model (*i.e.*, eroding) was 23%.

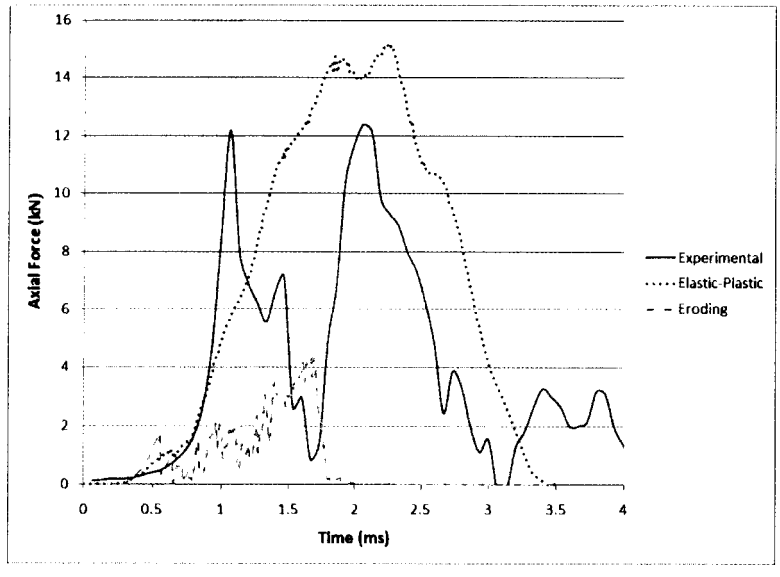

Figure 6.5: Axial Force for Material Models, Fracture
The peak force using the elastic-plastic material model was 121% of that attained experimentally, whereas the peak force using the elastic-plastic with damage material model (*i.e.*, eroding) was 35%.

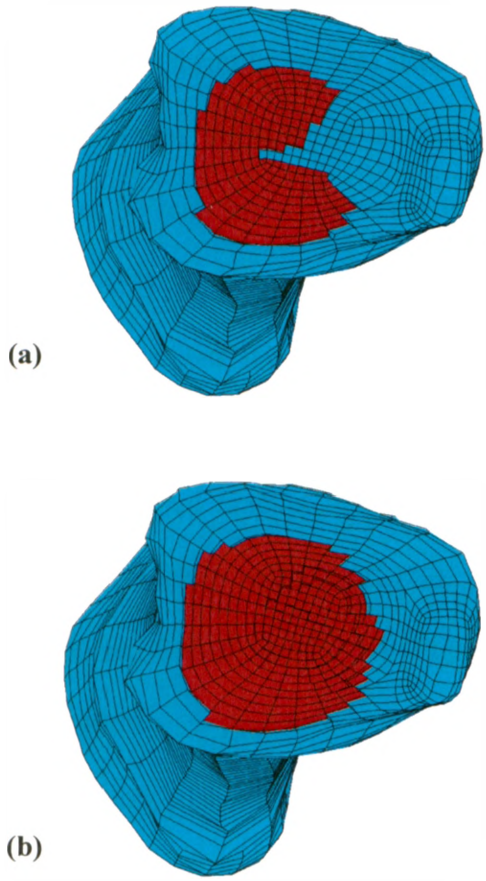

Figure 6.6: Element Erosion
Blue elements represent cortical bone, and pink represents cancellous bone. In both **(a)** the non-fracture and **(b)** the fracture simulations cortical elements exceeded the failure strain criterion (0.016). They were then eroded, exposing the cancellous bone. In the fracture simulation **(b)**, cancellous elements exceeded the failure strain criterion (0.134) and were eroded (*i.e.,* step-downs in pink region).

dramatic difference, the elastic-plastic material model (Section 6.3.1.1) was used for all other parameter assessments.

6.3.2 Element Formulation

The family of curves strain rate formulation was used for evaluation of the effect of element formulation. The constant stress solid element formulation (ELFORM 1) simulation ran in an average of 30 minutes, whereas the fully integrated 8 node element with nodal rotations (ELFORM 3) ran in an average of 3 hours. For the non-fracture simulation, ELFORM 1 achieved a peak force of 8.9 kN (74% of experimental) over a load duration of 3.2 ms (89%), resulting in an impulse of 14.5 Ns (91%) (Figure 6.7). This was with a corresponding distal bracket velocity of 2.45 m/s (122%). For the fracture simulation, ELFORM 1 reached 15.1 kN (121%), with a loading time of 3.1 ms (103%), and an applied impulse of 23.8 Ns (123%) (Figure 6.8). The velocity of the distal bracket reached 4 m/s (400%).

For the non-fracture simulation, ELFORM 3 achieved a peak force of 10.4 kN (87%), lasting 3.1 ms (86%), with an impulse of 17.0 Ns (106%). The distal bracket reached a speed of 2.86 m/s (143%). In the fracture case, the axial force reached 15.7 kN (125%), loading was applied over 3.3 ms (110%), creating an impulse of 25.4 Ns (132%). The distal bracket reached a peak velocity of 4.27 m/s (427%). ELFORM 3 was used for assessment of strain rate effects.

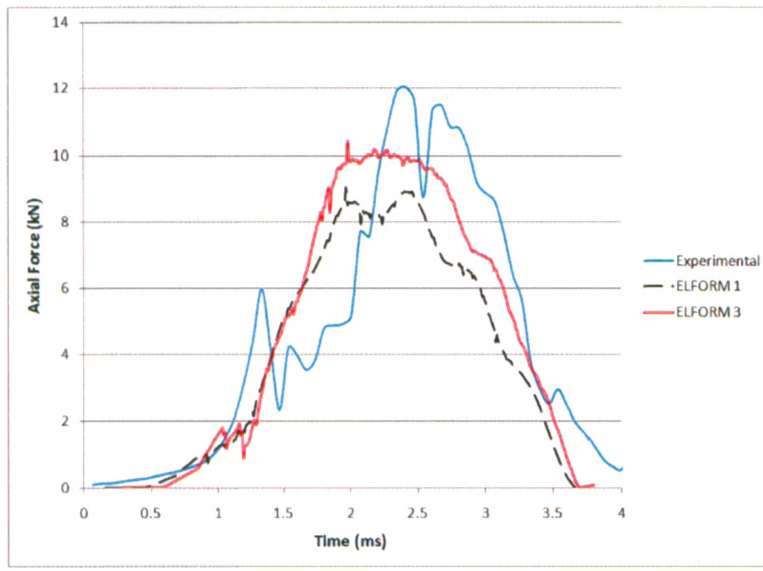

Figure 6.7: Axial Force for Element Formulation, Non-Fracture
The constant stress formulation (ELFORM 1) achieved a peak force 74% of that experimentally, whereas the fully integrated quadratic formulation (ELFORM 3) achieved a peak force 87% of the experimental.

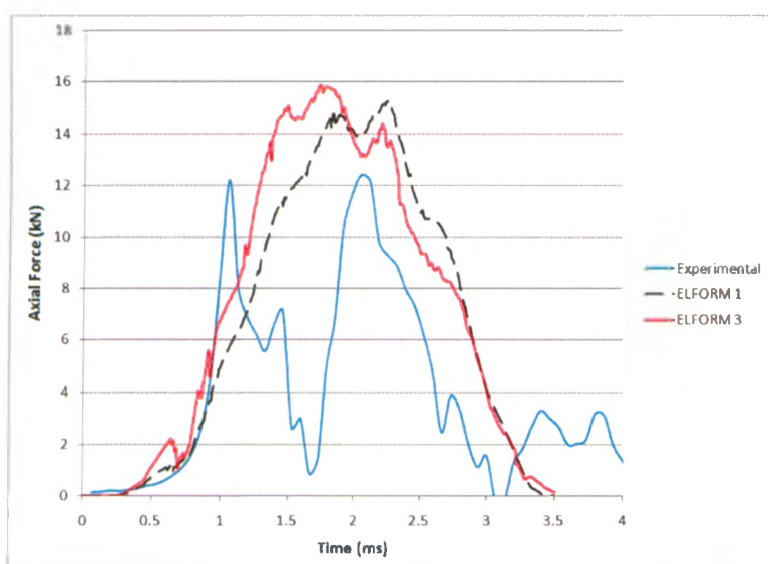

Figure 6.8: Axial Force for Element Formulation, Fracture
The constant stress formulation (ELFORM 1) achieved a peak force 121% of that experimentally, whereas the fully integrated quadratic formulation (ELFORM 3) achieved a peak force 125% of the experimental.

6.3.3 Strain Rate Formulation

6.3.3.1 Cowper-Symonds Equation Approach

The elastic-plastic material model with strain rate effects using the Cowper-Symonds yield stress scaling equation (Eq. 6.1) reached a peak axial force of 12.5 kN for the non-fracture simulation (104% of experimental) over a duration of 3 ms (83%), resulting in an impulse of 18.8 Ns (117%) (Figure 6.9). The distal bracket velocity attained in the simulation was 3.1 m/s (155%). For the fracture simulation, this formulation reached a peak force of 17.9 kN (143%) over a duration of 2.9 ms (97%) with a corresponding impulse of 27.0 Ns (140%) (Figure 6.10). The distal bracket velocity in the simulation was 4.5 m/s (450%).

6.3.3.2 Family of Strain Curves Approach

The family of strain rate curves attained a peak axial force for the non-fracture simulation of 10.4 kN (87%), with a loading duration of 3.1 ms (86%), resulting in an impulse of 17.0 Ns (106%). The distal bracket velocity was 2.9 m/s (143%). Likewise, for the fracture simulation, the peak force was 15.7 kN (126%), over a time span of 3.3 ms (110%), creating an impulse of 25.4 Ns (132%). The bracket velocity in this simulation reached 4.3 m/s (427%).

6.3.3.3 Effect on Strains at Strain Gauge Locations

At the distal-most gauge (Gauge 1) neither strain rate formulation predicted the strains well, with the Cowper-Symonds method overestimating the experimental principal strains by as much as 8 times, and the family of curves overestimating them by as much

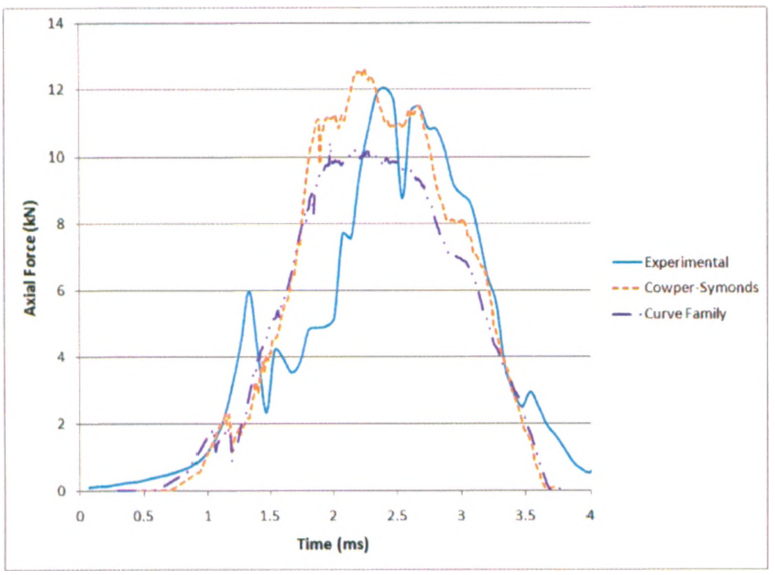

Figure 6.9: Axial Force for Strain Rate Formulations, Non-Fracture
The peak force using the Cowper-Symonds formulation was 104% of that attained experimentally, whereas the peak force using the family of strain rate curves was 87%.

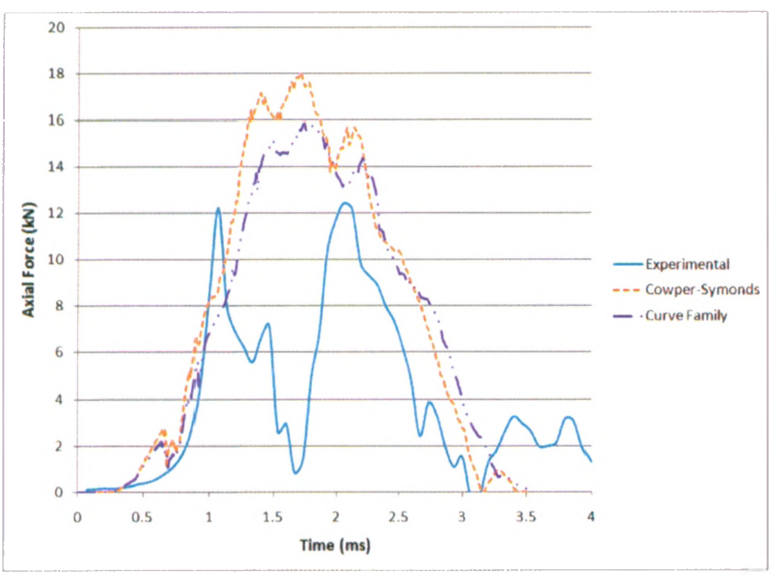

Figure 6.10: Axial Force for Strain Rate Formulations, Fracture
The peak force using the Cowper-Symonds formulation was 143% of that attained experimentally, whereas the peak force using the family of strain rate curves was 126%.

as 6 times (Figure 6.11). At the second gauge (Gauge 2), the Cowper-Symonds method overestimated the principal strains by a factor of 5, whereas the family of curves was worse, with predicted strains being up to 8.5 times the strains measured experimentally. At the third gauge (Gauge 3) the Cowper-Symonds formulation aligned well with experimental strains, with predicted values of 0.7 times the experimental values. The family of curves was closer as well, yet continued to over-predict the strains by a factor of 2. At the fourth strain gauge (Gauge 4) strains were negligible, and no difference between strain rate formulations was evident.

6.3.4 Optimal Bone Parameters

The results from the non-fracture studies conducted in sections 6.3.2 and 6.3.3 are summarized in Table 6.2, with the percent difference from experimental given in brackets. As it was understood that the fracture simulation would have limitations in its ability to represent the energy absorbed during a fracture, it was decided to select the optimal parameters based on the non-fracture study. The parameter closest to experimental for each factor examined is thus highlighted. The best material model was determined in section 6.3.1 to be an elastic-plastic material model. The fully integrated element formulation (ELFORM 3) appeared to better match experimental values than the constant stress solid (Section 6.3.2), and as such was selected for the final model. The best formulation for strain rate effects as presented in section 6.3.3 was selected to be the use of a family of strain rate curves defining viscoelastic effects, with the Cowper-Symonds scaling equation performing nearly as well.

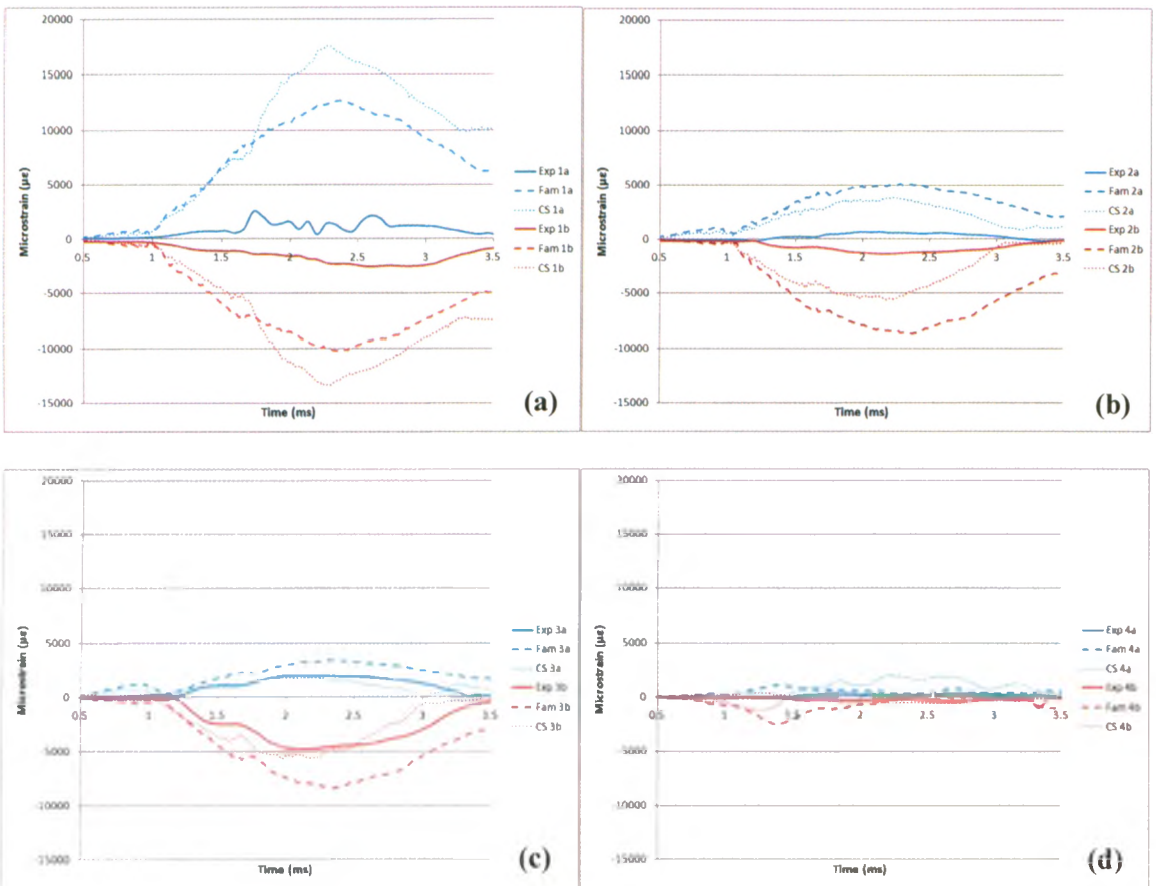

Figure 6.11: Principal Strains, Strain Rate Formulations
The principal strains corresponding to the gauges **(a)** Gauge 1, **(b)** Gauge 2, **(c)** Gauge 3, and **(d)** Gauge 4 for experimental (solid lines) and Cowper-Symonds and family of curve strain rate formulations. At Gauge 1 the family of curves was closer to experimental; while at Gauges 2 and 3 the Cowper-Symonds equation provided the best representation. There was little difference at Gauge 4.

Table 6.2: Summary of Parameters Evaluated

The two element formulations and the two strain rate formulations were compared to experimental values for peak axial force (F), impact duration (t), impulse (Imp), and bracket velocity (V). Values are presented with percentages of experimental values listed in brackets immediately following. The parameter which was closest to experimental is highlighted in blue. From this ELFORM 3 and the Family of Curves strain rate formulation were selected.

	F (kN)	t (ms)	Imp (Ns)	V (m/s)
ELFORM 1	8.9 (74)	3.2 (89)	14.5 (91)	2.4 (122)
ELFORM 3	10.4 (87)	3.1 (86)	17.0 (106)	2.9 (143)
Cowper-Symonds	12.5 (104)	3 (83)	18.8 (117)	3.1 (155)
Family of Curves	10.4 (87)	3.1 (86)	17.0 (106)	2.9 (143)

6.3.5 *FAILURE CRITERIA*

The two failure criteria (Von Mises stress and maximum principal strain) were assessed by plotting both the non-fracture and fracture conditions for the final model parameters (*i.e.,* elastic-plastic material, family of curves strain rate formulation, and fully integrated elements). Regions which exceeded the ultimate strain values (as defined in Section 6.2.4.4) were highlighted in red (Figure 6.12). A small number of elements exceeded the maximum principal strain level in the cortical bone in the non-fracture test, and a larger number in the fracture test. Cancellous strains never exceeded the critical level. A similar trend was noticed in the cortical bone for Von Mises stress (Figure 6.13), with a small number 'failing' in the non-fracture test and a larger number in the fracture simulation. The cancellous bone, however, exceeded the Von Mises criteria in a large number of elements for both tests.

Using the force-based injury curve (Figure 3.8), the injury risk from the non-fracture simulation was 32% and for the fracture simulation was 95%. Using the injury risk equation developed in Chapter 3 (Eq. 3.2, Figure 3.7), and the force and kinetic energy values from the present model, the injury risk from the non-fracture simulation was <1% and for the fracture simulation was 33% (Figure 6.14).

6.4 DISCUSSION

Finite element models are a promising tool for assessing injury potential to humans and for the design of protective measures. Many researchers have reported models to represent the response and injury risk to the lower leg (*e.g.,* Iwamoto *et al.*, 2005; Untaroiu *et al.*, 2005) but with very little validation. In order for the results from the

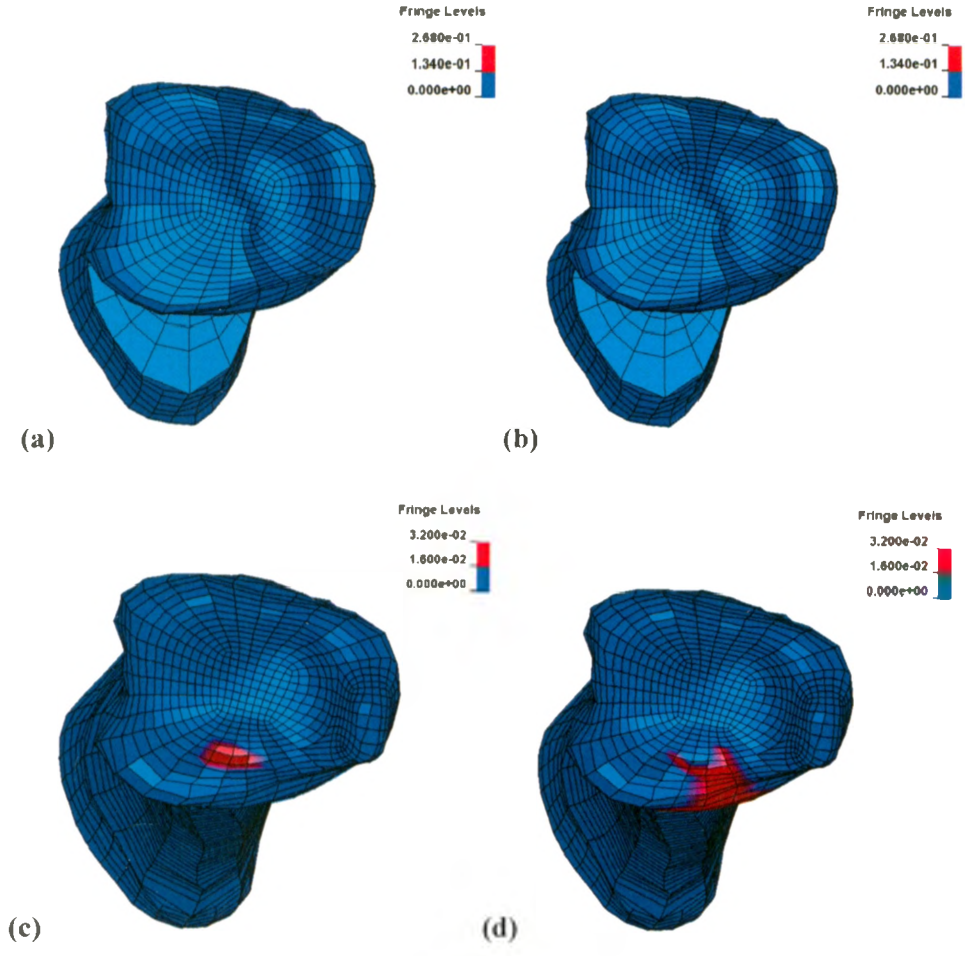

Figure 6.12: Maximum Principal Strains
Maximum principal strains which exceeded the critical level are shown in red. **(a)** non-fracture, cancellous **(b)** fracture, cancellous **(c)** non-fracture cortical **(d)** fracture, cortical. The critical cortical strain level was 0.016, and cancellous was 0.134.

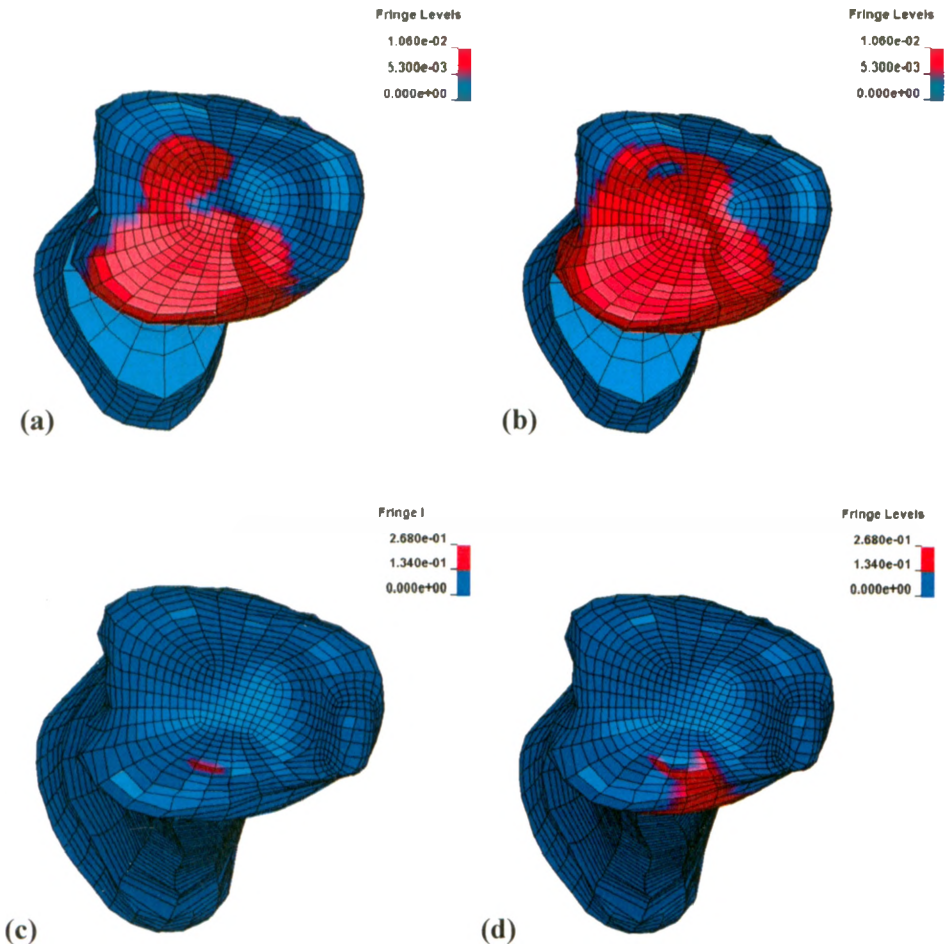

Figure 6.13: Von Mises Stress
Maximum Von Mises stresses which exceeded the critical level are shown in red. **(a)** non-fracture, cancellous **(b)** fracture, cancellous **(c)** non-fracture cortical **(d)** fracture, cortical. The critical cortical stress was 134 MPa, and was 5.3 MPa for cancellous bone.

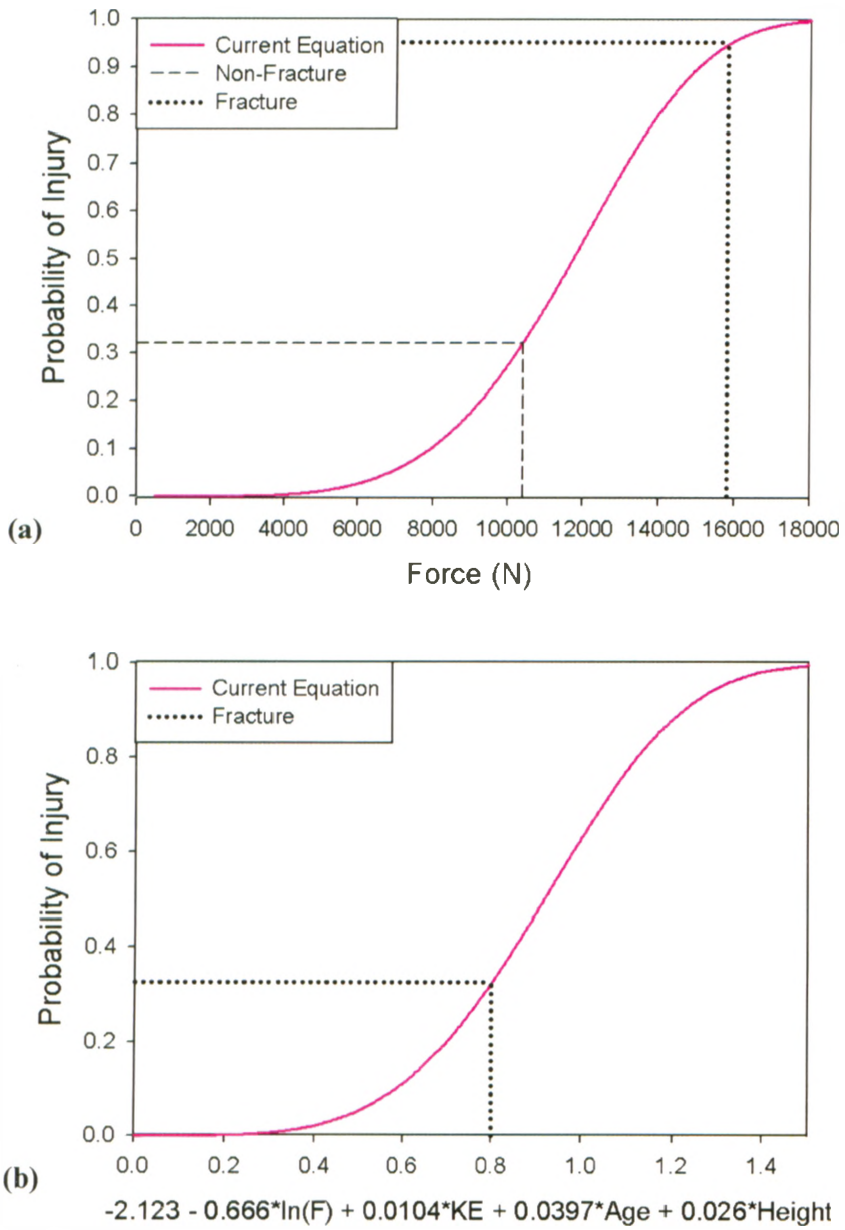

Figure 6.14: Application of Injury Risk Curves
The injury risk curves from Chapter 3 were applied to the non-fracture and fracture simulations, for **(a)** the force-only curve, and **(b)** the newly developed equation (Eq. 3.2).

model to be meaningful, a thorough investigation of its ability to represent the natural response of bone must be conducted.

The model built in this study has been developed to most represent natural cadaveric bone, as well as to predict the occurrence of injury in the specimen. It has the advantage of the geometry being taken from CT scans of the specimen which was actually tested, rather than from the Visible Human Project (Untaroiu *et al.*, 2005; Kim *et al.*, 2005). It was compared to the actual dynamic data from its impact testing (Chapter 3), rather than against previously published whole-bone response data (Tannous *et al.*, 1996; Untaroiu *et al.*, 2005), allowing for a more precise investigation into its response.

The representation of fracture, and the effect it has on geometry and energy absorption, is a difficult challenge in finite element modeling. The use of element deletion beyond a failure strain level was examined, but was found to be inappropriate. In the experimental testing conducted in Chapter 3, a crushing type of failure mechanism was noted. In such a case energy would be absorbed during the fracture, and then the resistance to loading would increase again as the "crushed" material built up behind the talus. This is the likely source of the double-hump of the experimental fracture curve (*e.g.*, Figure 6.5). If the elements are deleted, they cannot allow this "build up" of material to occur, and thus the ability to carry load is limited.

For the non-fracture impact level, the force, time duration, velocity, and impulse showed qualitatively good agreement between model and experimental responses. As evidenced by the small dip in the experimental curve, it is possible that small amounts of damage were occurring at this testing severity, which weren't represented in the model response. The model exceeded the experimental force for the fracture test, which is

unsurprising, but matched the time duration well. The velocity was likely higher in the model than experimentally for the fracture test because of the lack of energy absorption in combination with the "sticking" that occurred during the injury (as the talus drove into the distal region). Previous finite element models compared predicted fracture forces to experimentally obtained values, with an average difference of 10 – 15% (Untaroiu *et al.*, 2004; Iwamoto *et al.*, 2005) that could range up to 30 – 40% (Tannous *et al.*, 1996; Untaroiu *et al.*, 2005). The present model predicted experimentally-measured values within a maximum of 20%.

The agreement between experimental strain gauges and strains obtained in the simulation was not as good as expected; however, this could be attributed to the lack of regional variations in the model material properties. As well, strain rates as high as 5 per second were noted in the non-fracture simulation, so a family of strain rate curves that encompassed this range would likely improve accuracy of this formulation. LS-Dyna® presents maximum and minimum strains for the 3D volume, and in the current version of the software is unable to output surface strains. This may have contributed to the lack of agreement with the strain gauges. Strain gauge placement was limited experimentally, and as such only provided information about discrete locations for the non-fracture tests. Better agreement may have been attained at other locations along the bone which were not instrumented. Only one previous finite element investigation has looked at principal strains in comparison with a strain gauge experimentally (Untaroiu *et al.*, 2004; Untaroiu *et al.*, 2005). The maximum principal strain from this finite element study was compared to results from an experimental group, and was a maximum of 25% higher or lower than experimental strains (as calculated by the present author).

There were a number of limitations to this study, many of which are common with this type of dynamic finite element modeling. The bone properties were simplified for computational ease. Both cortical and cancellous bone models were isotropic and homogeneous, which is not a true representation of the properties of bone; however, this allowed a minimum number of materials to be defined. These are simplifications that have been used by most others in the dynamic modeling community (*e.g.*, Untaroiu, 2005; Iwamoto 2005), and has been shown to have little effect (Peng *et al.*, 2006). Only one specimen was examined, but it was selected as the most representative of those tested experimentally. As well, this model has only been validated for axial impact loads, and as such should not be used to simulate bending impacts such as those present in pedestrian strikes without further investigation. Finally, a convergence study to assess whether the mesh density was adequate should be performed, as decreasing the element size may improve the response of the model.

For the injury curves that were applied to the simulations, the force-only injury curve proved to be a good indicator of fracture risk. The poor performance of the newly-developed curve was the result of artificially high forces in the model (due to the inability to simulate fracture). Therefore, the model performs best for non-fracture scenarios.

As fractures cannot be actually simulated with the model, the maximum principal strain and the Von Mises stress values were examined for their applicability to determining injury risk. The cancellous values were not useful for predicting fractures, but the presence of 'failed' elements in the cortical bone for both criteria suggests that cortical values may be good indicators of injury risk.

This study has resulted in an optimized finite element model of the tibia's response to axial impact loading. The force-time profile represents the response of natural cadaveric bone up to the failure point, which is recommended to be defined as a maximal principal strain value for each bone material. This model can be implemented into future injury risk assessment studies, allowing better investigation into the effect of protective systems on injury potential.

6.5 REFERENCES

Austman, R.L., Milner, J.S., Holdsworth, D.W., and Dunning, C.E. (2008) The effect of the density-modulus relationship selected to apply material properties in a finite element model of long bone. *Journal of Biomechanics.* **41,** 3171-3176.

Beaugonin, M., Haug, E., and Cesari, D. (1997) Improvement of numerical ankle/foot model: modeling of deformable bone. *Stapp Car Crash Journal.* **41,** 225-237.

Beillas, P., Begeman, P.C., Yang, K.H., King, A.I., Arnoux, P.J., Kang, H.S., Kayvantash, K., Brunet, C., Cavallero, C., and Prasad, P. (2001) Lower limb: advanced FE model and new experimental data. *Stapp Car Crash Journal.* **45,** 469-494.

Burstein, A.H., Reilly, D.T., and Martens, M. (1976) Aging of bone tissue: mechanical properties. *Journal of Bone and Joint Surgery (American volume).* **58,** 82-86.

Carter, D.R. and Hayes, W.C. (1977) The compressive behavior of bone as a two-phase porous structure. *Journal of Bone and Joint Surgery (American volume).* **59,** 954-962.

Imai, K., Ohnishi, I., Bessho,M., and Nakamura, K. (2006) Nonlinear finite element model predicts vertebral bone strength and fracture site. *Spine* **31,** 1789-1794.

Iwamoto, M., Miki, K., and Tanaka, E. (2005) Ankle skeletal injury predictions using anisotropic inelastic constitutive model of cortical bone taking into account damage evolution. Society of Automotive Engineers, Inc.

Iwamoto, M., Tamura, A., Furusu, K., Kato, C., Miki, K., Hasegawa, J., and Yang, K.H. (2000) Development of a finite element model of the human lower extremity for analyses of automotive crash injuries. In *2000-01-0621.* Computer Applications for Crash, Optimization, and Simulation Research, Society of Automotive Engineers, Detroit, MI, USA.

Kim, Y.S., Choi, H.H., Cho, Y.N., Park, T.J., Lee, J.B., Yang, K.H., and King, A.I. (2005) Numerical investigations of interactions between the knee-thigh-hip complex with vehicle interior structures. *Stapp Car Crash Journal.* **49,** 85-115.

LSTC (2003) *LS-DYNA User's Manual, V.970.* Livermore, CA, USA.

Peng, L., Bai, J., Zeng, X., and Zhou, Y. (2006) Comparison of isotropic and orthotropic material property assignments on femoral finite element models under two loading conditions. *Medical Engineering & Physics* **28,** 227-233.

Sambamoorthy, B. and Halder, T. (2001) Characterization and component level correlation of energy absorbing (EA) polyurethane foams (PU) using LS-DYNA material models. 3rd European LS-DYNA User's Conference, Paris, France.

Taddei, F., Cristofolini, L., Martelli, S., Gill, H.S., and Viceconti, M. (2006) Subject-specific finite element models of long bones: An in vitro evaluation of the overall accuracy. *Journal of Biomechanics.* **39,** 2457-2467.

Takahashi, Y., Kikuchi, Y., Konosu, A., and Ishikawa, H. (2000) Development and validation of the finite element model for the human lower limb of pedestrians. *Stapp Car Crash Journal.* **44.**

Tannous, R.E., Bandak, F.A., Toridis, T.G., and Eppinger, R. (1996) A three-dimensional finite element model of the human ankle: development and preliminary application to axial impulsive loading. Society of Automotive Engineers, Inc.

Untaroiu, C., Darvish, K., and Crandall, J. (2004) Development and validation of a finite element model of the lower limb. ASME, Anaheim, California, USA.

Untaroiu, C., Darvish, K., Crandall, J., Deng, B., and Wang, J.T. (2005) A finite element model of the lower limb for simulating pedestrian impacts. *Stapp Car Crash Journal.* **49,** 157-181.

Valle, L. and Ray, M.H. (2005) Development and validation of a 50th percentile male human femur: Attachment A. Worcester Polytechnic Institute. Worcester, MA, USA. National Highway Traffic Safety Administration.

Yamada, H. (1970) *Strength of biological materials.* The Williams & Wilkins Company, Baltimore, MD, USA.

CHAPTER 7 – General Discussion and Conclusions

Overview: *In this chapter, the objectives and hypotheses from Chapter 1 are reviewed, and a summary of the main outcomes of the studies from this thesis is provided. The overall strengths and limitations of this work are discussed, and future directions for further investigations are presented.*

7.1 SUMMARY

Short-duration high-force axial loading of the tibia can lead to debilitating injuries, and the potential need for lower limb amputation. The current AV blast safety standard is taken from the car crash industry, but its applicability to these events was not previously examined. In order to properly assess the risk of tibia injury, an appropriate criterion and biofidelic surrogate are needed. The overall purpose of the studies presented in this thesis was to improve the assessment of tibia injury risk as a result of axial loading through the use of experimental and finite element techniques.

The first component of this research involved developing a testing apparatus capable of delivering these types of impact loads to specimens (*i.e.*, Objective #1, Chapter 2). A specialized pneumatic system was developed to apply impulses to cadaveric, synthetic, or ATD tibias over the range of forces, speeds, and time durations specified to represent anti-vehicular mine blasts (*i.e.*, 1 – 12 kN, 3 – 10 ms, 5 – 10 m/s). This system was instrumented to fully quantify the events, and was shown to be highly controllable and repeatable. This apparatus also allowed for forces to be applied at different velocities,

which permitted impulsive loads to be generated with different forces, momentums, and kinetic energies (*i.e.*, Hypothesis #1 accepted).

This apparatus was then used to investigate the injury tolerance of cadaveric tibias (*i.e.*, Objective #2, Chapter 3). Paired specimens were impacted until failure; one from each pair being impacted with a light projectile mass and the contralateral with a heavier mass. This allowed isolation of force effects from velocity-based (momentum and kinetic energy) effects on fracture tolerance. The average fracture force for all specimens was 12.6 kN, and a 10% risk of tibia fracture (according to the survivability curve generated) corresponded to an axial load of 7.9 kN. Other factors were examined for their influence on failure, and an injury equation was developed based on axial force, kinetic energy, age and height of the subject (*i.e.*, Hypothesis #2 accepted). The relationship between cadaveric and ATD response was also quantified, and a new ATD-based injury criterion of 12.6 kN proposed. This was much higher than the previous tolerance load of 5.4 kN in an ATD (Yoganandan *et al.*, 1996).

The results from the cadaveric specimens comprise the standard against which surrogates such as synthetic bones can be evaluated for their ability to represent natural response. Sawbone® synthetic bones were tested in a similar manner to the cadaveric tibias (*i.e.*, Objective #3, Chapter 4). Their fracture tolerance was much lower than cadaveric, and with altered strain distributions. Their failure was also dependent on different factors (such as momentum). Failure in the Sawbone® tibia consisted of fractures of the bone in combination with delamination of the epoxy resin cortical shell from interior cancellous foam. For these reasons, these surrogates were deemed

unacceptable for representing the response of human bones to impulse loading causing fracture (*i.e.,* Hypothesis #3 accepted).

After investigating the response of cadaveric, synthetic, and ATD tibias to impulse loading, the building of a finite element model of the tibia that could serve as a useful method for future assessments of injury risk was undertaken. Finite element modeling is the basis of many safety assessments in industry, and as such, a tibia model which correctly represented the natural lower leg would be a useful tool for their analyses. The construction of the necessary mesh of a representative tibia using TrueGrid® software was described in Chapter 5. It was rigorously evaluated to provide accurate and stable outputs during simulations. A finite element model was then developed using this mesh (*i.e.,* Objective #4, Chapter 6) to replicate the experimental tests that were conducted on the bone (Chapter 3). Numerous model parameters were examined to obtain the model which best represented both the non-fracture and fracture conditions, with particular emphasis on the non-fracture case. Peak axial force, load duration, impulse, and strain data were all used to optimize the model (*i.e.,* Hypothesis #4 accepted).

7.2 Strengths and Limitations

Specific strengths and limitations of each study were discussed in their respective chapters, but there were some that are generally applicable to this thesis. A major strength of this work is the large number of cadaveric specimens tested, and the use of paired specimens. This allowed investigation into the influence of parameters such as momentum and energy (which had not been previously examined) on fracture tolerance. The pneumatic testing apparatus developed in this work was designed specifically to

represent short-duration, high-impulse scenarios. The injury risk curves generated from this work demonstrated that previous car crash studies are not directly applicable to these events. This is also the only known study that has examined the impact response of Sawbone® synthetic bones, a feature that is of interest to many, including the manufacturer (personal communication).

The finite element model developed for dynamic simulations was rigorously tested, both for mesh quality and for evaluation of the parameters which influence a model's output. This type of evaluation is rarely seen in published dynamic finite element studies, and is a strength of the current work.

While this research addressed many of the problems in the literature pertaining to injury tolerance of the tibia, there are also several limitations. The use of *in-vitro* testing to approximate the *in-vivo* response is an approximation, but is a necessary one for the testing of fracture tolerance. Both the experimental and finite element tests examined loading in the axial direction only. In most impact scenarios, the loads applied to the tibia are combined with bending moments, which would dramatically alter the injury risk. The results from the current study are only applicable to axial loading events.

The research studies conducted within this thesis were all focused on the isolated cadaveric tibia. This allowed reduction in the complexity associated with full lower limb tests, and provided a more direct comparison to surrogates such as the ATD leg and the Sawbone® tibia. However, injuries to the bones of the foot (*e.g.*, the calcaneus and talus) are not insignificant, and can lead to debilitating injuries. The investigations in the current studies do not give any indication of the risk to these bones, which may have lower injury tolerances.

A final limitation of the results of this thesis is the large number of approximations necessary in the finite element model. The material properties (*e.g.*, modulus, Poisson's ratio) were selected using values from previous studies, but were not optimized for the specific specimen used in this study. As well, bone was modeled as homogeneous and isotropic, which were necessary assumptions to reduce the computational complexity of the model. Better agreement with experimental data may be obtained by further investigation and refinement of the material properties used.

7.3 Future Directions

The research conducted in this thesis has examined many aspects of tibia response to impulse loading, but there are many others still remaining to be investigated. This work on injury biomechanics represents a new area of research for the Jack McBain Biomechanical Testing Laboratory, and the equipment and methods developed within this thesis can be expanded to a wide variety of future studies on other regions of the body or different loading scenarios.

In order to better quantify the injury tolerance of the tibia, studies examining the tolerance of the lower leg to combined (axial + bending) loading would prove beneficial, and may result in injuries at different locations in the tibias. As well, further cadaveric testing examining the effect of varying the applied impulse on fracture tolerance could contribute to the injury criteria proposed herein, as this parameter was relatively constant in the current work (*i.e.*, to model in-vehicle mine blast events). Testing of full lower leg specimens would also provide a better appreciation of injury risk to other bones of the

lower leg (in particular the talus, calcaneus, and fibula), which may have different injury tolerances than those identified in the present work.

The ATD leg examined in the present study has been previously criticized for its ability to represent the response of a human lower leg (Kuppa *et al.*, 2001). The Denton leg is still widely used, but other options such as the Thor-Lx are growing in popularity. A new lower leg model, the Thor-Mx, has recently been released, and has been specifically designed for evaluation of the effects of landmine blasts. This leg has yet to be investigated, and testing of it using the methods described in this thesis would allow evaluation of its ability to represent cadaveric response.

The finite element model developed in this thesis was based on CT scans of a representative tibia, but models built from other scans would allow investigation into the range of responses present in the general population. As well, simulations using the other projectile mass used experimentally could provide further insight into the effect of momentum on bone response. The model will be used by our industrial collaborator for safety assessments using computer simulations.

7.4 SIGNIFICANCE

In conclusion, this work has contributed to the understanding of the response and tolerance of the tibia to axial impulsive loading. A new injury standard has been proposed that is specific to these types of short-duration, high-force loading events. Surrogates including the ATD and Sawbone® synthetic bones were examined for their ability to represent the body's response to loads at the fracture severity level. A finite element model of a representative cadaveric tibia was constructed and evaluated for its

quality and ability to match the parameters examined experimentally. The methods developed in this research, both experimental and finite element, can be easily applied to other areas of the body for future studies of injury risk. It is hoped that the results from this body of work will aid in the development of protective measures for the human body undergoing impulsive loading, to reduce the incidence of devastating lower leg fractures.

7.5 REFERENCES

Kuppa, S., Haffner, M., Eppinger, R., and Saunders, J. (2001) Lower extremity response and trauma assessment using the THOR-Lx/HIIIr and the Denton leg in frontal offset vehicle crashes. National Highway Traffic Safety Administration, The Netherlands.

Yoganandan, N., Pintar, F.A., Boynton, M., Begeman, P., Prasad, P., Kuppa, S., Morgan, R.M., and Eppinger, R. (1996) Dynamic axial tolerance of the human foot-ankle complex. Society of Automotive Engineers, Inc. 962426, 207-218.

APPENDICES

APPENDIX A – Glossary of Medical Terms

This appendix contains a list of the medical terms used through this thesis, to provide assistance to the reader who is unfamiliar with this terminology.

Achilles Tendon: A tendon of the posterior leg, attaches the calf muscles to the calcaneus.

Amputation: The removal of a body extremity by trauma or surgery.

Anatomical Position: Body upright, with the face and palms forward and the upper limbs placed at the sides.

Anterior: Situated towards the front of the body when in anatomical position.

Articulation: The contact junction between two bones.

Biofidelity: Ability to accurately represent the natural biological properties.

Cadaveric: Of, or pertaining to, a dead body preserved for anatomical study.

Calcaneus: The large bone of the heel.

Cancellous Bone: A spongy, lattice-like structure of bone. Synonymous with trabecular bone.

Cartilage: Connective tissue covering surfaces in joints, allows low-friction motion and absorbs shocks.

Collagen: The main protein in connective tissue.

Contralateral: Pertaining to the other side of the body (*i.e.*, left-right).

Cortical Bone: A dense bone structure. Synonymous with compact bone.

Diaphysis: The shaft of a long bone, a tube made of cortical bone.

Distal: Further from the point of reference; away from the midline of the body.

Epiphysis: The expanded articular end of a long bone; made of cancellous bone.

Femur: The large bone in the upper leg, extending from the pelvis to the knee.

Fibula: The smaller bone of the lower leg, extending between the knee and the ankle.

Frontal: The plane parallel to the long axis of the body separating the body into front and back portions.

Hind-foot: The portion of the foot comprising the talus and calcaneus.

***In Vitro*:** In an artificial environment outside a living body.

***In Vivo*:** In a living body of a plant or animal.

Intramedullary Canal: The canal down the center of a bone filled with marrow.

Joint: The location at which two bones make contact, permits relative movement.

Lateral: A position further away from the midline of the body.

Lower Leg: The portion of the leg between the knee and ankle joints.

Malleolus: A bony prominence on each side of the ankle.

Marrow: The soft tissue filling the cavities of bones.

Medial: A position closer to the midline of the body.

Osteon: The cylindrical structure forming the basis of cortical bone.

Pilon: The distal surface of the tibia, where articulation with the talus occurs. Synonymous with Plafond.

Plafond: The distal surface of the tibia, where articulation with the talus occurs. Synonymous with Pilon.

Plantar: Towards the bottom of the foot.

Plateau: A relatively flat surface in a joint, such as the knee.

Posterior: Located towards the back of the body.

Proximal: Closer to the point of reference; towards the center of the body.

Sagittal: The plane parallel to the long axis of the body separating the body into left and right portions.

Shank: The lower leg and foot.

Talocrural Joint: The joint between the talus and the tibia/fibula, allows the primary motion of the ankle.

Talus: The bone of the lower ankle, forms joints with the talus, fibula, calcaneus, and mid-foot.

Tarsal: Bone of the foot.

Tendon: A band of connective tissue connecting muscle to bone.

Tibia: The larger bone of the lower leg, extending between the knee and the ankle; the shinbone.

Tibiofibular Joint: The joint between the tibia and fibula (proximal and distal).

Trabecular: See cancellous bone.

Transverse: Placed crosswise, at a right angle to the long axis of a part.

Vascularization: Supply of blood vessels.

APPENDIX B – Injury Criteria for Various Areas of the Body

This appendix includes descriptions of some key injury criteria that have previously been developed for areas of the body other than the lower leg.

B.1 HEAD INJURY CRITERION

The Head Injury Criterion (HIC) is an index of injury as a result of head acceleration over a period of time (Mertz *et al.*, 1997). This weighted impulse criterion is widely used in a variety of industries, and is a linear fit to tolerance data from various cadaveric and animal injury studies plotting injury as a function of acceleration and time.

The HIC is calculated as follows:

$$HIC = MAX\left\{\left[\frac{1}{t_2 - t_1}\int_{t_1}^{t_2} a(t)dt\right]^{2.5}(t_2 - t_1)\right\} \quad \textbf{(Eq. B.1)}$$

Where a(t) is the head center of gravity resultant acceleration expressed in G's and t_1 and t_2 are the beginning and end points of time of the impulse (Bogosian and Der Avanessian, 2004).

Airbag regulations define a maximum HIC of 700 over a 15 ms period marks the border between acceptable and marginal, estimated to represent a 5% risk of a severe injury (Insurance Institute for Highway Safety, 2004). A HIC of 1000 is considered to represent the threshold of skull fracture for a large surface area. The HIC is only applicable for periods of acceleration greater than 2 ms. For shorter duration impulses, the peak acceleration is used as an injury predictor (Bogosian and Der Avanessian, 2004). As the

HIC was developed to predict injuries as a result of impacts (rather than inertial loading), no standard level is defined for the defense community (Manseau, 2005; NATO, 2007).

B.2 SPINE – DYNAMIC RESPONSE INDEX

The current method of predicting thoraco-lumbar spine injuries is the Dynamic Response Index (DRI), which was developed by the aircraft industry for ejection seats of pilots (Axelsson and Sundqvist, 2003). The DRI represents the maximum dynamic compression of the vertebral column by modeling the human body with a mass, spring and damper system (NATO, 2007).

The mathematical model of the spine is as follows:

$$\ddot{z}(t) = \ddot{\delta} + 2 \cdot \zeta \cdot \omega_n \cdot \dot{\delta} + \omega_n^2 \cdot \delta \qquad \textbf{(Eq. B.2)}$$

Where $\ddot{z}(t)$ is the pelvis acceleration in the vertical direction, δ is the compression of the spinal column, ζ is the damping coefficient with $\zeta = c/(2 \cdot m \cdot \omega_n)$, and ω_n is the natural frequency of the spine with $\omega_n = \sqrt{k/m}$. For the human body, the natural frequency (ω_n) has been determined to be 52.9 rad/s (8.4 Hz), and damping ratio (c) to be 0.224 (Axelsson and Sundqvist, 2003), and were determined using compressive tests on cadaveric vertebrae.

The DRI is calculated as follows:

$$DRI_z = \frac{\omega_n^2 \cdot \delta_{max}}{g} \qquad \textbf{(Eq. B.3)}$$

Where δ_{max} is the maximum compression of the spine, and g is the acceleration due to gravity (9.81 m/s^2).

Based on operational ejection seat experience, a DRI of 16 was found to correspond to a 1% risk of a fracture to the spine (Axelsson and Sundqvist, 2003). For a 10% risk of AIS 2+, the acceptable level for defense protection, the injury limit has been defined as a DRI of 17.7, which corresponds to a maximal spine compression of 6.2 cm (Manseau, 2005). The DRI is only applicable for axial head-ward acceleration, and is recommended to be used in conjunction with the Lumbar Load threshold, as factors such as position of the spine may impact susceptibility to vertebral injury. The Lumbar Load threshold is the peak force in pounds between the pelvis and lumbar spine, and equals 2065 pounds for a 50^{th} percentile male test dummy (Department of Army, 2000).

References

Axelsson, H. and Sundqvist, O. (2003) Mine clearance vehicles. Crew safety standard. Swedish Defence Material Administration.

Bogosian, D. and Der Avanessian, H. (2004) Blunt trauma from blast-induced building debris. 31st Explosives Safety Seminar San Antonio, Texas.

Department of Army. (2000) Occupant crash protection handbook for tactical ground vehicles. United States of America.

Insurance Institute for Highway Safety. (2004) Frontal offset crashworthiness evaluation. Guidelines for rating injury measures.

Manseau, J. (2005) Injury assessment method proposal for vehicle mine protection testing. TM 2004-241. Defence Research & Development Canada - Valcartier.

Mertz, J.H., Prasad, P., and Irwin, A.L. (1997) Injury risk curves for children and adults in frontal and rear collisions. Society of Automotive Engineers, Inc 973318.

NATO. (2007) Test methodology for protection of vehicle occupants against anti-vehicular landmine effects. Final Report of HFM-090 Task Group 25.

APPENDIX C – Detailed Operation of Apparatus

This appendix details the steps that should be taken to properly operate the test apparatus described in Chapter 2. These steps were used for the experimental studies conducted in Chapters 3 and 4.

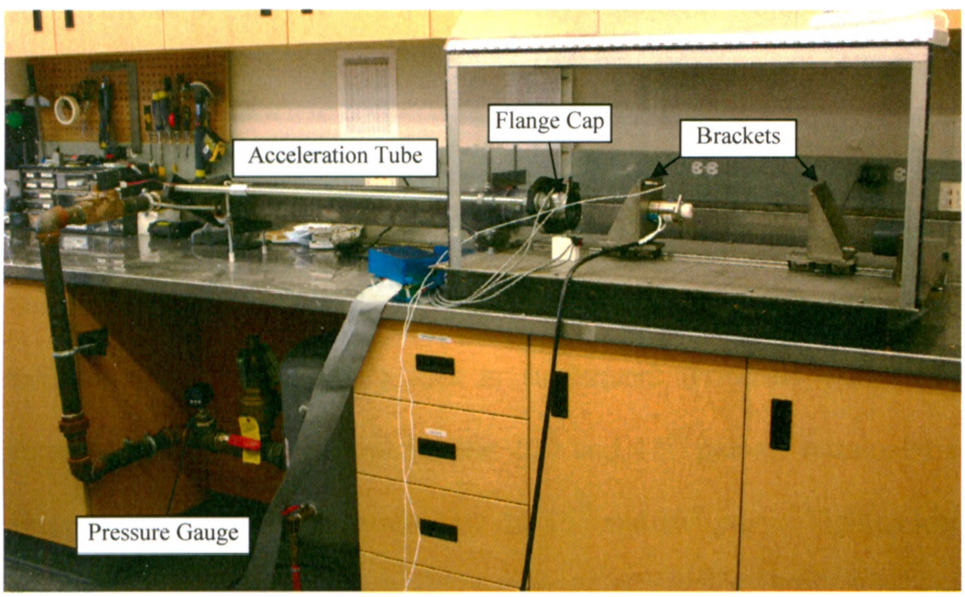

Figure C.1: Test Apparatus

Step 1: Initial Setup

a. Turn on PXI 1050 / SCXI 1010. Then turn on NI computer. Turn on second computer (connected to pressure regulator and cameras).

b. Select the projectile mass required. Typically leave a nut immediately behind the head of the projectile to ensure exits far enough to strike bracket. Use three large Fender washers for front support, polyethylene wiper for rear support. Double-nut as required.

c. Place projectile in tube, attach flange-cap. Tighten all nuts, double-nut as required. Only tighten down strapping over acceleration tube to finger-tight level – if you tighten this too much it will compress the tube, which will throw out all your calibration and you will lose the fine control over exit velocity.

d. Plug in two electronics boxes, ensure velocity sensors on cap are detecting reflective projectile (using indicator LEDs). If they don't activate, they may be turned on the peg they're mounted on. May require fine adjustment.

Step 2: Specimen Mounting

a. Connect instrumentation (strain gauges). Electronics box (Appendix F) is currently connected to the DAQ system with the accelerometer wired into the first two terminals, and strain gauges in subsequent terminals. The screw-down terminals for gauges 3c and 4a (the 10^{th} and 11^{th} pair of terminals) are to be skipped, and those gauges wired into the 15^{th} and 16^{th} pairs. Tighten screw-down terminals tightly – often a source of problems.

b. Mount specimen in potting jig, loosely mount to proximal bracket. Align within pot such that the distal articular surface of the tibia lines up with the polyethylene talus. Hand-tighten set screws, remove from bracket, fully tighten set screws. Remount on bracket and verify alignment is correct before tightening nuts.

c. Open Measurement & Automation Explorer, using task "cadaveric tibs". Calibrate strain gauges, not using shunt calibration.

d. If gauges don't calibrate, verify the screw-down terminals first. Secondly remove the gauge wires from the terminals and measure resistance of gauges to ensure they weren't damaged during installation.

Step 3: Software Initialization

a. On second computer, open vi that controls solenoid (solenoid.vi). On control box for the solenoid, set to "automatic". In LabVIEW®, set the solenoid vi to activate for 0.25 seconds. The first time it either won't run, or will stay open for several seconds, so make sure air tank pressure is zero first. Cycle a few times to make sure it's running smoothly.

b. On same computer, open vi that controls regulator (regulator.vi). Open valve to wall air, open ball valve next to air tank. Select AO1 from the drop-down menu, and set the voltage. Hit run. It's best if you aim lower than your final target pressure, and slowly build up so that you don't overshoot.

c. On same computer, open Measurement & Automation Explorer, activate the Sony Camera. Turn on the pressure gauge under the counter, turn on the light on it, and track the pressure using the camera while adjusting the voltage to the regulator.

d. Once pressure is stabilized, stop the camera acquisition.

e. On NI computer, open the vi for data collection (cadaverictibias.vi). Enter a folder and file name to save to, test it to make sure it collects and saves properly. Note: if there is an error in the file directory, it won't save. If you don't change the name of the file, it will overwrite it. Be careful.

Step 4: Testing Process

a. Push the projectile to the appropriate distance (easiest using a measuring tape). Apply two new layers of foam to the distal bracket (glue with strain gauge glue, replace after every 20 strikes or so). Push everything up so that the brackets are in contact with the end cap and the specimen is sandwiched. Close the shielding door.

b. The MotionScope camera needs to be started immediately prior to the tests (runs off a third computer). Set the frame rate (and thus the capture area), and preview it to center on the relevant area.

c. For the test itself, trigger the camera (as required), then the data collection (cadaverictibias.vi), followed by the solenoid (solenoid.vi). Always do a 3-2-1 countdown, wear hearing protection, and warn others in the lab prior to tests.

d. Use the data recording sheet to record the test parameters and results presented on the front panel, just in case files get erased (Figure C.2).

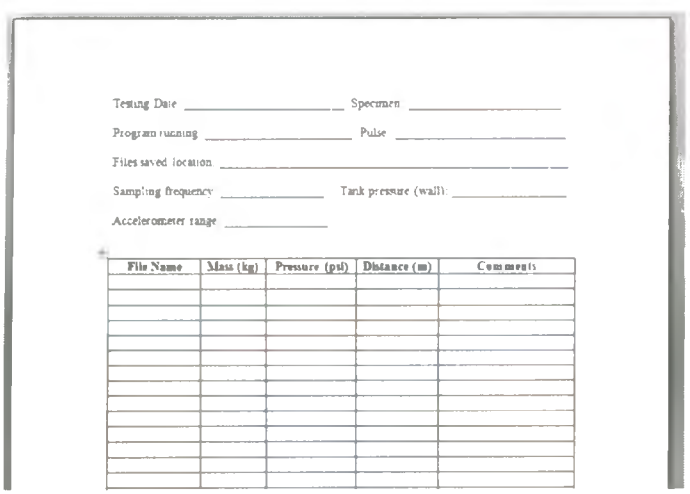

Testing Date _____ Specimen _____

Program running _____ Pulse _____

Files saved location _____

Sampling frequency _____ Tank pressure (wall) _____

Accelerometer range _____

File Name	Mass (kg)	Pressure (psi)	Distance (m)	Comments

Figure C.2: Testing Sheet

e. Every few hits, re-tighten everything.

Step 5: Shut Down

a. To close down, turn off the air at the wall, and then set the voltage going to the regulator to zero. Allow it to bleed out until not audible. Turn off the solenoid trigger, unplug the electronics boxes, turn off the computers, and clean up.

APPENDIX D – Technical Drawings

The detailed and dimensioned drawings of components for the apparatus described in Chapter 2 were created in Solidworks (Dessault Systems, Concord, Massachusetts, USA). The components were machined by The University of Western Ontario's University Machine Services (UMS). A list of components is also included.

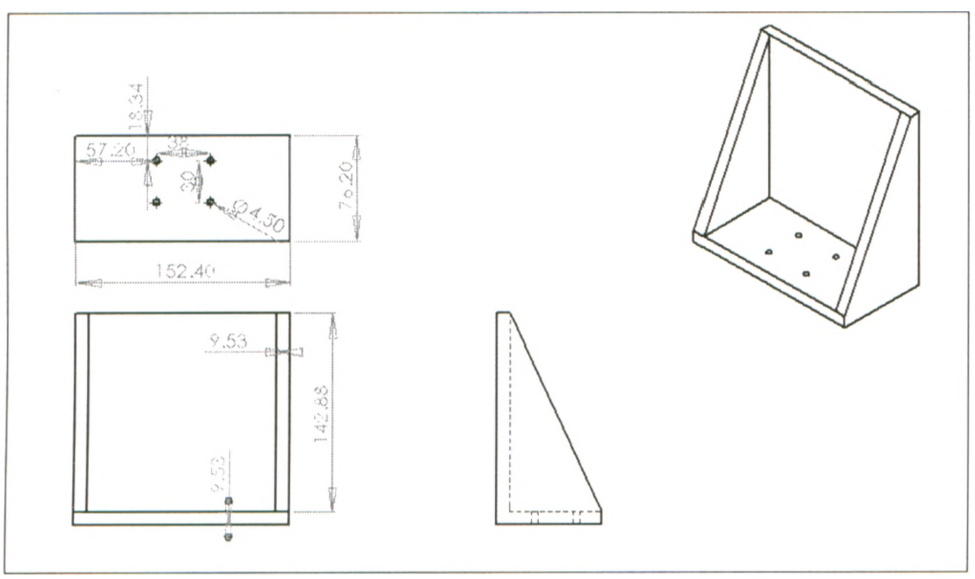

Figure D.1: Dimensioned Drawing of Bracket
All dimensions in mm, made of stainless steel.

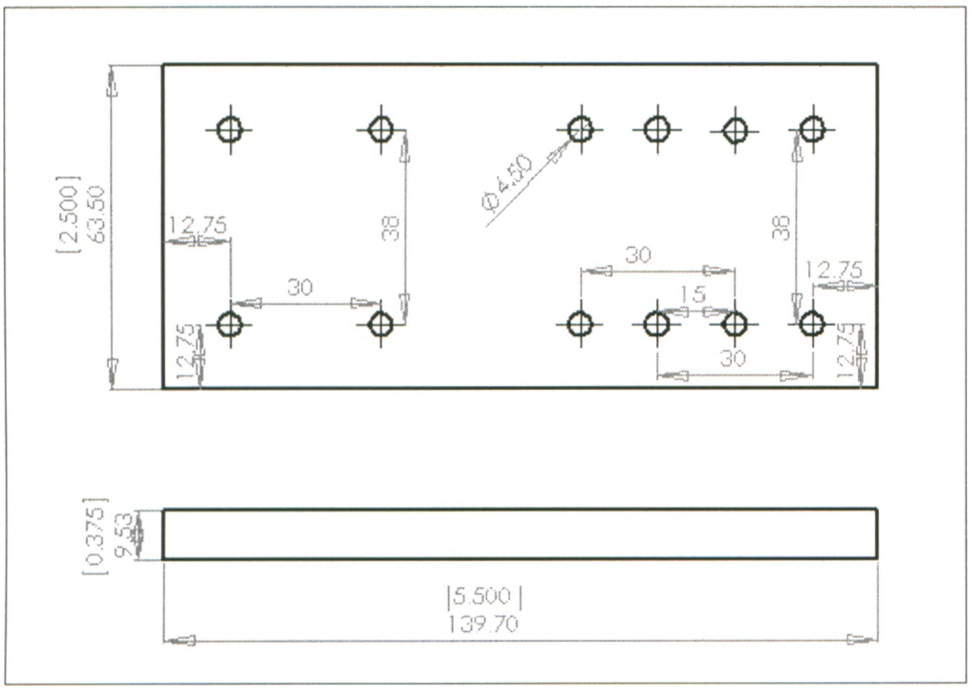

Figure D.2: Dimensioned Drawing of Bearing Plate
All dimensions in mm [inches], made of stainless steel.

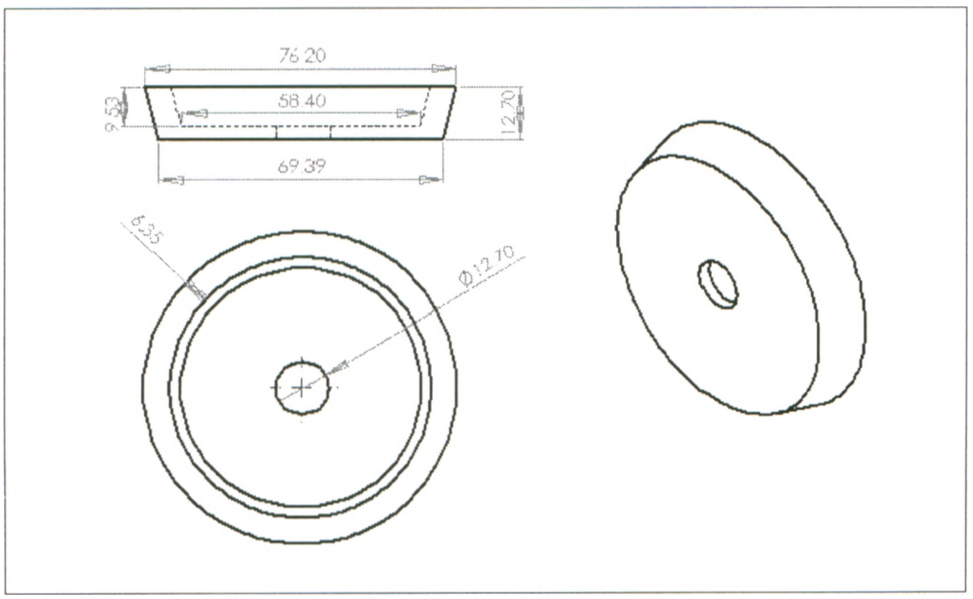

Figure D.3: Dimensioned Drawing of Wiper Disks
All dimensions in mm, made of polyethylene.

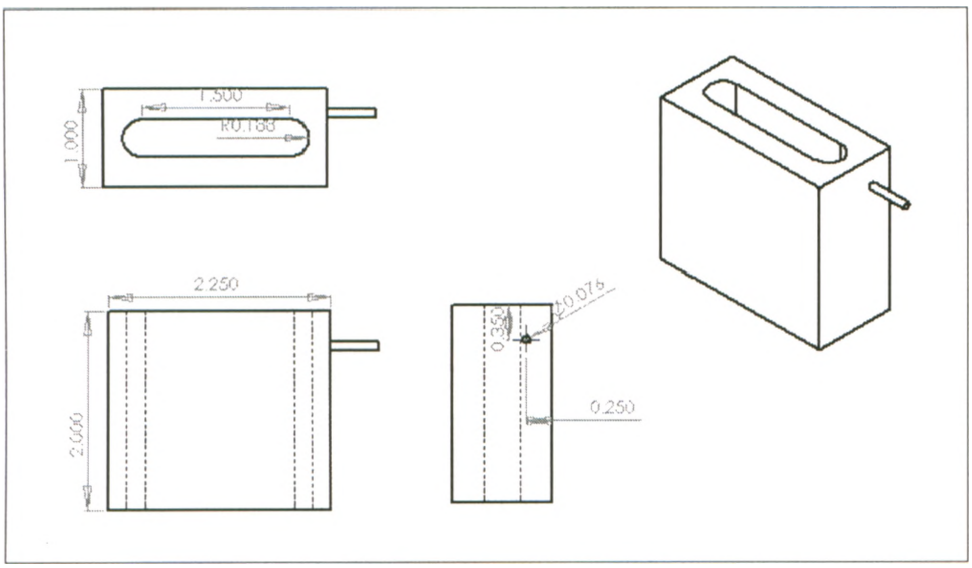

Figure D.4: Dimensioned Drawing of Velocity Block
All dimensions in inches, made of Delrin.

Table D.1: Itemized List of Components

Component	Description	Source
Bearings	6709K12	McMaster-Carr
Rail	6709K33, 820mm	McMaster-Carr
Acceleration Tube	100" long, 3" diameter, Lexan	UMS
Shielding	Lexan	UMS
Brackets (2)	Stainless Steel	UMS
Flange Cap	Aluminum	UMS
Digital Pressure Gauges (2)	2798K22, 0-100 psi	McMaster-Carr

APPENDIX E – LabVIEW® Programs

This appendix details the programming (i.e., LabVIEW back panels) for the custom-written software used for the operation of the regulator and solenoid, data collection, and analysis for Chapters 2 – 4.

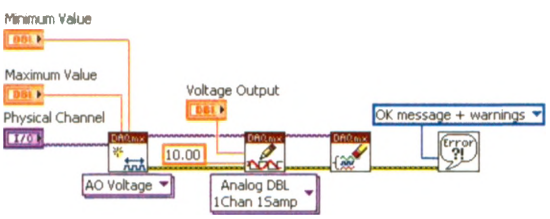

Figure E.1: Regulator Control Program Back Panel

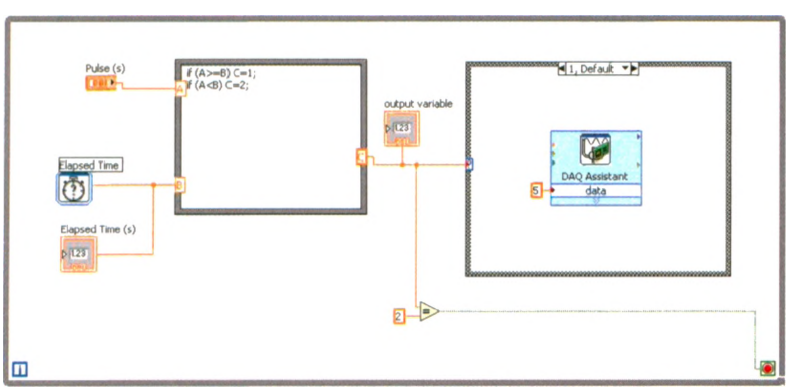

Figure E.2: Solenoid Triggering Program Back Panel

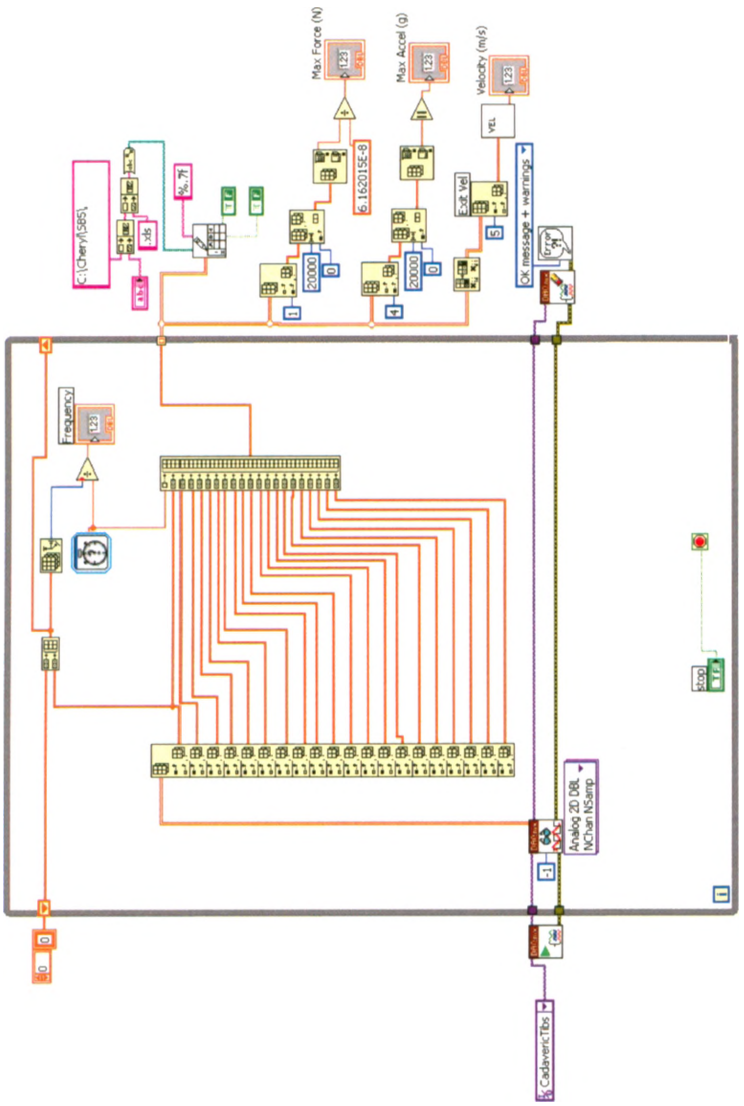

Figure E.3: Data Collection Program Back Panel

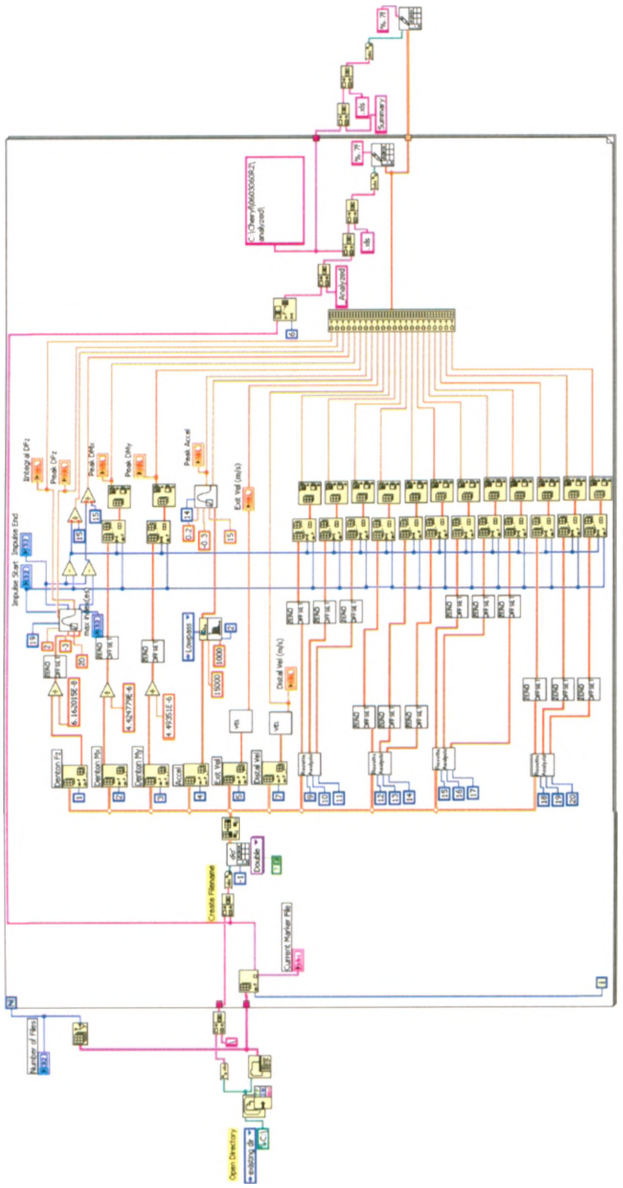

Figure E.4: Main Analysis Program Back Panel

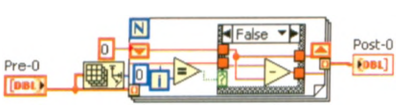

Figure E.5: Zero Offset Sub Program

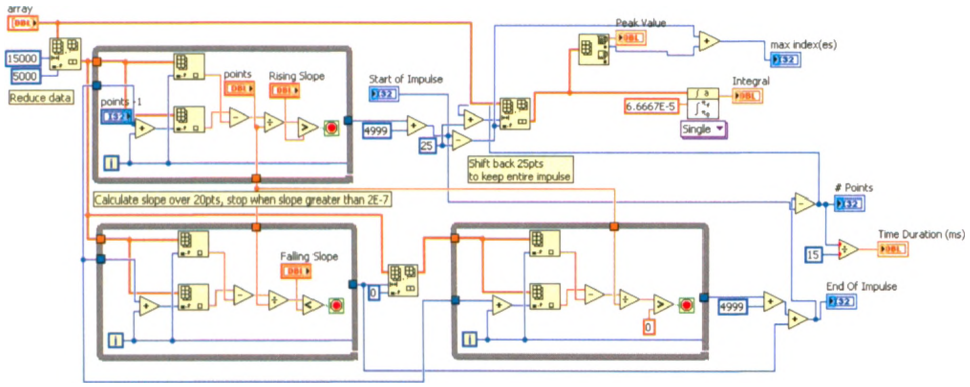

Figure E.6: Impulse Computing Sub Program

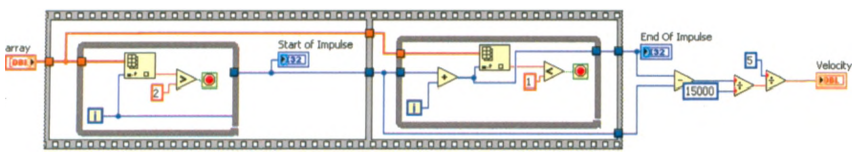

Figure E.7: Velocity Calculation Sub Program

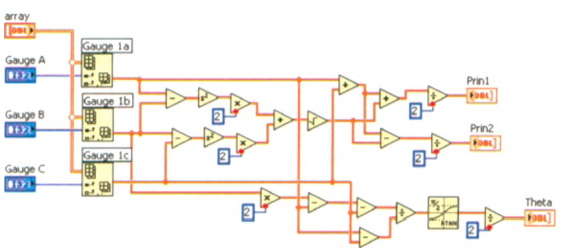

Figure E.8: Strain Gauge Rosette Analysis Sub Program

APPENDIX F – Electronics Box Schematics

This appendix details the schematics of the electronics box described in Chapter 2, and used throughout the experimental tests.

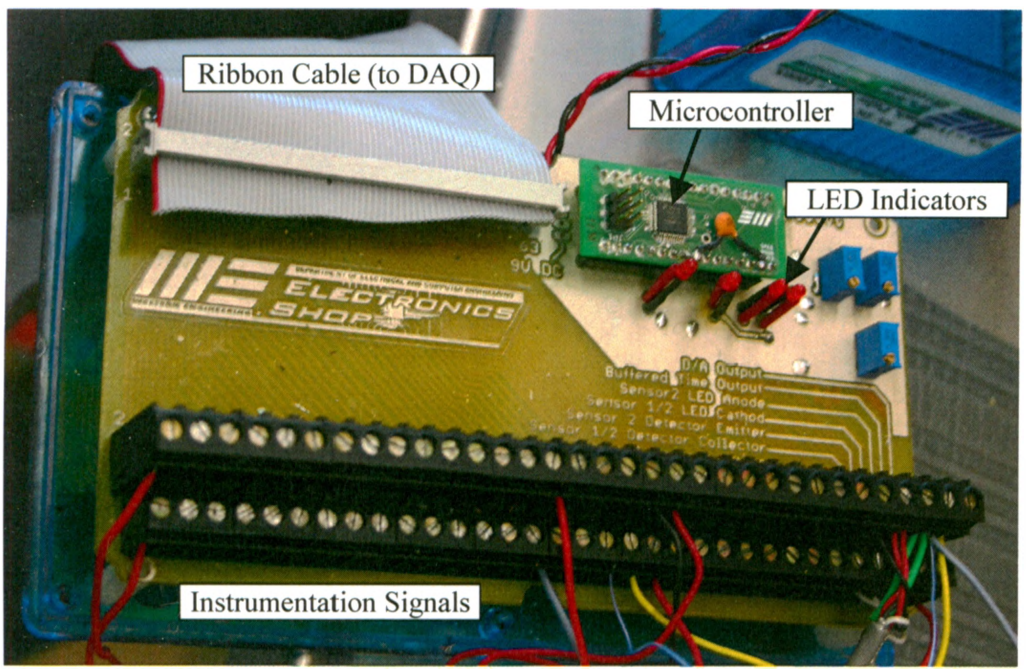

Figure F.1: Electronics Box
A custom-built electronics box collects the signals from all instrumentation (with room for further addition of signals) and passes them through a ribbon cable to the data collection system. A microcontroller on the box computes the velocity of the projectile, and LEDs are included to indicate the activation of the two reflective sensors for troubleshooting purposes.

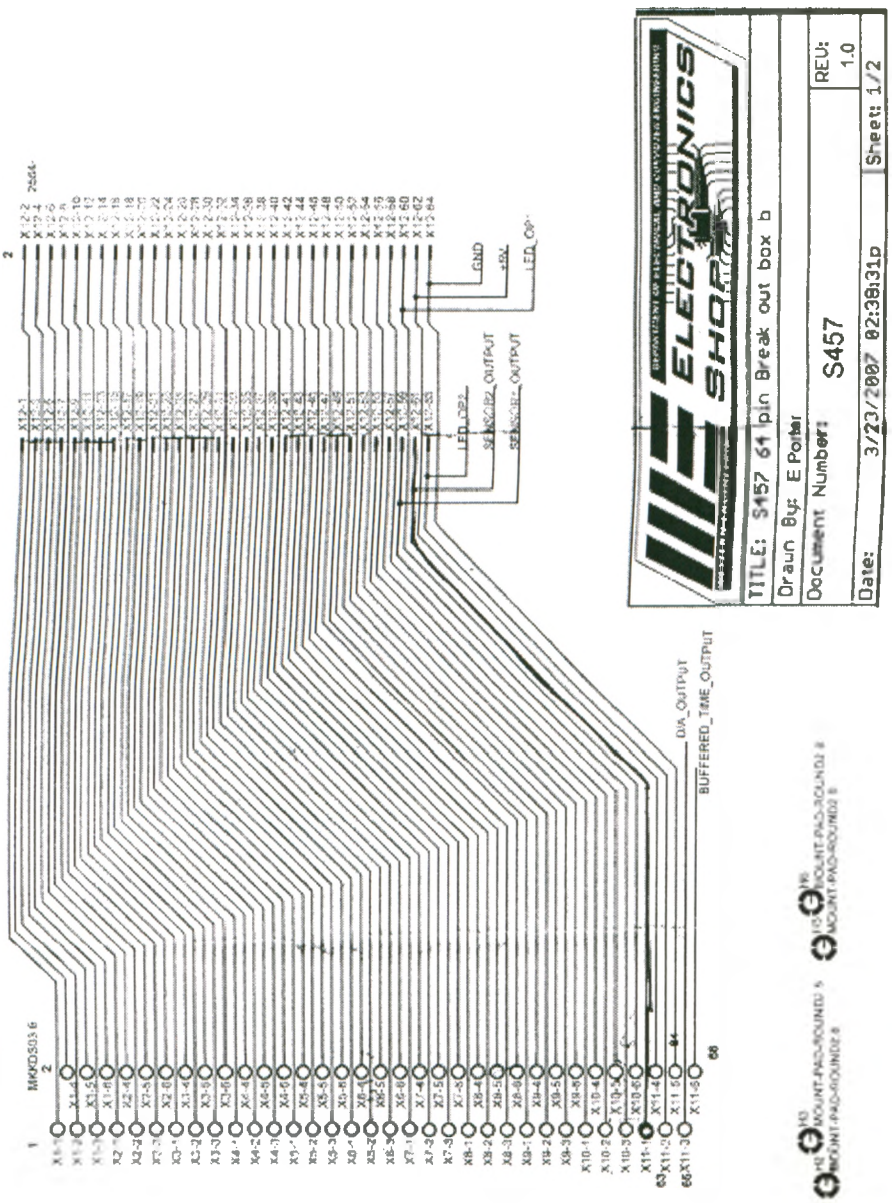

Figure F.2: Electronics Box Connection Terminals

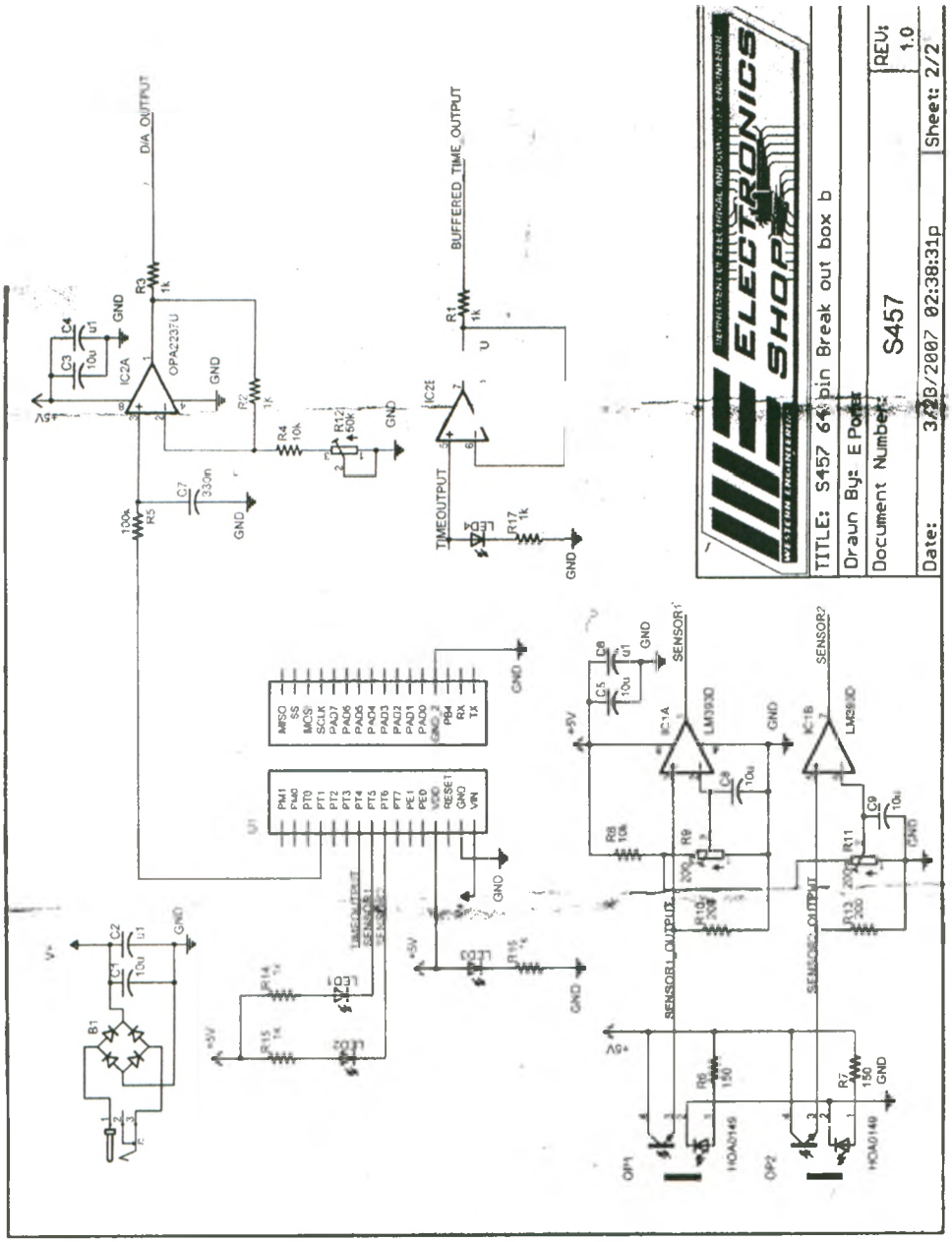

Figure F.3: Electronics Box Schematic

APPENDIX G – ATD Leg Schematic

This appendix includes the schematic of the ATD lower leg used in Chapter 2. This is courtesy of Robert A. Denton, Inc. (Rochester Hills, Michigan, USA), the manufacturer (with permission, Appendix M).

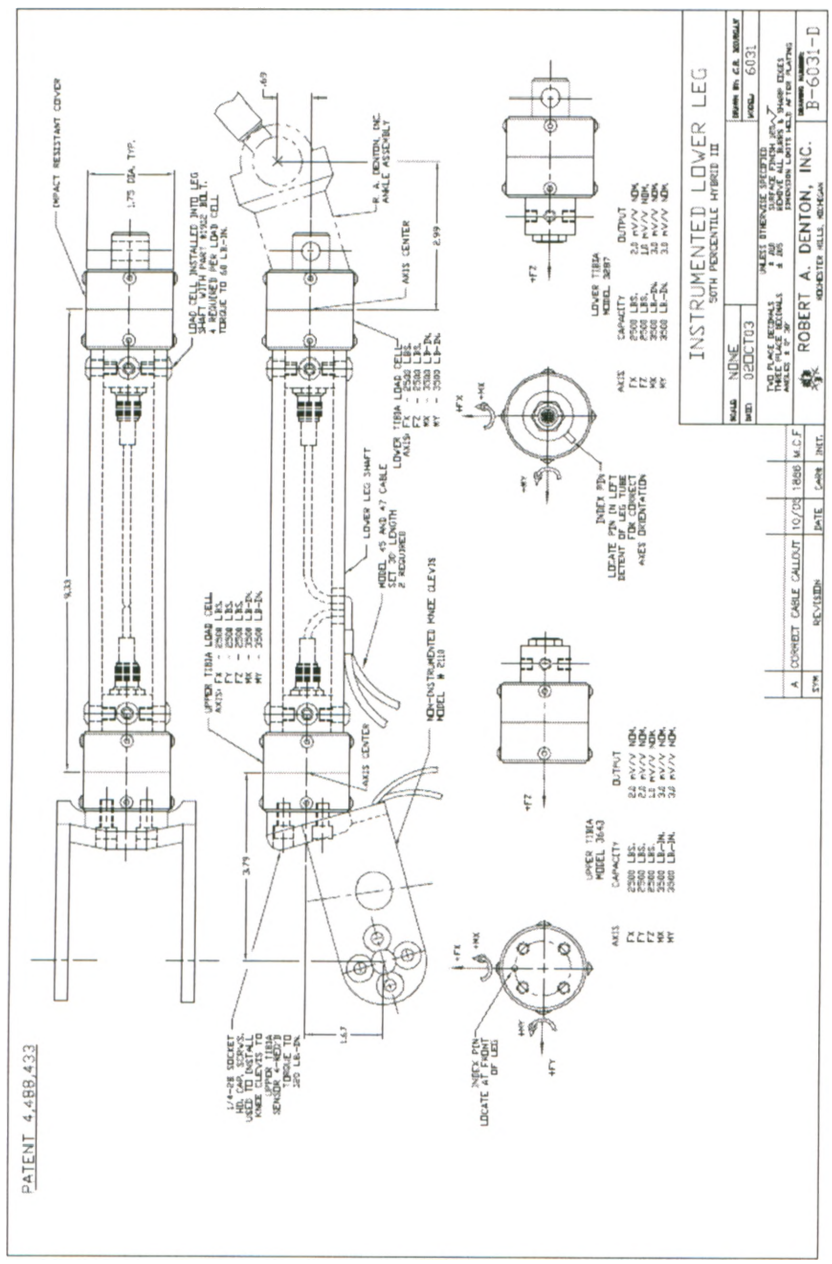

Figure G.1: Mechanical Structure of ATD Leg

APPENDIX H – Detailed Specimen Information

The specimen number, age, height, weight, and cause of death of each tibia that was tested in Chapter 3 are provided. All donors were male, and each provided a pair of tibias. Tabulated principle strain data are also provided for each specimen.

Table H.1: Donor Demographics

Specimen Number	Age (years)	Height (cm)	Weight (kg)	Cause of Death
06-06037	57	180.3	67.6	Prostate Cancer
08-07033	49	185.4	78.0	Congestive Heart Failure
08-07024	49	185.4	70.3	Cirrhosis
08-07085	47	188.0	59.6	Colon Cancer
08-08009	47	190.5	114.5	Renal Failure
06-08044	41	172.7	73.5	Heart Attack
06-10081	49	190.5	96.2	Melanoma
Average (±S.D.)	48 (4.7)	184.7 (6.3)	80.0 (19.0)	

Table H.2: 150 J Principal Strain Data
Principal strain values are presented for the 150 J tests, and are in the units of microstrain.

Specimen	1a	1b	2a	2b	3a	3b	4a	4b
06-06037L	11112	-10993	1943	-3952	318	-4525	462	-2214
06-06037R	2653	-6707	4023	-2382	1065	-1333	1677	-1514
08-07033L	3191	-4258	3304	-4734	2344	-5159	1269	-1463
08-07033R	2538	-3002	669	-1375	2095	-4838	1812	-1347
08-07024L	-	-	-	-	-	-	-	-
08-07024R	1532	-1538	608	-755	498	-732	420	-963
08-07085L	1723	-2806	1962	-3337	724	-4440	233	-327
08-07085R	1049	-1017	1852	-2394	1098	-1499	521	-1838
08-08009L	1993	-3729	2108	-3263	962	-3668	248	-657
08-08009R	244	-2308	1251	-1795	1761	-3079	1508	-1863
06-08044L	2962	-2375	764	-3845	2214	-3884	1680	-1392
06-08044R	1155	-1851	2501	-3909	631	-1928	1534	-1256
06-10081L	1258	-8449	2783	-2197	1250	-3025	1694	-1417
06-10081R	1102	-1864	1161	-1147	812	-1951	1084	-1107

Table H.3: 250 J Principal Strain Data
Principal strain values are presented for the 250 J tests, and are in the units of microstrain.

Specimen	1a	1b	2a	2b	3a	3b	4a	4b
06-06037L	10976	-11227	4804	-13294	4440	-13486	668	-22345
06-06037R	1249	-3074	1780	-4910	1789	-1856	204	-415
08-07033L	1144	-3352	378	-622	1305	-2772	1706	-1476
08-07033R	3611	-13268	511	-1255	1758	-5082	1698	-1392
08-07024L	-	-	-	-	-	-	-	-
08-07024R	5531	-1486	1834	-4991	7901	-19722	766	-876
08-07085L	204	-2400	1574	-3127	2554	-3869	290	-1255
08-07085R	161	-274	-41	-323	16	-117	-17	-132
08-08009L	5327	-4244	2962	-3717	1935	-4201	247	-733
08-08009R	13744	-7094	1178	-2065	2736	-4101	1127	-2447
06-08044L	781	-2223	1371	-4340	3019	-8404	12381	-10915
06-08044R	836	-2614	7311	-17559	747	-2139	1567	-1372
06-10081L	-	-	-	-	-	-	-	-
06-10081R	15724	-5014	1334	-1092	1448	-2586	1171	-865

APPENDIX I – Strain Gauge Application Technique

The following technique was used for application of all strain gauges to bone (both synthetic and cadaveric). It was developed based on previous studies on strain gauging bone (Finlay et al., 1982; Wright and Hayes, 1979) and further modified in the Jack McBain Biomechanical Testing Laboratory (Dunham, 2005). All supplies were purchased from Vishay Micro-Measurements (Raleigh, NC, USA).

1. Sand the surface of the bone where the gauge is to be laid with 400 grit sandpaper, rub with an alcohol pad to degrease.
2. Apply a thin layer of M-Bond 200 catalyst, let dry for 1 minute.
3. Add 2 drops of M-Bond 200 to the area and press into a thin layer using tape and finger pressure. Hold for 1 minute.
4. Wait 5 minutes.
5. Remove the tape, sand lightly to even surface. Wipe again with alcohol pad.
6. Place the strain gauge on a clean surface, and press a piece of installation tape onto top. Pick up gauge using tape.
7. Apply a thin layer of M-Bond 200 catalyst to both the back surface of the gauge and the surface of the bone, let dry for 1 minute.
8. Align the grid of the gauge with the laser line, and apply 1 drop of M-Bond 200 adhesive to the attachment site. Press down evenly, hold with finger pressure for 1 minute, pressing on all corners of the gauge.

9. Let sit for 5 minutes, remove tape.

10. Apply M-Coat A polyurethane coating to gauge and lead wire attachment points.

11. Let sit for 5 minutes.

References

Dunham, C.E. (2005) Biomechanical assessments of synthetic and cadaveric distal humeri for laboratory-based investigations. M.E.Sc. Thesis, *The University of Western Ontario*.

Finlay, J.B., Bourne, R.B., and McLean, J. (1982) A technique for the in vitro measurement of principal strains in the human tibia. *Journal of Biomechanics.* **15,** 723-729.

Wright, T.M. and Hayes, W.C. (1979) Strain gage application on compact bone. *Journal of Biomechanics.* **12,** 471-475.

APPENDIX J – Detailed Steps to Build a Bone Model

This appendix outlines the step-by-step methodology used to create a finite element model of a bone, as done in Chapter 5.

Mimics®:

Step 1: Defining Bone Regions

a. Import images from CT scan by creating a new project, selecting "Import Images", and navigating to the folder where the scan is located, then select "Convert". Assign a "top" and "bottom" to the model.

b. The model appears in three views, with a 3D rendering in the fourth quadrant. Adjust the contrast sliders (lower right corner of the screen) until the detail in the model is best visible.

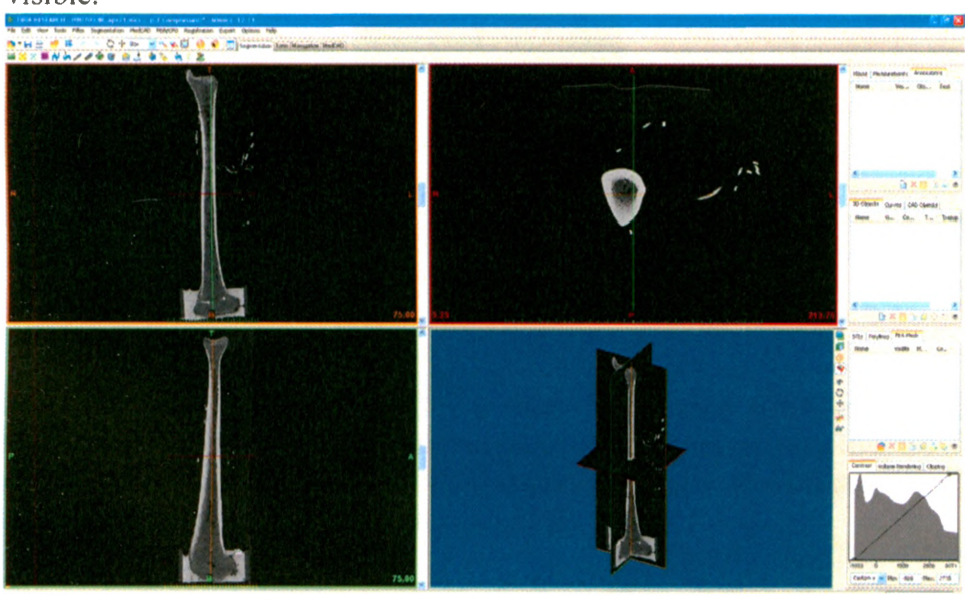

Figure J.1: The CT Scans in the Mimics Environment

c. Select the "Thresholding" tool (upper left corner of the screen)  to create a new mask based on the HU values in the model. This allows regions to be isolated based on certain density ranges. Adjust the slider bars until primarily cortical bone is highlighted, and select "Apply". This will segment the bone using a coloured mask.

Select the "Crop Mask" tool  and adjust cropping mask in all directions to leave only the bone region masked (eliminate the pot also).

Figure J.2: Thresholded Bone with Cortical Mask

d. Zoom in on the axial slices, and use the "Edit Mask" tool  to remove extra pixels from the mask and fill in any holes in the mask such that only cortical bone is included, and is one continuous region.

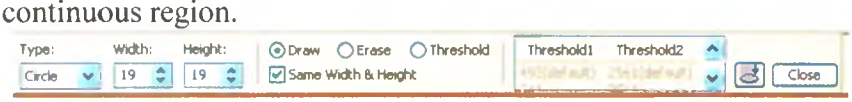

e. Once the bone is thresholded, polylines need to be generated defining the outer and inner surfaces of the bone. On the "Polylines" tab select "New" and select the mask generated in the previous step (d).

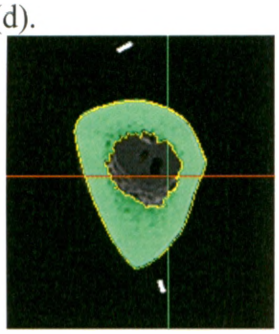

Figure J.3: Polylines Based on Cortical Mask

f. Select the "Polyline Growing" tool  to move the exterior polylines to a unique set and the interior polylines to a second unique set. This involves selecting the polyline, which will auto multi-select, but as the geometry changes several polylines may be needed to be selected in order to capture all of the required polylines.

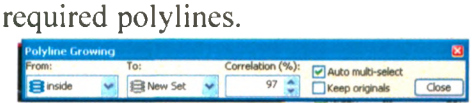

g. To define the transition from cancellous bone to marrow, scan through the axial slices until a hole larger than a few pixels is present. This defines the level where the transition occurs. Repeat at the proximal end, defining the transition back to cancellous bone. Copy the interior polylines from this area to a separate set.

h. Select the "Cavity Fill from Polylines" tool  and generate a mask for each set of polylines: outside, inside, and marrow.

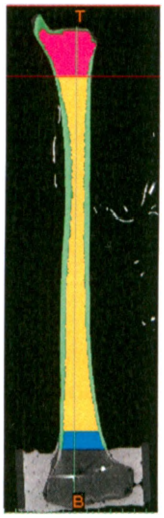

Figure J.4: Masks Defining Regions of the Bone

i. To output these regions so that they can be imported into TrueGrid® for mesh development, select the "STL+ Module" tool and create a binary STL file for each of the masks created in the previous step (h). Use "High Quality" settings.

Step 2: Strain Gauge Identification

a. To compare strains in the finite element model with those measured experimentally, the locations of the gauges need to be identified. On the "CAD Objects" tab select "New", "Point", "Draw". Navigate through the axial CT slices until the solder balls of the strain gauges are visible. Select the slice where the balls appear the largest (presumably the center slice) and place a point on each of the outer two solder balls. Repeat for each strain gauge.

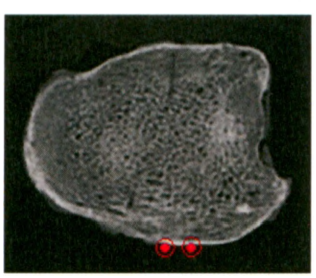

Figure J.5: Solder Ball Identification

b. On the "CAD Objects" tab select "Export txt" and add all points. This file will include the *x-y-z* coordinates of each point.

Step 3: Angle of Tip

a. Within the CT scanner the bone may not have been precisely aligned with the planes. In order to correct this, the On the "Measurements" tab select "New", "Measure Angle". In the sagittal and frontal views measure the angle that the PVC pot makes with the horizontal (see Figure 5.5). If not perfectly 90 degrees, this will be adjusted by rotating the STL files in TrueGrid®.

Step 4: Orient the Talus

a. Experimentally the talus sat within the depression of the distal articular surface. To locate the talus on the CT scans, on the "CAD Objects" tab select "New", "Circle", "Draw". Find a slice that is just off the articular surface of the bone, but still has some contours of the surrounding bone visible. Draw a circle, and go to the "Properties" of it to fix the radius to 1.25 inches.

b. Grab and drag the center point of the circle until it best approximates where the talus would sit experimentally (such that it doesn't penetrate the malleolus and sits in the slightly concave articular surface). Export the circle as a txt like was done for the strain gauges in Step 2.

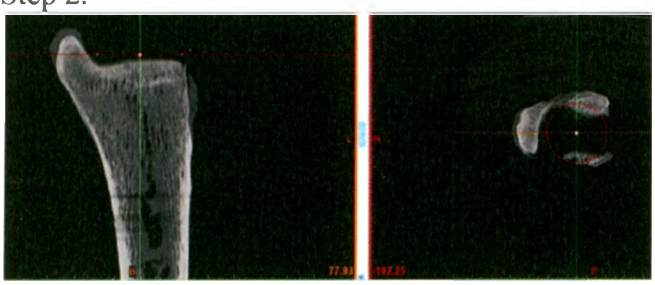

Figure J.6: Locating the Talus

TrueGrid®:

Step 5: Building the Distal Region

a. Import and number the three surfaces: inner, outside, and marrow.stl *(command: sd)*.

b. Create a part that is 3 blocks by 3 blocks by 1 block. Delete the corner blocks *(commands: block, dei)*.

c. Position blocks in area of distal-most bone, move vertices to approximate 45° angle and glue faces together *(commands: pb, mbi, bb)*.

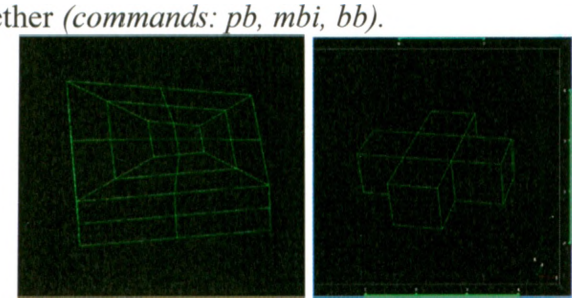

Figure J.7: Environment and Computation Views of Blocks

d. Create 3D splines on inner surface and outer surface approximating the distal ridge of the tibia, as well as the level at which the epiphysis begins to taper, and the level defining the transition from cancellous bone to marrow (and back). Also define

splines around the areas of curvature of the malleolus for future control of blocks *(command: curd).*

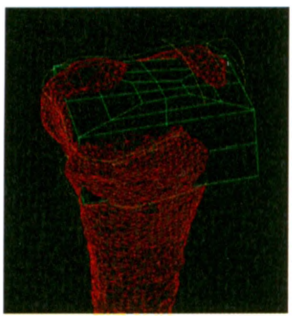

Figure J.8: Splines on a Surface

e. Create surfaces which describe the level at which transition regions will be implemented by offsetting the x-y plane *(command: sd).*

f. Attach the edges of the blocks to the cancellous curves defined in part (d). Project the outer faces onto the inner surface defined in part (a) *(commands: curs, sfi).*

g. Increase the mesh density in each direction, and apply smoothing algorithms to the faces and the volumes of the mesh *(commands: mseq, relax, unifm).*

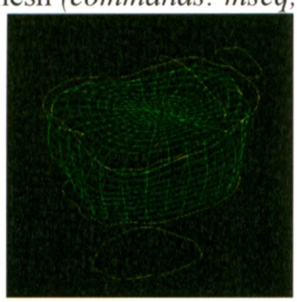

Figure J.9: The Cancellous Mesh

h. Insert a block on each exterior surface (x and y directions) that is one element thick, and a block in the distal z-direction for the cortical shell. Remove extraneous blocks *(commands: insprt, dei).*

i. Position vertices of faces on 45° angles (in all directions). Glue faces together to make continuous surface, attach edges to the curves previously defined (cortical curves), project exterior faces to the outside surface. Apply smoothing algorithms to the faces and the volumes of the cortical mesh *(commands: pb, mbi, bb, curs, sfi, relax, unifm).*

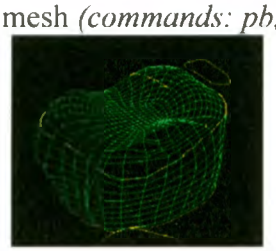

Figure J.10: The Cortical Mesh

j. Insert a block in the distal *z*-direction to represent the malleolus. Remove extraneous blocks, and attach edges to the curves, and project the exterior faces to the outside surface. Apply smoothing algorithms to the faces and volume *(commands: insprt, dei, pb, curs, sfi, relax, unifm)*

k. Assign material properties to individual blocks: cancellous blocks are material 1, cortical blocks are material 2 *(commands: mate, mt)*

l. Assign block boundary numbers to the regions on the proximal surface of the mesh, which will be attached to the next part *(command: bb)*

Step 6: The Second Part

a. Create a new part to represent the tapering section of the epiphysis. This new part is 5 blocks by 5 blocks by 1 block, and delete the corner blocks so it forms a cross shape. The exterior blocks (in *x* and *y* directions) are 1 element thick, and the interior ones (which will form the cancellous region) have 1/2 the elements as the cancellous blocks in the first distal-most region *(commands: merge, block, dei)*

b. Move vertices to 45° angles and glue corner faces together. Position blocks to be within appropriate region of the bone. Attach the edges to the previously-defined curves, and project the faces to the surfaces defined in Step 5(a). Assign block boundary numbers to the distal surfaces of the mesh to match those created in Step 5(l) to glue the parts together (as the number of elements is 1/2 that of the mating face, use transition block boundary command). Apply smoothing algorithms as before, and assign material properties as before. Assign block boundary numbers to regions on the proximal surface of the mesh, which will be attached to the next part *(commands: pb, mbi, bb, curs, sfi, trbb, relax, unifm, mt)*

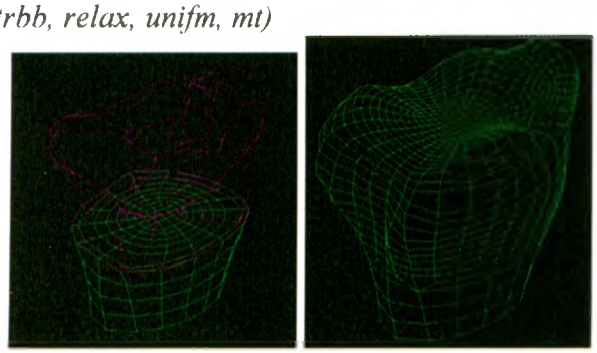

Figure J.11: Meshing the Second Part

Step 7: The Rest of the Bone

a. Create a new part to represent the diaphysis of the bone. This part is 5 blocks by 5 blocks by 1 block, with the same number of elements in each block as the previous part. Delete the corner blocks so it forms a cross shape *(commands: merge, block, dei, mbi, pb)*

b. Repeat Step 6(b). Increase the mesh density in the z-direction until elements are fairly square, apply smoothing algorithms and assign material properties as before (marrow is material 3). Assign block boundary numbers to regions on the proximal surface of the mesh, which will be attached to the next part *(commands: pb, mbi, bb, curs, sfi, mseq, relax, unifm, mt)*

c. Create a new part to represent the proximal-most region of the bone. This part is 5 blocks by 5 blocks by 1 block, with the same number of elements in the cortical blocks as the previous part, but double the elements in the cancellous region (due to the expansion in cross-section). Delete the corner blocks so it forms a cross shape *(commands: merge, block, dei, mbi, pb)*

d. Repeat Step6(b). Apply smoothing algorithms and assign material properties as before. Assign block boundary numbers to regions on the proximal surface of the mesh, which will be attached to the proximal bracket *(commands: pb, mbi, bb, curs, sfi, trbb, relax, unifm, mt)*

e. Enter merge phase. Define merged nodes tolerance as 0.0001 to remove duplicate nodes where blocks were glued together. Create a node set defining the nodes within 1.1mm of the proximal cut surface *(commands: merge, stp, nset)*

Step 8: Other Components

a. Create a part that is 3 blocks by 3 blocks by 1 block that will represent the polyethylene talus. Create a new cylindrical surface that is centered over the *x-y-z* coordinates as measured using Mimics®, with the same diameter as the experimental talus. Create two planar surfaces, the first being just off the distal articular surface of the bone, and the second being 1 inch distal to the first. Delete the corner blocks, position the vertices at 45° angles, and glue the faces together. Position the mesh within the newly created region, and project all faces of the talus to the surfaces. *(commands: block, dei, pb, mbi, sd, bb, sfi)*

b. Define a sphere centered within the talus to fillet the edge of the talus. Insert a partition 2 elements through the talus (in the *z*-direction) and project the proximal parts to the sphere. Apply smoothing algorithms, define the material (polyethylene is material 4), and assign block boundary numbers to the distal face of the talus where it will attach to the distal bracket *(commands: sd, sfi, relax, unifm, mt)*.

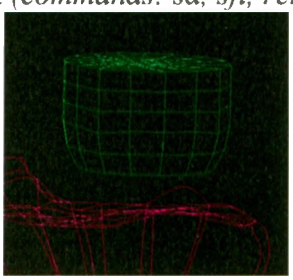

Figure J.12: The Talus

c. Create a node set at the distal face of the talus where it will attach to the distal bracket (where the load cell was positioned experimentally) *(command: nset).*

d. To create the distal bracket, create a part that is 3 blocks by 4 blocks by 1 block, delete the corners such that it forms a cross shape. Convert the short end into a cylinder shape by positioning the vertices and gluing faces, and attach it to the talus using the boundary numbers defined in part (b). Create a *x-z* surface that is offset in the *y* direction, and attach the face of the last block to it, representing the attachment point for bearings. Define a material (material 7 for the distal bracket) and apply smoothing algorithms. Assign block boundary numbers for the distal face (portion that forms the cylinder) for attachment to the foam *(commands: block, mbi, pb, dei, bb, sd, mt, relax, unifm)*

e. To create the foam, create a part that is 3 blocks by 3 blocks by 1 block, convert to a cylinder by deleting corners, positioning vertices and gluing faces. Attach it to the distal bracket using block boundary numbers. Create a *x-y* surface that is offset by 0.625 inches from the surface of the bracket, and project the faces of the mesh to the cylinder and the new surface. Define a material (material 5 for foam) and apply smoothing algorithms *(commands: block, mbi, pb, dei, bb, sd, mt, relax, unifm)*

f. To create the proximal bracket, create a part that is 5 blocks by 5 blocks by 1 block, convert to a cylinder by deleting corners, positioning vertices and gluing faces. Attach it to the block boundaries created in step 7(d). Define a *x-y* surface that is offset from the proximal surface of the bone, and project the faces of the mesh to this surface. Apply several smoothing algorithms, and define a material (material 16 for proximal bracket) *(commands: block, mbi, pb, dei, bb, sd, mt, relax, unifm)*

g. To create the projectile, create a part that is 3 blocks by 3 blocks by 2 blocks, convert to a hemisphere by deleting corners, positioning vertices and gluing faces *(commands: block, mbi, pb, dei, bb)*

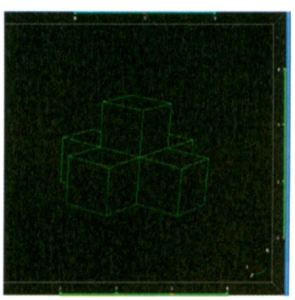

Figure J.13: Projectile Block Structure

h. Define a spherical surface located just off the surface of the foam with a diameter 3/4 that of the foam. Define a *x-y* surface that cuts through the center of the sphere. Project exterior faces of the mesh to these surfaces, apply smoothing algorithms, and assign a material (material 6 is the projectile). Define a node set that contains the nodes on the flat surface of the hemisphere *(commands: sd, sfi, unifm, relax, mt, nset)*

i. Write the output file containing node, element, and part information in LS-DYNA Keyword format *(commands: lsdyna keyword, write)*

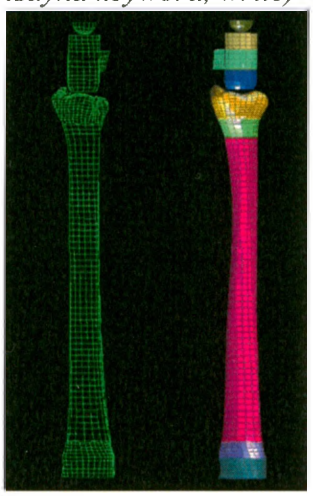

Figure J.14: The Complete Mesh

LS-DYNA®:

Step 9: Writing the Deck

a. Start writing a deck in notepad. Use *KEYWORD to define this as a keyword-written deck, *TITLE to define the title of the study, and *INCLUDE to reference the node and element data as output from TrueGrid®. Use *CONTROL_TERMINATION to set the simulated duration.

b. Write *DATABASE cards to output node data (*DATABASE_HISTORY_NODE) for specific nodes on components, force data for the set where the load cell was located (*DATABASE_NODAL_FORCE_GROUP) and element data for elements located underneath the strain gauges (*DATABASE_HISTORY_SOLID_SET).

c. Write a *PART card, a *SECTION card, and a *MAT card for each component. Select the appropriate mass for whichever projectile (3.9kg or 6.8kg) being simulated.

d. Using the *x-y-z* locations of the solder points of each strain gauge, compute the *x-y-z* coordinates of the corners of the strain sensing area of the gauge. In PrePost® import the keyword node and element file as output from TrueGrid®. Using the "Ident" feature, input the *x-y-z* coordinates of the corners of the strain sensing area of each gauge.

e. Using the "Ident" feature set to "Element" pick the elements that lie beneath the set of points. Create a set card for each strain gauge (*SET_SOLID_TITLE).

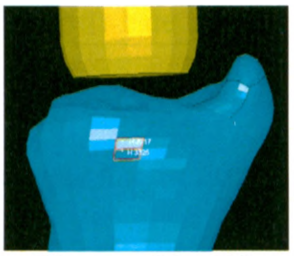

Figure J.15: Strain Gauge Element Identification

f. Write a *INITIAL_VELOCITY_RIGID_BODY card to specify the velocity of the projectile.

g. Define *CONTACT_AUTOMATIC_SURFACE_TO_SURFACE cards between all components that will come into contact (projectile-foam, talus-cortical bone, talus-cancellous bone, projectile-distal bracket).

h. Conclude with *END.

APPENDIX K – TrueGrid® Input File

This appendix includes the input file for the mesh that was constructed in Chapter 5. This input file is included as it is necessary to run further tests or alter the mesh in any way. It was also requested by the industrial collaborator on this project, General Dynamics Land Systems – Canada.

```
sd 1 stl inner.stl ;
sd 2 stl Marrow.stl ;
sd 3 stl outside.stl ;
sd 5 pl3 rt 7.6587270e+01 -8.0521985e+01 -1.5039968e+02
rt 8.7514178e+01 -7.0569206e+01 -1.5026136e+02 rt
9.5283942e+01 -8.1343137e+01 -1.5009658e+02 ;
sd 7 pl3 rt 75.671627 -54.868678 147.06598 rt 86.204893 -
75.45137 147.09288 rt 68.499807 -83.380167 147.12409 ;
sd 30 pl3 rt 8.0978298e+01 -4.6433953e+01 1.6345682e+02
rt 9.1057752e+01 -8.0185922e+01 1.6338828e+02 rt
6.0105103e+01 -7.9269842e+01 1.6347128e+02 ;
curd 1
 csp3 00
 8.4909510e+01 -5.9423919e+01 -1.8552969e+02
 8.2363709e+01 -5.9249503e+01 -1.8581836e+02
 7.5163665e+01 -5.9002083e+01 -1.8552953e+02
 7.0605865e+01 -6.1239596e+01 -1.8432106e+02
 6.6363787e+01 -6.4498247e+01 -1.8441223e+02
 6.6570895e+01 -7.3826961e+01 -1.8535071e+02
 6.7853050e+01 -7.6613912e+01 -1.8571329e+02
 6.8299933e+01 -8.1210963e+01 -1.8809501e+02
 6.7486847e+01 -8.7900150e+01 -1.8708163e+02
 6.7740273e+01 -9.2151715e+01 -1.8730578e+02
 6.8843243e+01 -9.4824959e+01 -1.8904861e+02
 8.5986367e+01 -9.8654898e+01 -1.8776145e+02
 9.2029252e+01 -9.7790019e+01 -1.8624001e+02
 1.0147598e+02 -9.4621420e+01 -1.8691939e+02
 1.1519588e+02 -8.3351227e+01 -1.8693920e+02
 1.1470076e+02 -7.8645470e+01 -1.8740285e+02
 1.1325859e+02 -7.4636901e+01 -1.8669097e+02
 1.0688315e+02 -6.6478985e+01 -1.8459532e+02
 1.0029294e+02 -6.4166643e+01 -1.8390858e+02
 9.5958523e+01 -6.2451439e+01 -1.8403057e+02
 8.8909833e+01 -6.0063674e+01 -1.8489964e+02
 8.4909510e+01 -5.9423919e+01 -1.8552969e+02
;;;
curd 2
 csp3 00
 7.8663358e+01 -6.8447093e+01 -1.5030911e+02
 7.5274520e+01 -7.0049067e+01 -1.5012289e+02
 7.1413956e+01 -7.3498863e+01 -1.4992351e+02
 7.0530176e+01 -7.7118314e+01 -1.5019280e+02
 7.0217523e+01 -8.1078093e+01 -1.5014190e+02
 7.3288119e+01 -8.4518594e+01 -1.5018523e+02
 7.6391609e+01 -8.7076522e+01 -1.5010870e+02
 7.9796773e+01 -8.9070802e+01 -1.5020579e+02
 8.4265964e+01 -8.9901158e+01 -1.5014561e+02
 9.0093717e+01 -9.0503124e+01 -1.5004302e+02
 9.3224064e+01 -8.8904071e+01 -1.5023562e+02
 9.5950007e+01 -8.5051582e+01 -1.4995418e+02
 9.7035341e+01 -7.8668903e+01 -1.4999863e+02
 9.7836216e+01 -7.5776063e+01 -1.4996432e+02
 9.6709100e+01 -7.2534916e+01 -1.5004622e+02
 9.5175596e+01 -6.9007492e+01 -1.4973519e+02
 9.0972049e+01 -6.7453865e+01 -1.4979549e+02
 8.6279061e+01 -6.6894117e+01 -1.5009409e+02
 8.1659208e+01 -6.7157612e+01 -1.5003110e+02
 7.8663358e+01 -6.8447093e+01 -1.5030911e+02
;;;
curd 3
 csp3 00
 6.8900780e+01 -5.3017182e+01 1.4659028e+02
 6.6189889e+01 -5.5912849e+01 1.4634244e+02
 6.3121453e+01 -6.0456731e+01 1.4660445e+02
 6.0511567e+01 -6.5045577e+01 1.4649944e+02
 5.9495258e+01 -6.8998034e+01 1.4642872e+02
 5.9127874e+01 -7.3831430e+01 1.4660785e+02
 6.0916153e+01 -7.8260406e+01 1.4679395e+02
 6.4804589e+01 -8.3677924e+01 1.4692362e+02
 6.7680924e+01 -8.7485265e+01 1.4698965e+02
 7.1933214e+01 -9.1037236e+01 1.4667208e+02
 7.5751204e+01 -9.2225787e+01 1.4662826e+02
 7.9809462e+01 -9.3132183e+01 1.4675383e+02
 8.4445735e+01 -9.2119223e+01 1.4695316e+02
 8.8918268e+01 -8.9382744e+01 1.4714645e+02
 9.0778226e+01 -8.5026993e+01 1.4709351e+02
 9.0546013e+01 -7.9132196e+01 1.4714581e+02
 8.9896849e+01 -7.3269263e+01 1.4695571e+02
 8.8989815e+01 -6.7729598e+01 1.4647143e+02
 8.7411788e+01 -6.2942717e+01 1.4694036e+02
 8.5374711e+01 -5.8252971e+01 1.4695006e+02
 8.4324444e+01 -5.5414121e+01 1.4710386e+02
 8.1206392e+01 -5.1538421e+01 1.4693117e+02
 7.6845313e+01 -5.0122100e+01 1.4702411e+02
 7.2403987e+01 -5.0643706e+01 1.4702527e+02
 6.8900780e+01 -5.3017182e+01 1.4659028e+02
;;;
curd 4
 csp3 00
 6.7933713e+01 -9.2578978e+01 1.6310776e+02
 6.9451276e+01 -9.4082831e+01 1.6291756e+02
 7.3658603e+01 -9.6534074e+01 1.6291625e+02
 7.9122003e+01 -9.8042351e+01 1.6323791e+02
 8.4072299e+01 -9.7873596e+01 1.6332119e+02
 8.7742223e+01 -9.7009800e+01 1.6326963e+02
 9.0923012e+01 -9.5203946e+01 1.6319148e+02
 9.3047605e+01 -9.1328376e+01 1.6284818e+02
 9.3478500e+01 -8.4674529e+01 1.6346521e+02
 9.2660664e+01 -7.9514492e+01 1.6281803e+02
 9.1880004e+01 -7.5131162e+01 1.6295486e+02
```

```
 9.0473291e+01 -7.0054320e+01 1.6290291e+02
 8.9322681e+01 -6.5927036e+01 1.6296212e+02
 8.7414364e+01 -6.0623136e+01 1.6295282e+02
 8.6613215e+01 -5.6175048e+01 1.6281864e+02
 8.4171029e+01 -5.0833618e+01 1.6277144e+02
 7.9870879e+01 -4.5171575e+01 1.6326576e+02
 7.4606969e+01 -4.5608596e+01 1.6332590e+02
 7.0656277e+01 -4.4941397e+01 1.6291385e+02
 6.7111842e+01 -4.6848482e+01 1.6324566e+02
 6.3733792e+01 -5.0259406e+01 1.6323154e+02
 6.1325145e+01 -5.4532225e+01 1.6324086e+02
 5.8556737e+01 -5.8278188e+01 1.6318615e+02
 5.5761934e+01 -6.4443438e+01 1.6339852e+02
 5.4016061e+01 -6.8844365e+01 1.6298995e+02
 5.3745570e+01 -7.3114925e+01 1.6303182e+02
 5.5138056e+01 -7.7489014e+01 1.6327459e+02
 5.7095664e+01 -8.0112770e+01 1.6322322e+02
 5.9052999e+01 -8.2131515e+01 1.6272650e+02
 6.1781680e+01 -8.4861013e+01 1.6318565e+02
 6.4591539e+01 -8.7445528e+01 1.6309637e+02
 6.6219066e+01 -9.0136300e+01 1.6298911e+02
 6.7933713e+01 -9.2578978e+01 1.6310776e+02
;;;
curd 6
 csp3 00
 6.6149332e+01 -4.3420907e+01 1.6260343e+02
 6.8963298e+01 -4.2308647e+01 1.6303186e+02
 7.4335665e+01 -4.0501174e+01 1.6309569e+02
 7.9640191e+01 -4.1045146e+01 1.6303948e+02
 8.4682797e+01 -4.4170446e+01 1.6309202e+02
 8.6603892e+01 -4.7065156e+01 1.6325660e+02
 8.7869944e+01 -5.2566362e+01 1.6260604e+02
 8.9064147e+01 -5.8541708e+01 1.6299031e+02
 9.0816324e+01 -6.3414959e+01 1.6273668e+02
 9.3125007e+01 -7.0660032e+01 1.6295442e+02
 9.4303524e+01 -7.4965127e+01 1.6292787e+02
 9.5277145e+01 -8.0304100e+01 1.6298779e+02
 9.5858539e+01 -8.4799777e+01 1.6264875e+02
 9.5789451e+01 -8.9522302e+01 1.6298314e+02
 9.4584083e+01 -9.5042688e+01 1.6311867e+02
 9.1173317e+01 -9.8510278e+01 1.6311852e+02
 8.7011573e+01 -1.0051218e+02 1.6318377e+02
 8.3024191e+01 -1.0160289e+02 1.6313514e+02
 7.8167968e+01 -1.0137750e+02 1.6326059e+02
 7.4462935e+01 -1.0044989e+02 1.6334218e+02
 7.0649307e+01 -9.8732193e+01 1.6289653e+02
 6.6128348e+01 -9.4149001e+01 1.6303342e+02
 6.3591912e+01 -9.1416659e+01 1.6301373e+02
 6.1266212e+01 -8.8535294e+01 1.6298492e+02
 5.9012151e+01 -8.6325993e+01 1.6312482e+02
 5.6074858e+01 -8.3041820e+01 1.6319059e+02
 5.3442855e+01 -8.0001424e+01 1.6306801e+02
 5.2137680e+01 -7.6098104e+01 1.6291305e+02
 5.2003499e+01 -7.0989938e+01 1.6321195e+02
 5.2451471e+01 -6.7442807e+01 1.6329842e+02
 5.4028584e+01 -6.2700936e+01 1.6316137e+02
 5.5110404e+01 -5.9341267e+01 1.6301951e+02
 5.6867189e+01 -5.6114575e+01 1.6273497e+02
 5.8682293e+01 -5.3583451e+01 1.6258362e+02
 6.0283536e+01 -5.1290956e+01 1.6243958e+02
 6.2551315e+01 -4.8644026e+01 1.6291676e+02
 6.4587881e+01 -4.6032773e+01 1.6295975e+02
 6.6149332e+01 -4.3420907e+01 1.6260343e+02
;;;
curd 40
 csp3 00
 1.0392704e+02 -9.5154604e+01 -1.9138772e+02
 1.0241343e+02 -9.3571276e+01 -1.9391412e+02
 1.0304916e+02 -8.9230487e+01 -1.9444097e+02
 1.0257104e+02 -7.1544236e+01 -1.9021131e+02
 1.0092884e+02 -6.5867435e+01 -1.8916127e+02
 9.9117146e+01 -6.3727513e+01 -1.8793996e+02
;;;
curd 11
 csp3 00
 1.0990590e+02 -6.5784734e+01 -1.8624755e+02
 1.0358508e+02 -6.4039059e+01 -1.8614657e+02
 9.9711423e+01 -6.3183784e+01 -1.8583176e+02
 9.5001176e+01 -6.2187665e+01 -1.8631427e+02
 9.0694721e+01 -6.0336770e+01 -1.8657428e+02
 8.6896607e+01 -5.9601264e+01 -1.8740634e+02
 8.1989470e+01 -5.8646850e+01 -1.8716201e+02
 7.6438265e+01 -5.8147058e+01 -1.8769951e+02
 7.2186473e+01 -5.8661098e+01 -1.8734053e+02
 7.0161194e+01 -5.9645576e+01 -1.8651577e+02
 6.6990073e+01 -6.2256592e+01 -1.8641736e+02
 6.4610975e+01 -6.4832506e+01 -1.8623859e+02
 6.3532153e+01 -6.8875239e+01 -1.8688825e+02
 6.7112069e+01 -8.7671200e+01 -1.8888832e+02
 6.6755764e+01 -9.1467750e+01 -1.8945225e+02
 6.6620621e+01 -9.4809755e+01 -1.9004358e+02
 6.9581438e+01 -9.7723052e+01 -1.9225104e+02
 7.3538172e+01 -9.9035456e+01 -1.9249075e+02
 7.8869365e+01 -1.0058332e+02 -1.9213605e+02
 8.8793424e+01 -9.8425137e+01 -1.9041089e+02
 9.5160218e+01 -9.7192702e+01 -1.8926304e+02
 9.9094987e+01 -9.6191766e+01 -1.8994910e+02
 1.0846346e+02 -9.3459322e+01 -1.9093728e+02
 1.1328033e+02 -9.2015791e+01 -1.9054845e+02
 1.1623301e+02 -8.7662926e+01 -1.8898735e+02
 1.1725734e+02 -8.5028799e+01 -1.8931276e+02
 1.1771571e+02 -7.9727248e+01 -1.8858431e+02
 1.1686790e+02 -7.3998525e+01 -1.8821925e+02
 1.1469125e+02 -6.9606071e+01 -1.8745247e+02
 1.0990590e+02 -6.5784734e+01 -1.8624755e+02
;;;
curd 20
 csp3 00
 8.3211156e+01 -9.5744824e+01 1.4698369e+02
 8.1237841e+01 -9.6098960e+01 1.4716567e+02
 7.6348470e+01 -9.6354636e+01 1.4726155e+02
 7.3213045e+01 -9.5640772e+01 1.4718872e+02
 6.9928387e+01 -9.3923935e+01 1.4721097e+02
 6.6225946e+01 -9.0363577e+01 1.4721740e+02
 6.2942754e+01 -8.6670853e+01 1.4691365e+02
 6.0342404e+01 -8.3039700e+01 1.4725538e+02
 5.8310535e+01 -8.0279154e+01 1.4719185e+02
 5.7195423e+01 -7.7287320e+01 1.4719878e+02
 5.6597646e+01 -7.2803796e+01 1.4713703e+02
 5.6879098e+01 -6.8714545e+01 1.4714634e+02
 5.7680915e+01 -6.5374940e+01 1.4714966e+02
 5.9244839e+01 -6.1785934e+01 1.4700237e+02
 6.2089651e+01 -5.7468002e+01 1.4711238e+02
 6.4710294e+01 -5.3846601e+01 1.4712843e+02
 6.6426192e+01 -5.0409000e+01 1.4705256e+02
 6.8005769e+01 -4.5961791e+01 1.4705126e+02
 7.1275607e+01 -4.2736300e+01 1.4703477e+02
 7.4510498e+01 -4.2017559e+01 1.4694096e+02
 7.7969315e+01 -4.2742641e+01 1.4691367e+02
 8.0491504e+01 -4.3896451e+01 1.4700805e+02
 8.3160010e+01 -4.5126595e+01 1.4699654e+02
 8.5104127e+01 -4.8556245e+01 1.4700314e+02
 8.7339013e+01 -5.4650472e+01 1.4697199e+02
 8.8655680e+01 -5.7907622e+01 1.4699456e+02
 9.0180513e+01 -6.2029252e+01 1.4697879e+02
 9.1283674e+01 -6.4824335e+01 1.4704214e+02
 9.2598764e+01 -6.9218303e+01 1.4704595e+02
 9.3605178e+01 -7.5121232e+01 1.4702202e+02
 9.4173064e+01 -7.8775046e+01 1.4707765e+02
 9.4660407e+01 -8.1967084e+01 1.4698951e+02
```

```
 9.4576984e+01 -8.5695582e+01 1.4701535e+02
 9.3642761e+01 -8.9991414e+01 1.4708445e+02
 9.1996619e+01 -9.2307991e+01 1.4704904e+02
 9.0565011e+01 -9.3924909e+01 1.4717543e+02
 8.8322312e+01 -9.4467963e+01 1.4710562e+02
 8.5706454e+01 -9.5166232e+01 1.4678719e+02
 8.3211156e+01 -9.5744824e+01 1.4698369e+02
;;;
block 1 3 5 7;1 3 5 7;1 3;1 3 5 7;1 3 5 7;1 3;
del 1 2 0 3 4; 1 2 0 3 4; 1 2;
rap
curd 44
 csp3 00
 1.0106995e+02 -6.2431754e+01 -1.6880212e+02
 9.4404917e+01 -6.0086443e+01 -1.6875549e+02
 8.9933892e+01 -5.9824247e+01 -1.6870223e+02
 8.1807100e+01 -6.0364778e+01 -1.6866886e+02
 7.4087303e+01 -6.2348775e+01 -1.6876163e+02
 6.9571869e+01 -6.6607793e+01 -1.6887887e+02
 6.5580893e+01 -6.8285620e+01 -1.6880182e+02
 6.4768891e+01 -7.3848449e+01 -1.6884552e+02
 6.4302331e+01 -7.7839791e+01 -1.6871231e+02
 6.5856808e+01 -8.0820879e+01 -1.6880260e+02
 6.6192726e+01 -8.4325775e+01 -1.6890204e+02
 6.7139287e+01 -8.8253577e+01 -1.6882361e+02
 7.0180201e+01 -9.2573371e+01 -1.6881758e+02
 7.5749465e+01 -9.4397707e+01 -1.6879744e+02
 8.0587403e+01 -9.6332164e+01 -1.6889661e+02
 9.0049461e+01 -9.6404842e+01 -1.6875835e+02
 9.5337137e+01 -9.7759818e+01 -1.6871208e+02
 1.0108241e+02 -9.6185473e+01 -1.6887018e+02
 1.0374268e+02 -9.1709896e+01 -1.6927395e+02
 1.0601949e+02 -8.7219928e+01 -1.6897915e+02
 1.0779789e+02 -8.2814360e+01 -1.6880382e+02
 1.0826572e+02 -7.6639909e+01 -1.6894458e+02
 1.0777944e+02 -7.0434556e+01 -1.6928480e+02
 1.0466125e+02 -6.5371974e+01 -1.6903968e+02
 1.0106995e+02 -6.2431754e+01 -1.6880212e+02
;;;
curd 39
 csp3 00
 1.1484617e+02 -7.9224560e+01 -1.9783276e+02
 1.1539493e+02 -7.8025761e+01 -1.9792348e+02
 1.1583022e+02 -7.5902674e+01 -1.9740705e+02
 1.1540572e+02 -7.1463546e+01 -1.9638605e+02
 1.1448720e+02 -6.8377424e+01 -1.9590719e+02
 1.1337081e+02 -6.6747655e+01 -1.9527312e+02
 1.1139355e+02 -6.6056637e+01 -1.9557058e+02
 1.0923730e+02 -6.7139205e+01 -1.9591623e+02
 1.0819691e+02 -6.9431999e+01 -1.9634525e+02
 1.0827392e+02 -7.4098670e+01 -1.9746607e+02
 1.0821243e+02 -7.5832107e+01 -1.9775758e+02
 1.0843799e+02 -7.8179876e+01 -1.9793630e+02
 1.0989824e+02 -8.0128523e+01 -1.9803750e+02
 1.1191423e+02 -8.0537493e+01 -1.9771114e+02
 1.1358134e+02 -8.0430574e+01 -1.9735808e+02
 1.1484617e+02 -7.9224560e+01 -1.9783276e+02
;;;
mbi -4; -2; 1 2; xyz 0.365140e-01 -0.146980 -0.699395
mbi -4; -3; 1 2; xyz -0.700058 1.27982 0.972671
mbi -3; -4; 1 2; xyz 1.03446 0.269584 0.357254
mbi -2; -4; 1 2; xyz -1.46979 0.243299 0.125857e-01
mbi -1; -3; 1 2; xyz -0.657301e-02 1.09993 0.912673
mbi -1; -2; 1 2; xyz 0.544699 -1.08987 -0.834944
mbi -2; -1; 1 2; xyz -0.946058 -0.169897 -0.263065
mbi -3; -1; 1 2; xyz 1.78855 0.436747e-01 0.266846
bb 3 3 1 3 4 2 1;
bb 3 3 1 4 3 2 1;
bb 1 3 1 2 3 2 2;
bb 2 3 1 2 4 2 2;
bb 2 1 1 2 2 2 3;
bb 1 2 1 2 2 2 3;
bb 3 2 1 4 2 2 4;
bb 3 1 1 3 2 2 4;
mbi -4; -2; 1 2; xyz -0.989922e-01 -0.627252 -0.576127
mbi 1 4; 1 4; 1 2; y -83.5106
mbi 1 4; 1 4; 1 2; x 101.102
mbi 1 4; 1 4; 1 2; z -186.064
mbi 1 4; 1 4; 1 2; z -16.9364
mbi -4; 2 3; 1 2; xyz 8.45633 -2.55267 0.522909
mbi 2 3; -1; 1 2; xyz -20.3915 -14.5656 -0.834384
mbi -1; 2 3; 1 2; xyz -23.1771 6.51339 -1.42324
mbi -1; 2 3; 1 2; xyz -13.7505 1.64953 -0.798792
mbi 2 3; -1; 1 2; xyz -8.71279 -6.31193 -0.354692
mbi 2 3; -4; 1 2; xyz 6.95643 12.2446 0.134872
mbi 2 3; -4; 1 2; xyz -1.13729 3.61204 -0.137614
mbi 2 3; -4; 1 2; xyz -1.10283 2.52703 -0.113362
mbi -3; -3;; xyz -1.52751 5.76996 -0.203741
mbi -2; -3;; xyz -17.0606 3.43095 -1.01958
mbi -2; -2;; xyz -14.9450 -5.36382 -0.720858
mbi -3; -2;; xyz -5.17098 0.356338 -0.294957
mbi -3; -3;; xyz -5.23358 0.992208 -1.20531
mbi ;; -2; z 32.2363
mbi ;; -1; z 13.5237
curs 1 2 1 1 3 1 1
curs 2 1 1 3 1 1 1
curs 4 2 1 4 3 1 1
curs 2 4 1 3 4 1 1
sd 9 xyplan mz -168.7 ; ;
dap
curs 4 2 2 4 3 2 44
curs 2 1 2 3 1 2 44
curs 1 2 2 1 3 2 44
curs 2 4 2 3 4 2 44
mbi -2; -3; 1 2; xyz -6.83346 1.93448 -0.284763
mbi -2; -2;; xyz -4.91276 -0.848815 -0.107489
mbi -3; -2;; xyz -1.70899 -3.69647 0.110277
mbi -3; -3;; xyz -6.38628 -1.09134 -0.140253
mbi -2; -3;; xyz 1.09446 -2.45794 1.88307
sfi -1; 2 3; 1 2;sd 1
sfi 2 3; -4; 1 2;sd 1
sfi -4; 2 3; 1 2;sd 1
sfi 2 3; -1; 1 2;sd 1
sfi 1 4; 2 3; -1;sd 1
sfi 2 3; 1 4; -1;sd 1
sfi 1 4; 2 3; -2;sd 9
sfi 2 3; 1 4; -2;sd 9
relax 2 1 1 3 4 1 & 1 2 1 2 3 1 & 3 2 1 4 3 1 5 0 1 ;
relax 2 1 1 3 4 1 & 1 2 1 2 3 1 & 3 2 1 4 3 1 5 0 1 ;
pb 2 3 1 2 3 1 xyz 84.3176 -75.0147 -185.475
relax 2 1 2 3 4 2 & 1 2 2 2 3 2 & 3 2 2 4 3 2 10 0 1 ;
relax 2 4 1 3 4 2 & 1 2 1 1 3 2 & 4 2 1 4 3 2 & 2 1 1 3 1 2 10
0 1 ;
unifm 1 2 1 4 3 2 & 2 3 1 3 4 2 & 2 1 1 3 2 2 10 0 1 ;
mseq k 6
mseq i 6 0 6
mseq j 6 0 6
mseq i 0 6 0
mseq j 0 6 0
c distal most cancellous region finished
insprt 1 5 1 2
del 1 2 0 3 4; 1 2 0 3 4; 1 2;
mbi ;; -1; z -7.95850
bb 2 1 1 2 2 2 9;
bb 1 2 1 2 2 2 10;
undo
bb 1 2 1 2 2 2 9;
bb 3 2 1 4 2 2 10;
bb 3 1 1 3 2 2 10;
bb 3 3 1 3 4 2 11;
```

```
bb 3 3 1 4 3 2 11;
bb 1 3 1 2 3 2 12;
bb 2 3 1 2 4 2 12;
curs 1 2 1 1 3 1 11
curs 2 4 1 3 4 1 11
curs 4 2 1 4 3 1 11
curs 2 1 1 3 1 1 11
insprt 1 1 1 2
dei 1 2; 1 2 0 3 4; 1 3;
dei 1 2; 2 3; 1 2;
mbi -1; 2 3; 2 3; x -14.0397
bb 2 2 1 2 3 2 13;
bb 1 2 2 2 3 2 13;
insprt 1 2 5 2
dei 5 6; 1 4; 1 2;
dei 5 6; 1 2 0 3 4; 2 3;
mbi -6; 2 3; 2 3; x 9.53819
bb 5 2 1 5 3 2 14;
bb 5 2 2 6 3 2 14;
insprt 1 3 1 2
dei 1 6; 1 2; 1 2;
dei 1 3 0 4 6; 1 2; 2 3;
mbi 3 4; -1; 2 3; y -28.8405
mbi 3 4; -1; 2 3; y 13.0797
bb 3 2 1 4 2 2 15;
bb 3 1 2 4 2 2 15;
insprt 1 4 5 2
dei 1 6; 5 6; 1 2;
dei 1 3 0 4 6; 5 6; 2 3;
mbi 3 4; -6; 2 3; y 21.5299
mbi 3 4; -6; 2 3; y -5.98436
bb 3 5 1 4 5 2 16;
bb 3 5 2 4 6 2 16;
bb 4 5 2 4 6 3 17;
bb 5 4 2 6 4 3 17;
bb 5 3 2 6 3 3 18;
bb 4 1 2 4 2 3 18;
bb 3 1 2 3 2 3 19;
bb 1 3 2 2 3 3 19;
bb 1 4 2 2 4 3 20;
bb 3 5 2 3 6 3 20;
curs 1 3 3 1 4 3 44
curs 3 6 3 4 6 3 44
curs 6 3 3 6 4 3 44
curs 3 1 3 4 1 3 44
sfi -6; 3 4; 2 3;sd 3
sfi 3 4; -1; 2 3;sd 3
sfi 3 4; -6; 2 3;sd 3
sfi -1; 3 4; 2 3;sd 3
sfi 3 4; 5 6; -3;sd 9
sfi 1 2; 3 4; -3;sd 9
sfi 3 4; 1 2; -3;sd 9
sfi 5 6; 3 4; -3;sd 9
sfi 3 4; 2 5; -1;sd 3
sfi 2 5; 3 4; -1;sd 3
relax 2 3 1 5 4 1 & 3 4 1 4 5 1 & 3 2 1 4 3 1 10 0 1 ;
relax 3 6 2 4 6 3 & 6 3 2 6 4 3 & 1 3 2 1 4 3 & 3 1 2 4 1 3 10
0 1 ;
unifm 5 3 3 6 4 3 & 3 5 3 4 6 3 & 1 3 3 2 4 3 & 3 1 3 4 2 3 10
0 1 ;
decmd 165
undo
sfi 2 4; 3 4; -1;sd 3
unifm 3 2 1 4 5 2 & 2 3 1 3 4 2 & 4 3 1 5 4 2 & 5 3 2 6 4 3 &
3 1 2 4 2 3 & 1 3 2 2 4 3 & 3 5 2 4 6 3 10 0 1 ;
insprt 1 2 4 4
mbi -5; 3 4; -1; xyz 6.36690 1.34420 -0.655879
unifm 2 3 1 6 4 2 & 1 3 2 7 4 3 & 3 2 1 4 3 3 & 3 1 2 4 2 3 &
3 4 1 4 5 3 & 3 5 2 4 6 3 15 0 1 ;
unifm 2 3 1 6 4 2 & 1 3 2 7 4 3 & 3 2 1 4 3 3 & 3 1 2 4 2 3 &
3 4 1 4 5 3 & 3 5 2 4 6 3 15 0 1 ;
mbi -5; 3 4; -1; z -3.43443
unifm 2 3 1 6 4 2 & 1 3 2 7 4 3 & 3 2 1 4 3 3 & 3 1 2 4 2 3 &
3 4 1 4 5 3 & 3 5 2 4 6 3 15 0 1 ;
mseq i 0 4 0 2 2 0
mseq j 0 4 0 4 0
relax 3 1 3 4 6 3 & 1 3 3 3 4 3 & 4 3 3 7 4 3 10 0 1 ;
relax 3 1 3 4 6 3 & 1 3 3 3 4 3 & 4 3 3 7 4 3 10 0 1 ;
relax 1 3 2 7 4 2 & 3 4 2 4 6 2 & 3 1 2 4 3 2 10 0 1 ;
curf 3 1 3 4 1 3 44
relax 3 1 2 4 1 3 5 0 1 ;
unifm 2 3 1 6 4 2 & 1 3 2 7 4 3 & 3 2 1 4 3 3 & 3 1 2 4 2 3 &
3 4 1 4 5 3 & 3 5 2 4 6 3 15 0 1 ;
unifm 2 3 1 6 4 2 & 1 3 2 7 4 3 & 3 2 1 4 3 3 & 3 1 2 4 2 3 &
3 4 1 4 5 3 & 3 5 2 4 6 3 40 0 1 ;
mseq i -1 0 0 0 0 -1
mseq j -1 0 0 0 -1
mseq k -1 0
dap
mate 1
mt 2 3 1 6 4 2 2
mt 3 2 1 4 5 2 2
mt 3 1 2 4 2 3 2
mt 6 3 2 7 4 3 2
mt 3 5 2 4 6 3 2
mt 1 3 2 2 4 3 2
bb 1 3 3 2 4 3 100;
bb 3 1 3 4 2 3 101;
bb 6 3 3 7 4 3 102;
bb 3 5 3 4 6 3 103;
bb 3 2 3 4 5 3 104;
bb 2 3 3 3 4 3 105;
bb 4 3 3 6 4 3 106;
insprt 1 5 1 4
dei 1 5 0 6 7; 1 3 0 4 6; 1 2;
dei 1 5 0 6 7; 3 4; 1 2;
dei 5 6; 1 3 0 4 6; 1 2;
mbi 5 6; 3 4; -1; z -9.55522
curd 39
 csp3 00
 1.1484617e+02 -7.9224560e+01 -1.9783276e+02
 1.1539493e+02 -7.8025761e+01 -1.9792348e+02
 1.1583022e+02 -7.5902674e+01 -1.9740705e+02
 1.1540572e+02 -7.1463546e+01 -1.9638605e+02
 1.1448720e+02 -6.8377424e+01 -1.9590719e+02
 1.1337081e+02 -6.6747655e+01 -1.9527312e+02
 1.1139355e+02 -6.6056637e+01 -1.9557058e+02
 1.0923730e+02 -6.7139205e+01 -1.9591623e+02
 1.0819691e+02 -6.9431999e+01 -1.9634525e+02
 1.0827392e+02 -7.4098670e+01 -1.9746607e+02
 1.0821243e+02 -7.5832107e+01 -1.9775758e+02
 1.0843799e+02 -7.8179876e+01 -1.9793630e+02
 1.0989824e+02 -8.0128523e+01 -1.9803750e+02
 1.1191423e+02 -8.0537493e+01 -1.9771114e+02
 1.1358134e+02 -8.0430574e+01 -1.9735808e+02
 1.1484617e+02 -7.9224560e+01 -1.9783276e+02
;;;
pb 6 4 1 6 4 1 xyz 113.681 -65.2124 -194.397
pb 6 3 1 6 3 1 xyz 116.286 -79.6665 -198.259
pb 5 3 1 5 3 1 xyz 109.285 -79.5197 -203.172
pb 5 4 1 5 4 1 xyz 107.478 -67.0531 -196.506
curs 5 3 1 5 4 1 39
curs 5 3 1 6 3 1 39
curs 6 3 1 6 4 1 39
curs 5 4 1 6 4 1 39
sfi 5 6; 3 4; -1;sd 3
sfi -6; 3 4; 1 2;sd 3
sfi 5 6; -4; 1 2;sd 3
sfi 5 6; -3; 1 2;sd 3
```

```
sfi -5; 3 4; 1 2;sd 3
sfi 4 5; 3 4; -2;sd 3
relax 5 3 1 6 4 1 & 5 4 1 6 4 2 & 5 3 1 5 4 2 & 6 3 1 6 4 2 &
5 3 1 6 3 2 7 0 1 ;
unifm 5 3 1 6 4 2 5 0 1 ;
unifm 5 3 1 6 4 2 & 2 3 2 6 4 3 & 1 3 3 7 4 4 & 3 4 2 4 5 4 &
3 5 3 4 6 4 & 3 2 2 4 3 4 & 3 1 3 4 2 4 10 0 1 ;
unifm 5 3 1 6 4 2 10 0 1 ;
mt 5 3 1 6 4 2 2
c distalmost section complete
merge
block 1 2 8 12 18 19;1 2 8 12 18 19;1 5;1 2 8 12 18 19;1 2 8
12 18 19;1 5;
dap
mbi ;; 1 2; y -92.9273
mbi ;; 1 2; x 78.1869
mbi ;; 1 2; z -163.365
dei 1 3 0 4 6; 1 3 0 4 6; 1 2;
mbi -4; 1 2; 1 2; xy 3.19672 1.38723
mbi 5 6; -3; 1 2; xy -2.20587 -4.69069
mbi 5 6; -4; 1 2; xy -1.44613 4.64706
mbi -4; 5 6; 1 2; xy 3.61880 -0.755530
mbi -3; 5 6; 1 2; xy -4.95921 -0.671114
mbi 1 2; -4; 1 2; xy 0.949881 4.56264
mbi 1 2; -3; 1 2; xy 0.527800 -4.69069
mbi -3; 1 2; 1 2; xy -5.21245 -0.478460e-01
bb 1 3 1 3 3 2 30;
bb 3 1 1 3 3 2 30;
bb 4 1 1 4 3 2 31;
bb 4 3 1 6 3 2 31;
bb 4 4 1 6 4 2 32;
bb 4 4 1 4 6 2 32;
bb 3 4 1 3 6 2 33;
bb 1 4 1 3 4 2 33;
bb 1 3 1 3 3 2 34;
bb 3 1 1 3 3 2 34;
mbi -6; -4;; xyz 0.717056e-01 1.08669 0.406502e-01
mbi -4; -1;; xyz 1.24063 -0.701654 -0.499851e-02
mbi -1; -4; 1 2; xyz -1.70844 0.502175 -0.997005e-02
mbi -1; -4;; xyz -0.779860 -0.257474 -0.222272e-01
mbi -3; -6; 1 2; xyz -0.864265 -0.257437 -0.236194e-01
mbi -6; -4;; xyz 0.421996 0.168540 0.130886e-01
mbi -1; -3; 1 2; xyz -0.961789 -1.03327 -0.534061e-01
mbi ;; -2; z 7.73965
mbi ;; -1; z -4.31828
curs 3 5 2 4 5 2 2
curs 5 3 2 5 4 2 2
curs 3 2 2 4 2 2 2
curs 2 3 2 2 4 2 2
mbi 3 4; -2; -1; xyz 1.74527 -6.44895 0.550009
mbi -5; 3 4; -1; xyz 10.0938 5.08149 3.34771
mbi 3 4; -5; -1; xyz -6.29490 10.0920 -2.03560
mbi -2; 3 4; -1; xyz -9.50527 -4.30399 -3.15062
pb 5 3 2 5 3 2 xyz 95.0804 -79.7531 -150.109
pb 4 2 2 4 2 2 xyz 95.1642 -81.4742 -149.093
pb 2 4 2 2 4 2 xyz 76.4363 -74.5884 -149.573
pb 3 5 2 3 5 2 xyz 76.3877 -74.8127 -149.709
pb 5 4 2 5 4 2 xyz 90.8394 -70.8510 -149.438
pb 4 5 2 4 5 2 xyz 91.6785 -67.7813 -149.710
trbb 2 3 1 3 4 1 105 ; ;
trbb 3 2 1 4 5 1 104 ; ;
trbb 4 3 1 5 4 1 106 ; ;
relax 2 3 2 5 4 2 & 3 4 2 4 5 2 & 3 2 2 4 3 2 10 0 1 ;
mbi 3 4; 3 4; -2; xyz -1.04357 2.57443 0.175631
pb 4 4 2 4 4 2 xyz 88.2626 -74.5001 -151.182
pb 3 3 2 3 3 2 xyz 84.0436 -82.8885 -148.873
sfi -5; 3 4; 1 2;sd 1
sfi 3 4; -2; 1 2;sd 1
sfi 3 4; -5; 1 2;sd 1
sfi -2; 3 4; 1 2;sd 1
unifm 3 2 1 4 5 2 & 4 3 1 5 4 2 & 2 3 1 3 4 2 10 0 1 ;
sfi -6; 3 4; 1 2;sd 3
sfi 3 4; -1; 1 2;sd 3
sfi -1; 3 4; 1 2;sd 3
sfi 3 4; -6; 1 2;sd 3
pb 1 4 2 1 4 2 xyz 71.3933 -69.1719 -151 084
pb 1 3 2 1 3 2 xyz 79.3027 -91.6250 -150.465
pb 4 1 2 4 1 2 xyz 98.0731 -87.6342 -150.014
pb 4 1 2 4 1 2 xyz 99.3916 -82.7957 -149.942
pb 6 4 2 6 4 2 xyz 96.1335 -66.3403 -150.477
pb 6 4 2 6 4 2 xyz 93.1905 -64.7906 -151.135
pb 6 4 2 6 4 2 xyz 92.1203 -64.7162 -151.384
relax 3 1 2 4 6 2 & 4 3 2 6 4 2 & 1 3 2 3 4 2 5 0 1 ;
curs 1 3 1 1 4 1 44
curs 3 6 1 4 6 1 44
curs 6 3 1 6 4 1 44
curs 3 1 1 4 1 1 44
relax 3 1 1 4 6 1 & 1 3 1 3 4 1 & 4 3 1 6 4 1 10 0 1 ;
trbb 1 3 1 2 4 1 100;
pb 1 4 1 1 4 1 xyz 67.7154 -64.9820 -168.524
pb 1 4 1 1 4 1 xyz 67.7350 -71.5653 -166.818
pb 6 4 1 6 4 1 xyz 109.139 -68.5672 -166.292
pb 6 4 1 6 4 1 xyz 106.744 -65.0295 -166.308
pb 6 4 1 6 4 1 xyz 104.091 -62.3097 -165.451
pb 6 4 1 6 4 1 xyz 101.613 -61.4206 -166.220
trbb 3 5 1 4 6 1 103;
pb 6 4 1 6 4 1 xyz 99.8360 -62.3723 -168.026
pb 6 4 1 6 4 1 xyz 99.3226 -62.4149 -168.552
trbb 5 3 1 6 4 1 102;
pb 4 1 1 4 1 1 xyz 104.618 -91.6037 -169.585
trbb 3 1 1 4 2 1 101;
pb 4 1 1 4 1 1 xyz 107.719 -81.6409 -168.246
unifm 1 3 1 2 4 2 & 3 5 1 4 6 2 & 5 3 1 6 4 2 & 3 1 1 4 2 2 10
0 1 ;
sfi -1; 3 4; 1 2;sd 3
sfi 3 4; -1; 1 2;sd 3
sfi 3 4; -6; 1 2;sd 3
sfi -6; 3 4; 1 2;sd 3
sfi 3 4; 1 6; -2;sd 5
sfi 1 6; 3 4; -2;sd 5
pb 1 4 2 1 4 2 xyz 69.6433 -70.8346 -150.704
pb 2 4 2 2 4 2 xyz 72.0370 -72.2560 -150.198
pb 2 4 2 2 4 2 xyz 72.1454 -72.5308 -150.671
relax 3 1 1 4 1 2 & 1 3 1 1 4 2 & 6 3 1 6 4 2 & 3 6 1 4 6 2 5 0
1 ;
pb 3 3 1 3 3 1 xyz 86.5526 -84.1563 -168.598
mt 2 3 1 5 4 2 1
mt 3 2 1 4 5 2 1
mt 3 1 1 4 2 2 2
mt 1 3 1 2 4 2 2
mt 5 3 1 6 4 2 2
mt 3 5 1 4 6 2 2
relax 1 3 2 6 4 2 & 3 1 2 4 3 2 & 3 4 2 4 6 2 10 0 1 ;
bb 2 3 2 5 4 2 107;
bb 3 2 2 4 3 2 108;
bb 3 4 2 4 5 2 109;
bb 1 3 2 2 4 2 110;
bb 3 1 2 4 2 2 111;
bb 5 3 2 6 4 2 112;
bb 3 5 2 4 6 2 113;
c second distal region done
merge
block 1 2 8 12 18 19;1 2 8 12 18 19;1 11;1 2 8 12 18 19;1 2 8
12 18 19;1 11;
mbi ;; 1 2; x 67.1929
mbi ;; 1 2; y -82.4632
mbi ;; -1; z -144.310
mbi ;; -2; z 116.416
mbi ;; -2; z 13.0700
mseq k 20
```

```
dei 1 3 0 4 6; 1 3 0 4 6; 1 2;
dap
mbi 5 6; -3; 1 2; xyz -0.974912 -5.03033 -0.266454e-14
mbi -4; 1 2; 1 2; xyz 4.33491 -0.963542e-01 -0.266454e-14
mbi 5 6; -4; 1 2; xyz -1.53868 5.00125 -0.266454e-14
mbi -4; 5 6; 1 2; xyz 3.89642 -0.559139 -0.266454e-14
mbi -3; 5 6; 1 2; xyz -3.62952 -1.93724 -0.266454e-14
mbi 1 2; -4; 1 2; xyz 1.86823 3.68579 -0.266454e-14
mbi 1 2; -3; 1 2; xyz 1.68031 -4.96769 -0.266454e-14
mbi -3; 1 2; 1 2; xyz -4.25593 0.915687e-01 -0.266454e-14
bb 3 4 1 3 6 2 60;
bb 1 4 1 3 4 2 60;
bb 1 3 1 3 3 2 61;
bb 3 1 1 3 3 2 61;
bb 4 1 1 4 3 2 62;
bb 4 3 1 6 3 2 62;
bb 4 4 1 6 4 2 63;
bb 4 4 1 4 6 2 63;
mbi -6; -4; 1 2; xyz -0.236302 0.232974 -0.831531e-03
mbi -6; -4; 1 2; xyz -0.313205 0.438482 -0.194495e-02
mbi -6; -4; 1 2; xyz 0.375845 -0.187925 0.135746e-03
mbi -4; -1; 1 2; xyz 0.889849 -0.332269 -0.410757e-03
mbi -3; -6; 1 2; xyz -1.30237 -0.893432 0.956761e-02
mbi -3; -6; 1 2; xyz -0.187918 -0.125276 0.135687e-02
mbi -3; -6; 1 2; xyz 0.438483 0.626389 -0.533712e-02
mbi -1; -3; 1 2; xyz -0.509114e-01 -1.89711 0.124758e-01
bb 2 3 1 5 4 1 107 ;
bb 3 4 1 4 5 1 109 ;
bb 3 2 1 4 3 1 108 ;
mt 2 3 1 5 4 2 3
mt 3 2 1 4 5 2 3
sfi -5; 3 4; 1 2;sd 1
sfi 3 4; -2; 1 2;sd 1
sfi 3 4; -5; 1 2;sd 1
sfi -2; 3 4; 1 2;sd 1
mbi 3 4; -6; 1 2; xyz -1.23461 14.2855 -0.666134e-15
mbi -6; 3 4; 1 2; xyz 8.22428 0.598601 -0.444089e-15
mbi 3 4; -1; 1 2; xyz -0.232112 -14.9049 0.133227e-14
mbi -1; 3 4; 1 2; xyz -9.19898 -7.35850 0.111022e-14
mbi -1; 3 4; 1 2; xyz -8.99398 -1.69191 0.111022e-14
bb 3 1 1 4 2 1 111 ;
bb 1 3 1 2 4 1 110 ;
bb 3 5 1 4 6 1 113 ;
bb 5 3 1 6 4 1 112 ;
sfi -1; 3 4; 1 2;sd 3
sfi 3 4; -6; 1 2;sd 3
sfi 3 4; -1; 1 2;sd 3
sfi -6; 3 4; 1 2;sd 3
pb 1 4 2 1 4 2 xyz 62.1028 -58.4752 141.230
pb 4 1 2 4 1 2 xyz 88.8053 -92.3772 140.087
pb 6 3 2 6 3 2 xyz 89.8220 -91.9103 139.915
pb 6 3 2 6 3 2 xyz 91.9646 -89.2626 139.405
pb 6 3 2 6 3 2 xyz 93.6744 -86.7262 138.877
pb 6 3 2 6 3 2 xyz 94.5846 -84.1187 138.486
pb 6 3 2 6 3 2 xyz 94.2611 -82.6229 138.313
pb 6 3 2 6 3 2 xyz 94.4745 -81.2375 138.122
pb 6 4 2 6 4 2 xyz 89.9268 -63.0116 140.327
pb 6 4 2 6 4 2 xyz 89.7686 -62.2025 140.295
relax 3 1 2 4 6 2 & 1 3 2 3 4 2 & 4 3 2 6 4 2 10 0 1 ;
relax 3 6 1 4 6 2 & 6 3 1 6 4 2 & 1 3 1 1 4 2 & 3 1 1 4 1 2 10
0 1 ;
pb 3 1 2 3 1 2 xyz 63.3661 -85.3950 142.613
mbi ;; -2; z 4.06674
sfi 3 4; 1 6; -2;sd 7
sfi 1 6; 3 4; -2;sd 7
pb 4 1 2 4 1 2 xyz 91.9020 -82.9355 147.619
pb 6 3 2 6 3 2 xyz 92.1778 -84.5731 148.181
pb 6 3 2 6 3 2 xyz 92.0514 -86.1673 147.431
pb 6 4 2 6 4 2 xyz 90.5904 -58.5985 146.746
unifm 3 1 1 4 6 2 & 4 3 1 6 4 2 & 1 3 1 3 4 2 10 0 1 ;
mt 3 5 1 4 6 2 2
mt 5 3 1 6 4 2 2
mt 1 3 1 2 4 2 2
mt 3 1 1 4 2 2 2
mseq k 20
unifm 2 3 1 5 4 2 & 3 4 1 4 5 2 & 3 2 1 4 3 2 15 0 1 ;
unifm 2 3 1 5 4 2 & 3 4 1 4 5 2 & 3 2 1 4 3 2 15 0 1 ;
unifm 2 3 1 5 4 2 & 3 4 1 4 5 2 & 3 2 1 4 3 2 15 0 1 ;
unifm 2 3 1 5 4 2 & 3 4 1 4 5 2 & 3 2 1 4 3 2 15 0 1 ;
unifm 2 3 1 5 4 2 & 3 4 1 4 5 2 & 3 2 1 4 3 2 25 0 1 ;
unifm 2 3 1 5 4 2 & 3 4 1 4 5 2 & 3 2 1 4 3 2 25 0 1 ;
unifm 2 3 1 5 4 2 & 3 4 1 4 5 2 & 3 2 1 4 3 2 25 0 1 ;
unifm 2 3 1 5 4 2 & 3 4 1 4 5 2 & 3 2 1 4 3 2 25 0 1 ;
bb 3 2 2 4 5 2 114;
bb 4 3 2 5 4 2 115;
bb 2 3 2 3 4 2 116;
bb 3 1 2 4 2 2 117;
bb 5 3 2 6 4 2 118;
bb 3 5 2 4 6 2 119;
bb 1 3 2 2 4 2 120;
c shaft region done
merge
block 1 2 11 17 26 27;1 2 11 17 26 27;1 6;1 2 11 17 26 27;1
2 11 17 26 27;1 6;
dei 1 3 0 4 6; 1 3 0 4 6; 1 2;
mbi -4; 1 2; 1 2; xy 6.85415 1.90414
mbi 5 6; -3; 1 2; xy -1.74521 -6.96010
mbi 5 6; -4; 1 2; xy -1.37435 7.48990
mbi -4; 5 6; 1 2; xy 6.90713 -0.155828
mbi -3; 1 2; 1 2; xy -7.11904 2.01010
mbi 1 2; -3; 1 2; xy 0.950517 -6.64223
mbi -3; 5 6; 1 2; xy -5.42371 -0.473704
mbi 1 2; -4; 1 2; xy 1.58627 6.69521
bb 1 3 1 3 3 2 70;
bb 3 1 1 3 3 2 70;
bb 4 1 1 4 3 2 71;
bb 4 3 1 6 3 2 71;
bb 4 4 1 6 4 2 72;
bb 4 4 1 4 6 2 72;
bb 3 4 1 3 6 2 73;
bb 1 4 1 3 4 2 73;
mbi -1; -4; 1 2; xyz -0.842964 0.281652 -0.399215e-01
mbi -3; -6; 1 2; xyz -1.42447 0.493705 -0.670218e-01
mbi -6; -4; 1 2; xyz 0.538171 1.07556 0.565178e-01
mbi -4; -1; 1 2; xyz 0.976278 0.274360 0.610798e-01
mbi -1; -3; 1 2; xyz 0.733107e-02 -1.06901 -0.260164e-01
dap
mbi ;; 1 2; x 58.7408
mbi ;; 1 2; y -81.7085
mbi ;; 1 2; z 154.232
mbi ;; -1; z -5.51188
mbi ;; -2; z 4.77508
mbi 3 4; -2; 1 2; xyz 4.29565 -17.4635 -0.284217e-13
mbi -5; 3 4; 1 2; xy 5.13036 8.84235
mbi -2; 3 4; 1 2; xyz -5.99367 -10.7825 -0.284217e-13
mbi 3 4; -5; 1 2; xyz -7.24541 5.57511 -0.284217e-13
mseq i 0 3 2 3 0
mseq j 0 3 2 3 0
trbb 3 2 1 4 5 1 114 ; ;
trbb 2 3 1 3 4 1 116 ; ;
trbb 4 3 1 5 4 1 115 ; ;
sfi -2; 3 4; 1 2;sd 1
sfi 3 4; -5; 1 2;sd 1
sfi -5; 3 4; 1 2;sd 1
sfi 3 4; -2; 1 2;sd 1
trbb 1 3 1 2 4 1 120 ; ;
trbb 3 5 1 4 6 1 119 ; ;
trbb 5 3 1 6 4 1 118 ; ;
trbb 3 1 1 4 2 1 117 ; ;
sfi -1; 3 4; 1 2;sd 3
```

```
sfi 3 4; -6; 1 2;sd 3
sfi 3 4; -1; 1 2;sd 3
sfi -6; 3 4; 1 2;sd 3
curs 2 3 2 2 4 2 4
curs 3 2 2 4 2 2 4
curs 5 3 2 5 4 2 4
curs 3 5 2 4 5 2 4
curs 3 6 2 4 6 2 6
curs 1 3 2 1 4 2 6
curs 3 1 2 4 1 2 6
curs 6 3 2 6 4 2 6
pb 4 2 2 4 2 2 xyz 92.2729 -89.5993 163.280
pb 4 1 2 4 1 2 xyz 95.3386 -91.9353 162.875
pb 5 4 2 5 4 2 xyz 84.8809 -53.0350 162.864
pb 6 4 2 6 4 2 xyz 87.6742 -51.1514 162.469
curs 3 5 2 4 5 2 4
relax 3 1 2 4 6 2 & 1 3 2 3 4 2 & 4 3 2 6 4 2 10 0 1 ;
relax 3 6 1 4 6 2 & 6 3 1 6 4 2 & 1 3 1 1 4 2 & 3 1 1 4 1 2 10
0 1 ;
relax 2 3 1 2 4 2 & 3 2 1 4 2 2 & 5 3 1 5 4 2 & 3 5 1 4 5 2 10
0 1 ;
sd 77 xyplan mz 163 ; ;
sfi 3 4; 1 6; -2;sd 77
sfi 1 6; 3 4; -2;sd 77
curf 1 3 2 1 4 2 6
curf 6 3 2 6 4 2 6
curf 3 1 2 4 1 2 6
curf 3 6 2 4 6 2 6
unifm 3 1 1 4 6 2 & 1 3 1 3 4 2 & 4 3 1 6 4 2 10 0 1 ;
mt 3 2 1 4 5 2 1
mt 2 3 1 5 4 2 1
mt 3 5 1 4 6 2 2
mt 1 3 1 2 4 2 2
mt 3 1 1 4 2 2 2
mt 5 3 1 6 4 2 2
bb 3 2 2 4 5 2 294;
bb 4 3 2 5 4 2 295;
bb 2 3 2 3 4 2 296;
bb 3 1 2 4 2 2 297;
bb 5 3 2 6 4 2 298;
bb 3 5 2 4 6 2 299;
bb 1 3 2 2 4 2 300;
c all bone done
merge
stp 0.0001
nset 1 = srf 30 0.1
nset 2 = srf 30 0.3
nset 3 = srf 30 0.5
nset 4 = srf 30 1.1
block 1 3 5;1 3 5;1 5;1 3 5;1 3 5;1 5;
dap
insprt 1 2 3 2
insprt 1 4 3 2
dei 1 2 0 3 4; 1 2 0 3 4; 1 2;
mbi 2 3; -4; 1 2; y 1.58318
mbi -4; 2 3; 1 2; x 2.43333
mbi -3; -1; 1 2; xyz 1.36601 0.589891 -0.939999
mbi -4; -2; 1 2; xyz -0.308392e-01 -1.05314 -0.176266
mbi -4; -3; 1 2; xyz -0.620434e-01 1.47441 0.327810
mbi -3; -4; 1 2; xyz 1.06287 0.330344 -0.755832
mbi -1; -3; 1 2; xyz 0.207978 1.07518 0.440282e-01
mbi -2; -4; 1 2; xyz -1.02421 -0.167055 0.757067
mbi -2; -1; 1 2; xyz -0.904810 -0.164520 0.665594
mbi -1; -2; 1 2; xyz -0.189538 -1.31247 -0.103299
bb 3 1 1 3 2 2 123;
bb 3 2 1 4 2 2 123;
bb 3 3 1 4 3 2 124;
bb 3 3 1 3 4 2 124;
bb 2 3 1 2 4 2 125;
bb 1 3 1 2 3 2 125;
bb 1 2 1 2 2 2 126;
bb 2 1 1 2 2 2 126;
mbi ;; 1 2; z -149.774
mbi ;; 1 2; z -58.2775
mbi ;; 1 2; x 36.3020
mbi ;; 1 2; y -82.0334
mbi ;; 1 2; x 46.6086
sd 29 cy 85.54 -77.93 -192.05 0 0 1 15.9 ;
mbi -1; 2 3; 1 2; xyz -6.89429 0.240706e-01 -0.168376e-01
mbi 2 3; -1; 1 2; xyz 4.76335 -11.6753 -0.134040e-01
mbi -4; 2 3; 1 2; xyz 8.97760 6.61995 0.362094e-01
mbi 2 3; -4; 1 2; xyz -5.34691 5.48061 -0.132886e-02
mbi 2 3; -4; 1 2; xyz 1.20215 4.35979 0.123077e-01
mbi -1; 2 3; 1 2; xyz -4.35922 -6.18660 -0.239649e-01
mbi 2 3; -1; 1 2; xyz 5.58227 -3.98830 0.511021e-02
sfi 2 3; -1; 1 2;sd 29
sfi -1; 2 3; 1 2;sd 29
sfi 2 3; -4; 1 2;sd 29
sfi -4; 2 3; 1 2;sd 29
unifm 3 2 1 4 3 2 & 2 1 1 3 4 2 & 1 2 1 2 3 2 10 0 1 ;
mbi -2; -2; 1 2; xyz -2.13333 -5.06389 -0.773728e-01
mbi -3; -2; 1 2; xyz 5.05742 -2.83758 -0.148389e-01
mbi -3; -3; 1 2; xyz 4.01155 2.97700 0.580622e-01
mbi -2; -3; 1 2; xyz -2.72917 1.98233 0.140330e-01
unifm 2 1 1 3 4 2 & 1 2 1 2 3 2 & 3 2 1 4 3 2 10 0 1 ;
relax 2 1 2 3 4 2 & 3 2 2 4 3 2 & 1 2 2 2 3 2 10 0 1 ;
sd 31 plan 85.54 -77.93 -192.05 0 0 1 ;
sd 32 plan 85.54 -77.93 -216.48 0 0 1 ;
sfi ;; -2;sd 31
sfi ;; -1;sd 32
mseq i 2 2 2;
mseq j 2 2 2;
pb 3 3 1 3 3 1 xyz 94.0967 -74.0098 -217.089
pb 2 3 1 2 3 1 xyz 85.5228 -74.4537 -216.237
pb 2 2 1 2 2 1 xyz 86.5358 -83.3076 -216.053
pb 3 2 1 3 2 1 xyz 95.1223 -81.7592 -216.976
pb 2 2 1 2 2 1 xyz 86.1553 -81.1107 -215.911
pb 2 3 1 2 3 1 xyz 86.5708 -73.1392 -216.788
pb 3 2 1 3 2 1 xyz 92.8879 -83.4238 -215.630
pb 2 2 1 2 2 1 xyz 85.2310 -80.7304 -215.945
relax 2 1 1 3 4 1 & 3 2 1 4 3 1 & 1 2 1 2 3 1 10 0 1 ;
trsd 31 mz 5 ;
trsd 31 mz -5 ;
trsd 31 mz -5 ;
trsd 31 mz 2 ;
trsd 31 mz -1 ;
trsd 31 mz -.5 ;
trsd 31 mz -.5 ;
mt 2 1 1 3 4 2 4
mt 1 2 1 4 3 2 4
pb 2 2 1 2 2 1 xyz 81.8409 -81.7766 -216.551
pb 2 3 1 2 3 1 xyz 83.4456 -74.1460 -215.872
bb 2 1 1 3 4 1 160;
bb 3 2 1 4 3 1 161;
bb 1 2 1 2 3 1 162;
sd 78 sp 85.54 -77.93 -206 15.9 ;
insprt 1 5 2 1
mseq k 0 1;
sfi -4; 2 3; 2 3;sd 78
sfi 2 3; -1; 2 3;sd 78
sfi -1; 2 3; 2 3;sd 78
sfi -1; 2 3; 1 2;sd 29
sfi 2 3; -1; 1 2;sd 29
sfi -4; 2 3; 1 2;sd 29
sfi 2 3; -4; 1 2;sd 29
decmd 49
decmd 50
decmd 51
decmd 52
pb 1 3 2 1 3 2 xyz 79.8619 -62.8396 -203.818
```

```
pb 1 3 2 1 3 2 xyz 79.7352 -63.1517 -203.991
sfi 2 3; -4; 2 3;sd 78
merge
nset talus = srf 32 0.1
sd 33 plan 85.54 -77.93 -236.48 0 0 1 ;
block 1 3 5;1 3 5;1 5;1 3 5;1 3 5;1 5;
insprt 1 2 3 2
insprt 1 4 3 2
dei 1 2 0 3 4; 1 2 0 3 4; 1 2;
mbi ;; 1 2; x 73.9161
mbi ;; 1 2; y -79.1745
mbi ;; 1 2; z -230.097
mbi ;; 1 2; xyz 5.95720 -0.897980 -1.54643
mbi -4; 2 3; 1 2; x 2.50869
mbi 2 3; -4; 1 2; y 2.49144
mbi -3; -4; 1 2; xyz 1.53600 0.850100e-01 -0.170147
mbi -4; -3; 1 2; xyz -0.191240 0.513235 0.750960
mbi -2; -4; 1 2; xyz -1.48640 -0.182601 0.248660e-01
mbi -1; -3; 1 2; xyz 0.250027 0.573656 0.752233
mbi -4; -2; 1 2; xyz -0.780841 -0.823604 -1.00073
mbi -3; -1; 1 2; xyz 1.03485 -0.135752 -0.383554
mbi -2; -1; 1 2; xyz -1.23799 -0.281192 -0.159160
mbi -1; -2; 1 2; xyz -0.268402e-01 -0.772189 -1.07076
bb 2 1 1 2 2 2 200;
bb 1 2 1 2 2 2 200;
bb 1 3 1 2 3 2 201;
bb 2 3 1 2 4 2 201;
bb 3 3 1 3 4 2 202;
bb 3 3 1 4 3 2 202;
bb 3 2 1 4 2 2 203;
bb 3 1 1 3 2 2 203;
mseq i 2 2 2;
mseq j 2 2 2;
mbi -4; 2 3; 1 2; xyz 10.6435 1.48706 0.319267
mbi 2 3; -1; 1 2; xyz -2.08921 -4.99288 -5.24021
mbi 2 3; -4; 1 2; xyz 0.275494 4.06705 4.44521
mbi -1; 2 3; 1 2; xyz -6.44577 2.04134 3.04679
sfi -1; 2 3; 1 2;sd 29
sfi 2 3; -1; 1 2;sd 29
sfi 2 3; -4; 1 2;sd 29
sfi -4; 2 3; 1 2;sd 29
bb 2 1 2 3 4 2 160;
bb 3 2 2 4 3 2 161;
bb 1 2 2 2 3 2 162;
sd 33 plan 85.54 -77.93 -236.48 0 0 1 ;
y
unifm 1 2 1 2 3 2 & 2 1 1 3 4 2 & 3 2 1 4 3 2 10 0 1 ;
pb 4 3 1 4 3 1 xyz 94.3788 -62.8756 -238.691
pb 2 3 1 2 3 1 xyz 81.1445 -74.6981 -235.884
pb 3 3 1 3 3 1 xyz 86.1608 -72.9321 -235.132
pb 3 2 1 3 2 1 xyz 87.0635 -78.0225 -237.587
pb 2 2 1 2 2 1 xyz 80.9685 -79.7795 -238.134
relax 2 1 1 3 4 1 & 3 2 1 4 3 1 & 1 2 1 2 3 1 10 0 1 ;
relax 2 4 1 3 4 2 & 4 2 1 4 3 2 & 1 2 1 1 3 2 & 2 1 1 3 1 2 10
0 1 ;
relax 2 4 1 3 4 2 & 4 2 1 4 3 2 & 1 2 1 1 3 2 & 2 1 1 3 1 2 10
0 1 ;
unifm 1 2 1 4 3 2 & 2 3 1 3 4 2 & 2 1 1 3 2 2 5 0 1 ;
sfi 2 3; 1 4; -1;sd 33
sfi 1 4; 2 3; -1;sd 33
relax 2 4 1 3 4 2 & 4 2 1 4 3 2 & 1 2 1 1 3 2 & 2 1 1 3 1 2 10
0 1 ;
unifm 1 2 1 4 3 2 & 2 3 1 3 4 2 & 2 1 1 3 2 2 5 0 1 ;
pb 3 1 1 3 1 1 xyz 98.4440 -84.7187 -236.261
pb 4 3 1 4 3 1 xyz 89.2661 -61.9864 -234.353
pb 4 3 1 4 3 1 xyz 90.7939 -62.7918 -234.102
pb 4 3 1 4 3 1 xyz 93.1426 -67.4991 -231.458
pb 1 3 1 1 3 1 xyz 74.9646 -67.6334 -236.464
pb 2 1 1 2 1 1 xyz 74.2313 -88.0485 -236.476
pb 3 1 1 3 1 1 xyz 95.6814 -90.4775 -236.686
pb 4 3 1 4 3 1 xyz 94.8986 -65.1760 -236.225
pb 3 2 1 3 2 1 xyz 88.1424 -79.3841 -235.518
pb 3 2 1 3 2 1 xyz 88.9807 -79.8077 -235.643
mbi 2 3; 2 3; -1; xyz 1.29820 -0.208731 0.826865e-01
bb 1 2 1 4 3 1 163;
bb 2 3 1 3 4 1 164;
bb 2 1 1 3 2 1 165;
mt 1 2 1 4 3 2 7
mt 2 1 1 3 4 2 7
pb 4 3 1 4 3 1 xyz 96.4136 -65.4480 -237.114
pb 4 3 1 4 3 1 xyz 97.2940 -66.1146 -236.723
pb 4 3 1 4 3 1 xyz 97.6531 -67.0557 -237.357
pb 2 1 1 2 1 1 xyz 72.9474 -88.4326 -236.384
pb 2 1 1 2 1 1 xyz 73.1051 -88.0057 -236.314
relax 1 2 1 1 3 2 & 2 4 1 3 4 2 & 4 2 1 4 3 2 & 2 1 1 3 1 2 10
0 1 ;
insprt 1 1 1 4
insprt 1 2 5 4
dei 1 2 0 5 6, 1 2 0 3 4; 1 2;
insprt 1 3 1 4
insprt 1 4 5 4
dei 1 3 0 4 6; 1 2 0 5 6; 1 2;
mbi 3 4; -1; 1 2; y -13.5450
mbi 3 4; -6; 1 2; y 8.48157
mbi -6; 3 4; 1 2; x 15.6683
mbi -1; 3 4; 1 2; x -14.2368
mbi -3; -6; 1 2; xyz -8.41200 0.457541 -0.391134
mbi -1; -4; 1 2; xyz 0.832080 5.77270 -0.461763
mbi -1; -3; 1 2; xyz 5.15080 -9.03173 0.992295
mbi -3; -1; 1 2; xyz -6.53807 1.76708 -0.425414
mbi -4; -1; 1 2; xyz 9.54926 2.15775 0.213728
mbi -6; -3; 1 2; xyz -4.22665 -8.02635 0.513664
mbi -6; -4; 1 2; xyz -6.97690 7.60990 -0.946356
mbi -4; -6; 1 2; xyz 7.18555 2.62668 0.745449e-01
bb 5 4 1 6 4 2 331;
bb 4 5 1 4 6 2 331;
bb 3 5 1 3 6 2 332;
bb 1 4 1 2 4 2 332;
bb 1 3 1 2 3 2 333;
bb 3 1 1 3 2 2 333;
bb 4 1 1 4 2 2 334;
bb 5 3 1 6 3 2 334;
sfi 3 4; 1 6; -1;sd 33
sfi 1 6; 3 4; -1;sd 33
sfi 1 6; 3 4; -2;sd 32
sfi 3 4; 1 6; -2;sd 32
sfi 4 6; 3 4; -1;sd 33
pb 5 4 1 5 4 1 xyz 97.6531 -67.0557 -236.116
pb 5 3 1 5 3 1 z -236.48
pb 5 4 1 5 4 1 z -236.48
sfi 5 6; 3 4; -1;sd 33
sd 15 yzplan mx 110 ; ;
sfi -6; 3 4; 1 2;sd 15
sd 100 yzplan mx 60 ; ;
sfi -1; 3 4; 1 2;sd 100
sd 101 zxplan my -100 ; ;
sfi 3 4; -6; 1 2;sd 101
sd 102 zxplan my -100 ; ;
sfi 3 4; -1; 1 2;sd 102
mbi -3; -1; 1 2; xyz -0.917929e-02 -3.76986 0.428411
mbi -3; -1; 1 2; xyz -0.280669 -3.42710 0.838058e-01
mbi -1; -3; 1 2; xyz 0.795097 -4.08101 -0.663294
pb 1 3 1 1 3 1 xyz 59.8909 -98.3056 -234.027
pb 1 3 1 1 3 1 xyz 59.9043 -100.157 -236.423
pb 3 6 1 3 6 1 xyz 58.2599 -54.8936 -236.531
pb 3 6 1 3 6 1 xyz 59.8904 -54.8463 -236.467
pb 3 6 1 3 6 1 xyz 59.5152 -55.1453 -236.484
pb 6 4 1 6 4 1 xyz 109.649 -55.1232 -236.425
pb 4 1 1 4 1 1 xyz 110.318 -101.015 -236.456
curd 101 twsurf 102 33 85.159 -100.0 -236.48
```

```
sfi 3 4; -1; -1;sd 102
sfi 3 4; -6; -1;sd 101
sfi -1; 3 4; -1;sd 100
sfi -1; 3 4; -2;sd 100
sfi -1; 3 4; 1 2;sd 100
sfi -3; -6; 1 2;sd 100
sfi -4; -1; 1 2;sd 15
sfi -1; -3; 1 2;sd 102
sfi -6; -4; 1 2;sd 101
sfi -3; -5; -1;sd 29
sfi -3; -5; 1 2;sd 29
sfi -2; -4; 1 2;sd 29
mbi -3; -5; 1 2; xyz -3.87874 -1.51273 0.705886e-02
mbi -3; -5; 1 2; xyz -4.56842 -0.733167 0.462599e-02
pb 3 5 1 3 5 1 xyz 73.2755 -66.5934 -236.467
pb 3 5 1 3 5 1 xyz 73.5363 -66.4674 -236.465
bb 1 3 1 6 4 1 170;
bb 3 1 1 4 3 1 171;
bb 3 4 1 4 6 1 172;
mt 1 3 1 6 4 2 7
mt 3 1 1 4 6 2 7
merge
block 1 5 9 13 17 21;1 5 9 13 17 21;1 6;1 5 9 13 17 21;1 5 9
13 17 21;1 6;
dei 1 3 0 4 6; 1 3 0 4 6; 1 2;
mbi 1 2; -4; 1 2; xyz -0.438411 3.43366 0.518623
mbi -1; -4; 1 2; xyz 0.425027 3.19313 0.489495
mbi -3; -5; 1 2; xyz -2.67225 0.591964 0.669521e-01
mbi -3; -6; 1 2; xyz -7.18768 0.708564 0.456382e-01
mbi -4; -5; 1 2; xyz 4.12945 -0.123632 0.169056e-01
mbi -4; -6; 1 2; xyz 5.87579 0.346993 0.103613
mbi -5; -4; 1 2; xyz 0.585579e-01 2.65931 0.405108
mbi -6; -4; 1 2; xyz -0.898138 7.04438 1.06400
mbi -5; -3; 1 2; xyz -0.594768 -3.62098 -0.556059
mbi -6; -3; 1 2; xyz -0.667134 -7.04714 -1.07796
mbi -4; -2; 1 2; xyz 2.02210 -0.980714e-01 0.256815e-02
mbi -4; -1; 1 2; xyz 6.11499 0.286905 0.965399e-01
mbi -3; -2; 1 2; xyz -2.63798 0.310945 0.244928e-01
mbi -3; -1; 1 2; xyz -5.28327 0.839042 0.819611e-01
mbi -2; -3; 1 2; xyz 0.220621 -2.24990 -0.340402
mbi -1; -3; 1 2; xyz 1.16293 -5.83166 -0.877200
bb 3 1 1 3 3 2 260;
bb 1 3 1 3 3 2 260;
bb 1 4 1 3 4 2 261;
bb 3 4 1 3 6 2 261;
bb 4 4 1 4 6 2 262;
bb 4 4 1 6 4 2 262;
bb 4 3 1 6 3 2 263;
bb 4 1 1 4 3 2 263;
mbi ;; 1 2; x 58.1737
mbi ;; 1 2; y -85.2590
mbi ;; 1 2; z -223.965
mbi ;; 1 2; z -25.0589
mbi ;; 1 2; z 1.92605
mbi ;; 1 2; x 15.5714
bb 1 3 2 6 4 2 170;
bb 3 1 2 4 3 2 171;
bb 3 4 2 4 6 2 172;
sfi -1; 3 4; 1 2;sd 100
sfi -6; 3 4; 1 2;sd 15
sfi 3 4; -1; 1 2;sd 102
sfi 3 4; -6; 1 2;sd 101
sfi -6; -4; 1 2;sd 101
mbi -4; -6; 1 2; x -2.46822
sfi -4; -6; 1 2;sd 101
sfi -4; -1; 1 2;sd 102
sfi -6; -3; 1 2;sd 102
sfi -1; -4; 1 2;sd 101
sfi -4; -6; 1 2;sd 101
sfi -6; -4; 1 2;sd 101
sfi -1; -4; 1 2;sd 101
sfi -3; -6; 1 2;sd 101
sfi -3; -1; 1 2;sd 100
sfi -4; -6; 1 2;sd 15
unifm 1 3 1 6 4 2 & 3 4 1 4 6 2 & 3 1 1 4 3 2 15 0 1 ;
relax 1 3 1 6 4 1 & 3 1 1 4 3 1 & 3 4 1 4 6 1 15 0 1 ;
pb 3 4 1 3 4 1 xyz 81.0425 -71.3181 -245.176
pb 4 3 1 4 3 1 xyz 88.6417 -77.6412 -247.198
pb 3 3 1 3 3 1 xyz 81.6954 -77.7713 -246.989
pb 4 4 1 4 4 1 xyz 89.0856 -71.2674 -245.438
mt 1 3 1 6 4 2 5
mt 3 1 1 4 6 2 5
sd 34 plan 85.54 -77.93 -252.355 0 0 1 ;
sfi 1 6; 3 4; -1;sd 34
sfi 3 4; 1 6; -1;sd 34
merge
block 1 2 11 17 26 27;1 2 11 17 26 27;1 6;1 2 11 17 26 27;1
2 11 17 26 27;1 6;
dei 1 3 0 4 6; 1 3 0 4 6; 1 2;
mbi -4; 1 2; 1 2; xyz 5.36279 2.42140 0.128407
mbi 5 6; -3; 1 2; xyz -2.08055 -5.85616 -0.149300
mbi 5 6; -4; 1 2; xyz -2.15477 6.91373 0.107980
mbi -4; 5 6; 1 2; xyz 4.88533 -1.04878 0.511231e-01
mbi -3; 1 2; 1 2; xyz -5.04912 2.12257 -0.318219e-01
mbi 1 2; -3; 1 2; xyz 3.83075 -5.54168 -0.554005e-01
mbi -3; 5 6; 1 2; xyz -6.53432 -2.23848 -0.142054
mbi 1 2; -4; 1 2; xyz 1.59348 5.88255 0.142621
bb 1 3 1 3 3 2 301;
bb 3 1 1 3 3 2 301;
bb 4 1 1 4 3 2 302;
bb 4 3 1 6 3 2 302;
bb 4 4 1 6 4 2 303;
bb 4 4 1 4 6 2 303;
bb 3 4 1 3 6 2 304;
bb 1 4 1 3 4 2 304;
mbi ;; 1 2; z 172.824
mbi ;; 1 2; x 65.5262
mbi ;; 1 2; y -86.5695
mseq i 0 3 2 3 0
mseq j 0 3 2 3 0
bb 3 2 1 4 5 1 294;
bb 4 3 1 5 4 1 295;
bb 2 3 1 3 4 1 296;
bb 3 1 1 4 2 1 297;
bb 5 3 1 6 4 1 298;
bb 3 5 1 4 6 1 299;
curd 33 lp3
 66.149332 -43.420907 162.60343
 66.465872 -43.298617 162.65979
 67.0099 -43.087807 162.75483
 67.554298 -42.8751 162.84486
 68.099302 -42.659297 162.92673
 68.645144 -42.439196 162.99727
 68.963298 -42.308647 163.03186
 69.258746 -42.185844 163.05914
 69.55463 -42.061925 163.08197
 70.064288 -41.848393 163.1117
 70.575897 -41.637098 163.13078
 70.832564 -41.533383 163.13681
 71.089877 -41.431539 163.14076
 71.347888 -41.332002 163.14283
 71.606649 -41.23521 163.14322
 71.866214 -41.1416 163.14212
 72.126634 -41.051609 163.13972
 72.387962 -40.965674 163.13622
 72.650251 -40.884232 163.13183
 72.913554 -40.80772 163.12672
 73.177922 -40.736575 163.12111
 73.443409 -40.671235 163.11518
 73.576588 -40.640878 163.11216
```

73.710067 -40.612135 163.10913
73.865819 -40.580787 163.10564
74.021996 -40.551786 163.10221
74.178608 -40.52522 163.09888
74.335665 -40.501174 163.09569
74.483823 -40.480916 163.09285
74.632358 -40.462945 163.09016
74.781243 -40.447241 163.08762
74.93045 -40.433783 163.08522
75.058874 -40.424 163.08325
75.187499 -40.415848 163.08139
75.316308 -40.409315 163.07961
75.445284 -40.404387 163.07791
75.57441 -40.401051 163.07629
75.703668 -40.399296 163.07475
75.833042 -40.399108 163.07327
75.962514 -40.400475 163.07186
76.092068 -40.403384 163.07051
76.221685 -40.407822 163.06922
76.481045 -40.421235 163.06678
76.740456 -40.440614 163.06452
76.999781 -40.465856 163.06239
77.258885 -40.496859 163.06035
77.517629 -40.533524 163.05838
77.775877 -40.575747 163.05643
78.033492 -40.623428 163.05447
78.290338 -40.676464 163.05246
78.546277 -40.734755 163.05037
78.801173 -40.798199 163.04816
79.054889 -40.866693 163.0458
79.201951 -40.908842 163.04433
79.34854 -40.952647 163.0428
79.494629 -40.998088 163.04118
79.640191 -41.045146 163.03948
79.801483 -41.09938 163.03748
79.962055 -41.155588 163.0354
80.12187 -41.21377 163.03324
80.280893 -41.273924 163.03106
80.552185 -41.381887 163.02728
80.820858 -41.495663 163.02361
81.086733 -41.615247 163.02016
81.349631 -41.740631 163.01708
81.609374 -41.87181 163.0145
81.865783 -42.008778 163.01254
82.11868 -42.151529 163.01135
82.367886 -42.300056 163.01105
82.613221 -42.454353 163.01177
82.854509 -42.614414 163.01365
83.091569 -42.780232 163.01682
83.324223 -42.951802 163.02142
83.552293 -43.129118 163.02757
83.775599 -43.312173 163.03541
83.993964 -43.500961 163.04507
84.207208 -43.695475 163.05668
84.328886 -43.811315 163.06439
84.448733 -43.92909 163.07283
84.566715 -44.048801 163.08203
84.682797 -44.170446 163.09202
84.816433 -44.315522 163.10471
84.947349 -44.463175 163.11828
85.057604 -44.592023 163.13045
85.16577 -44.722663 163.14292
85.27181 -44.855044 163.15555
85.375685 -44.989114 163.16817
85.477358 -45.124823 163.18064
85.576791 -45.26212 163.1928
85.673948 -45.400953 163.2045
85.76879 -45.541273 163.21557
85.86128 -45.683027 163.22588
85.951381 -45.826166 163.23525
86.039054 -45.970637 163.24354
86.124262 -46.11639 163.2506
86.206968 -46.263375 163.25626
86.287134 -46.411539 163.26038
86.364723 -46.560833 163.26279
86.439696 -46.711205 163.26335
86.523621 -46.887525 163.26146
86.603892 -47.065156 163.2566
86.66673 -47.211181 163.2503
86.727165 -47.358002 163.24198
86.785271 -47.505595 163.23175
86.841122 -47.653936 163.21973
86.932037 -47.910495 163.19526
87.01689 -48.169061 163.16647
87.096058 -48.429509 163.13396
87.169916 -48.691714 163.09833
87.238841 -48.955549 163.06019
87.303209 -49.220889 163.02015
87.363396 -49.487609 162.97879
87.419778 -49.755582 162.93673
87.472732 -50.024684 162.89457
87.522633 -50.294789 162.85291
87.569857 -50.565771 162.81236
87.614782 -50.837504 162.77351
87.699235 -51.382723 162.70334
87.739517 -51.655957 162.67323
87.779002 -51.929441 162.64724
87.824461 -52.247917 162.62297
87.869944 -52.566362 162.60604
87.919436 -52.908297 162.59677
87.969867 -53.249911 162.59614
88.014117 -53.543098 162.60178
88.059371 -53.83597 162.6125
88.105771 -54.128488 162.62771
88.153462 -54.420618 162.6468
88.25329 -55.003564 162.69426
88.305712 -55.294307 162.72143
88.359999 -55.584515 162.7501
88.416292 -55.874152 162.77967
88.474737 -56.163181 162.80955
88.535474 -56.451565 162.83913
88.598649 -56.739268 162.86782
88.664405 -57.026254 162.89503
88.732884 -57.312486 162.92015
88.80423 -57.597928 162.94259
88.878586 -57.882543 162.96175
88.969117 -58.212739 162.97913
89.064147 -58.541708 162.99031
89.148479 -58.82008 162.99442
89.235948 -59.097603 162.99385
89.313395 -59.335408 162.98999
89.392787 -59.57269 162.98333
89.556722 -60.045881 162.96279
89.726383 -60.517563 162.93464
89.900402 -60.988123 162.90126
90.256031 -61.927428 162.8284
90.434904 -62.396948 162.7937
90.612656 -62.866896 162.76335
90.816324 -63.414959 162.73668
90.962506 -63.81802 162.72475
91.105879 -64.221955 162.71912
91.22694 -64.569648 162.71882
91.34616 -64.91792 162.72227
91.579505 -65.616082 162.73881
91.806773 -66.316194 162.76543
92.028821 -67.018013 162.79884
92.246507 -67.721293 162.83577
92.46069 -68.425789 162.8729
92.672227 -69.131256 162.90694
92.881976 -69.837449 162.93461

93.003564 -70.248683 162.94648
93.125007 -70.660032 162.95442
93.267394 -71.142878 162.95826
93.50996 -71.973184 162.95417
93.629264 -72.38885 162.94889
93.746617 -72.804989 162.94261
93.861542 -73.221697 162.93623
93.973567 -73.639071 162.93061
94.082217 -74.05721 162.92664
94.187017 -74.476208 162.9252
94.303524 -74.965127 162.92787
94.371226 -75.263059 162.93222
94.436632 -75.561498 162.93842
94.544073 -76.075385 162.9523
94.645901 -76.590527 162.96862
94.742854 -77.106771 162.98549
94.835668 -77.623966 163.00102
94.925083 -78.141959 163.01331
95.011836 -78.660599 163.02047
95.096663 -79.179734 163.02059
95.180304 -79.699211 163.01179
95.228728 -80.001638 163.00181
95.277145 -80.3041 162.98779
95.3583 -80.810783 162.95508
95.427324 -81.246092 162.91963
95.494817 -81.681404 162.87962
95.55994 -82.116716 162.83717
95.621852 -82.552024 162.79439
95.679714 -82.987326 162.7534
95.732684 -83.422619 162.71633
95.779924 -83.857899 162.68527
95.820593 -84.293163 162.66236
95.840904 -84.546474 162.65361
95.858539 -84.799777 162.64875
95.873936 -85.063616 162.64814
95.886376 -85.327491 162.65182
95.894795 -85.554256 162.65813
95.901202 -85.78111 162.6671
95.908296 -86.235197 162.69205
95.908288 -86.68998 162.72476
95.901813 -87.145687 162.76333
95.889501 -87.602545 162.80584
95.871985 -88.060782 162.85039
95.849896 -88.520626 162.89507
95.823869 -88.982305 162.93798
95.789451 -89.522302 162.98314
95.742711 -90.170401 163.02737
95.719773 -90.449341 163.04318
95.694504 -90.728223 163.0572
95.666476 -91.006778 163.06955
95.635264 -91.284739 163.0803
95.600443 -91.561841 163.08957
95.561586 -91.837816 163.09745
95.518269 -92.112396 163.10404
95.470066 -92.385316 163.10943
95.416551 -92.656307 163.11373
95.357299 -92.925104 163.11702
95.291883 -93.191439 163.11942
95.219879 -93.455046 163.121
95.140861 -93.715657 163.12188
95.098588 -93.844755 163.12209
95.054402 -93.973005 163.12216
95.00825 -94.100372 163.12209
94.960078 -94.226823 163.12191
94.909833 -94.352326 163.12163
94.857463 -94.476846 163.12126
94.793756 -94.620502 163.12072
94.727013 -94.76273 163.1201
94.65715 -94.903476 163.11941
94.584083 -95.042688 163.11867
94.518594 -95.161224 163.11801
94.450724 -95.278582 163.11732
94.380527 -95.394759 163.11663
94.308059 -95.509753 163.11593
94.17839 -95.70457 163.11472
94.042449 -95.895872 163.11353
93.90051 -96.083645 163.11238
93.752849 -96.267876 163.1113
93.599741 -96.44855 163.11032
93.441461 -96.625654 163.10945
93.278285 -96.799173 163.10873
93.110487 -96.969096 163.10818
92.938343 -97.135406 163.10782
92.762129 -97.298091 163.10768
92.582119 -97.457138 163.1078
92.398589 -97.612531 163.10818
92.211814 -97.764258 163.10886
92.022069 -97.912305 163.10986
91.82963 -98.056658 163.1112
91.634771 -98.197303 163.11293
91.405279 -98.356322 163.11543
91.173317 -98.510278 163.11852
90.951106 -98.651798 163.122
90.727118 -98.788917 163.12596
90.53331 -98.903346 163.12967
90.33827 -99.014781 163.13362
90.142036 -99.12334 163.13774
89.944644 -99.229139 163.14198
89.746133 -99.332296 163.14629
89.546538 -99.432929 163.15062
89.345898 -99.531154 163.1549
89.14425 -99.62709 163.15909
88.94163 -99.720853 163.16314
88.738076 -99.812562 163.16697
88.328314 -99.990283 163.17382
87.915261 -100.16119 163.17921
87.499215 -100.32623 163.18269
87.011573 -100.51218 163.18377
86.572314 -100.6737 163.18169
86.192895 -100.80784 163.17795
85.811584 -100.93655 163.17286
85.428377 -101.05875 163.16684
85.236062 -101.11706 163.16363
85.043271 -101.17334 163.16034
84.850004 -101.22745 163.15703
84.65626 -101.27925 163.15376
84.462039 -101.32861 163.15059
84.267341 -101.37539 163.14755
84.072165 -101.41946 163.14472
83.876509 -101.46067 163.14213
83.680375 -101.4989 163.13985
83.483761 -101.53401 163.13793
83.254302 -101.57076 163.13621
83.024191 -101.60289 163.13514
82.752691 -101.63456 163.13479
82.480391 -101.65976 163.13542
82.245892 -101.6764 163.13674
82.010945 -101.68858 163.13876
81.775616 -101.69642 163.14147
81.539969 -101.70008 163.14485
81.304071 -101.69969 163.1489
81.067987 -101.6954 163.15361
80.831782 -101.68734 163.15896
80.595522 -101.67567 163.16493
80.359272 -101.66051 163.17153
80.123099 -101.64203 163.17873
79.887067 -101.62035 163.18652
79.651242 -101.59561 163.1949
79.415689 -101.56797 163.20384
79.180475 -101.53756 163.21334

78.945664 -101.50453 163.22339
78.711322 -101.46901 163.23396
78.439231 -101.42473 163.24693
78.167968 -101.3775 163.26059
77.743602 -101.29776 163.28314
77.380723 -101.22398 163.30267
77.019303 -101.14541 163.32131
76.659231 -101.06214 163.3381
76.300398 -100.97425 163.35205
75.942694 -100.88181 163.36221
75.58601 -100.78492 163.36759
75.230234 -100.68365 163.36723
74.875258 -100.57808 163.36016
74.462935 -100.44989 163.34218
74.010109 -100.30203 163.30936
73.622953 -100.16847 163.27192
73.238531 -100.02789 163.22798
73.047643 -99.954679 163.20419
72.857794 -99.879363 163.1795
72.669103 -99.801827 163.15415
72.481689 -99.721953 163.12839
72.295671 -99.639624 163.10246
72.111167 -99.554724 163.07661
71.928296 -99.467135 163.05107
71.747177 -99.376742 163.02609
71.567928 -99.283427 163.00191
71.390667 -99.187074 162.97877
71.215514 -99.087566 162.95691
71.042587 -98.984786 162.93658
70.844265 -98.860877 162.91517
70.649307 -98.732193 162.89653
70.502443 -98.630385 162.88434
70.357581 -98.525781 162.87392
70.214644 -98.418488 162.86521
70.073552 -98.308616 162.85812
69.835207 -98.114118 162.84952
69.601684 -97.912876 162.8451
69.372587 -97.705439 162.84449
69.147521 -97.49236 162.8473
68.926088 -97.27419 162.85314
68.707892 -97.051478 162.86164
68.492536 -96.824776 162.87241
68.279624 -96.594635 162.88505
68.06876 -96.361606 162.8992
67.859547 -96.126239 162.91446
67.444488 -95.650698 162.94678
66.61674 -94.695808 163.00789
66.373618 -94.420941 163.02203
66.128348 -94.149001 163.03342
65.841192 -93.838453 163.04263
65.592456 -93.574694 163.04732
65.342664 -93.312847 163.04936
64.843026 -92.791472 163.04671
64.594742 -92.530239 163.04262
64.34852 -92.267505 163.03711
64.105141 -92.002417 163.03048
63.865385 -91.734121 163.02303
63.727826 -91.576162 163.01844
63.591912 -91.416659 163.01373
63.458633 -91.256608 163.00901
63.326887 -91.095094 163.0043
63.103397 -90.814812 162.99644
62.882494 -90.532026 162.98917
62.443553 -89.963524 162.97776
62.223065 -89.680101 162.97432
62.000265 -89.398758 162.97283
61.773928 -89.120641 162.97364
61.542829 -88.846897 162.9771
61.405655 -88.690048 162.98047
61.266212 -88.535294 162.98492
61.145319 -88.405036 162.9896
61.022774 -88.276307 162.99504
60.808862 -88.058227 163.00597
60.591478 -87.843375 163.01856
60.371515 -87.63094 163.03246
60.14986 -87.420108 163.0473
59.705039 -87.000002 163.0783
59.483651 -86.789101 163.09374
59.264132 -86.576552 163.10864
59.012151 -86.325993 163.12482
58.839259 -86.148707 163.13511
58.668607 -85.969387 163.14453
58.379868 -85.657127 163.15876
58.095665 -85.340551 163.17055
57.814684 -85.020726 163.18
57.535609 -84.698721 163.18715
56.977921 -84.052446 163.19492
56.696679 -83.730314 163.19567
56.412086 -83.410278 163.19443
56.244392 -83.225408 163.19283
56.074858 -83.04182 163.19059
55.760532 -82.709982 163.1849
55.214208 -82.144632 163.1703
54.942701 -81.861147 163.16071
54.67525 -81.575137 163.1496
54.543737 -81.43072 163.14347
54.414069 -81.285114 163.13697
54.286522 -81.138132 163.13008
54.161374 -80.989588 163.12281
54.0389 -80.839297 163.11517
53.919378 -80.687071 163.10714
53.803084 -80.532726 163.09873
53.690296 -80.376074 163.08994
53.563795 -80.190584 163.07923
53.442855 -80.001424 163.06801
53.383231 -79.903097 163.06207
53.325157 -79.803762 163.05601
53.268615 -79.703447 163.04986
53.213583 -79.602184 163.04362
53.122493 -79.426059 163.03278
53.035701 -79.247372 163.02185
52.953103 -79.066275 163.01094
52.874597 -78.882917 163.00012
52.80008 -78.697452 162.98951
52.729449 -78.510029 162.97919
52.662602 -78.320801 162.96926
52.599435 -78.129919 162.9598
52.539847 -77.937534 162.95093
52.483734 -77.743797 162.94272
52.430993 -77.54886 162.93528
52.381523 -77.352874 162.9287
52.33522 -77.155991 162.92308
52.291981 -76.958361 162.9185
52.251704 -76.760136 162.91506
52.214286 -76.561468 162.91286
52.174197 -76.329865 162.91198
52.13768 -76.098104 162.91305
52.097048 -75.810134 162.91723
52.061473 -75.522271 162.92438
52.034788 -75.275034 162.93269
52.011545 -75.027853 162.9428
51.991611 -74.780715 162.95454
51.974853 -74.533609 162.96775
51.961136 -74.286526 162.98223
51.950328 -74.039452 162.99783
51.942293 -73.792377 163.01435
51.936899 -73.545289 163.03163
51.934012 -73.298178 163.04948
51.933497 -73.051031 163.06774
51.935222 -72.803838 163.08623

```
51.939052 -72.556588 163.10477
51.944854 -72.309269 163.12318
51.952494 -72.06187 163.14129
51.961839 -71.814379 163.15893
51.972753 -71.566785 163.17592
51.987258 -71.278448 163.19463
52.003499 -70.989938 163.21195
52.028968 -70.586532 163.23342
52.054007 -70.239961 163.24932
52.082653 -69.893655 163.26293
52.115556 -69.547866 163.2743
52.153367 -69.202841 163.28349
52.196737 -68.858832 163.29056
52.22071 -68.687285 163.29332
52.246317 -68.516087 163.29557
52.273638 -68.345266 163.29731
52.302757 -68.174855 163.29856
52.333753 -68.004885 163.29932
52.366708 -67.835388 163.2996
52.407643 -67.638732 163.29932
52.451471 -67.442807 163.29842
52.517683 -67.17021 163.29613
52.589287 -66.898996 163.29272
52.65472 -66.666987 163.28896
52.723431 -66.435807 163.2845
52.795095 -66.205364 163.27939
52.869387 -65.975571 163.27369
52.945984 -65.746337 163.26745
53.02456 -65.517573 163.26075
53.186354 -65.061099 163.24613
53.519423 -64.149858 163.2137
53.685507 -63.693662 163.1968
53.847829 -63.236129 163.18006
53.939539 -62.968951 163.17057
54.028584 -62.700936 163.16137
54.149462 -62.320664 163.14893
54.249773 -61.992952 163.13847
54.348157 -61.664787 163.12788
54.544241 -61.008918 163.10504
54.644487 -60.682126 163.09213
54.7479 -60.356704 163.07781
54.855755 -60.033107 163.06175
54.911745 -59.872136 163.05297
54.969324 -59.711792 163.04363
55.038555 -59.526021 163.03201
55.110404 -59.341267 163.01951
55.188354 -59.149697 163.00551
55.269328 -58.959326 162.99062
55.341236 -58.796725 162.9772
55.415244 -58.634999 162.9633
55.491288 -58.474145 162.94899
55.569308 -58.314157 162.93434
55.649242 -58.155032 162.91944
55.731027 -57.996766 162.90437
55.814603 -57.839355 162.8892
55.899907 -57.682793 162.87401
55.986878 -57.527078 162.85888
56.075454 -57.372204 162.84389
56.257173 -57.064967 162.81464
56.444571 -56.761048 162.78689
56.637154 -56.460414 162.76128
56.867189 -56.114575 162.73497
57.06619 -55.825215 162.71611
57.239748 -55.578628 162.70194
57.415178 -55.333477 162.68904
57.769666 -54.845879 162.66482
58.125676 -54.359222 162.63895
58.479232 -53.870304 162.6069
58.682293 -53.583451 162.58362
58.862347 -53.323975 162.5593
59.473356 -52.426618 162.47189
59.6267 -52.203165 162.45474
59.781241 -51.980945 162.44167
59.93746 -51.760398 162.43377
60.095835 -51.541964 162.43213
60.283536 -51.290956 162.43958
60.403567 -51.135297 162.44999
60.525182 -50.981137 162.4646
60.737483 -50.719359 162.49827
60.953455 -50.460904 162.54092
61.172464 -50.205072 162.59039
61.393874 -49.951164 162.64454
61.841359 -49.446322 162.75825
62.066163 -49.193989 162.81351
62.290828 -48.940783 162.86484
62.551315 -48.644026 162.91676
62.794728 -48.361873 162.95562
63.002002 -48.11713 162.98115
63.207222 -47.87018 162.99976
63.410058 -47.620981 163.01179
63.61018 -47.369493 163.01754
63.807259 -47.115672 163.01735
64.000964 -46.859478 163.01153
64.190965 -46.600868 163.00041
64.376934 -46.3398 162.98432
64.483179 -46.186714 162.97279
64.587881 -46.032773 162.95975
64.777488 -45.745728 162.93187
64.936461 -45.497015 162.90439
65.092223 -45.246579 162.87401
65.245168 -44.994629 162.8411
65.395688 -44.741379 162.80599
65.544176 -44.487037 162.76906
65.691027 -44.231817 162.73065
65.981389 -43.719583 162.65083
66.149332 -43.420907 162.60343 ;
;
mbi 3 4; -6; -2; xyz 4.58165 17.0873 5.14131
mbi -6; 3 4; -2; xyz 3.96509 0 190302 3.60824
mbi 3 4; -1; -2; xyz 5.34213 -14.0506 4.23681
mbi -1; 3 4; -2; xyz -1.70744 -3.97144 9.32747
mbi -1; 3 4; -2; xyz -3.36506 6.60488 0.165933
curs 1 3 2 1 4 2 33
curs 3 6 2 4 6 2 33
curs 3 1 2 4 1 2 33
curs 6 3 2 6 4 2 33
pb 1 4 2 1 4 2 xyz 61.0300 -50.1941 182.639
sd 78 xyplan mz 183 ; ;
y
sfi ;; -2;sd 78
mt 1 3 1 6 4 2 16
mt 3 1 1 4 6 2 16
bb 1 3 1 2 4 1 300;
nset 1 3 2 6 4 2 = proxend
nset 3 4 2 4 6 2 = proxend
nset 3 1 2 4 3 2 = proxend
relax 1 3 2 6 4 2 & 3 1 2 4 3 2 & 3 4 2 4 6 2 15 0 1 ;
pb 3 4 2 3 4 2 xyz 70.0986 -62.2703 183.000
pb 3 3 2 3 3 2 xyz 69.2948 -81.3009 183.000
pb 4 3 2 4 3 2 xyz 85.4269 -81.7280 183.000
pb 4 4 2 4 4 2 xyz 83.3665 -62.0648 183.000
unifm 1 3 1 6 4 2 & 3 1 1 4 3 2 & 3 4 1 4 6 2 10 0 1 ;
pb 3 5 2 3 5 2 xyz 64.1612 -54.0184 183.000
pb 4 2 2 4 2 2 xyz 88.9826 -90.4329 183.000
pb 3 2 2 3 2 2 xyz 61.9880 -84.1224 183.000
relax 1 3 2 6 4 2 & 3 1 2 4 3 2 & 3 4 2 4 6 2 10 0 1 ;
merge
block 1 3 5;1 3 5;1 5;1 3 5;1 3 5;1 5;
insprt 1 1 1 2
insprt 1 3 1 2
```

```
dei 1 2 0 3 4; 1 2 0 3 4; 1 2;
mbi -1; 2 3; 1 2; x -1.83967
mbi 2 3; -1, 1 2; y -1.57785
mbi -1; -3; 1 2; xy 0.117073 1.18602
mbi -2; -4; 1 2; xy -1.09807 -0.407970
mbi -3; -4; 1 2; xy 1.46803 -0.437471
mbi -4; -3; 1 2; xy 0.202208 1.13052
mbi -4; -2; 1 2; xy 0.202896 -0.816408
mbi -3; -1; 1 2; xy 1.03525 0.262996
mbi -2; -1; 1 2; xy -1.09472 0.488499
mbi -1; -2; 1 2; xy 0.185477 -1.05451
mbi ;; 1 2; z -266.345
mbi ;; 1 2; x 85.8118
mbi ;; 1 2; y -79.4479
insprt 1 6 1 2
sd 89 cy 8.55400e+01 -7.79300e+01 -1.92050e+02 0 0 1
11.9 ;
sd 91 sp 85.54 -77.93 -305 50 ;
dei 2 3; 3 4; 2 3;
dei 3 4; 2 3; 2 3;
dei 2 3; 1 2; 2 3;
dei 1 2; 2 3; 2 3;
pb 2 4 2 2 4 2 xyz 84.8885 -75.3175 -262.473
pb 4 3 2 4 3 2 xyz 89.8208 -75.3140 -262.227
pb 1 2 2 1 2 2 xyz 85.7996 -78.9023 -262.328
mbi 2 3; 2 3; -3; z 1.26461
pb 3 1 2 3 1 2 xyz 91.0147 -79.2643 -262.765
mbi 2 3; 2 3; -3; z 10.5400
mbi 2 3; 2 3; -3; z 10.6326
mbi ;; -2; z 9.19598
mbi ;; -1; z 1.34445
mbi 2 3; 2 3; -1; z 4.35640
mbi -1; 2 3; -1; xyz -9.89750 -0.107699 -1.71140
mseq i 2 2 2
mseq j 2 2 2
mseq k 2 2
pb 2 2 1 2 2 1 xyz 82.5055 -81.3689 -261.528
pb 2 3 1 2 3 1 xyz 84.1224 -74.9245 -262.167
pb 3 3 1 3 3 1 xyz 89.1355 -74.7917 -260.080
pb 3 2 1 3 2 1 xyz 88.3255 -80.1259 -259.315
pb 2 2 1 2 2 1 xyz 84.0962 -81.6351 -260.291
pb 2 2 1 2 2 1 xyz 83.9402 -81.5881 -262.702
pb 3 2 1 3 2 1 xyz 87.3141 -81.0726 -261.769
pb 2 1 1 2 1 1 xyz 74.2693 -80.0391 -263.091
sd 94 xyplan mz -265 ; ;
sfi 2 3; 1 4; -1;sd 94
sfi 1 4; 2 3; -1;sd 94
sfi 2 3; 2 3; -3;sd 91
sfi 2 3; -1; 1 2;sd 91
sfi -1; 2 3; 1 2;sd 91
sfi 2 3; -4; 1 2;sd 91
sfi -4; 2 3; 1 2;sd 91
sfi 2 3; 1 4; -1;sd 94
sfi 1 4; 2 3; -1;sd 94
mbi 2 3; 2 3; -2; z 1.45382
bb 1 2 1 2 2 2 501;
bb 2 1 1 2 2 2 501;
bb 3 1 1 3 2 2 502;
bb 3 2 1 4 2 2 502;
bb 3 3 1 4 3 2 503;
bb 3 3 1 3 4 2 503;
bb 2 3 1 2 4 2 504;
bb 1 3 1 2 3 2 504;
pb 1 2 1 1 2 1 xyz 86.1086 -102.777 -265.918
pb 2 4 1 2 4 1 xyz 74.2116 -52.1139 -264.588
pb 4 3 1 4 3 1 xyz 107.023 -59.3780 -265.264
pb 3 1 1 3 1 1 xyz 115.444 -76.9150 -265.542
bb 2 2 2 3 2 3 510;
bb 2 1 2 3 2 2 511;
bb 2 2 2 2 3 3 512;
bb 1 2 2 2 3 2 512;
bb 2 3 2 3 3 3 513;
bb 2 3 2 3 4 2 513;
bb 3 2 2 3 3 3 514;
bb 3 2 2 4 3 2 514;
pb 1 2 2 1 2 2 xyz 79.8695 -89.6584 -260.394
pb 1 3 2 1 3 2 xyz 78.3644 -76.2268 -255.038
pb 3 1 2 3 1 2 xyz 94.9791 -83.9245 -252.083
pb 3 1 2 3 1 2 xyz 93.9065 -86.6346 -253.669
pb 3 1 1 3 1 1 xyz 115.269 -82.5365 -260.715
pb 2 2 1 2 2 1 xyz 82.9679 -84.3144 -262.962
pb 2 3 1 2 3 1 xyz 81.2854 -71.4932 -260.540
pb 3 3 1 3 3 1 xyz 91.6559 -70.2977 -266.301
pb 3 2 1 3 2 1 xyz 92.8703 -84.0704 -268.502
pb 2 1 1 2 1 1 xyz 79.2030 -104.411 -259.650
pb 3 1 1 3 1 1 xyz 111.125 -94.2568 -263.480
pb 1 3 1 1 3 1 xyz 67.9017 -58.0219 -261.930
pb 4 3 1 4 3 1 xyz 104.506 -53.5723 -261.823
pb 2 1 1 2 1 1 xyz 72.8683 -101.456 -260.345
pb 1 3 2 1 3 2 xyz 78.2736 -71.5642 -254.142
pb 4 3 2 4 3 2 xyz 89.7710 -71.6792 -252.904
pb 4 3 2 4 3 2 xyz 90.8561 -70.9263 -253.650
mbi 2 3; 2 3; -2; xyz -0.755755 -0.183527e-01 1.50720
sfi -1; 2 3; -1;sd 89
sfi 2 3; -4; -1;sd 89
sfi -4; 2 3; -1;sd 89
sfi 2 3; -1; -1;sd 89
pb 2 1 2 2 1 2 xyz 85.5886 -85.1915 -256.425
pb 1 3 2 1 3 2 xyz 79.8891 -73.0636 -253.227
pb 4 3 2 4 3 2 xyz 88.2522 -74.5751 -254.632
pb 3 1 2 3 1 2 xyz 89.3081 -83.5980 -254.863
decmd 149
decmd 150
decmd 151
decmd 152
pb 3 2 1 3 2 1 xyz 92.3093 -82.4453 -265.099
pb 2 2 1 2 2 1 xyz 83.4950 -82.2961 -263.834
pb 2 3 1 2 3 1 xyz 82.2486 -72.7835 -264.441
pb 3 3 1 3 3 1 xyz 91.5217 -71.4903 -265.511
insprt 1 5 1 3
dei 1 2 0 3 4; 1 2 0 3 4; 1 2;
mbi ;; -1; z -8.54638
sfi -1; 2 3; 1 2;sd 89
decmd 105
decmd 106
sfi -1; 2 3; -2;sd 89
sfi 2 3; -4; -2;sd 89
sfi -4; 2 3; -2;sd 89
sfi 2 3; -1; -2;sd 89
mbi 2 3; -1; -2; z -1.82618
sfi 2 3; -1; -1;sd 89
sfi -4; 2 3; -1;sd 89
sfi 2 3; -4; -1;sd 89
sfi -1; 2 3; -1;sd 89
sfi 2 3; 1 4; -1;sd 94
sfi 1 4; 2 3; -1;sd 94
mbi 2 3; 2 3; -2; z 3.08365
mbi 2 3; 2 3; -2; z 0.733864
mbi 2 3; 2 3; -3; z 3.12931
unifm 2 1 1 3 4 3 & 3 2 1 4 3 3 & 1 2 1 2 3 3 & 2 2 3 3 3 4 10
0 1 ;
unifm 2 2 3 3 3 4 & 1 2 2 4 3 3 & 2 1 2 3 2 3 & 2 3 2 3 4 3 10
0 1 ;
relax 1 2 1 4 3 1 & 2 1 1 3 2 1 & 2 3 1 3 4 1 10 0 1 ;
unifm 2 1 2 3 4 2 & 1 2 2 2 3 2 & 3 2 2 4 3 2 10 0 1 ;
relax 2 1 3 3 4 3 & 3 2 3 4 3 3 & 1 2 3 2 3 3 10 0 1 ;
relax 2 1 2 3 4 2 & 1 2 2 2 3 2 & 3 2 2 4 3 2 10 0 1 ;
relax 2 4 2 3 4 3 & 1 2 2 1 3 3 & 2 1 2 3 1 3 & 4 2 2 4 3 3 &
2 2 4 3 3 4 10 0 1 ;
pb 2 2 4 2 2 4 xyz 83.6458 -83.1066 -254.255
```

```
pb 4 2 3 4 2 3 xyz 88.3337 -82.0146 -254.812
mbi 2 3; 2 3; -3; z -1.25741
mate 6
```

```
nset 1 1 1 4 4 1 = projectile
merge
lsdyna keyword
```

APPENDIX L – LS-DYNA® Input Deck

This appendix includes the program file for the entire LS-DYNA® model that was detailed in Chapter 6. It calls a separate file which includes the node and element data that were previously output as the last step of the TrueGrid® file (from Appendix K).

```
$ This program takes a tibia bone mesh as output from TrueGrid, applies material properties, and creates a simulation of the
$experimental impact using projectile mass and velocity as inputs, and modeling the bracket and foam. The load applied to the tibia
$and strain at specific sets corresponding to strain gauge locations are used for validation purposes.
$ This program was created October 1, 2009 by Cheryl E. Quenneville
$ UNITS: millimeter, millisecond, kilogram, kiloNewton
$
*KEYWORD
$ deck is written in keyword format
$
$
*TITLE
Tibia Smashing Test
$
$
*INCLUDE
repo.k
$ this includes node and element data for the bone, talus, foam, projectile, distal and $proximal brackets as well as sets for the
proximal cut surface of the bone, the proximal $surface of the distal bracket, and the back surface of the projectile (to limit to z travel
$only)
$
$
$$$$$$$$$$$$$$$$$$$$$$$$$$ CONTROL CARDS $$$$$$$$$$$$$$$$$$$$$$$$$$$$$$$$
$
*CONTROL_TERMINATION
$ termination time (in milliseconds)
3.5
$
*CONTROL_TIMESTEP
$#  dtinit    tssfac      isdo     tslimt     dt2ms      lctm      erode     ms1st
 0.196e-4  0.700000
$#  dt2msf   dt2mslc     imscl
    0.000         0         0
$
$
$$$$$$$$$$$$$$$$$$$$$$$$$$$$ DATABASE CARDS $$$$$$$$$$$$$$$$$$$$$$$$$$$$
$
*DATABASE_BINARY_INTFOR
0.01
$ gives contact interface data
$
*DATABASE_EXTENT_BINARY
,,,1,,,,
,,,,1,,
$
*DATABASE_BINARY_D3PLOT
0.01
$ time interval between outputs. Writes output files in binary format for complete output states, plotting info to plot data over the 3D
$geometry of the model.
```

```
$
*DATABASE_NCFORC
0.01,3
$
*DATABASE_HISTORY_NODE
$ first on dist bracket, second on prox bracket, third on projectile, fourth on dist bone
18510,24924, 27396, 1281
$
*DATABASE_HISTORY_NODE_SET
$ Defines node set that outputs - talus
5
$
*DATABASE_NODAL_FORCE_GROUP
$ Defines a nodal force group for output - talus
5
$
*DATABASE_HISTORY_SOLID_SET
$ Defines an output for solid sets (each gauge)
11,12,13,14
$
*DATABASE_NODOUT
0.01
$
*DATABASE_NODFOR
0.01,3
$
*DATABASE_ELOUT
0.01,3
$
*DATABASE_GLSTAT
0.01,3
$
$
$$$$$$$$$$$$$$$$$$$$$$$$$ PART CARDS $$$$$$$$$$$$$$$$$$$$$$$$$$$$$$$$
$ A part is defined for each material region
$
*PART
Cancellous
1,1,1
$
*PART
Cortical
2,2,2
$
*PART
Marrow
3,3,3
$
*PART
Talus
4,4,4
$
*PART
Foam
5,5,5
$
*PART
Projectile
6,6,6
$
*PART
Distal
7,7,7
$
*PART
Proximal
16,16,16
$
$
$$$$$$$$$$$$$$$$$$$$$$$$$$$$ SECTION CARDS $$$$$$$$$$$$$$$$$$$$$$$$$$$$
```

```
$
*SECTION_SOLID
$Cancellous section
1,3
$
*SECTION_SOLID
$Cortical section
2,3
$
*SECTION_SOLID
$ Marrow section
3,1
$
*SECTION_SOLID
$Talus section
4,1
$
*SECTION_SOLID
$Foam section
5,2
$
*SECTION_SOLID
$ Projectile section
6,1
$
*SECTION_SOLID
$ Distal section
7,1
$
*SECTION_SOLID
$ Proximal section
16,1
$
$
$$$$$$$$$$$$$$$$$$$$$$$$$$$$$$ SET CARDS $$$$$$$$$$$$$$$$$$$$$$$$$$$$$$$$
$
$ Sets for strain gauges.
$
*SET_SOLID_TITLE
Gauge 1
11
3317,3325
$
*SET_SOLID_TITLE
Gauge 2
12
3357,3358,5415,5417
$
*SET_SOLID_TITLE
Gauge 3
13
5427,5431
$
*SET_SOLID_TITLE
Gauge 4
14
10694,10695
$
*SET_NODE
4,
16890,16891,16892,16893,16894,16910,16911,16912
16913,16914,16930,16931,16932,16933,16934,16950
16951,16952,16953,16954,16970,16971,16972,16973
16974
$
*SET_NODE_LIST
$#    sid      da1      da2      da3      da4
      5
$#   nid1     nid2     nid3     nid4     nid5     nid6     nid7     nid8
   17957    17978    17999    18020    18041    18062    18083    18461
```

```
    18458   18455   18452   18449   18446   17180   17156   17132
    18440   18437   18434   18431   18428   17183   17159   17135
    18422   18419   18416   18413   18410   17186   17162   17138
    18404   18401   18398   18395   18392   17189   17165   17141
    18386   18383   18380   18377   18374   17192   17168   17144
    18368   18365   18362   18359   18356   17195   17171   17147
    18350   18347   18344   18341   18338   17198   17174   17150
    18443   18080   18059   18038   18017   17996   17975   17954
    18425   18077   18056   18035   18014   17993   17972   17951
    18407   18074   18053   18032   18011   17990   17969   17948
    18389   18071   18050   18029   18008   17987   17966   17945
    18371   18068   18047   18026   18005   17984   17963   17942
    18353   18065   18044   18023   18002   17981   17960   17939
    17201   17624   17627   17630   17633   17636   17639   17642
    17621   17618   17615   17612   17609   17606   17603   17177
    17600   17597   17594   17591   17588   17585   17582   17153
    17579   17576   17573   17570   17567   17564   17561   17129
    17558   17555   17552   17549   17546   17543   17540   17105
    17537   17534   17531   17528   17525   17522   17519   17081
    17516   17513   17510   17507   17504   17501   17498   17057
    16697   16694   16691   16688   16685   16682   16679   16676
    17126   17102   17078   17054   17123   17099   17075   17051
    17120   17096   17072   17048   17117   17093   17069   17045
    17114   17090   17066   17042   17111   17087   17063   17039
    17108   17084   17060   17036   16508   16511   16514   16517
    16652   16655   16658   16661   16664   16667   16670   16673
    16628   16631   16634   16637   16640   16643   16646   16649
    16604   16607   16610   16613   16616   16619   16622   16625
    16601   16598   16595   16592   16589   16586   16583   16580
    16556   16532   16559   16535   16562   16538   16565   16541
    16577   16553   16529   16574   16550   16526   16571   16568
    16547   16544   16523   16520
$
*SET_NODE_LIST
$ set for friction load
6
18533,20997,18526,20990,18463,18470,19534,19527
$
$
$$$$$$$$$$$$$$$$$$$$$$$$$$$$ MATERIAL CARDS $$$$$$$$$$$$$$$$$$$$$$$$$$$$
$
$
*MAT_PIECEWISE_LINEAR_PLASTICITY
$ Cancellous bone: mid, ro, E, PR, sigy, etan
1, 0.000001, 0.5, 0.3, 0.01, 0.025
360.7,4.605


$
*MAT_PIECEWISE_LINEAR_PLASTICITY
$ Cortical bone: mid, ro, E, PR, sigy, etan
2, 0.00000185, 20, 0.3, 0.129, 1
360.7,4.605


$
*MAT_ELASTIC
$ Marrow
3,0.000001,0.02,0.499,,,
$
*MAT_ELASTIC
$ Polyethylene talus
4,0.000001,170,0.35,,,
$
*MAT_ELASTIC
$ Polyurethane foam (52 kg/m3, 2.5 MPa E)
5,0.0004,2.5,0.2,,
$
*MAT_RIGID
$ measure projectile volume as 4017.4 mm3
```

```
$ Projectile density (rho=m/vol = 0.00169 for 6.8kg, 0.000971 for 3.9kg)
6,0.00169,210,0.3,,,,
1,4,7

$
*MAT_RIGID
$ measure distal bracket volume as 44995.5 mm3
$ Distal bracket with density set based on volume (rho = 4.314kg/44995.5mm3)
7,0.0000959,210,0.3,,,,
1,4,7

$
*MAT_RIGID
$ measure proximal bracket volume as 37964 mm3
$ Proximal bracket with density set based on volume (rho = 5.602kg/37964.3mm3)
16,0.0001476,210,0.3,,,,
1,4,7

$
$
$$$$$$$$$$$$$$$$$$$$$$$$$$ CONSTRAINT CARDS $$$$$$$$$$$$$$$$$$$$$$$$$$
$
$
*INITIAL_VELOCITY_RIGID_BODY
$ Initial velocity of 8.58 m/s for non-fx, 11.37 m/s for fx
6,0,0,11.37,0,0,0
$
*LOAD_NODE_SET
$ corners of distal bracket
6,3,1,1
$
*DEFINE_CURVE
1
0,-2
10000,-2
$
$
$$$$$$$$$$$$$$$$$$$$$$$$$$ CONTACT CARDS $$$$$$$$$$$$$$$$$$$$$$$$$$
$
*CONTACT_AUTOMATIC_SURFACE_TO_SURFACE
5,6,3,3,,,1,1
0.2,0.2,
0.8,0.8
1
$
*CONTACT_AUTOMATIC_SURFACE_TO_SURFACE
2,4,3,3,,,1,1
0.02,0.02,

$
*CONTACT_AUTOMATIC_SURFACE_TO_SURFACE
1,4,3,3,,,1,1
0.02,0.02,

$
*CONTACT_AUTOMATIC_SURFACE_TO_SURFACE
6,7,3,3,,,,
0.2,0.2,

$
*CONTACT_INTERIOR
1
$
*SET_PART
1
5
$
$$$$$$$$$$$$$$$$$$$$$$$$$$$$$$$$$$$$$$$$$$$$$$$$$$$$$$$$$$$$$$$$$$$$$$$
$
*END
```

APPENDIX M – Letters of Permission

This appendix includes letters of permission for Figures 1.7, 1.8, and G.1.

Figure 1.7:

Subject: copyright permission ISSUE=201416 PROJ=12
From: "NHTSAHotline@telesishq.com" <NHTSAHotline@Telesishq.com>
Date: Thursday, November 5, 2009 2:11 am

Project: NHTSA Hotline Center
Case: copyright permission
Case Number: 201416

Date: 11/02/2009 **Time:** 10:15:02
Creation Date: 10/31/2009 **Creation Time:** 17:32:10

Description:
Entered on 11/02/2009 at 10:15:02 EST (GMT-0500) by Kiianah Johnson:
Thank you for contacting the U.S. Department of Transportation's Vehicle Safety Hotline Information Center.

The information presented on this Web site and our publications is considered to be public domain and therefore has no copyright. While the information and may be distributed or copied in any format, please do not change the content or its meaning, and attribute the information to the correct source.

We hope that you find this information helpful. However, if you need additional information on our services please feel free to contact us at 1-888-327-4236.

Thank you,

NHTSA.dot.gov Response Team

Disclaimer: "This response is for information purposes only and does not constitute an official communication of the U.S. Department of Transportation. For an official response, please write U.S. Department of Transportation, National Highway Traffic Safety Administration, 1200 New Jersey Ave, SE, West Building, Washington, DC 20590.

APPENDIX N – Specimen Measurements

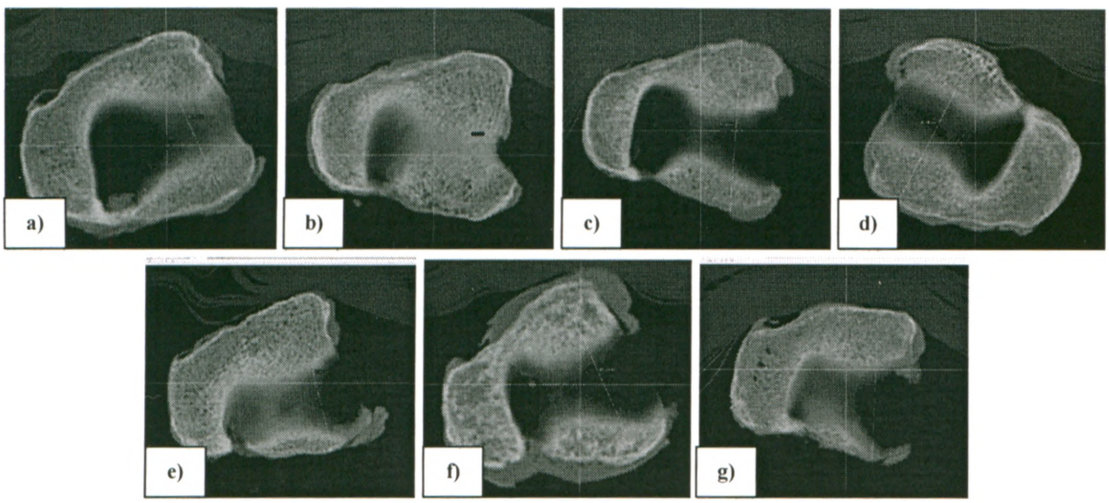

a) 06-06037R	b) 08-07033R	c) 08-07024R	d) 08-07085R	e) 08-08009R	f) 06-08044R	g) 06-10081R
40.16 mm	41.78 mm	41.88 mm	42.05 mm	43.06 mm	41.27 mm	41.63 mm

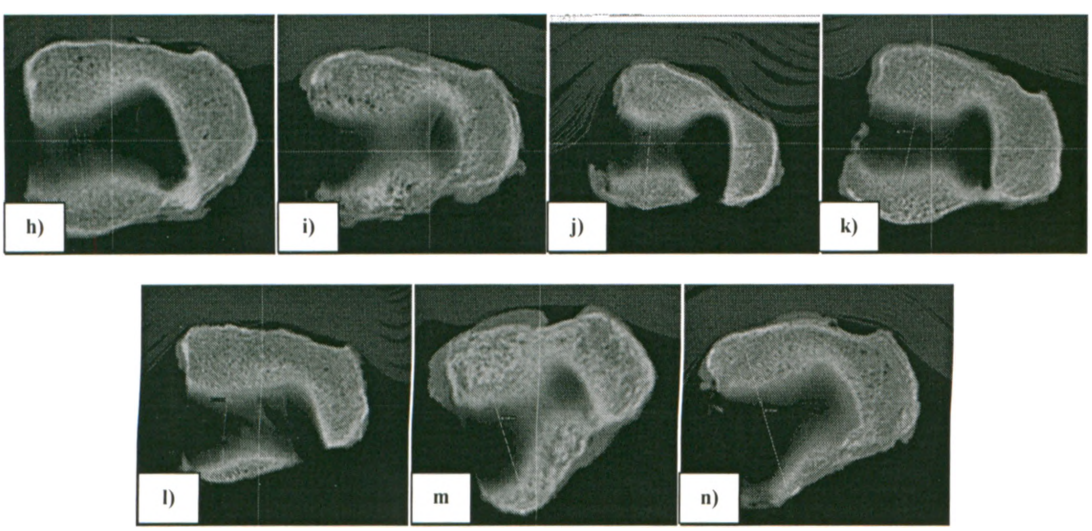

h) 06-06037L	i) 08-07033L	j) 08-07024L	k) 08-07085L	l) 08-08009L	m) 06-08044L	n) 06-10081L
41.40 mm	39.34 mm	41.26 mm	42.09 mm	41.33 mm	40.64 mm	41.98 mm